

# *Synthesis, Characterization and Modifications of Nanocomposite Thin Films*

*Submitted in*

*fulfillment of the requirements for the degree of*

*Doctor of Philosophy*

by

**Shushant Kumar Singh**

**(ID No. 2013RPH9001)**

Under the supervision of

Dr. Rahul Singhal



**DEPARTMENT OF PHYSICS  
MALAVIYA NATIONAL INSTITUTE OF TECHNOLOGY  
JAIPUR  
February 2019**



**©Malaviya National Institute of Technology Jaipur (India)**

**2019**

***All Right Reserved.***



*Dedicated to My Family  
and friends*



## **DECLARATION**

I, **Shushant Kumar Singh**, declare that this thesis titled “**Synthesis, Characterization and Modifications of Nanocomposite Thin Films**” and the work presented in it, are my own. I confirm that:

- This work was done wholly or mainly while in candidature for a research degree at this university.
- Where any part of this thesis has previously been submitted for a degree or any other qualification at this university or any other institution, this has been clearly stated.
- Where I have consulted the published work of others, this is always clearly attributed.
- Where I have quoted from the work of others, the source is always given. With the exception of such quotations, this thesis is entirely my own work.
- I have acknowledged all main sources of help.
- Where the thesis is based on work done by myself, jointly with others, I have made clear exactly what was done by others and what I have contributed myself.

Date:

Shushant Kumar Singh  
(2013RPH9001)





## **CERTIFICATE**

This is to certify that the thesis entitled “**Synthesis, Characterization and Modifications of Nanocomposite Thin Films**” being submitted by **Shushant Kumar Singh (2013RPH9001)** is a bonafide research work carried out under my supervision and guidance in fulfillment of the requirement for the award of the degree of **Doctor of Philosophy** in the **Department of Physics**, Malaviya National Institute of Technology, Jaipur, India. The matter embodied in this thesis is original and has not been submitted to any other University or Institute for the award of any other degree.

**Place:** Jaipur

**Date:**

Dr. Rahul Singhal  
Assistant Professor  
Department of Physics  
Malaviya National Institute of Technology Jaipur,  
Jaipur-302017 (Rajasthan)



## ACKNOWLEDGEMENTS

“The power of God is with you at all times; through the activities of mind, senses, breathing, and emotions; and is constantly doing all the work using you as a mere instrument.” (Bhagavad Gita)

First, my sincere and warmest thank to my thesis supervisor Dr. Rahul Singhal, for his endless support and endurance in guiding me throughout the research work. I am very thankful to him to encourage and support me during my journey of research.

I would like to express my sincere thanks to Dr. V.V. Siva Kumar (Scientist-E, IUAC New Delhi) who always supported and encouraged me during my research work. He was always available to solve my problems with his kind behaviour. I especially thank him to provide synthesis facility without any deferment.

I am very thankful to Dr. D. Kanjilal, Dr. D. K. Avasthi, Dr. K. Asokan, Dr. Fouran Singh, Dr. D. Kabiraj, Dr. P. Kulriya, Dr. Parveen Kumar, Mr. Sunil Ojha, Mrs. Devarani Devi, Mr. Abhilash for help and discussion about my research plan and give the chance to avail different characterization and synthesis facility. During my research carrier works experience at IUAC was very graceful and their door were always open for synthesis facility and beam facility.

I am highly thankful to all faculties of Department of Physics, MNIT Jaipur for their continuous support and encouragement. I am especially thankful to Dr. K. Sachdev and Dr. S. N. Rao for moral support and always discussing my problems and give the solutions. I am also thankful to departmental staff members Mr. Khem Singh, Mr. Sunil Kumar, Mr. Ritesh, Mr. Firoj Khan and Ramkishor Ji for their support to make the departmental activities easy and cheerful.

I wish my sincere gratitude to Dr. Beer Pal Singh, Head, Department of Physics, CCS University, Meerut, and Dr. Ritu Vishnoi for the fruitful discussion regarding my research.

I pay my sincere thanks to all staff members of Material Research Center MNIT Jaipur especially Mr. M. Reza, Mr. Ramesh Kumar, Dr. Srinivas Yadav, Mr. Sachin Survey, Mr.

Hitesh Sharma, Mr. Bhupesh who always helped me to solve the problems facing with the characterization facilities.

I express my heartiest thanks to my seniors; Dr. Rishi Vyas, Dr. Vikas Sharma, Dr. Yogita Kumari, Dr. Anil Kumar, Dr. Sandeep Garg, Dr. Promod Kumar, Dr. D.C. Agrawal, Dr. Praveen Kumar, Dr. Mohit Sharma, Dr. Rajkumar, Ms. Ruchi Tomer who always show me a path in the dark side of this journey. I also thank to my colleagues Dr. Veeresh Kumar, Dr. Himanshu Sharma, Dr. Trupti Sharma, Pooja Sharma, Dr. Lokesh Kumar Jangir, Rajesh Kumar, Rini Singh, Anoop M D, Pooja Kumari, Arun Vinod, Dr. Satyavir Singh, Dr. Mahendra Singh and all research scholars of the Department.

I am fortunate enough to have many good friends who always support me in every aspect throughout my Ph.D. career. I am especially grateful to Mr. Gyanendra Panchal, Mr. Sat Kumar, Mr. Anuj Kumar, Mr. Dheeraj Sharma, Mr. Anurag Sharma, Mr. Hemant Kumar and my MNIT friends Dr. Sachin Rathi, Dr. Diwakar Gautam, Dr. Dheeraj Mehta, Dr. Pawan Chauhan, Mr. Nitesh Kumar for their moral support.

From deep of my heart, I am thankful to my parents, Mr. Ramesh Kumar Singh and Mrs. Saroj Singh who always encouraged me to pursue my goals and for always being my strength to face every difficulty and challenge in my life. I pay my regards to my brother Mr. Prashant Kumar Singh and Mrs. Anjali Singh and love to champ of our family Trisha.

**Date:**

**(Shushant Kumar Singh)**

## Abstract

The metal-oxide nanocomposites possess various physical properties which makes them of great scientific interest for different applications. Among all, ZnO based nanocomposites are very promising due to its wide band gap (3.34 eV) and large exciton energy (60 meV). In present thesis, initially pure ZnO thin films have been synthesized by RF-magnetron sputtering technique. Then prepared films have been irradiated with 100 MeV Ag<sup>7+</sup> at the fluences of  $3 \times 10^{12}$ ,  $1 \times 10^{13}$  and  $3 \times 10^{13}$  ions/cm<sup>2</sup>. Pure ZnO thin films were also annealed at temperatures 400 °C and 500 °C for 1 hour with continuous flow of oxygen gas. Ion-induced and thermally induced structural and optical modifications of nanocrystalline ZnO films have been investigated using various characterization techniques such as X-ray diffraction (XRD), UV-visible spectroscopy, atomic force microscopy (AFM), scanning electron microscopy (SEM) and Raman spectroscopy. The crystalline behaviour of the films was enhanced in particular c-axis direction due to impact of high energetic ions. Lattice defects were also influenced by ion irradiation as well as thermal annealing confirmed by Raman spectra. Optical transparency were found to be decreased with ion fluence. The Structural and optical properties of the films have been improved with thermal annealing and ion irradiation.

Metal-oxide nanocomposites have attracted considerable attention because of their tunable structural and optical properties affected by incorporation of metal. Ag-ZnO nanocomposite thin films were synthesized by two different approaches; RF-magnetron sputtering and Ag ion implantation. Ag-ZnO nanocomposite thin films with three different Ag concentration (8%, 15% & 40%) were deposited by RF-magnetron sputtering technique. The composite nature of the films have been confirmed by Rutherford backscattering spectroscopy (RBS) and Ag fraction has been calculated using simulation with Rutherford universal manipulation program (RUMP). The formation of hexagonal wurtzite structure of ZnO and Ag-ZnO films was confirmed by XRD. Raman spectroscopy revealed the information of lattice defects and disordering during Ag incorporation into ZnO. The enhancement in electrical conductivity in Ag-ZnO thin films than that of pure ZnO was observed by I-V and Hall measurements and the nature of conductivity was altered from n-type to p-type at higher Ag concentration. This property of nanocomposite

thin films can be very useful for the device fabrication. Another approach, ion implantation has been used for the formation of Ag nanoparticles in ZnO matrix. Ion implantation is unique technique to grow metal nanoparticles in any matrix with precise control of depth and selective area for the implantation. 120 keV Ag ion beam was used for Ag implantation with different implantation dose from  $3 \times 10^{14}$  to  $3 \times 10^{16}$  ions/cm<sup>2</sup> by negative ion implantation facility at Inter University Accelerator center, New Delhi (IUAC). Surface stoichiometry and thickness of the films were estimated by RBS and X-ray photoelectron spectroscopy (XPS). Ag nanoparticles was found to be asymmetrically distributed on the surface of ZnO. XRD results revealed the formation of hexagonal wurtzite structure with good crystalline nature along c-axis. However, the crystalline behavior of the film was affected by implantation dose which may be attributed to the lattice strain induced in the matrix. The specific c-axis orientation of the film is unique feature for immense technological importance for various applications.

Further, SHI and thermally induced modifications in Ag-ZnO nanocomposite thin films have been carried out in systematical manner. Ag-ZnO nanocomposite films were irradiated with 100 MeV Ag ions with three different fluences  $3 \times 10^{12}$ ,  $1 \times 10^{13}$  and  $3 \times 10^{13}$  ions/cm<sup>2</sup>. The presence of Ag and formation nanocomposite was confirmed by XPS analysis. Surface plasmon resonance (SPR) band at 475 nm corresponding to Ag nanoparticles was appeared in Ag-ZnO nanocomposites thin films and shifts towards the lower wavelength (30 nm) with ion irradiation. Thermal induced SPR tuning has also been studied for Ag-ZnO nanocomposite thin films. The prepared Ag-ZnO thin films were annealed at three different temperatures 300 °C, 400 °C and 500 °C in the vacuum environment (order of vacuum  $10^{-2}$ ) to prevent the oxidation of Ag nanoparticles. XRD revealed the monocrystalline behaviour of the as-synthesized Ag-ZnO thin films and the crystallinity of the films have been improved with annealing temperature. The average particle size of Ag nanoparticles was estimated as 8.2 nm by transmission electron microscopy (TEM). Presence of Ag in the form of nanoparticles depicts the SPR band in optical spectra observed at 565 nm. This SPR band was observed to be red shifted remarkably (22 nm) at the higher temperature. These high quality Ag-ZnO nanocomposite thin films with minimum strain and tunable SPR frequency could be useful in plasmonic applications.

## Table of contents

<b>Acknowledgements</b>	V
<b>Abstract</b>	VII
<b>Contents</b>	IX
<b>List of Tables</b>	XV
<b>List of Figures</b>	XVII
<b>List of Abbreviations</b>	XXV

### **Chapter 1: Introduction**

1.1. Introduction.....	2
1.2. Nanocomposites.....	2
1.2.1. Nano-composites thin films .....	4
1.3. Metal nanoparticles.....	4
1.3.1. Silver (Ag) nanoparticles and their surface plasmon resonance (SPR).....	5
1.4. Zinc Oxide (ZnO).....	8
1.4.1. Crystal structure.....	8
1.4.2. Band structure.....	9
1.4.3. Defects and impurities.....	10
1.4.4. Properties and applications.....	11
1.5. Approaches for modifications of Nano-composite thin films.....	12
1.5.1. SHI irradiation induced modifications.....	12
1.5.2. Thermally induced modifications.....	15
1.6. Objectives of thesis.....	15
1.7. Organization of thesis.....	15

### **Chapter 2: Literature Review**

2.1. Background.....	18
2.2. Effect of SHI irradiation on ZnO thin films.....	18
2.3. Effect of thermal annealing on ZnO thin films.....	22
2.4. SHI irradiation of metal-ZnO nano-composite thin films.....	26
2.5. Studies on thermally induced modifications of metal-ZnO nano-composite thin films.....	27
2.6. Motivation of thesis.....	32

### **Chapter 3: Materials and Methods**

3.1. Thin film deposition techniques.....	36
3.1.1. RF-magnetron sputtering.....	36
3.1.2. Negative ion implantation.....	38
3.2. Modification techniques for engineering the properties of materials.....	39
3.2.1. Swift heavy ion irradiation.....	40
3.2.2. Thermal annealing.....	43
3.3. Characterization techniques.....	43
3.3.1. Rutherford backscattering spectroscopy.....	43
3.3.2. X-ray diffraction spectroscopy.....	45
3.3.3. UV-visible spectroscopy.....	46
3.3.4. Atomic force microscopy.....	48
3.3.5. Scanning electron microscopy.....	50
3.3.6. Transmission electron microscopy.....	52
3.3.7. Raman spectroscopy.....	54
3.3.8. Photo-luminescence spectroscopy.....	55
3.3.9. X-ray photoelectron spectroscopy.....	56
3.3.10. Electrical measurements.....	58



## **Chapter 4: SHI and Thermally Induced Modifications of ZnO Films as a Host Matrix**

4.1. Introduction.....	62
4.2. SHI irradiation studies of host matrix.....	63
4.2.1. Experimental details.....	63
4.2.2. Results and discussion.....	63
4.2.2.1. X-ray diffraction analysis.....	64
4.2.2.2. UV-visible spectroscopy.....	65
4.2.2.3. Atomic force microscopy.....	67
4.2.2.4. Scanning electron microscopy.....	70
4.2.2.5. Micro-Raman spectroscopy.....	71
4.3. Thermal annealing studies of host matrix.....	73
4.3.1. Experimental details.....	73
4.3.2. Results and discussion.....	73
4.3.2.1. Rutherford backscattering spectroscopy.....	73
4.3.2.2. X-ray diffraction analysis.....	74
4.3.2.3. UV-visible spectroscopy.....	75
4.3.2.4. Micro-Raman spectroscopy.....	76
4.4. Summary.....	77

## **Chapter 5: Synthesis and Characterization of Ag-ZnO Nano-composites Thin Films Using Two Different Approach**

5.1. Introduction.....	80
5.2. Synthesis of Ag-ZnO nano-composite thin films using RF-magnetron sputtering.....	81
5.2.1. Experimental details.....	81
5.2.2. Results and Discussion.....	82
5.2.2.1. Rutherford backscattering spectroscopy.....	82
5.2.2.2. X-ray diffraction analysis.....	83

5.2.2.3. Scanning electron microscopy.....	85
5.2.2.4. Micro-Raman spectroscopy.....	87
5.2.2.5. Electrical measurement.....	88
5.3. Synthesis of Ag-ZnO nano-composite thin films using negative ion implantations technique.....	90
5.3.1. Experimental details.....	90
5.3.2. Results and discussion.....	91
5.3.2.1. Rutherford backscattering spectroscopy.....	91
5.3.2.2. X-ray diffraction analysis.....	93
5.3.2.3. UV-visible spectroscopy.....	94
5.3.2.4. Atomic force microscopy.....	95
5.3.2.5. Micro-Raman spectroscopy.....	97
5.3.2.6. X-ray photoelectron spectroscopy.....	98
5.4. Summary.....	99

## **Chapter 6: SHI and Thermally Induced Modifications of Ag-ZnO Nano-composites Thin Films**

6.1. Introduction.....	102
6.2. SHI irradiation studies of nano-composites thin films.....	102
6.2.1. Experimental details.....	103
6.2.2. Results and discussion.....	103
6.2.2.1. Rutherford backscattering spectroscopy.....	103
6.2.2.2. X-ray diffraction analysis.....	105
6.2.2.3. UV-visible absorption spectroscopy.....	108
6.2.2.4. Atomic force microscopy.....	110
6.2.2.5. Micro-Raman spectroscopy.....	112
6.2.2.6. Photo-luminescence measurement.....	112
6.2.2.7. X-ray photoelectron spectroscopy.....	113
6.3. Thermal annealing studies of nano-composites thin films.....	115

6.3.1. Experimental details.....	115
6.3.2. Results and discussion.....	115
6.3.2.1. X-ray diffraction analysis.....	115
6.3.2.2. UV-visible spectroscopy.....	118
6.3.2.3. Atomic force microscopy.....	121
6.3.2.4. Micro-Raman spectroscopy.....	123
6.3.2.5. Transmission electron microscopy.....	124
6.3.2.6. X-ray photoelectron spectroscopy.....	125
6.4. Summary.....	126

## **Chapter 7: Conclusion and Future Scope**

7.1. Conclusions.....	130
7.2. Future scope.....	132

<b>References</b> .....	133
-------------------------	-----

## **Appendix**

A- List of publications.....	157
B- Research articles.....	161

## **Bio-data**



## List of Tables

<b>Table 1.1</b>	Properties of the Silver.....	6
<b>Table 1.2</b>	Properties of ZnO.....	11
<b>Table 4.1</b>	Variation of crystallite size with different ion irradiation fluences.....	65
<b>Table 4.2</b>	Grain size and roughness of the film with different fluences.....	70
<b>Table 5.1</b>	The sputtering parameters for thin film deposition.....	82
<b>Table 5.2</b>	Lattice parameter and crystallite size for pure ZnO and Ag-ZnO nanocomposite thin film.....	85
<b>Table 5.3</b>	The electrical parameter for pure ZnO and Ag-ZnO nanocomposite thin film.....	90
<b>Table 6.1</b>	Lattice parameters, crystallite size and stress of the pristine and irradiated thin films estimated by X-ray diffraction spectra.....	108
<b>Table 6.2</b>	Band gap, roughness and grain size of pristine and irradiated thin films.....	110
<b>Table 6.3</b>	Structural parameters of as-deposited and annealed Ag-ZnO NCs thin films.....	118
<b>Table 6.4</b>	Optical parameter with different annealing temperatures.....	121
<b>Table 6.5</b>	Variation in roughness and grain size with annealing for the Ag-ZnO NCs thin films.....	122



## List of Figures

<b>Figure 1.1</b>	Block diagram for the nanocomposite material.....	3
<b>Figure 1.2</b>	FCC lattice structure for the silver.....	6
<b>Figure 1.3</b>	Resonant excitation of collective oscillations of the conduction electrons in the nanoparticles .....	7
<b>Figure 1.4</b>	Crystal structure of the ZnO (wurtzite and zinc blende).....	9
<b>Figure 1.5</b>	Band diagram (with splitting of valence band) for the ZnO at 4.2 K.....	10
<b>Figure 1.6</b>	Flow diagram for the ion beam irradiation.....	14
<b>Figure 3.1</b>	Schematic diagram for the RF sputtering.....	37
<b>Figure 3.2</b>	Negative ion implantation facility at the IUAC New Delhi.....	38
<b>Figure 3.3</b>	MC-SNICS ion source of the accelerator.....	41
<b>Figure 3.4</b>	Schematic diagram of the 15 UD pelletron accelerator at IUAC New Delhi.....	42
<b>Figure 3.5</b>	High vacuum irradiation chamber of Material Science beam line at IUAC New Delhi.....	42
<b>Figure 3.6</b>	Schematic representation of RBS setup.....	45
<b>Figure 3.7</b>	Schematic representation for the Bragg's diffraction.....	46

<b>Figure 3.8</b>	Schematic for the working of UV-visible spectrophotometer.....	47
<b>Figure 3.9</b>	Schematic for working of AFM.....	49
<b>Figure 3.10</b>	A look inside SEM.....	51
<b>Figure 3.11</b>	Interaction volume for the interaction of electron beam with the specimen.....	52
<b>Figure 3.12</b>	Schematic diagram of the TEM.....	53
<b>Figure 3.13</b>	Schematic diagram of Raman spectrophotometer.....	55
<b>Figure 3.14</b>	Schematic diagram of the PL System.....	56
<b>Figure 3.15</b>	Schematic representation of the XPS with basic components.....	58
<b>Figure 3.16</b>	(a) Image of Sample holder used for Hall-measurements (b) different components of Hall measurement apparatus.....	59
<b>Figure 4.1</b>	XRD spectra of the pristine and irradiated ZnO thin films with different fluences, Inset shows the zoomed behaviour of (002) plane with ion irradiation.....	64
<b>Figure 4.2</b>	Variation of the lattice strain and crystallite size with different ion fluences.....	65
<b>Figure 4.3</b>	UV-visible transmission spectra for pristine and 100 MeV Ag ion irradiated films of ZnO and the optical band gap variation of pristine and irradiated film calculated by Tau'c plot (inset).....	66



<b>Figure 4.4</b>	AFM micrographs of (a) Pristine (b) $3 \times 10^{12}$ ions/cm <sup>2</sup> (c) $1 \times 10^{13}$ ions/cm <sup>2</sup> and (d) $3 \times 10^{13}$ ions/cm <sup>2</sup> .....	68
<b>Figure 4.5</b>	Variation of grain size with different ion fluences calculated by atomic force microscopy.....	69
<b>Figure 4.6</b>	Variation of roughness and grain size with different ion irradiation fluences.....	69
<b>Figure 4.7</b>	FESEM micrographs of pristine and 100 MeV Ag ion irradiated film of ZnO at different fluences.....	70
<b>Figure 4.8</b>	Raman spectra of pristine and 100 MeV Ag irradiated at different fluences.....	72
<b>Figure 4.9</b>	RBS spectra of the as deposited ZnO thin film on Si substrate.....	74
<b>Figure 4.10</b>	XRD pattern of as deposited ZnO thin film.....	75
<b>Figure 4.11</b>	Transmittance spectra of as deposited and annealed ZnO thin films.....	75
<b>Figure 4.12</b>	Band gap variation of as deposited and annealed film calculated by Tau'c plot.....	76
<b>Figure 4.13</b>	Raman spectra of as deposited and annealed ZnO thin films.....	77
<b>Figure 5.1</b>	RBS spectra for the (a) pure ZnO (b) Ag-ZnO (8%) and (c) Ag-ZnO (15%) (d) Ag-ZnO (40%) nanocomposite thin films.....	83

<b>Figure 5.2</b>	XRD diffraction pattern for the pure (a) and Ag-ZnO nanocomposite thin film with three different doping concentration (b) 8%, (c) 15% and (d) 40% Ag.....	85
<b>Figure 5.3</b>	Scanning electron micrograph for (a) pure ZnO (b) 8% Ag-ZnO (c) 15% Ag-ZnO and (d) 40% Ag-ZnO nanocomposite thin films.....	86
<b>Figure 5.4</b>	Raman spectra for the pure (a) and Ag-ZnO nanocomposite thin film with different doping concentration (b. 8% c. 15% and d. 40% Ag concentration).....	88
<b>Figure 5.5</b>	I-V spectra for the pure and Ag-ZnO nanocomposite thin films.....	89
<b>Figure 5.6</b>	Variation of resistance and conductivity with Ag doping concentration....	89
<b>Figure 5.7</b>	(a) RBS spectra of the Ag implanted ZnO thin film (b) Depth profile of Ag implanted ZnO thin film and (c) Depth distribution curve of Ag ion implanted in ZnO thin film estimated by SRIM-TRIM simulation (d) Enlarge view shows the experimental distribution of Ag ions by RBS.....	92
<b>Figure 5.8</b>	(a) X-ray diffraction pattern of the pure ZnO and 120 keV Ag implanted thin film with different dose (b) Variation in crystallite size and lattice strain with implantation dose.....	93
<b>Figure 5.9</b>	(a) UV-visible transmittance spectra of the pure ZnO and 120 keV Ag implanted ZnO thin film with different dose (b) Variation in band gap of the pure and implanted ZnO thin films.....	94
<b>Figure 5.10</b>	3-D AFM micrographs of as-deposited and 120 keV Ag implanted ZnO thin film with different implantation dose.....	95

<b>Figure 5.11</b>	Variation in roughness and grain size of the pure and 120 keV Ag implanted ZnO thin film with different implantation dose.....	96
<b>Figure 5.12</b>	Raman spectra of the pure ZnO and 120 keV Ag implanted ZnO thin film with different implantation dose.....	97
<b>Figure 5.13</b>	XPS spectra of the pure ZnO and Ag implanted ZnO nanocomposite thin film at the dose $3 \times 10^{16}$ ions/cm <sup>2</sup> .....	99
<b>Figure 6.1</b>	Rutherford backscattering spectrum (RBS) of Ag-ZnO nanocomposite thin film.....	105
<b>Figure 6.2</b>	The nuclear and electronic energy losses of 100 MeV Ag <sup>7+</sup> ions as the function of incident ion energy.....	105
<b>Figure 6.3</b>	XRD spectra of pristine and irradiated films at three different fluences.....	107
<b>Figure 6.4</b>	Crystallite size of pristine and 100 MeV Ag <sup>7+</sup> irradiated thin film.....	108
<b>Figure 6.5</b>	UV- visible absorption spectra of pristine and 100 MeV Ag <sup>7+</sup> irradiated films.....	109
<b>Figure 6.6</b>	Band gap variation of pristine and irradiated films, calculated by Tauc's relation.....	110
<b>Figure 6.7</b>	AFM micrographs (2D) of pristine and irradiated Ag-ZnO nanocomposite thin films.....	111

<b>Figure 6.8</b>	Raman spectra of pristine and irradiated films at different fluences.....	112
<b>Figure 6.9</b>	PL spectra of pristine and irradiated films at different fluences.....	113
<b>Figure 6.10</b>	XPS spectra of Ag-ZnO nanocomposite thin film (Survey as well as core spectra of Zn, O and Ag).....	114
<b>Figure 6.11</b>	X-ray spectra of as-deposited and annealed Ag-ZnO nanocomposite thin film at three different temperatures of 300 °C, 400 °C and 500 °C.....	117
<b>Figure 6.12</b>	UV-visible absorption spectroscopy of the as-deposited and annealed Ag-ZnO thin films.....	118
<b>Figure 6.13</b>	Band gap variation of the as-deposited and annealed Ag-ZnO thin films at different temperatures.....	120
<b>Figure 6.14</b>	2D (1×1 μm <sup>2</sup> ) AFM micrographs of (a) as-deposited and annealed (b) 300 °C (c) 400 °C (d) 500 °C Ag-ZnO nanocomposite thin films.....	122
<b>Figure 6.15</b>	Raman spectra of as-deposited and annealed Ag-ZnO nanocomposite thin films.....	123
<b>Figure 6.16</b>	TEM micrographs of as-deposited Ag-ZnO nanocomposite thin film (a) surface image (b) Ag nanoparticle (c) HRTEM image with d-spacing (d) SAED pattern.....	124

**Figure 6.17** XPS spectra of the as-deposited Ag-ZnO nanocomposite thin film (a) survey scan (b) high resolution spectra of Zn (c) O and (d) Ag.....126



## List of abbreviations

<b>Ag</b>	Silver
<b>SPR</b>	Surface plasmon resonance
<b>ZnO</b>	Zinc oxide
<b>S<sub>n</sub></b>	Nuclear energy loss
<b>S<sub>e</sub></b>	Electronic energy loss
<b>SHI</b>	Swift heavy ion
<b>NPs</b>	Nanoparticles
<b>NC</b>	Nanocomposite
<b>RBS</b>	Rutherford backscattering spectroscopy
<b>XRD</b>	X-ray diffraction
<b>RUMP</b>	Rutherford universal manipulation program
<b>SAED</b>	Selected area electron diffraction
<b>XPS</b>	X-ray photoelectron spectroscopy
<b>PL</b>	Photo-luminescence spectroscopy
<b>SEM</b>	Scanning electron microscopy
<b>AFM</b>	Atomic force microscopy





# Chapter 1

## Introduction

---

*In this chapter, the overview about the nanomaterials and nanocomposites is presented. The chapter introduces the fundamental properties of the dopant metal Ag and matrix material ZnO in detailed. A brief discussion about the optical properties especially surface plasmon resonance for the noble metal nanoparticles has been done. The objectives of the thesis have also been mentioned in this chapter.*

## 1.1. Introduction

“Nanotechnology is the principle of atom manipulation atom by atom, through control of the structure of matter at a molecular level. It entails the ability to build the molecular system with atom-by-atom precision, yielding a variety of nano-machines.” by Drexler [1].

Nanotechnology is the creation and utilization of materials through the control of matter on the nanometer length scale at the level of atoms, molecules and supramolecular structures [2–5]. This field includes the structures which have a typical dimension in the range of nanometer scale (one billionth or  $10^{-9}$  of a meter) [6]. One nanometer is equal to 4 gold atom or 10 hydrogen atom aligned in a line. At this length scale, materials show exciting chemical and physical properties which are drastically diverse from the bulk properties of material. Although this field is very new for human society, but there are many examples which exist in our nature from the beginning of life. Flagella bacteria is a good example of the biological molecular nano-machine, where an electro-chemical potential difference across the membranes is applied and responsible for the proton flow which eventually drives nano-motors [7]. So nanotechnology is not only the basic field in the tuning of the properties of materials but also yielding a more technical knowledge about the device fabrication as well as in biomedical applications [8–11]. Nowadays, “nano-scale science and technology” offers the new era for modern research and developing new ideas which is growing day by day. There are two approaches to synthesize the nano-materials; (a) top-down and (b) bottom-up approach. In the top-down approach, the bulk material is processed with appropriate techniques to achieve the desired structure and shape of the final product. Ball milling, Ion implantation, lithography and chemical etching are mainly used as a top-down approach for the nanomaterial synthesis. Whereas bottom-up approach is widely applied for the nano-device fabrication. In this process, the parent material is assembled molecule by molecule or atom by atom. Sol-gel technology, physical and chemical vapor deposition, electro-deposition and epitaxial growth are some examples of this approach.

## 1.2. Nanocomposites

Nanocomposites (NC) are the special class of nanomaterials which offer new possibilities which could not be found in two different materials separately (**Figure 1.1**). The nanocomposite materials are the solid solution of two different materials wherein one is reinforcing phase and other one act as matrix phase with one of the phase in the nano-region. Reinforcing phase consists of different forms of the material such as fibers, nanoparticles and sheets (also known as filler) while the matrix phase occupies the main volume of the composite. This type of structure provides more desirable properties than those of the single host material. The size and shape of the filler material show a significant role in various applications. The essential features of nano-composites are as follows:

- The properties of nanocomposite materials also depend on morphology and interfacial characteristics of parent material as well incorporated noble metals.
- The nanocomposite offer combine diverse properties which produce from the combination of both filler and matrix material which are unknown with parent constituent materials.
- Drastically enhance optical, electrical, mechanical and other properties depending on the properties of Nano-particulates.
- Generate many exciting new materials with novel properties.

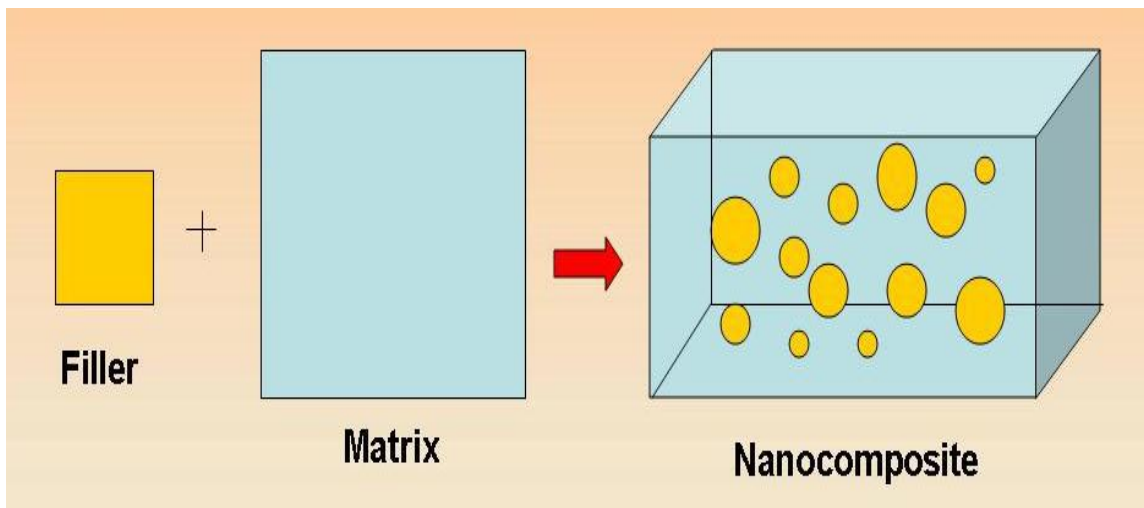


*Figure 1.1* Block diagram for the nanocomposite material.

Based on the matrix material the nanocomposites can be categorized as follows;

- (1) Ceramic matrix nanocomposite
- (2) Metal matrix nanocomposite
- (3) Polymer matrix nanocomposite

The present thesis deals with the first category of the nanocomposites. Ceramics possess good thermal and chemical stability and wear resistance and widely used in industry. Here, metal-metal oxide nanocomposites have been investigated.

### **1.2.1. Nanocomposite thin film**

Nanocomposite thin film is the vastly growing research fields for different applications such as device fabrication, sensing and optical applications. In the present scenario, NC thin film technology plays a major role in various industrial applications such as optical devices, coatings, memory devices because of their improved electrical, optical and mechanical properties [12–17].

NC thin films with metal nanoparticles as filler can effectively tune the properties of NCs which is applicable in the field of device fabrication [18,19]. Incorporation of the metal nanoparticles in the parent matrix makes it very useful in different optical applications since metal particles show good optical properties. Furthermore, the size and shape of nanoparticles are the two crucial parameters in enhancing the optical properties of the material. Small filler size provides the high surface to volume ratio. This increased reinforced surface area can affect the macro-scale properties of matrix remarkably. The optical characteristics of the nanocomposite thin films are depends on the noble metal as well as matrix material. It is well known that film properties for example grain growth, surface morphology, epitaxial stress/strain, crystalline quality and composition could be affected by the deposition methods and parameters. The ductility of the films can be increased in NC without decreasing its strength. Usually, the filler is dispersed into the host matrix during the synthesis processing and amount of the filler can be varied, though the uniform dispersion of filler is desirable. Several deposition techniques have been used for the synthesis of the nanocomposite thin film such as RF-sputtering, ion beam deposition, electron beam evaporation and ion implantation [20–22].

In the present thesis, RF-sputtering has been used for the synthesis of metal oxide thin film whereas RF co-sputtering as well as ion implantation techniques have been used for metal-metal oxide NC thin film.

### **1.3. Metal nanoparticles**

Nanoparticles show interesting properties, due to their high surface area to volume ratio and have the potential applications in the bio-medical field, laser application, medicinal application and optical application [23–25]. As per definition, at least one dimension of the nanoparticles should be less than 100 nm. In the case of bulk material, physical properties of the material do not change with the size of the material while such properties are much affected by the size and shape of the material when it is in nano-scale. Nanoparticles can be considered as a bridging between atomic structure and bulk material. Many nano-scale size dependent properties are observed in various cases such as quantum confinement of semiconducting nanoparticles, super-paramagnetism properties in magnetic nanoparticles and surface plasmon resonance in noble metal nanoparticles. At the nano-scale regime, surface to volume ratio (S/V ratio) of the material show the significant role in tuning the physical and chemical properties of the material which is attributed to large surface energy of the atoms present on the surface as compared to bulk. In the present thesis, the silver nanoparticles have been embedded as filler by using RF co-sputtering and ion implantation techniques.

#### **1.3.1. Silver (Ag) nanoparticles and their surface plasmon resonance (SPR)**

Silver is the metallic element and has atomic number 47, which is denoted by Ag and belongs to group 11 with Au and Cu metals. Ag has two naturally isotopes  $^{107}\text{Ag}$  and  $^{108}\text{Ag}$ , an atomic mass of 108 and crystallizes in the face-centered cubic lattice structure (**Figure 1.2**). It has three oxidation states which are 0, +1 and +2 with a very large electrical conductivity [26]. Apart from that, higher reflectivity, thermal conductivity and electrical conductivity make Ag advantageous element in comparison with other metals. Ag paste has been widely used in solar cell contacts, electrical contacts, microelectronics,

catalysis and medical instruments. The important properties of Ag are summarized in **Table 1.1**.

**Table 1.1** Properties of the Silver

Material name	Silver (Ag)
Chemical formula weight	107.87
System	Cubic ( $\alpha=\beta=\gamma = 90^\circ$ )
Melting temperature ( $^\circ\text{C}$ )	961.71 $^\circ\text{C}$
$a$ ( $\text{\AA}$ )= $b$ ( $\text{\AA}$ )= $c$ ( $\text{\AA}$ )	4.0862
Unit cell volume ( $\text{\AA}^3$ )	68.23
Calculated density ( $\text{g/cm}^3$ )	10.50

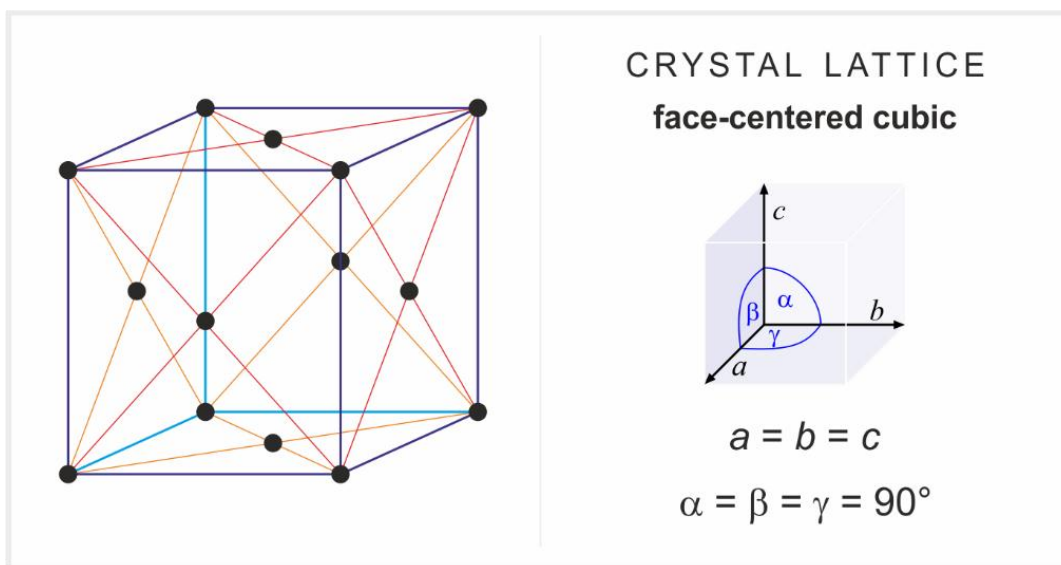


**Figure 1.2** FCC lattice structure for the silver.

Ag nanoparticles exhibit interesting optical properties compared to the bulk material. If the electromagnetic light imposed on these nanoparticles, they show strong absorption band at a certain frequency of the incident light. This strong band arises due the resonance between oscillation frequency of the free electron cloud of the atoms and the frequency of the incident radiation. This band is known as SPR band for the given

nanoparticles and shown in **Figure 1.3** [27]. The optical properties of nanocomposite thin films can be tailored by embedding these nanoparticles in the host matrix.

Incident electromagnetic (EM) light on the nanoparticles causes an electronic charge separation and atom goes to change own equilibrium state during light irradiation. This charge separation generates a restoring force which leads to an oscillatory motion of the electrons of the atom at a certain characteristic frequency. At the same time, oscillations induced polarization originates in the opposite direction which helps in reducing the restoring force of the electrons.

The SPR band of the NC thin films depends on:

- The amount of the metal content present in host medium (matrix).
- Shape as well as size of metal nanoparticles.
- Inter-particle separation between the nanoparticles dispersed in the matrix.
- Properties of the matrix material surrounding the nanoparticles.

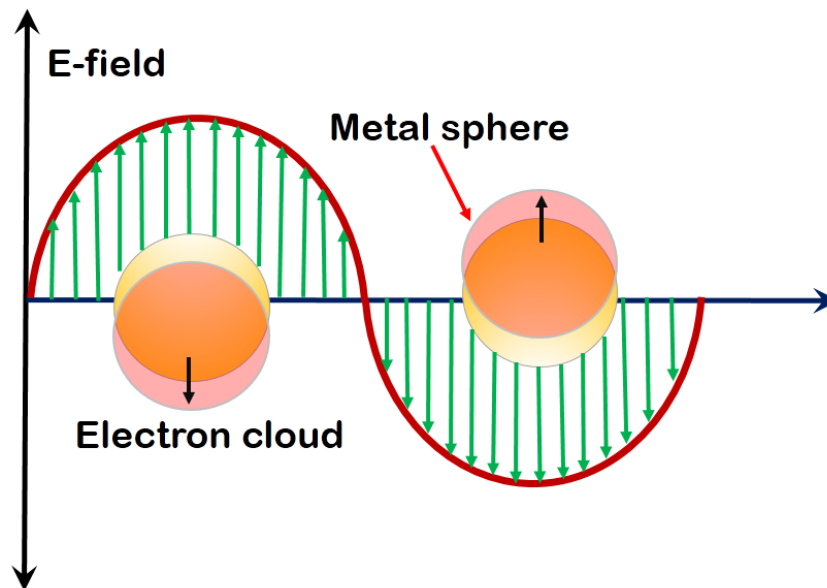


**Figure 1.3** Resonant excitation of collective oscillations of the conduction electrons in the nanoparticles.

The formation of the SPR band also depends on the nanoparticles size. If the size of nanoparticles is smaller than the wavelength of the incident electromagnetic radiation, a uniform EM radiation exists across the nanoparticles which yield the narrow band of SPR. If the size of nanoparticles is larger than wavelength of the incident electromagnetic

radiation, the EM field distribution becomes non-uniform and show multi-pole resonances which yield broad peaks in the absorption spectra of the nanoparticles. Also the dielectric constant of the host matrix affects the optical properties of the nanoparticles.

## **1.4. Zinc oxide (ZnO)**

ZnO (N-type semiconductor) is a very promising material of II-VI group with wide band gap (3.34 eV) and high exciton binding energy (60 meV) [28]. A great scientific interest has been received due to their transmission properties in visible region, and piezoelectric properties [29,30]. In recent years, ZnO is very encouraging and competitive material that is utilized in various fields; solar cells, transparent conductive contacts, spintronic devices, light emitting devices, laser deflectors, paints, antibacterial activity, bio-sensors, gas sensors, and piezoelectric transducers [31–36]. Great efforts have been made to modify the properties of ZnO by doping of noble metal and ion irradiation so that it can be widely used in various research areas. In the present study, ZnO has been used as host matrix and the modifications by ion irradiation in their properties have been investigated.

### **1.4.1. Crystal structure**

Zinc oxide is a semiconducting material with space group  $C_{6mc}$ . The ultraviolet luminance and exciton emission have been observed in ZnO nanoparticles as well in the thin film, due to its large exciton binding energy. Generally, ZnO has been found in the two forms:

- (a) Hexagonal wurtzite structure
- (b) Cubic zinc blende structure.

Hexagonal wurtzite structure is the more stable structure of the ZnO. Tetrahedral coordination has been found for both structures which indicate the  $sp^3$  hybridization and leads to covalent bonding. The tetrahedral coordination in ZnO results in a non-central symmetric structure. As a result, it can be used as piezoelectricity and pyro-electricity applications. The presence of ionic character makes ZnO responsible for the ionic bonding between Zn and O (Zn-O bond). Therefore, ZnO shows both type of behavior covalent as well as ionic [37].



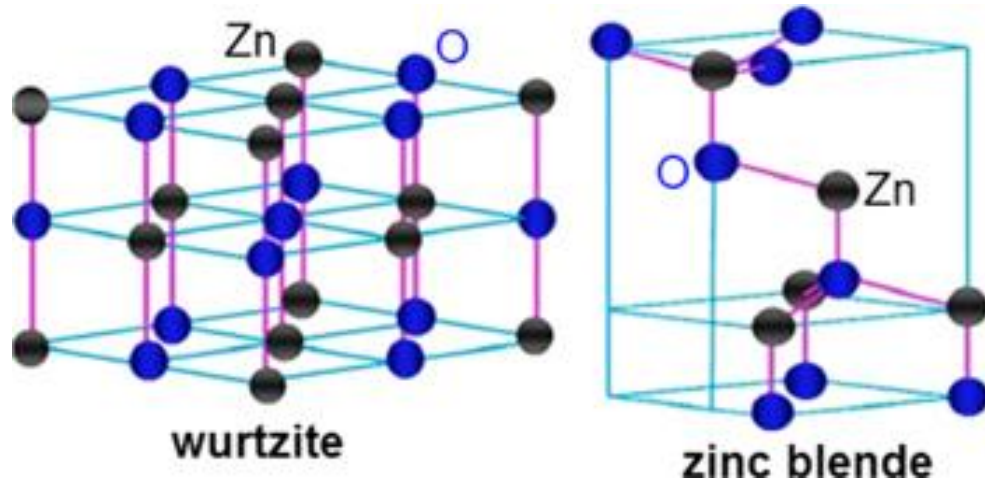


*Figure 1.4 Crystal structure of the ZnO (wurtzite and zinc blende).*

### 1.4.2. Band structure

The band structure of a semiconducting material is the crucial parameter which decides the overall performance of the device. The theoretical results of the band structure have been calculated by local density approximation (LDA). The electronic band diagram for the ZnO is shown in **Figure 1.5**. In the given figure, band structure shows high symmetry lines in the hexagonal Brillouin zone. The lower edge of the conduction band (minima) and higher edge of the valence band (maxima) match exactly at  $k = 0$  which clearly reveal that ZnO is a direct band gap material. The value of band gap for the ZnO has been calculated  $\sim 3.7$  eV by the local density approximation. The calculated value of the band gap is closer to experimental value of the ZnO i.e. 3.44 eV. The theoretical calculations for the band structure of ZnO (bulk) have been extensively studied by many researchers. Ivanov and Pollmann et al. analyzed the electronic structure of wurtzite ZnO by using empirical tight binding method (ETBM). The observed data was found to be consistent with the experimental data which obtained by ultra-violet photoelectron spectroscopy (UPS) and electron-energy-loss spectroscopy (EELS) [38]. The valence band of ZnO splits into three sub-bands referred as A, B and C as can be seen in the figure. The spin-orbit splitting and crystal-field splitting are the responsible for the sub-bands formation. The sub-band A and C are known to possess  $\Gamma_7$  symmetry whereas sub-band B is related to  $\Gamma_9$  symmetry as mentioned. The experimental band gap of the ZnO is close to  $\sim 3.44$  eV at the temperature of 4.2 K.

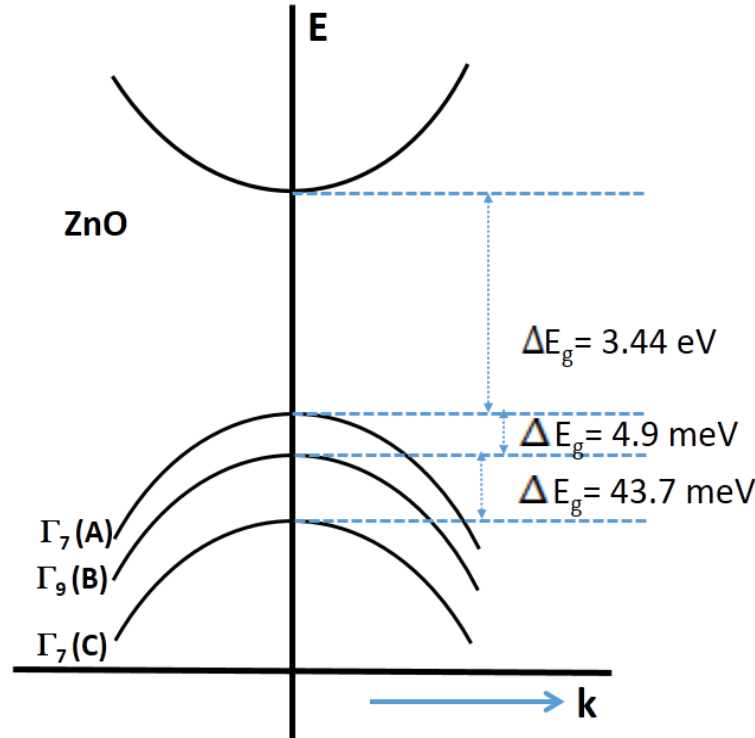


*Figure. 1.5 Band diagram (with splitting of valence band) for the ZnO at 4.2 K.*

The band structure of the ZnO also correlates with the optical properties. Thus band gap engineering is an emerging and interesting field for the different optical applications and electronic device development.

### 1.4.3. Defect and impurities

Native (intrinsic) defects are imperfections which occurs in the crystal during the growth process. Only the constitute elements are participating in these defects. Interstitials (extra atoms occupying interstices in lattice structure of ZnO), vacancies (missing of any atom from its own position) and antisites (O atom occupied by Zn sites and vice versa) are the main native defects which commonly exist in the crystal lattice. These native defects can effectively change the electronic and optical properties of the ZnO and may be controlled by deposition parameter, and doping of the metal elements. These defects are directly associated to the compensation of the predominant donor and acceptor dopants. For the formation of p-type materials donor defects take place in the materials whereas n-type behaviour is controlled by the acceptor defects. Generally, ZnO has n-type conductivity

due to oxygen vacancies or zinc interstitials and it can be easily tune with the doping of different noble metal Ag, Au, Cu as well as Ga and In impurities etc. These defects can strongly related with the electrical and optical properties of the material. So the understanding of incorporation of the metals and behavior of the defects are essential to its application in semiconductor devices [39,40].

#### 1.4.4. Properties and applications

In the present scenario, zinc oxide (ZnO) has become a promising material for the various optoelectronic devices and thin film applications, because of the large exciton binding energy as well direct band gap. Different mechanical, thermal, optical, electrical and vibrational properties of the ZnO are tabulated in **Table 1.2**.

*Table 1.2 Properties of ZnO*

<i>Sl. No.</i>	<i>Properties</i>	<i>Value</i>
1.	Chemical formula	ZnO (zinc oxide)
2.	Colour and nature	White solid
3.	Density	5.606 g/cm <sup>3</sup>
4.	Band gap	3.44 eV
5.	Space group/ coordination geometry	<i>C6v4-P63mc</i> , Tetrahedral
6.	Lattice structure	Hexagonal wurtzite (cubic)
7.	Vibrational bands	12 (9 optical modes and 3 acoustic modes)
8.	Lattice constant	$a = b = 3.25 \text{ \AA}$ , $c = 5.2 \text{ \AA}$ , $c/a = 1.63$
9.	Bulk Young's modulus	111.2 GPa
10.	Bulk hardness	5 GPa
11.	Thermal expansion coefficient	$\alpha_a = 4.31 \times 10^{-6} \text{ K}^{-1}$ and $\alpha_c = 2.49 \times 10^{-6} \text{ K}^{-1}$ at 300 K
12.	Specific heat capacity	$C_p = 40.3 \text{ J mol}^{-1} \text{ K}^{-1}$ at constant pressure
13.	Refractive index	2.004

ZnO has become an alternate to indium tin oxide in solar cell industry used as transparent conductive electrodes owing to its transparency in visible region, low cost, a high degree of chemical stability, and less toxicity. In the last few years, ZnO-based nanomaterials have attracted considerable attention because of their dimensionality and size of their structural features, electrical and optical properties and also motivate towards its utilization in various nano-device fabrication realm.

Radiation hardness properties of the ZnO is very much useful in space application. Thus ZnO provides the huge opportunities for the modern research due to its unique properties which are applicable in potential application for industry and society. Indeed, many researchers are struggling to improve their properties by applying different procedures for example incorporation of the metal as a dopant, ion implantation and interplay with annealing etc.

## **1.5. Approaches for modifications of the nanocomposite thin films**

### **1.5.1. SHI irradiation induced modifications**

Ion beam technology offers the flexibility to tune the materials properties as per requirement and also support the developing a new class of material. Size dependent properties of materials can be effectively enhanced by this technique and leads to the better understanding of the nanotechnology. The ion beam is a very powerful technique in the field of thin film science because of easy controlled beam parameters; incident ion energy, ion fluence, beam size and scanning area. This technique has been used for material modifications as well as material characterizations and the energy of incident ion beam plays the major role for the same [41–45]. Possible applications of the ion beam on the basis of energy regime are the classified in following manner:

- Material synthesis: DC/RF sputtering, atom beam sputtering, plasma based deposition (applicable for low energy eV to few keV) and doping, ion implantation and ion beam mixing (applicable for few keV to MeV).
- Material characterization: Rutherford backscattering-spectroscopy (RBS), elastic recoil detection analysis (ERDA), particle-induced X-ray emission (PIXE),

channeling, nuclear reaction analysis (low energy regime few MeV) and, blocking (high energy regime up to 100 MeV).

- Material modifications: low energy ion irradiation ( $< \text{MeV}$ ) and high energy ion irradiation ( $> 10 \text{ MeV}$ ).

The interaction of incident ions with the target material is the fundamental need for understanding of the role of ion beam in Material Science. When energetic ions interact with the target material, they loss their energy to the material by elastic and inelastic collisions. There are two basic transformation mechanism for the loss of energy into the material due to atomic collisions with target atoms [46]:

- Elastic collisions between nuclei of the target atom and incoming ions. It is denoted as nuclear energy loss  $S_n$ , which dominates in lower energy regime from  $\sim \text{few keV}$  to  $1 \text{ MeV/nucleon}$ .
- Inelastic collisions between electron cloud of the target atom and incident ions and it is termed as electronic energy loss  $S_e$ , which dominates in higher energy regime, especially for Swift heavy ion (SHI) irradiation  $> 1 \text{ MeV/nucleon}$ .

A large amount of energy deposited by incident ions into the target material is responsible for the atomic displacement along the beam path and described by two different models; (i) Coulomb spike model (CSM) and (ii) Thermal spike model (TSM). Due to high energy acquired from incident SHI ions, excitations/ionizations along the ion track within very short time scale of  $10^{-17}$  second occurred in the material. This excitations/ionizations is responsible for the coherent radial atomic movements along the ion tracks. These movements lead to modifications in the material such as defects and mixing under the Coulomb force and explained as CSM. On the other hand, when the atomic subsystem of the material attains the energy from electronic subsystem due to SHI irradiation by electron-phonon coupling (EPC) phenomena, then it leads to increasing local lattice-temperature rapidly up to  $10^4 \text{ K}$  (formed the thermal spikes) and quenched very fast (rate  $\sim 10^{14} \text{ K/s}$ ). This process is also responsible for modifications in the material and known as thermal spike model (TSM) [46–48].

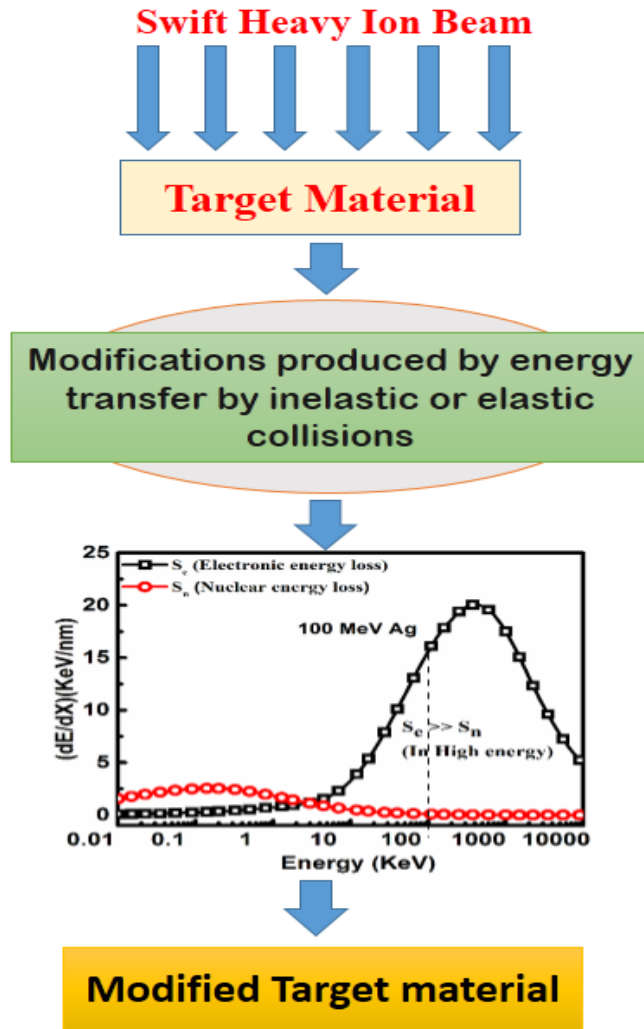


*Figure. 1.6 Flow diagram for the ion beam irradiation.*

In the case of SHI irradiation,  $S_e$  is more important and depends on many factors such as charge, mass and energy of the incident ions. In the present thesis, low energy ion beam (100 keV) has been used for material synthesis by ion implantation facility and high energy beam (MeV range) for the material modifications. When the velocity of incident ion is nearly comparable to the Bohr velocity of the electron of the target material, the incident ions are known as swift heavy ions (SHI) and is used for the material modifications. In the case of SHI irradiation, huge amount of energy deposited into the target material during irradiation is responsible for the modifications (**Figure 1.6**). These modifications depend on the nature of incoming ions, energy of the ion and fluences of the ion. So SHI irradiation provides the controlled way to modify the material

in specific regime by simply changing the energy and fluence of the ion beam. Controlled energy deposition with spatial selectivity is the unique feature for the modification which is only possible with ion beam technology. Due to this remarkable feature, ion beam provides the unique facility to engineer the materials for potential applications.

### **1.5.2. Thermally induced modifications**

In the case of thin films, thermal annealing is a process used for structural, optical, electrical improvements and intrinsic stress liberation. In this process, direct heat energy supplied to the target material for selective time to modify the material properties. Different annealing parameter such as annealing temperature, annealing environment, annealing time and ramp rate are directly related with the alteration of properties. In present thesis, role of thermal annealing over the pure ZnO and metal-ZnO nanocomposite have been discussed in detail. Furthermore, comparison of thermal annealing and SHI irradiation induced modifications have been observed for the both ZnO and Ag-ZnO nanocomposite thin films.

### **1.6. Objectives of the thesis**

The objective of the present thesis are as follows:

1. Synthesis and characterizations of pure ZnO thin films as a host matrix by RF sputtering technique and the investigation of modifications in their properties by SHI irradiation and thermal annealing.
2. Synthesis and characterizations of Ag-ZnO nanocomposite thin films by RF sputtering and ion implantation.
3. Investigation of SHI irradiation and thermal induced modifications in the structural and optical properties of Ag-ZnO nanocomposite thin films.

### **1.7. Organization of thesis**

**Chapter 1.** Describes the introduction for the nano-science and nanotechnology. Brief introduction about the nanocomposite thin film and nanoparticles followed by the structure and properties of Ag as a filler and ZnO as matrix have been presented. Ion-matter interaction has also been described briefly in this chapter.

**Chapter 2.** Includes the extensive literature for the annealing study of the pure ZnO and Ag-ZnO NC thin film as well as ion induced modifications.

**Chapter 3.** Introduces the experimental techniques used for the synthesis and characterization of NC thin films. RF sputtering and ion implantation were used for the synthesis of NC thin films. Various characterization techniques used in the present study such as RBS, X-ray diffraction, UV-visible spectroscopy, scanning electron microscopy, atomic force microscopy, Raman spectroscopy, photo-luminance spectroscopy, x-ray photoelectron analysis, transmission electron microscopy are described in this chapter.

**Chapter 4.** It covers the detailed discussion about the synthesis of pure ZnO thin film (as a host matrix) by RF sputtering and modifications induced by thermal annealing and ion irradiation.

**Chapter 5.** It explains the detail about the synthesis methods by two different approaches: RF sputtering and ion implantation.

**Chapter 6.** It describes the annealing and SHI irradiation induced modifications in the Ag-ZnO NCs thin film in detail.

**Chapter 7.** It is about the overall conclusion of the thesis work and future scope of the present study.



# Chapter 2

## Literature Review

---

*In this chapter, detailed reports about the nanocomposite thin films has been discussed. Previously reported studies on the thermal and SHI induced modifications in nanocomposite thin films have also been summarized in systematic manner.*

## 2.1. Background

During the last decades, ZnO has been extensively used for various applications such as transparent conductive electrodes, solar cell window, optical devices, piezoelectric transducers and gas sensors because of their remarkable structural, optical and electrical properties. ZnO is a multi-functional material of II-VI group with the large band gap (~3.3 eV). The improvement in the properties of ZnO thin films using different treatments such as doping of novel metal, ion implantation, thermal induced modifications and SHI irradiation techniques is the current area of interest. ZnO thin films show very fascinating properties in comparison to bulk material due to different nanostructured formation and large surface to volume ratio and play the major role to enhance their own properties with reduced cost of the devices as well less material consumption. A detailed literature study on thermal as well SHI induced modifications in pure ZnO thin films and ZnO based nanocomposite thin films is presented in following sections.

## 2.2. Effects of SHI irradiation on ZnO thin films

Ion irradiation is unique technique for the modification in the structural, optical, electrical properties of material in a controlled way. Irradiation induced modifications in ZnO thin films have been extensively observed by many researchers. Some of investigations are summarized below:

- The effect of thermal annealing as well as SHI induced annealing on the structural and morphological behavior of the ZnO thin film was studied by Agrawal *et al.* [49]. The X-ray diffraction confirmed the hexagonal wurtzite structure of ZnO film with preferential orientation in (002) plane. The grain size of the film was increased due to thermal and irradiation induced annealing and lead to better crystallinity due to strain relaxation between film and the substrate. No considerable changes were found in the surface roughness of the film during annealing. The effect on the bonding between Zn-O due to annealing was observed by Fourier transformation infrared spectroscopy (FTIR). It was concluded that SHI induced annealing gives highly textured c-axis oriented ZnO

thin film in comparison of thermal annealing which is much more suitable for the device fabrication.

- P.M Ratheesh Kumar *et al.* [50] prepared spray pyrolyzed ZnO thin film and irradiated using 120 MeV Au ion beam. The SHI induced modifications in structural, electrical and optical properties were investigated in this study. The absorption edge of the film was not affected by SHI irradiation but transmittance of the film was slightly decreased with ion irradiation. The intensity of major peak (002) in X-ray diffraction pattern was continuously decreasing with increasing the irradiation fluence. During irradiation, generation of oxygen vacancies take place and could be responsible for the lower resistivity with higher carrier concentration. Electrical resistivity of the film drastically decreases from 78 to 0.71  $\Omega$  during ion irradiation at higher ion fluence. Metal to oxygen (Zn/O) ratio was increased during ion irradiation confirmed by X-ray photo electron spectroscopy (XPS) due to swift heavy ion irradiation. Antisites oxygen was responsible for the depletion of the defect level which lead to the decrement in the intensity of the PL spectra of the as-deposited and irradiated ZnO thin films.
- S. Rehman *et al.* [51] synthesized nc-ZnO thin films by RF-magnetron sputtering technique and irradiated using 120 MeV Au ion beam. The SHI induced structural and spectroscopic modifications in nc-ZnO thin films were studied in this work. The nanocrystals become more oriented at the lower ion fluence while the grain size was decreased with higher ion fluence. The topographical features of the pristine and irradiated films were estimated using atomic force microscopy and found the agglomerated grains at the higher irradiation fluence. Micro-Raman study of the pristine and irradiated ZnO thin films revealed the modifications in phonon-structure due to disorder and phonon-localization. SHI irradiation is the responsible for lattice defects generation during irradiation and contributes to the phonon-structure of the material. The red shift in longitudinal optical (LO) mode induced by irradiation was observed by FTIR study. Under the SHI irradiation, the amorphization of crystallites was not observed, so such type of films may be useful in radiation harsh environment for optoelectronic device fabrication.

- V. Kumar *et al.* [52] synthesized ZnO/Si thin films by using RF-magnetron sputtering and irradiated with 80 MeV Br ion beam with different ion fluences. X-ray diffraction pattern confirmed stable hexagonal wurtzite structure of ZnO and the shifting in the peak position were observed peak shifting during irradiation. For the lower fluences films goes tensile to rest position and again move to tensile at higher ion fluences confirmed by peak shifting in X-ray and Raman spectra. At the optimal ion fluence  $5 \times 10^{13}$  ions/cm<sup>2</sup> film showed the maximum PL intensity with lower surface roughness. The defects formation in the pristine and irradiated ZnO thin films were investigated by the XPS study and described in details. PL spectra of the film revealed the strong UV emission for the pristine film however the irradiated films showed the strong blue-green coupled emission specially of the above optimal ion fluence. All the structural, morphological and luminescent modifications induced by SHI irradiation have been explained on the basis of thermal spike model.
- Siddharth Mal *et al.* [53] explained modifications in magnetic properties of ZnO epitaxial thin film induced by 300 MeV Ag ion beam. They observed the room temperature ferromagnetic behavior in pure ZnO thin film in the controlled manner by using ion beam irradiation and also increase this nature with increasing the irradiation dose without significant change in structural properties of the film. Electrical and optical modifications were also studied in this report. Raman spectra of the pristine and irradiated films showed the dramatic changes in vibration modes which was subjected to the lattice disorder and non-linear point defects. These results were responsible for the room temperature ferromagnetism and also leads to the generation of the defects during ion irradiation. They also proposed a unified mechanism to explain the room temperature ferromagnetism and n-type conductivity of ZnO thin film after irradiation on the basis of different defects and vacancies induced by SHI irradiation.
- P. Prabukanthan *et al.* [54] successfully deposited ZnO thin films using RF-magnetron sputtering and then irradiated using 100 MeV O ion beam with the fluence of  $5 \times 10^{13}$  ions/cm<sup>2</sup> at two different temperatures: room temperature and liquid nitrogen temperature. The structural modifications were observed by X-ray

diffraction and revealed the reduced intensity of (002) plane with higher FWHM for the film irradiated at liquid nitrogen temperature (LNT) in comparison of the both pristine and room temperature irradiated. The change in transmittance and band gap for the both irradiated film in RT and LNT were estimated by UV-visible transmission spectroscopy. Dramatic change was found in grain size with lower roughness for the case of RT irradiation and it may be due to strain relaxation between the grains during irradiation while in the case of LNT irradiation roughness of the film was increase. The Photo-luminescence analysis of the pristine film confirmed the two strong emissions at 403 nm and 472 nm. However, in the case of irradiation of the film, emission at 472 nm was disappear for both RT as well as LNT irradiation. Concentration of the zinc and oxygen was estimated by the augur electron spectroscopy. Conclusively, structural and optical modifications were found better in the case of RT irradiation.

- D.C. Agrawal *et al.* [55] studied the SHI irradiation induced effects in thermally evaporated ZnO thin film. The ZnO thin films were irradiated by 100 MeV Au ion beam at the fluence range from  $5 \times 10^{11}$  to  $5 \times 10^{13}$  ions/cm<sup>2</sup>. X-ray diffraction spectra for the pristine and irradiated ZnO thin films confirmed the formation of c-axis oriented ZnO thin films with hexagonal wurtzite structure. At the lower ion fluence, the thin film showed the good crystalline behaviour with lower roughness because of the line arrangement of the grains due to irradiation. While the higher ion fluence increases surface disordering which lead to the grain agglomeration on the surface. The agglomeration of the grains is responsible for the higher roughness value. The optical properties of the film were not very much affected by ion irradiation confirmed by the UV-visible absorption spectroscopy and FTIR study. The blue shift was observed in the PL spectra of the film after irradiation which may be due to anti-site oxygen or oxygen vacancies. It was concluded that the ion irradiation at lower ion fluence was more beneficial for enhancement in the properties of ZnO thin film.
- The SHI irradiation induced stress variation in pure ZnO thin films were investigated by Fouran Singh *et al.* [56]. The ZnO thin films were synthesized using pulse laser deposition at room temperature. Further, ZnO thin films were

irradiated by 120 MeV Ag ion beam at various ion fluences. The change in lattice parameter and stress between the grains was observed due to the SHI induced oxygen vacancies. The nature of the stress was found compressive for the pristine and irradiated films and it may be due to defects and dislocation which was confirmed by the micro-Raman spectroscopy and FTIR results. SHI irradiation induced stress shows a good relationship with the ferromagnetism which is responsible for the modifications.

### **2.3. Effect of thermal annealing on ZnO thin films**

Thermal annealing is an effective technique to enhance the material properties such as grain growth, crystalline behaviour and optical nature due to their thermal energy. ZnO thin films exhibit very interesting structural and optical modifications induced by thermal annealing. Some reports related to thermally induced modifications are summarized below:

- The ZnO thin films in amorphous phase were synthesized by Daniel *et al.* [57] using RF magnetron sputtering technique. Thermally induced structural and optical modifications have been observed at different annealing temperatures using different characterization tools like X-ray diffraction analysis, UV-visible absorption spectroscopy and atomic force microscopy. The transformation from amorphous to crystalline was observed at 400 °C and the crystallinity was increased with increasing the annealing temperature. Preferential growth was found in (002) direction with thermal annealing. Particle size was also found to be increased (16 to 27 nm) with increasing the temperature. The average roughness of the films was found to decrease with increasing the temperature which indicated the better optical quality. Band gap of the film also decreased with annealing (3.28 to 3.25 eV) which was confirmed by the band gap analysis on the basis of UV-visible spectroscopy.
- Elilarassi *et al.* [58] prepared ZnO thin films by using liquid-flow deposition method (LF method) and then annealed in the temperature range of 350-550 °C. The annealing effects on the optical properties and surface morphology were observed by different characterization techniques. Polycrystalline behaviour with

(100), (002) and (101) orientations of hexagonal wurtzite structure was observed by X-ray diffraction measurements and crystallite size was increased with higher annealing temperature. Atomic force microscopy has been confirmed the improvement in the grain size with post annealing process. The shape of nanocrystals was estimated by scanning electron microscopy and found to be near hexagonal in nature. The removal of the impurities with thermal annealing were studied in this report. The band gap of the film was found to be increased (blue shift) initially (350°C) and then decreased with increasing (red shift) the temperature (350-550°C). The photo-luminescence (PL) spectroscopy showed the UV emission and defect induced deep-level emission in visible region of the light.

- Zhou *et al.* [59] synthesized the thin films of ZnO by RF sputtering technique. The investigations of the different oxygen/argon flow ratio as well as annealing temperature on the behaviour of ZnO films were studied. XPS results confirmed the shifting of the peak positions in opposite direction with increasing the oxygen/argon flow ratio. Raman spectra of the films revealed the hexagonal wurtzite structure and found the good crystallinity at 420 °C. The band gap of the film decreased first and then increased with annealing temperature confirmed by UV-visible spectroscopy. The PL spectra revealed the change in both violet and green emission peak for the ZnO thin film with annealing as well as intensity of flow ratio (O<sub>2</sub>/Ar).
- The structural and optical properties of sputtered ZnO thin films were studied by Mina Jung *et al.* [60]. The thin film of ZnO were synthesized using sputtering on the silicon (111) substrate and annealed in three different temperatures 700, 800, and 900 °C under oxygen atmosphere. The crystalline behavior of the ZnO thin films were enhanced with annealing temperature up to 800 °C. However, crystalline behaviour found to be deteriorated as the temperature was increased above 800 °C. This behavior of the thin films suggested the inter-diffusion of ZnO layers into silicon substrate and also responsible for poor crystalline behavior at the temperature 900 °C. The understanding of inter-diffusion phenomena between ZnO and silicon was observed on the basis of findings from transmission electron

microscopy and Auger electron spectroscopy. It was observed that the thickness of ZnO layer was reduced with the thermal annealing.

- M. G. Mendez *et al.* [61] have successfully deposited thin films of the ZnO on the glass substrate using RF sputtering. Further, the annealed of the films were performed at the temperature range 100-300 °C in the vacuum. The X-ray diffraction and UV-visible spectroscopy were used to study the structural and optical properties. The various optical parameters were calculated by Drude-Lorentz model with the fitting of transmittance spectra of the films. The crystallinity of the thin films were found to be enhanced with thermal annealing. The optical band gap of ZnO was calculated and observed the decrement with increasing the temperature. This decrement in the band gap have been explained on the basis of Burstein-Moss shift effect. The variation in plasma frequency and frequency with respect to annealing temperature was also studied in this report.
- Y. E. Jeong *et al.* [62] were grown ZnO thin films by RF-magnetron sputtering and annealed at different temperatures to investigate the structural and optical properties. The X-ray diffraction study confirmed the enhancement in structural parameters due to lattice relaxation at the higher temperature. The thermal expansion coefficient of the ZnO film and substrate was different which may be directly affected to the lattice mismatch of the film. As the annealing temperature increases, the crystalline quality of the film increases and the peak corresponding to (002) orientation of the film become sharper and move towards the bulk values of ZnO (34.4°). This enhancement was also subjected to reduction in the stress of the film. The optical band gap and transmittance of the films were improved with increasing the temperature of annealing. This enhancement in the optical band gap might be related to in-plane stress effect.
- P. Murkute *et al.* [63] have synthesized ZnO thin films on silicon substrate at 400 °C using RF sputtering. To remove the defects occurred during the film deposition, high temperature annealing was performed in the temperature range 700-900 °C in constant oxygen gas flow during annealing. The high temperature annealing helps in the removal of the different zinc vacancies, oxygen interstitials and defects which is subjected to the improvement in the film quality. X-ray



diffraction spectra confirmed the formation of the c-axis orientated ZnO films with hexagonal wurtzite structure. The PL properties were improved with annealing temperature and low temperature PL spectra was also performed for study the near-band-edge emission and found highest peak intensity (for 3.37 eV) at 900 °C and show high quantum yield which is very beneficial for the various device fabrication.

- The effect of annealing temperatures of 400 °C, 600 °C and 800 °C on the RF sputtered ZnO thin films were studied by M. F. Al-Kuhaili *et al.* [64]. The X-ray diffraction analysis revealed the presence of highly (002) orientation of the films. It was also revealed from the X-ray results that, crystallite size of the film increase from 6 nm to 28 nm with the thermal annealing. The average surface roughness ( $R_{rms}$ ) of the films were increased with thermal annealing however, it drastically increases at higher annealing temperatures which may be attributed to grain growth during the annealing. The transparency of the film was reduced with annealing. The reason was attributed to the oxygen vacancies and scattering due to higher roughness of the film. The refractive index of the film was decreased and extinction coefficient was increased at 600-800°C, which was ascribed to the increment in absorption and scattering.
- Duy-Thach Phan *et al.* [65] synthesized ZnO thin film via RF-magnetron sputtering technique and annealed at different temperature. The basic characteristics of the ZnO films were examined with different characterization techniques. These studies were performed to use these films to fabricate the surface acoustic wave (SAW) resonators and found that 600 °C is the optimal temperature for the good SAW devices. In this study, they observed the small grain size and porosity in the film at low annealing temperature with the low surface roughness. At the higher temperature, roughness and cracks were observed to be increased which were responsible for the reduction in resistivity of the film. It leads to the insertion loss or SAW velocity of the ZnO film at higher temperature and shows very weak response of the device.
- The thin films of ZnO were synthesized by sol-gel spin coated method on glass substrate by U. Chitra *et al.* [66]. Further, annealing of the films were performed

at different temperatures 300 °C, 400 °C and 500 °C. The topographical features of annealed films were estimated by atomic force microscopy and found the columnar growth of the film on the surface. The average roughness ( $R_{rms}$ ) of the film enhanced with annealing temperature. The X-ray measurements revealed the polycrystalline nature of the annealed films with increasing in crystallite size. The enhanced optical transparency and reduced band gap were observed after thermal annealing. Other optical parameters (band gap, refractive index and urbach energy etc.) were also calculated by transmittance spectra by the help of single-oscillator Wemple di Domenico model. The band gap of the film was decreased with annealing.

#### **2.4. SHI irradiation of Metal-ZnO nanocomposite thin films**

Some detailed studies describing the modifications induced by ion irradiation in metal-oxide nanocomposite thin films are summarized below:

- The 100 MeV Ni induced modifications in cobalt doped ZnO thin films were studied by Sunil Kumar *et al.* [67]. The Co-ZnO thin film was irradiated with a fluence of  $1 \times 10^{13}$  ions/cm<sup>2</sup> with 100 MeV Ni<sup>7+</sup> ion beam. The film showed single phase corresponding to (002) plane with higher crystallinity while as-deposited film showed three phase and lower crystallinity comparative to irradiated film. FTIR analysis revealed that the bond structure of Zn-O was not affected by cobalt doping as well as irradiation. The decrement in the band gap of the irradiated film was observed which may be due to *sp-d* interaction between the Co<sup>2+</sup> ions and ZnO band electrons. The slight increment in roughness and grain size after ion irradiation was observed by AFM.
- Vinod Kumar *et al.* [68] synthesized boron doped ZnO (ZnO:B) thin film by sol-gel method. They prepared ZnO:B thin film on silicon substrate using spin-coating technique. The prepared films were irradiated by 80 MeV Br<sup>6+</sup> ion beam at the fluence range from  $3 \times 10^{11}$  to  $3 \times 10^{13}$  ions/cm<sup>2</sup>. XRD spectra of the films revealed the hexagonal wurtzite structure and suggested the transformation from the compressive stress to tensile stress with increasing the irradiation fluence. Chemical composition of the film was examined by XPS and the decrement in the

oxygen defects was observed after ion irradiation. Defect level emission (DLE) was observed in pristine ZnO:B thin film while the strong UV emission was found in irradiated film which was confirmed by luminance spectra. These emission band was exponentially associated with the defects and stress in the film which was subjected to swift heavy ion irradiation. So these films could be beneficial in white light emission application.

- The magnetic and structural properties enhancement by SHI irradiation in pure and V doped ZnO thin films deposited by RF sputtering were investigated by G. Jayalakshmi *et al.* [69]. XRD results confirmed the crystalline nature of the thin films and showed a marginal change in the peak intensity and peak position after irradiation. Raman spectra of the films revealed the degradation of crystallinity with SHI irradiation which was also supported by XRD results. The arrangement of the smaller grains during ion irradiation was clearly estimated by AFM. The oxygen defects density was found to be increased with ion irradiation confirmed by photo-luminance analysis. The enhanced ferromagnetism was observed in the case of higher V doping as well as irradiated film. The reason may be assigned to oxygen vacancies produced by swift heavy ion irradiation.

## **2.5. Studies on thermally induced modifications of Metal-ZnO nanocomposite thin films**

Thermal annealing induced modifications in metal-ZnO nanocomposite thin film are described by many researchers. Some reports are present here to understand the thermal induced modifications in Ag-ZnO nanocomposite thin film.

- M. H. Habibi *et al.* [70] synthesized Ag-ZnO nanocomposite thin films by spin-coating method on the glass substrate. The various properties of Ag-ZnO thin films of the films were controlled by the silver content, annealing temperature and preheating temperature. The Ag-ZnO thin films were preheated at the temperatures from 200 to 300 °C and annealed at 550 to 850 °C. The crystallinity of the film increases with annealing temperature while the optical absorbance of the film decreases with increasing the annealing temperature. The amount of silver also plays a major role in absorption properties and observed the maximum

absorption for the Ag content 0.068 M and 0.110 M at 430 nm (surface plasmon band). The variation in the porosity and grain size (68 nm for pure and 370 nm for Ag doped) of the film with the variation in content of Ag were estimated by SEM and AFM. The particle size for the Ag and ZnO was found to be 5 nm and 58 nm, respectively. X-ray photoelectron spectroscopy showed the considerable lower shift in the binding energy of the Ag 3d<sub>5/2</sub> due to interaction between Ag and ZnO in comparison of pure metallic Ag.

- X.B. Wang *et al.* [71] systematically investigated the microstructure, photoluminance and Raman scattering of the DC sputtered Ag-ZnO thin film with different Ag concentration (1.6 - 5.7 at.%). XRD results revealed the presence of stable wurtzite structure in pure and Ag doped ZnO thin films. The wurtzite structure of the film retained after Ag incorporation while the preferred orientation of the ZnO (c-axis) was decreased with increasing the Ag doping. The near band edge emission (NBE) was enhanced for the moderate Ag doping and then quenched with higher doping value. The NBE band also shifted towards the lower wavelength with Ag doping. Raman spectra of the films was confirmed the Ag incorporation into ZnO matrix which evidence by appearance of local vibrational mode at 411 cm<sup>-1</sup>.
- Myung-Ki Lee *et al.* [72] successfully synthesized Au-ZnO and Ag-ZnO composite nanocrystals having a dumbbell-like structure. These nanostructures were synthesized through the nucleation as well as decomposition of zinc hydroxide at the surface of pre-existing Ag and Au nanoparticles. The transmission electron microscopy results confirmed the size of the Au/Ag and ZnO nanoparticles and found to be 4 nm and 10 nm respectively. The very good crystalline behaviour of the Au/Ag nanoparticles with face centered cubic structure and wurtzite structure of the ZnO confirmed by TEM images. The photo-luminance study of the films showed very high PL intensity in lower wavelength region, compared to Au because of higher refractive index and showed strong light scattering effect. The green emission band corresponding to ZnO nanocrystals found to be suppressed due to surface plasmon band of the Au in Au-ZnO composite while remain unaffected in the case of Ag-ZnO composite.

The maximum absorbance for Ag nanoparticles lies in the region 400-420 nm. The enhanced UV-emission was observed in the both case Au or Ag-ZnO composite. It depends on the surface electron transfer from metal to ZnO as well as the extension of the Fermi level to the ZnO.

- L.N. Wang *et al.* [73] prepared Ag doped ZnO thin films by pulse laser deposition method at different substrate temperature 500 °C and 600 °C and observed the effect of annealing on the composite films annealed at temperature 700 °C. The Raman spectra was studied in detail and found the strong  $A_1$  (LO) mode due to oxygen vacancies and zinc interstitials in the Ag-ZnO thin film. An additional mode at  $493\text{ cm}^{-1}$  was also found in the spectra and confirmed the presence of Ag and indicated the Ag incorporation into the ZnO lattice. X-ray diffraction study of the films confirmed monocrystalline behaviour of the film and c-axis orientation during deposition as well as annealing process.
- The Ag doped ZnO thin films were synthesized by A. Tripathi *et al.* [74] by using sol-gel method. The polycrystalline behaviour of the undoped and Ag-ZnO thin films were confirmed by XRD. It was also confirmed that from XRD, the intensity of all the peaks decreased with Ag doping. The particle size was estimated by the Debye-Scherrer formula and found to be 10 to 28 nm. The surface features of the film estimated by the Atomic force microscopy and found the smooth surface of the film. Transparency of the films were very high (70-90%) in the visible and IR region and found the good absorption at 370 nm which was blue shifted in the comparison of bulk ZnO. Two major peaks were found at 393 and 485 nm in UV and visible region as confirmed by PL spectroscopy. The intensity of both the peaks were enhanced with Ag doping which was attributed to the free-hole concentration due to Ag incorporation in ZnO. So they found that Ag is a suitable candidate for the doping in ZnO which lead the free charge carriers which play major role in UV light emission.
- Ag-ZnO thin films were successfully synthesized by RF sputtering technique by R. Deng *et al.* [75]. Furthermore, the effects of variation of oxygen/argon gas ratio on the different properties of the Ag-ZnO thin film were investigated. The composite thin film alters its semiconducting behaviour from n-type to p-type

with increases the oxygen/argon gas ratio. X-ray photoelectron spectroscopy revealed the substitution of the Ag to Zn sites ( $\text{Ag}_{\text{Zn}}$ ) in the ZnO which leads to p-type conductivity. The p-type Ag-ZnO thin films with O-rich conditions was responsible for the depression in donor defects and low formation energy of  $\text{Ag}_{\text{Zn}}$  acceptor. The p-ZnO: Ag/n-ZnO homojunction showed very good rectification properties in the I-V results.

- The thermal induced modifications in RF sputtered Al doped ZnO thin film were studied by Y.S. Park *et al.* [76]. They observed the effect of substrate temperature range from 100 °C to 500 °C on the Al doped ZnO thin film for the organic thin film transistor performance. The conductivity of the thin films was affected by the substrate temperature which affects the transistor performance. The conductivity and crystallinity of the film were found to be increased with increasing the substrate temperature while the surface properties of the film degraded at the substrate temperature 300 °C.
- W.H. Zhang *et al.* [77] synthesized RF sputtered Mo-doped ZnO thin films on Si (111) substrate at different substrate temperatures of 200 °C, 300 °C and 400 °C. The substrate temperature induced modifications in structural and optical modifications were observed in this study. It was found that, the microstructural and optical properties of the Mo-ZnO thin films strongly related to the growth temperature. At the temperature of 200 °C, higher crystalline nature of the film was found. The optical band gap of the films was calculated as 3.18 eV, 3.22 eV, 3.25 eV and 3.21 eV at room temperature and 200 °C, 300 °C and 400 °C respectively. The PL intensity of the broad violet-blue emission was found to be increase with increasing the temperature of the substrate. Surface chemical composition of the films was estimated by the XPS. They observed the substrate temperature play the major role in change the amount of defects which leads the crystalline behavior. These enhanced properties of the Mo-doped ZnO thin film makes them suitable for the modulating the performance of the obtained TCOs.
- Su-Shia Lin *et al.* [78] was prepared pure and Ti doped ZnO thin films by simultaneous sputtering for the ZnO and DC magnetron sputtering for Ti. The XRD spectra of the Ti-ZnO films revealed the formation of the wurtzite structure

and found two major diffraction planes at (002) and (103) while (002) was observed as a preferential orientation. They observed the substrate temperature dependent modification in the Ti doped ZnO thin film in the range of 50 °C to 200 °C. The crystalline behaviour of the film was improved up to 150 °C, and then it slightly decreased at the temperature 200 °C. The surface properties significantly affected by the temperature of the substrate and it leads to the enhancement in the carrier mobility in the film. The free electrons in Ti doped ZnO thin films may be originated from Ti donors and oxygen vacancies and mean free path of the charge carriers was found very shorter. Therefore, grain boundary scattering could be accusers there. The resistivity of the Ti-doped ZnO film at 100 °C was estimated  $9.69 \times 10^{-3} \Omega \text{ cm}$ . This low value is due to the higher carrier-concentration and mobility at the certain temperature. At the higher temperature 200 °C, re-evaporation process takes place which is responsible for the reduction in the vacancies and affects the carrier concentration and resulted in the lower resistivity of the films. The Transmittance of the film was decreased with increasing the substrate temperature.

- Li Li *et al.* [79] was synthesized highly conductive and transparent Al-doped ZnO thin film by DC and RF sputtering and study the structural and electrical properties of the film with annealing treatment. The crystallinity of the film improved by annealing treatment for the both cases DC sputtered and RF sputtered Al doped ZnO thin films. However, the RF sputtered film are more optically transparent (85%) than DC sputtered films (80%). The electrical resistivity was found to be lower in the case of DC sputtering. Therefore, RF reactive magnetron sputtering was found to be more suitable technique to achieve the better structural and optical properties as compared to DC sputtering.
- In Soo Kim *et al.* [80] was deposited Ag-doped ZnO thin films by e-beam evaporation technique. The various properties of the films were studied as a function of annealing temperature range from 350 °C to 650 °C in air atmosphere. As-deposited and annealed film at 350 °C showed the p-type conduction and then lost the p-type behaviour with increasing the post annealing temperature. At the annealing temperature 350 °C, film showed the lower resistivity  $7.25 \times 10^{-2} \Omega \text{ cm}$

with hole concentration  $5.09 \times 10^{19} \text{ cm}^{-3}$  and mobility  $1.69 \text{ cm}^2/\text{V s}$ . The presence of Ag with p-type conductivity confirms by the acceptor states which was observed in low temperature PL spectra.

- Hong Seong Kang *et al.* [81] have fabricated Ag doped ZnO thin film (p-type) on the  $\text{Al}_2\text{O}_3$  substrate using pulse laser deposition (PLD). The effect of deposition temperature on different properties were investigated systematically in this report. The substitution of  $\text{Ag}^+$  for  $\text{Zn}^+$  was observed by the shift in (002) plane in XRD pattern. They observed that, a narrow range of deposition temperature from 200-250 °C was suitable for the fabrication of p-type Ag doped ZnO thin films with hole concentration  $4.9 \times 10^{16} - 6.0 \times 10^{17} \text{ cm}^{-3}$ . The PL spectra of the film confirmed the presence of neutral acceptor bound exciton for the p-type Ag doped ZnO thin film.
- Y.K Mishra *et al.* [82] reported the tunability of localized surface plasmon resonance (LSPR) of Au nanoparticles in ZnO matrix by thermal processing. The Au-ZnO nanocomposite thin films were synthesized by atom beam sputtering technique and annealed in Ar environment at the different temperatures from 200 °C to 600 °C. The UV-visible absorption spectroscopy of the film showed the tuning in the LSPR from 505 to 615 nm (red shift  $\sim 110 \text{ nm}$ ) with increasing the annealing temperature. The formation of Au nanoparticles was confirmed by transmission electron microscopy. At the higher annealing temperature (600 °C), Au nanoparticles attached on the top of ZnO which was form in like nano-rod which was clearly seen in the TEM micrographs. The significant enhancement in the Raman signal was also observed by Raman spectroscopy. This tuning in LSPR band of the Au nanoparticles might be useful in plasmonic devices.

## 2.6. Motivation of thesis

After extensive literature survey, it was found that, ZnO based nanocomposite materials have been vastly applicable for the different technological applications. The tailoring of structural and optical properties of this material by different approaches are very effective way to enhance its use in different areas. The energy of SHI beam and the incident fluence are the key parameter to tune the materials properties. Different annealing



parameter also responsible for the material modifications. After go through the extensive literature survey, we found following research gap which is need to do more investigations:

- ✚ *There is no reports on comparative study between the thermal and SHI induced modifications in Ag-ZnO nanocomposite thin films.*
- ✚ *There is no reports to formation of metal nanoparticles in ZnO matrix by negative ion implantation facility.*
- ✚ *Few investigations are reported on implantation induced modifications in oxide matrix.*

The motivation of this study is to elaborate the understanding about the thermal and ion induced modifications in nanocomposite thin films. Therefore, the effect of SHI irradiation and thermal annealing on structural and optical properties of film is required. The current research work is devoted to optical properties enhancement of the nanocomposite film which can be very much advantageous for the different plasmonic applications.



# Chapter 3

## Materials and Methods

---

*This chapter deals with the synthesis and characterization techniques which has been used to carry out this work. Diverse characterization techniques are used and described along with the brief introduction to the swift heavy ion accelerator as well implantation facility.*

### **3.1. Thin film deposition techniques**

Thin film possess attractive properties due to the size and structure. When the materials have been synthesized in form of a layer ranging from fraction of nanometer to micrometer in thickness, known as thin film. Less material requirement, controlled synthesis and less space are required for the formation of thin film which makes it can have versatile applications [83,84]. Thin film play the important role in modern research area for the study of material with unique properties due to nano-scale region. There are different physical vapour deposition (PVD) and chemical vapour deposition (CVD) techniques which are used for the synthesis of the thin film but every method of deposition has unique advantage and disadvantage. So it is necessary to know the appropriate technique for the film deposition on the basis of required characteristics and application of interest. For example Sol-gel method is very cheap and easy to synthesize the thin film where no requirement for the vacuum and sophisticated instruments but the failure of this technique is uniformity and controlled thickness of the film. Second, pulse laser deposition is the very good technique for the homogenous and higher crystalline thin film for different device fabrication application but is very expensive and required very costly instrument and installation facility.

Physical vapour deposition is the very ancient and effective technique to fabricate the nanocrystalline thin film with controlled thickness and composition of the material. Electron beam sputtering, DC/RF sputtering, Arc deposition and pulse laser deposition are the major technique under the PVD for film deposition. Among the different technique, sputtering is more advantageous technique due to very good control of stoichiometry and deposition rate which is necessary for the large area uniform thin film deposition. In the present case, Pure and Ag-ZnO nanocomposite thin film synthesized by RF magnetron sputtering. The detailed structure and working of the RF sputtering describe below:

#### **3.1.1. RF magnetron sputtering**

Sputtering is a very efficient physical vapour deposition technique for the good quality thin film fabrication. In this technique, energetic non-reactive ion of inert gas bombard on the target material which created by potential difference between the electrodes (**Figure**

**3.1).** During this process, atom of the target material eject out form the target due to collision between gas ions and target material fly from the target in straight line and accumulate on the substrate in the vacuum chamber. Standard physical sputtering is driven by basic physical phenomena, momentum exchange between gas ions and atom of the target material during the collision. The main factor which involve in the sputtering process summarize following manner:

- Generation of the plasma which contains the inert gas ions and electrons in the vacuum chamber by applying the huge potential between anode and cathode.
- Ejection of the target atoms due to bombardment of ions
- Involves vaporization of target atoms by momentum transfer from energetic ions.
- Motion of ejected target atoms through the plasma towards the substrate.
- Accumulation of the target atoms on the substrate leads the formation of high quality thin film of the material.

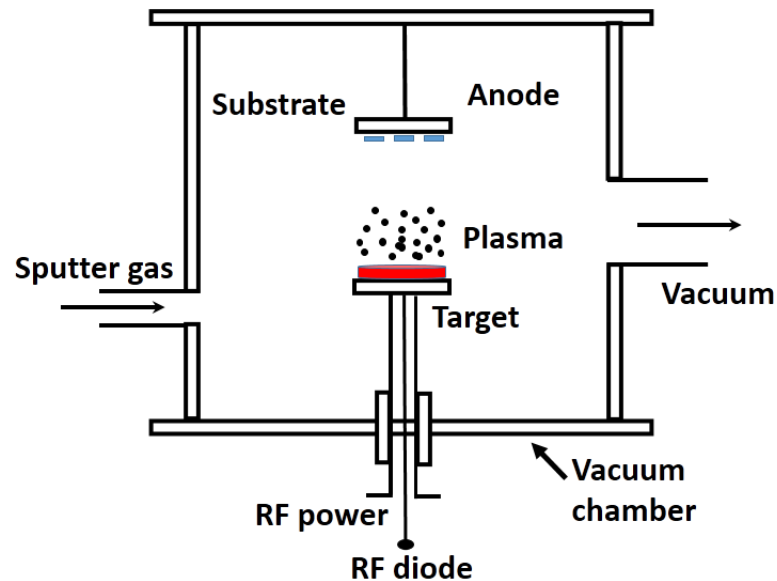


*Figure 3.1 Schematic diagram for the RF sputtering.*

**Sputtering configuration parameters:**

- Power supply
- Target design
- Substrate geometry
- Working gas

**Advantage of sputtering:**

- High uniformity of the film at large area.
- Ability to deposit the films with the stoichiometry of the original target composition
- Good adhesion with thickness control
- Increased deposition rate
- Reduced substrate heating from electron bombardment during deposition
- Reduced working gas pressure requirement
- Ease of conversion to industrial-scale processing

**3.1.2. Negative ion implantation**

Ion implantation is unique technique whereby the energetic ions of the energy of 10 to 500 keV introduce into near-surface region of the target material. The range of incoming ions is usually from 100 Å to 1 μm which depends on the incident ion energy and target material. So it is universal technique of the surface modification in controlled manner.

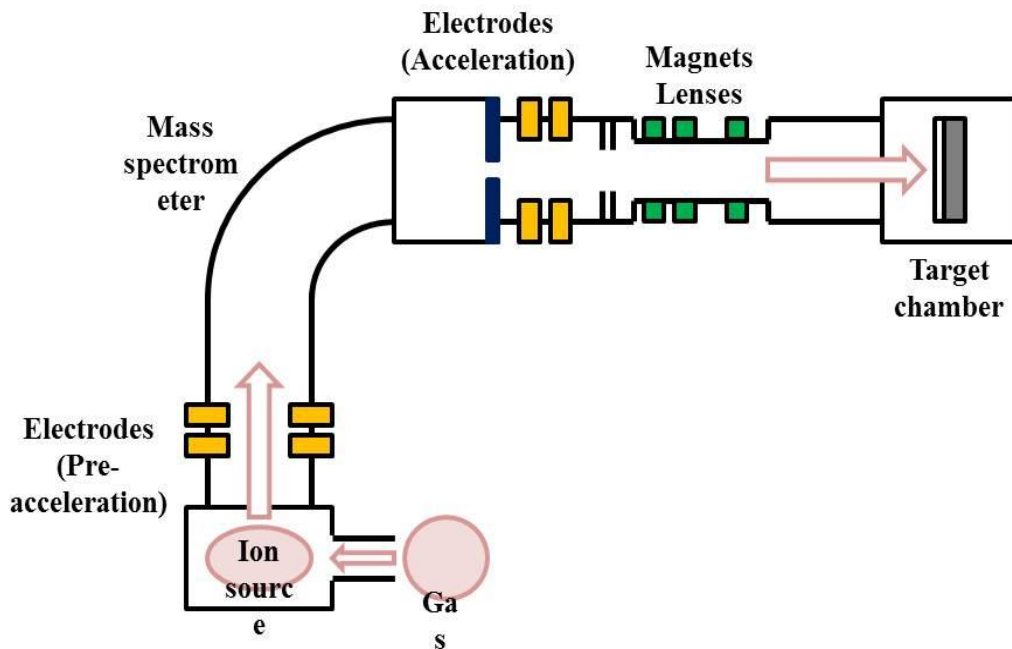


*Figure 3.2 Negative ion implantation facility at the IUAC New Delhi.*

In the semiconducting industry, implantation is widely used for the device fabrication because it provided the facility of selected area impanation with required dose which is not possible in other method. For generate the metal ion beam, inert argon gas is ionized and generate the positive ions which are attract by the negatively biased metal target. Due to this interaction between positively charged ions and metal target, the pure metal atoms and ion are come out form the target. These metal ions are extracted and focused into a beam and imposed on the sample material. **Figure 3.2** is showing the schematic diagram of the ion implanter facility at IUAC, New Delhi. In the present research scenario, ion implantation has very attractive to research community because its unique feature. The well-directed metal ion beam is buried into the surface of the target material which produced a selective doped region and modify the material properties with very high lateral resolution using conventional masking technique. This technique is very much useful in device fabrication, power surface modifications, nanoparticles formation in different material, catalysis and light emitting devices and quantum devices. In the present study, 100 keV Ag ion beam was use for the implantation in the ZnO thin film for the formation of the Ag-ZnO nanocomposite material with Ag nanoparticles.

### **3.2. Modification techniques for engineering the properties of the materials**

When the energy of accelerated charged particle is  $> 1$  MeV and the velocity of particles more than the velocity of Bohr electron, is called swift heavy ions. In the case of swift heavy ions, electronic energy loss ( $S_e$ ) is greater than the nuclear energy loss ( $S_n$ ). SHI has been extensively used for modify of the different properties such as (structural, magnetic, electrical and optical) of the materials in controlled manner. These modifications in the material are appraised by interaction between incoming ions and target atoms which is followed by the energy of incident ion, nature of ion species and irradiation dose. Depending the energy of the ions, accelerators are divided mainly in two part (a) low energy accelerator (few keV to few hundred keV) based on elastic collision with higher nuclear energy loss (b) high energy accelerator (few MeV to GeV) based on inelastic collision with higher value of electronic energy loss. In the SHI, when incoming ions passes through the material, they lose their energy along the ion path in the target

material. This huge amount of energy is the responsible for the material modifications like creation of defects, rapid annealing, track formation and crystallization/amorphization through the ion path. The energy and dose of incident ions are play a major role in the material modification and can be easily controlled. So SHI irradiation provides the unique facility to tailoring the properties of the materials as per the requirement.

### **3.2.1. Swift heavy ion (SHI) irradiation**

In the present study, 15 UD pelletron accelerator facility at IUAC, New Delhi (India) was used of sample irradiation. This tandem Van de Graaff type electrostatic accelerator provides the higher energy (few MeV to hundred MeV) beam of different ion species. The different ion species are available and controlled by the MC-SNICS (multi cathode source of negative ions by cesium sputtering) ion source which present at the top of accelerator. The MC-SNICS ion source can produce the negative ions of the energy range from few  $\mu\text{A}$  to several mA with almost 40 different ion species. The schematic diagram of the 15 UD pelletron accelerator is shown in **Figure 3.3** with the MC-SNICS ion source. This sputtered source is use for accelerate the cesium ion which striking on cold cathode and produce a negative ion beam (energy  $\sim 250$  keV) of cathode material. A thin layer of the cesium ion condensed on the surface of the cathode which leads to more negative ion production from the cathode.

The negative ion beam of the metal pass through the pelletron which is installed in the vertical stainless steel tank with height 26.5 m and diameter 5.5 m. In the middle of the tank, there is very high potential terminal (with potential gradient 4 to 16 MV) while the top and bottom of the tank are grounded. To avoid the spark inside the tank due to very high voltage, the tank is filled with sulfur hexafluoride ( $\text{SF}_6$ ) gas at the pressure of 6-7 bar which is always maintain in the tank.



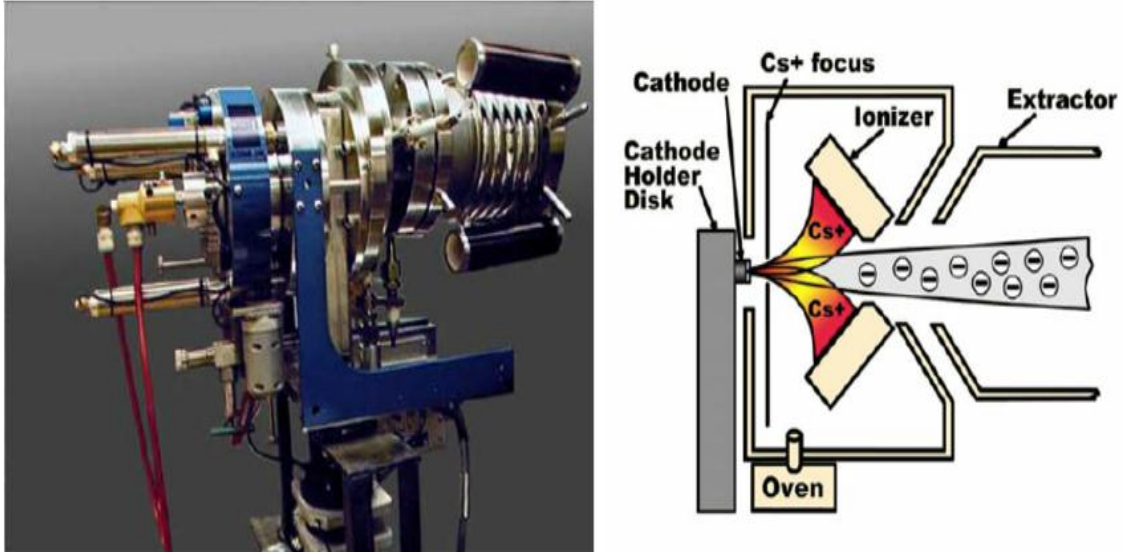


*Figure 3.3 MC-SNICS ion source of the accelerator.*

The ejected negative ions from the ion source are turned in the downward direction to the terminal by the  $90^\circ$  dipole magnet called “injector magnet” (shown in **Figure 3.4**). These negative ions travel from the top of the tank to the positive terminal. This positive potential accelerates the incoming negative ions. At the terminal, the accelerated negative ions pass through a stripper ( $N_2$  gas or C foil) which knocks out the electrons from the negative ions, and then these negative ions transform into positive ions. After the electron ejection, the transformed positive ion beam is again repelled by the applied positive voltage. Due to this repulsion, the positive ion beam travels with double acceleration from the terminal to the bottom of the tank and finally passes through the “analyzing magnet” which selects the final energy and charge state of the ion beam. One more switching magnet is also installed there for switching the beam to the selected area. The final energy of the ion beam is calculated by the given formula:

$$E_{Total} = E_{injector} + (1 + q) V \quad (3.1)$$

where  $q$  is the charge state after stripping at the terminal,  $V$  is the terminal voltage and  $E_{injector}$  is the energy of the ion from the deck. The charge state  $q$  depends on the terminal voltage and the stripper material.

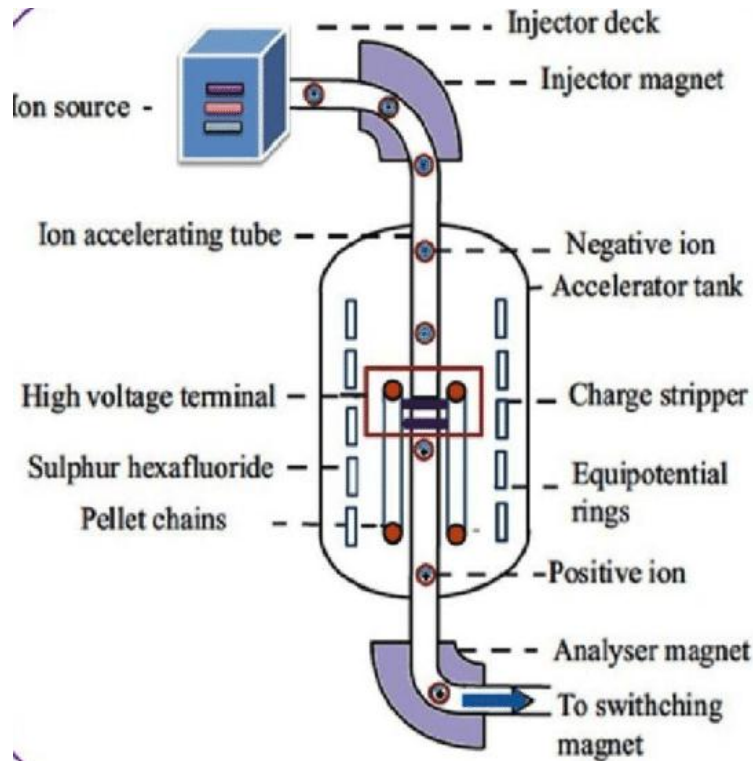


**Figure 3.4** Schematic diagram of the 15 UD pelletron accelerator at IUAC New Delhi.

**Material Science beam line at IUAC New Delhi**

In the IUAC New Delhi, there are 7 different beam line which divided by the switching magnet. Among of them, one beam line is devoted to the material science experiment which is at 15° form the zero degree beam line. Material science beam line has ultra-high vacuum irradiation chamber with the 68 cm diameter and made by stainless steel.



**Figure 3.5** High vacuum irradiation chamber of Material Science beam line at IUAC New Delhi.

This chamber is connected with the turbo molecular pump backed by rotary pump to create the high vacuum (order of  $10^{-7}$  mbar) in the irradiation chamber during sample irradiation. A four sided sample holder (usually called target ladder) is use for hold the sample for the irradiation which made by copper. The CCD camera is also installed in the irradiation chamber to see the sample position during the experiment. The beam is scan over the sample in X and Y area within the dimension of  $10 \times 10$  cm<sup>2</sup> with the help of electromagnetic scanner. The irradiation dose (fluence) for sample irradiation is the crucial parameter for the modifications. This fluence is calculated by the number of count using the Faradey cup by using given formula:

$$Time = \frac{fluence \times A \times e}{(i/q)} \quad (3.2)$$

Where q is the ionic charge state, A is the area of the sample, (i/q) beam current in pA and fluence in calculate in the ions/cm<sup>2</sup>. In the present sturdy, 100 MeV Ag ion beam with different irradiation fluence was used for the sample irradiation and observed the ion induced structural, electrical and optical modifications. The photograph of the irradiation chamber facility at IUAC is shown in **Figure 3.5**.

### **3.2.2 Thermal annealing**

Thermal annealing is also good technique for the material modifications. It is simple technique to modify the material properties. Different annealing temperature and annealing environment can change to alter the material properties as per requirement. In the case of thermal annealing, atoms of the material acquire the energy from thermal treatment and play the major role in tuning the properties.

## **3.3. Characterization techniques**

### **3.3.1. Rutherford backscattering spectroscopy**

Rutherford backscattering spectroscopy is widely used for the determination of atomic species, concentration of species and thickness of the film with very good accuracy because it's directly based on the collision between atomic nuclei of the target materials. It is quantitative, non-destructive technique with very good resolution of the order of nm and very sensitive for the heavy elements. In this technique, when the incident ions

(energy typically in the range of 500 keV to 5 MeV) passes through the target material, they lose their energy and scattered by target atoms of the different masses. The energy of back scattered ions are detected by solid state detectors which kept at a small solid angle in the instrument and provide the direct information about the target atoms and various facets of the sample. The interaction between incoming ions and target atom can be explain on the basic of elastic collision between them. The number of backscattered ions form the target atom for a given number of incident ion collected in a certain solid angle is called differential scattering cross-section and explain in given manner:

$$\frac{d\sigma}{d\Omega} = \left[ \frac{Z_1 Z_2 e^2}{4E} \right] \frac{4}{\sin^4 \theta} \frac{\left[ \sqrt{1 - \left[ \frac{M_1 \sin \theta}{M_2} \right]^2} + \cos \theta \right]^2}{\sqrt{1 - \left[ \frac{M_1 \sin \theta}{M_2} \right]^2}} \quad (3.3)$$

Where

$M_1$  = Mass of incident ion

$M_2$  = Mass of target atom

$Z_1$  = Atomic number of incident ion

$Z_2$  = Atomic number of target atom

$E$  = Energy of incoming ions

$e$  = Charge of electron ( $1.6 \times 10^{-19}$  C)

$\theta$  = Scattering angle

The energy of backscattered particle change due to elastic collision with the target atom, this loss of the energy directly depend on the stopping power of the material and also influenced by inter-collision of incident ions. The ratio of scattered ion energy and incident ion energy is called the kinematic factor and explain in such manner:

$$K = \frac{E_{scattered}}{E_{incident}} = \left[ \frac{\left[ \sqrt{1 - \left[ \frac{M_1 \sin \theta}{M_2} \right]^2} + \frac{M_1 \cos \theta}{M_2} \right]}{1 + \frac{M_1}{M_2}} \right]^2 \quad (3.4)$$

All symbols are explain in above expression. In the RBS setup, three major components are present for the compositional analysis of the target film which are describe following manner:

- (1) Ion source (usually alpha particles  $\text{He}^{2+}$  ions)
- (2) A linear particles accelerator (energy range 0.5 – 3 MeV)
- (3) A solid state detector for the energy measurement of scattered ions

A schematic diagram of experimental setup of RBS spectroscopy is shown in **Figure 3.6**. RBS is very unique technique for the compositional analysis without need of any reference material. The different software such as RUMP, SIMNRA and XRUMP are available for the simulation and analyze the RBS spectrum for getting the different material information like thickness and composition [85].

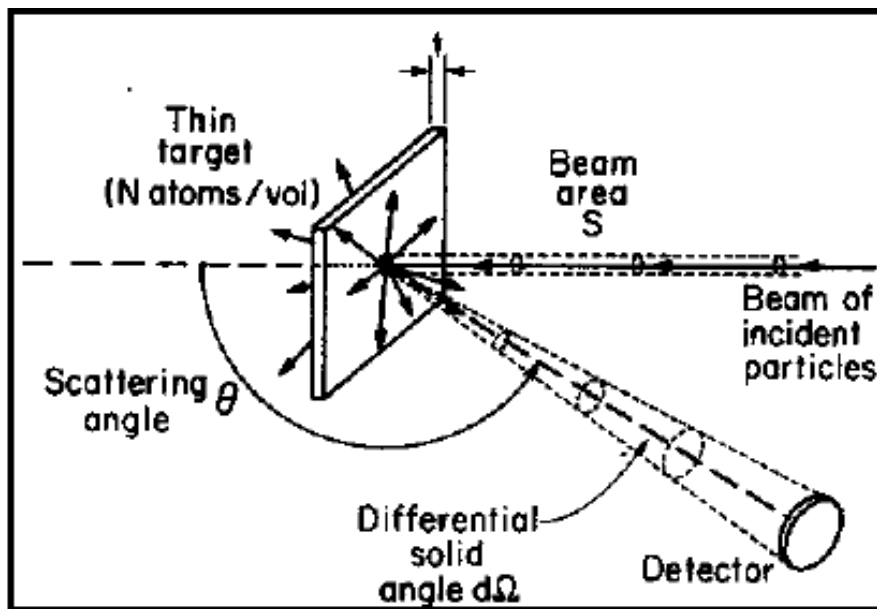


*Figure 3.6 Schematic representation of RBS setup.*

### 3.3.2 X-ray diffraction spectroscopy

X-ray diffraction, a fundamental technique, is used to gather the crystallographic information about the material to be investigated. A material acts as 3D grating for the X-ray diffraction as the wavelength of the beam is nearly comparable to the atomic size and it is well explained by W. Bragg. According to Bragg's diffraction, when a monochromatic X-ray beam incidents on the material at an angle  $\theta$ , it gets diffracted at

angle  $2\theta$  with the incident beam (as shown in **Figure 3.7**). The diffracted beam interferes constructively or destructively depending on the path difference. The diffracted beam is collected by the detector and the crystallographic information of the material can be extracted. A very well-known equation known as Bragg-relation which is corresponding to the constructive interference, is as follows [86]:

$$n\lambda = 2d \sin \theta \quad (3.5)$$

Where,  $n$  = order of reflection,  $\lambda$  = wavelength of incident X-rays,  $d$  = interatomic spacing between lattice plane and  $\theta$  = diffraction angle. Debye-Scherrer's formula have been used in the present study to calculate the grain size ( $D$ ) of pure and Ag-ZnO composite thin films [87]:

$$D = \frac{0.9\lambda}{\beta \cos \theta} \quad (3.6)$$

Where,  $\lambda$  = wavelength of X-rays,  $\beta$  = full width at half maxima of diffracted peak,  $\theta$  = diffraction angle. The strain was also estimated by following relation:

$$\varepsilon = \frac{\beta \cos \theta}{4 \sin \theta} \quad (3.7)$$

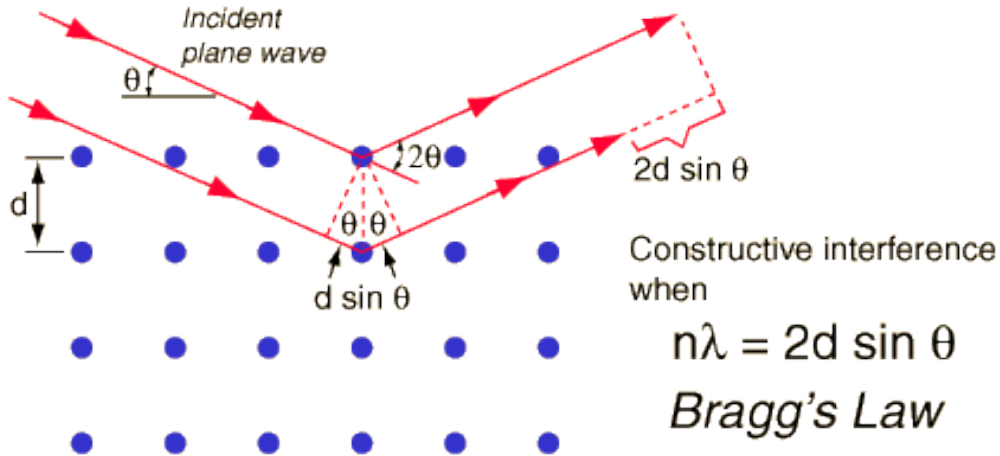


**Figure 3.7** Schematic representation for the Bragg's diffraction.

### 3.3.3 UV-visible spectroscopy

When the radiation is incident on the materials it gets absorbed by the electrons and they get excited from ground state to higher states. In UV-visible spectroscopy, the radiation consists of UV and visible part of electromagnetic spectrum and generally in ranges from

190 nm to 900 nm. UV-visible spectroscopy is greatly used for quantitative analysis of the materials and using for determine of the band gap of the material. As the energy is quantized and the transition occurs at the fixed value of energy so the peak obtained in the spectrum should be sharp peaks. But, only broad peaks are observed because of the number of vibrational energy levels for each electronic energy level and the transitions occur among the different vibrational energy levels. The set up for the UV-visible spectrophotometer is shown in **Figure 3.8**. Usually two lamps are required for both UV and visible radiation; deuterium lamp for the UV radiation and tungsten lamp for visible radiation. The function of diffraction grating is to separate the required radiation and the slit ensures the narrow waveband. The radiation passing through the reference cell and the sample are incident on the photodiode or photomultiplier which converts the photons into current. The spectrum is generated by comparing the current produced by reference cell and the sample. Modern instruments are self-calibrating.

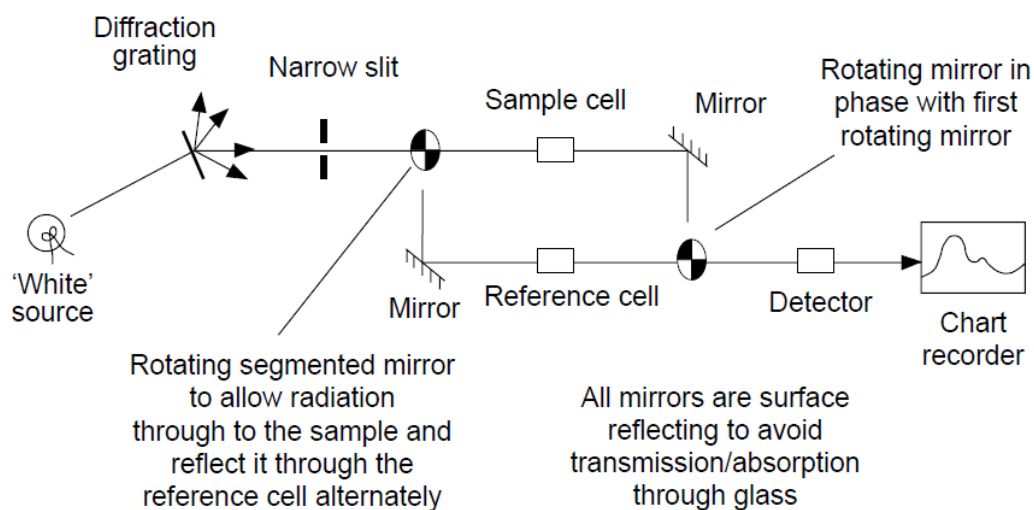


**Figure 3.8** Schematic of the working of UV-visible spectrophotometer.

The principle of absorption spectroscopy is based on Beer's and Lambert law [88]. According to Beer's law the absorption is directly proportional to the concentration of absorbing molecules (i.e. the number of absorbing molecules in path of radiation). Lambert's law states that the radiation absorbed by the molecules does not depend on the intensity of radiation. By combining these two, Beer-Lambert law described as:

$$\log_{10} \left( \frac{I_0}{I} \right) = \epsilon \cdot b \cdot c \quad (3.8)$$

Where,  $\epsilon$  = wavelength dependent absorptive coefficient known as molar absorption coefficient (molar extinction coefficient),  $b$  = path length in cm,  $I_0$  = intensity of incident radiation,  $I$  = intensity of transmitted radiation and  $c$  = concentration in mol/dm<sup>3</sup>.  $\text{Log}_{10}(I_0/I)$  refers to the absorbance of the material and can be directly found from the absorbance spectrum (a plot between absorbance and wavelength) referred as “absorbance unit”. Absorbance is a function of concentration and the path length while  $\epsilon$  (molar extinction coefficient) is independent of them. Other important information is the wavelength ( $\lambda_{\text{max}}$ ) at which the maximum absorbance occurs. It is used to identify the material. On the other hand, if  $\epsilon$  and  $\lambda_{\text{max}}$  are known then the concentration of the solution can be measured which is a common application of this spectroscopy. Another application is to calculate the band gap. The optical energy band gap of a material can be calculated using Tauc’s relation [89]:

$$(\alpha h\nu)^{1/n} = A(h\nu - E_g) \quad (3.9)$$

Where  $E_g$  is the energy band gap,  $A$  is absorption coefficient and  $h\nu$  is the energy of incident photon. Extrapolation of the tangent at the absorbance edge in Tauc’s plot gives the value of the band gap of the material.

### 3.3.4 Atomic force microscopy

AFM is an important part of scanning probe microscopy (SPM) which has been widely used in the field of material science, medical science and nano-technological applications. It was invented by Binnig, Quate and Gerber in 1986 with an aim of imaging the non-conducting samples also. Generally, it is used to observe the morphological behaviour of the thin films of almost all the materials [90]. In the AFM, a sharp metallic tip (at the end of cantilever) interacts with the surface of the thin films and produce the Vander Waals force between tip and surface of the sample depending on the undulation in the surface of the thin films. Tip scan the sample with the help of a piezoelectric scanner as a raster scan. There are three modes of operation of AFM; contact, non-contact and tapping.

In the contact mode (repulsive force), tip scans over the sample surface during imaging in a close contact with the surface. During the raster-scan, metallic tip goes along the surface of the material and found the vertical deflection of the cantilever, these deflections indicate the material height as well the features of the material’s surface. This



deflection is sensed and if it is different from the set value the feedback circuit comes into to play. In noncontact mode (attractive force), the metallic tip does not touch the sample surface and gives the topographic images of the material due to attractive forces.

In the tapping mode, the cantilever is driven to oscillate up and down close to the resonance frequency due to presence of piezoelectric material which is mounted on the scanner. This is an advance mode of AFM. The tip intermittently touches the surface. This mode is very much effective for the scanning of the soft material like polymer and membranes due to its non-destructive nature in comparison of contact mode. Surface damage possibilities are reduced in this mode because tip does not drag across the sample during scanning [3].

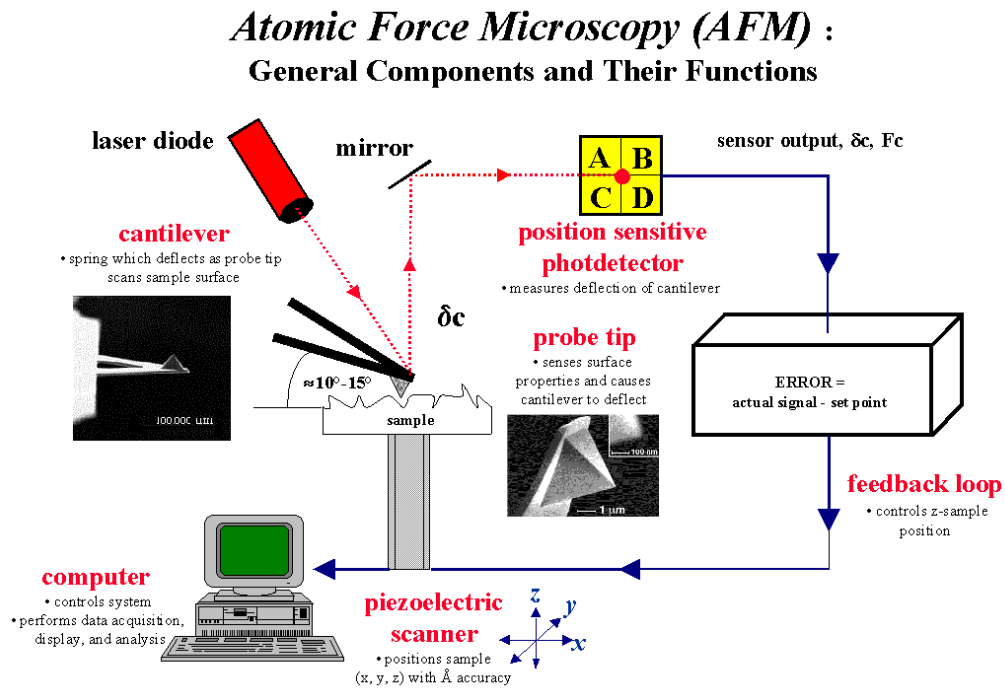


**Figure 3.9** Schematic for working of AFM.

**Figure 3.9** shows the schematic diagram for the working of the AFM. When the cantilever bends due to the undulation in the surface of the sample, the path of laser beam also deflected which leads to deviation in the position of central spot in the photodiode. The force between the tip and sample is responsible for the fluctuations in cantilever.

$$F = ks \tag{3.10}$$

Where,  $k$  = spring constant and  $s$  = bending distance for the cantilever during imaging [2]. The cantilever of the AFM is made up of silicon nitride or silicon material with a

very sharp tip (width of few  $\sim 10$  nm) which provide the facility to observe very high-resolution image on nanometer scale.

In the present thesis, the pure and Ag doped ZnO thin films were characterized using AFM (Bruker, spring constant  $\sim 0.4$  N/m, resonant frequency  $\sim 70$  kHz) in scan-assist mode which is similar to the tapping mode.

### **3.3.5 Scanning electron microscopy**

SEM is another electron microscope launched in 1938 by Von Ardenne and was first commercial in 1965 due to the additional feature of scanning the beam over the surface of sample. The highly energetic and focused electron beam interacts with surface of sample get the structural and chemical information of the sample. Scattering of the electron beam can be avoided by maintaining the required vacuum in the system. Following information about the specimen can be produced from SEM; Topography, Morphology, Compositions and Crystallographic information [91].

The image of instrument along with the schematic is represented in **Figure 3.10**. At the top of instrument, electron gun is present which produces a very fine electron beam (diameter  $\sim 0.01$  mm) in the range of 2-40 kV. The first condenser lens is used for controlling the beam. To eliminate the high-angle electrons from the beam, condenser lens works in conjunction with condenser aperture. The second condenser lens utilized to form the very thin, tight and coherent beam and is controlled by the “fine probe current knob”. Generally, minimum probe diameter and maximum probe current is to be optimized which depends on spherical aberration, brightness and accelerating voltage. Probe diameter directly affects the resolution and it can be optimized by optimizing the brightness. Brightness is directly proportional to accelerating voltage. However, high accelerating voltage limits the resolution, as the volume of generation X-rays becomes more. A set of scan coils are used for the scanning of electron beam on the surface of specimen during imaging. The electron beam interacts with the surface of the sample and this interaction were displayed on CRT monitor with the help of detectors. When the electron beam interact with the sample a number of signals produced and broadly divided in two categories; electron signals and photon signals.

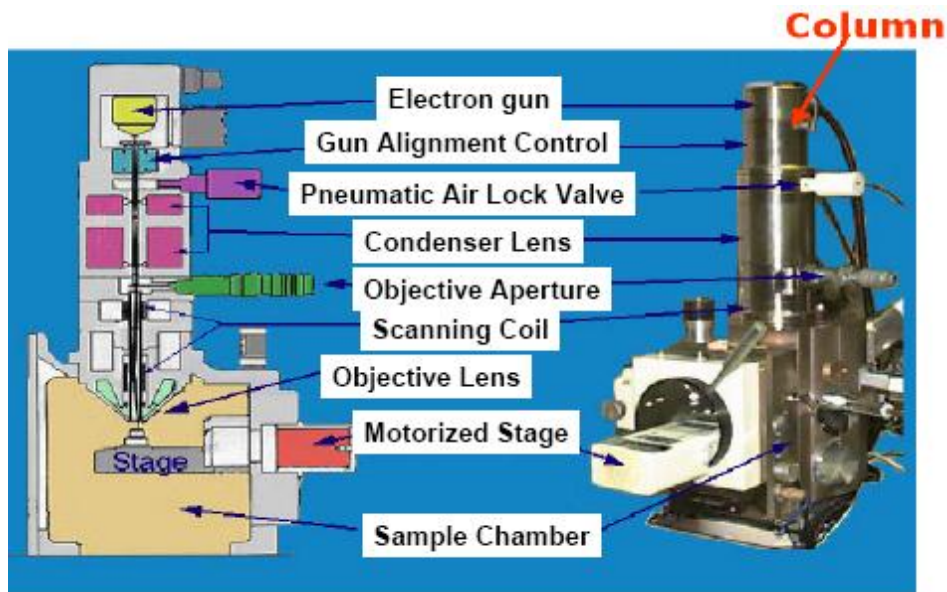


*Figure 3.10 A look inside SEM.*

Mainly two type of the signals are considered for the imaging in SEM and; (a) Secondary electrons (b) Backscattered electrons and for elemental analysis, EDX is used.

Secondary electrons provide the topographical information about the specimen as they are the low energy electrons (5 eV) and are emitted from a depth of nearly 10 nm from the surface. The yield of secondary electrons depends on the atomic number of the material to be investigated and the angle of incidence of electron beam. The electrons are collected by a separate detector used for secondary electrons. Backscattered electrons are comparatively high energy electrons and are backscattered from the specimen from higher depth. Their production rate directly depends on the specimen's atomic number. When the elections are emitted from the surface the vacancies are created which are to be filled from the electrons present in higher shells. As a result, X-rays are produced which are collected by EDX detector and provides the information which element is present in the specimen and their relative abundance also. For imaging point of view, secondary electron mode is the most commonly used (**Figure 3.11**). In the present work, pure and nanocomposite thin films were characterized by SEM (Nova Nano FE-SEM 450 FEI) with an accelerating voltage of 15 kV.

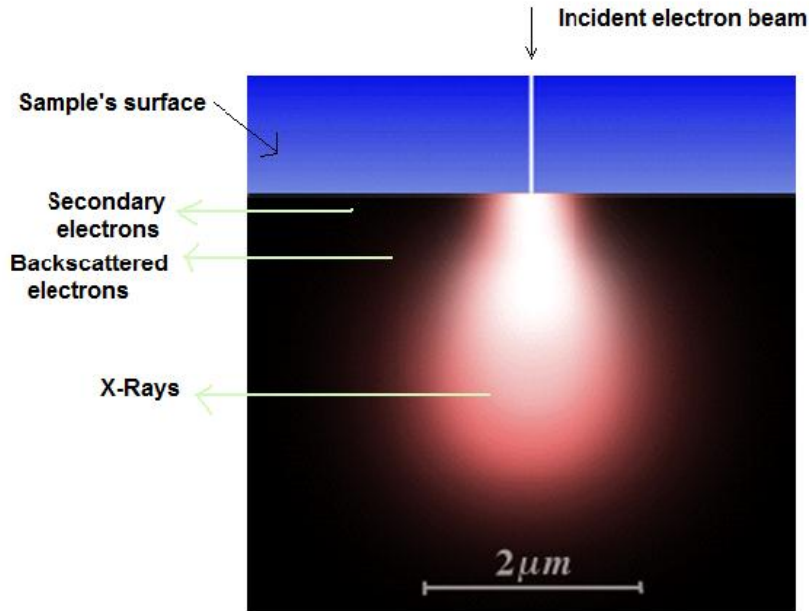


*Figure 3.11 Interaction volume for the interaction of electron beam with the specimen.*

### 3.3.6 Transmission electron microscopy

TEM is a technique used to collect the structural and chemical information about the sample, for which an electron beam is transmitted through the sample. The sample is need to be ultrathin, less than 100 nm so that the electrons can gets transmitted through the samples and image is formed as a result of the interaction of the electrons with the sample. Figure shows the schematic representation of TEM. An electron beam is generated by electron gun, which consists of filament, basic circuit and extraction anode and the electron beam is accelerated at high potential  $\sim 100\text{-}400$  kV. Generally, tungsten and  $\text{LaB}_6$  filament are used due to their high melting point and low work function respectively. Further, a fine beam is obtained with the help of different condenser lenses (magnetic lens). This collimated beam is incident on the sample and the electrons interact with matter and transmitted through the sample. Transmitted beam of electrons again collimated with help of another lenses and made to fall on CCD sensor which response to form a very high-resolution image of the sample [92]. There are the different imaging methods in TEM which attempts to modify the electron beam transmitted through the sample in such a way that the different information can be extracted about the sample; contrast formation, diffraction and three dimensional imaging. On the basis of contrast

formation, two modes are considered: (a) Bright-filed image mode (b) Dark-filed image mode. In these modes the image is formed on the basis of contrast formation of diffracted and not diffracted electrons from the samples.

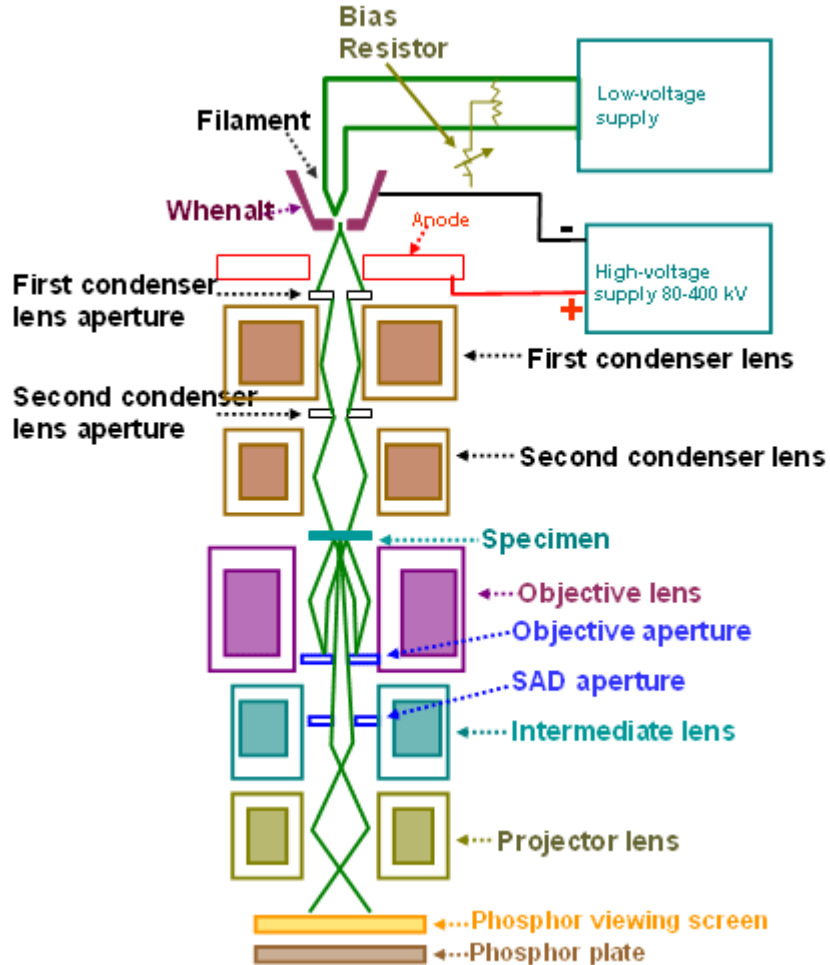


*Figure 3.12 Schematic diagram of the TEM.*

In bright field imaging, the word “bright field” is used for the bright background which means the thicker regions or the higher density regions of samples appear dark and the thinner or no sample regions appear bright. While, in dark field imaging, the diffracted beam appears bright and not diffracted beam appears bright. This can be done with the tilting of sample and it is used to observe the diffracted beam (**Figure 3.12**).

In the present study, imaging have been done with most commonly used bright-field mode. A diffraction pattern can also be generated by adjusting the magnetic lenses. The image consists of either a pattern of dots (in case of single crystal) or series of rings

(polycrystalline). The diffraction pattern of a single crystal mainly depends on the orientation and the structure of sample illuminated by the electron beam. The lattice planes and interplanar distances can be easily observed with the help of selected area diffraction pattern (SEAD) mode [7]. The wavelength of incident electron beam can easily be controlled by accelerating voltage.

$$\lambda = h/p = 12.25 \times 10^{-10} / \sqrt{V} \quad (3.11)$$

In present study, we have used TEM, Technai T20 FEI at 200 kV which is equivalent to 2.51 pm wavelength. For such low wavelength, very high-resolution images were obtained. There are many advantages and disadvantages with this technique. It produces the high resolution images with the possibility of real and reciprocal space information from the same region of the sample. It provides the chemical information about the sample using some additional attachment like energy dispersive X-ray scattering (EDX) and electron energy loss scattering (EELS). There are some disadvantages also like high running cost, difficult sample preparation. Here, for the sample preparation, an easy way has been adopted and the thin film was deposited on the TEM grid itself at the same time.

### **3.3.7 Raman spectroscopy**

Raman spectroscopy is one of spectroscopic technique that can be used for quantitative and qualitative application about the specimen. It is used to observe the different modes of vibrations like vibrational, rotational and other low-frequency modes. It is based on inelastic scattering of monochromatic light (usually a laser source is used) from the specimen. When the beam incident on the specimen, major amount of photons is scattered with the same frequency as that of incident photons known as Rayleigh scattering. A small number of photons are scattered with a shifted frequency; higher or lower than that of incident photons. This shifting arises because of the interactions between the incident radiation and the vibrational levels of the molecules of the specimen. This shifting in frequency gives the information about the modes of the samples and this effect is called Raman Effect [93]. Raman spectrum is the plot of this shift versus the frequency and it is plotted with the Rayleigh frequencies lies at  $0 \text{ cm}^{-1}$ . Then the different functional groups in the specimen correspond to the different band

positions are obtained in the spectrum. This technique is very much useful for most molecular samples like liquids, gels, powders, slurries, some metals and thin films. It is a non-destructive technique. The Raman instrument typically made with four major components: (a) Excitation laser source, (b) light collection optics geometry, (c) Filter for select the desired wavelength, and (d) Detector which is clearly showing in **Figure 3.13**.

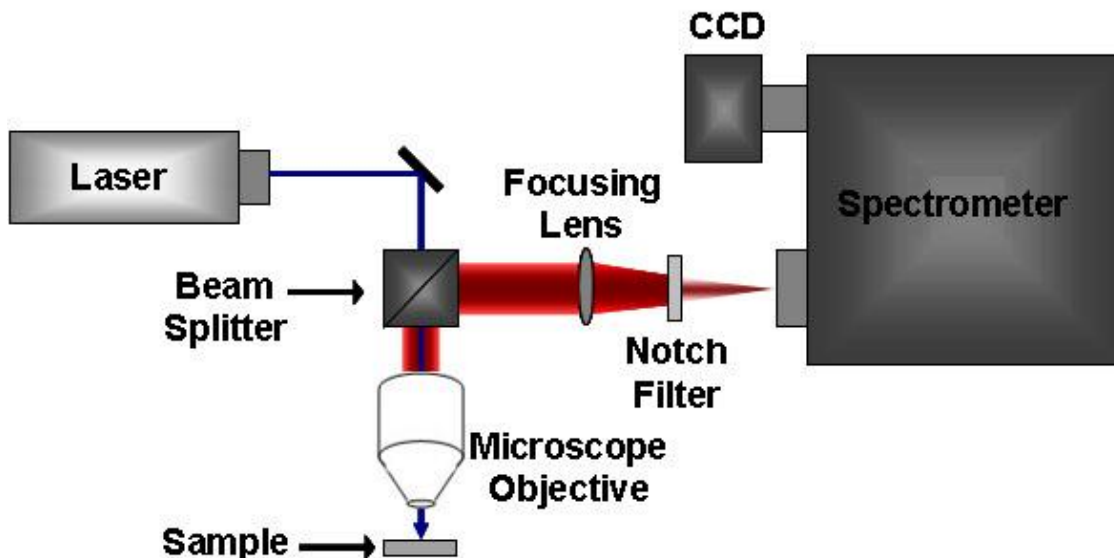


*Figure 3.13 Schematic diagram of Raman spectrophotometer.*

The laser line at 532 nm of He-Cd laser was used with an output of 50 mW. The power of the laser at the sample was 5mW. The Raman spectra were accumulated over 50 sec.

### **3.3.8. Photoluminescence spectroscopy**

Photoluminescence (PL) has become a merit of excellence for evaluating semiconductors properties. PL is defined as the light emission from any form of matter after absorption of photons or it is the result of transition of electrons. Optical characterization methods is having advantage that they are non-destructive, not requiring any further treatment like making electrical contacts or sample preparation and they have very high sensitivity [94]. Photo luminescent materials are characterized on the basis of mechanism involved in-

- (a) Inter-band transitions
- (b) Transitions including impurities or defects

(c) Hot carrier intra-band transitions

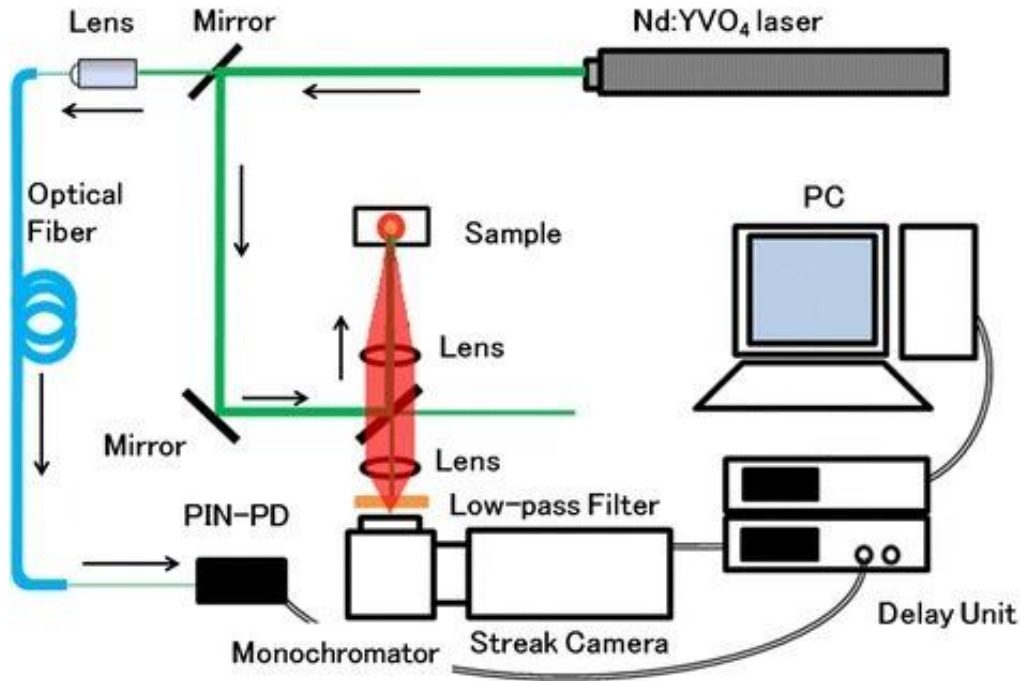


*Figure 3.14 Schematic diagram of the PL System.*

Furthermore, inter-band transitions are divided into two different ways (i) near band edge band-to-band transition and (ii) hot carrier band-to-band transition. Conduction band to acceptor level, bound exciton transition and deep level transition are related to impurities and defects in the material. The electron and hole pair generate by the mobile concentration of energy which is responsible for common center of mass, called exciton. These generated exciton can only exist for a significant length of time at very low temperatures. When the electron and hole combine each other, that time an exciton has less potential energy than a free pair of charge carriers. Therefore when an exciton recombines, any photon which is emitted has rather less energy than the bandgap. Later this photon doesn't have quite sufficient energy to re-excite an electron from the valance band to conduction band, it has a much better possibility to escape from the crystal than photons created by transition at or above the bandgap. Here the schematic for the PL is showing in the **Figure 3.14**.

### 3.3.9 X-ray photo-electron spectroscopy



XPS is very sensitive technique used to find the chemical state, elemental composition, electronic state of the elements present in the material and empirical formula. It is used to analyze the surface of the sample with a depth of 1-10 nm from surface. XPS spectra are observed when the material is irradiated with the X-rays and electrons escaped from the surface of the material are collected by the detector. XPS spectra is the plot between the number of electrons detected by the detector and their binding energy. Each element present in the material can be identified easily as it produces the characteristic set of peaks at particular binding energy of electrons. The number of electrons (directly related to the intensity of peaks) detected estimates the amount of the element present in the material. So it provides the more reliable information about the electronic structure as well as chemical composition/bonding of the material [95]. The experiment is to be performed in the ultra-high vacuum to minimize the error and maximize the number of electrons collected.

The binding energy of the electrons depends upon work function of the electron. As we move towards the inner shell of the atom, greater the binding energy and lesser the kinetic energy of emitted electron. The schematic diagram for the XPS is shown in **Figure 3.15**. This binding energy also shift to higher or lower energy when an atom makes bond with other atoms. Shifting depends upon the electron affinity of the sharing atom. The XPS measurements has been taken at ultra-high vacuum. The energy and intensity of electron further analyzed with the help of the detector and analyze the surface chemistry of the material. The electron binding energy of the each emitted electron is given by fundamental relation [15]:

$$E_{binding} = E_{photon} - (E_{kinetic} + \Phi) \quad (3.12)$$

Where  $E_{binding}$  = binding energy of emitted electrons,  $E_{photon}$  = energy of X-ray photons,  $E_{kinetic}$  = kinetic energy of the emitted electrons, and  $\phi$  is the work function. In present study, XPS (Omicron nanotechnology) measurements were performed at a pressure of  $10^{-10}$  torr. The general scan and core level spectra of O (1s), Zn (2p), and Ag (2p) are obtained with monochromatized Al radiation (photon energy 1486.6 eV) with a pass energy of 50 eV for survey and 20 eV for core level spectra. Electron take-off angle was  $90^\circ$ . The background correction in core level spectra are done using the Shirley

algorithm. Baseline correction and peak fitting are done using the software Casa-XPS. The core level spectra are analyzed with respect to the C (1s) binding energy of 284.8 eV.

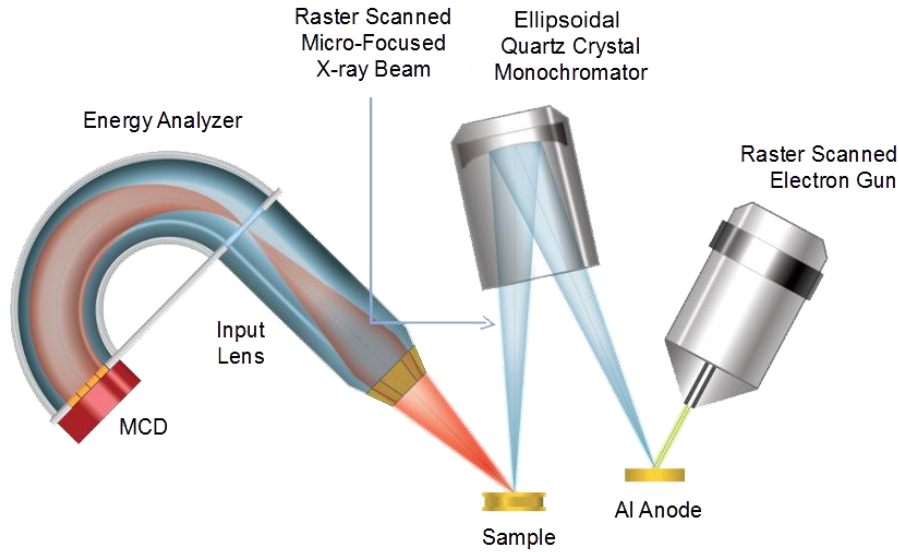


*Figure 3.15 Schematic representation of the XPS with basic components.*

### 3.3.10. Electrical measurements

I-V and Hall measurements are good techniques to measure the electrical conductivity and resistance of the bulk and thin films. The schematic diagram for the Hall-probe method is shown in **Figure 3.16**. Hall measurement is very well-known and comprehensive method to obtain the different electrical parameter such as conductivity, sheet resistance, and carrier concentration of the sample. It can also be used to find out the nature of semiconductor whether sample is n-type or p-type. In this method, current carrying sample is subjected to a magnetic field, then a voltage is produced in perpendicular direction to the current and magnetic field both. The generated voltage is known as Hall voltage and it helps to decide the nature of conductivity. The Vander Pauw method is commonly used for the connections with the sample material to calculate the hall coefficient and resistivity. The Vander Pauw method employ the four-probe geometry to calculate the average resistivity of the sample.

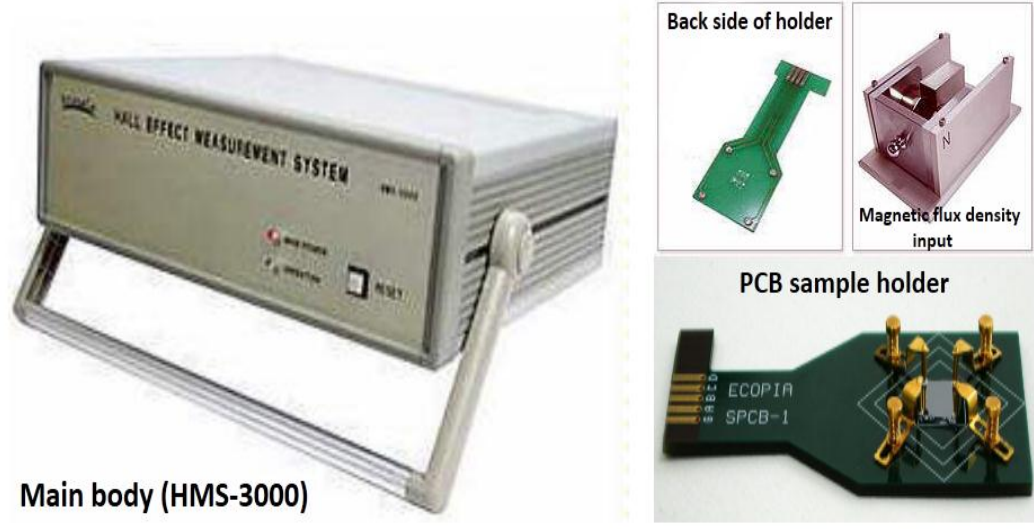


*Figure 3.16 (a) Image of Sample holder used for Hall-measurements (b) different components of Hall measurement apparatus.*



# Chapter 4

## SHI and Thermally Induced Modifications of ZnO Films as a Host Matrix

---

In this chapter, we are discussing about the swift heavy ion irradiation and thermally induced modifications in ZnO films as a host matrix. ZnO thin films were synthesized by RF-magnetron sputtering. The prepared films were irradiated with 100 MeV Ag ions and annealed at different temperature of 400 and 500 °C. SHI and thermal induced structural and optical modifications have been discussed in detail.

## 4.1. Introduction

The oxide semiconductors possess various physical properties such as transparency, conductivity and piezoelectricity which makes them of great scientific interest for optoelectronic and piezoelectric device applications. Among all, ZnO (*n*-type) semiconductor is a very promising material due to its wide optical band gap and large exciton binding energy [96,97]. The larger band gap of ZnO in comparison to Si and Ge, makes it more promising to use at high temperature in electronic devices. The physical properties of ZnO are widely influenced by deposition conditions and parameters. To analyze the effects of deposition on film's property, many techniques such as sol-gel method, spray pyrolysis, metal organic chemical vapour deposition, pulse laser deposition and RF/DC sputtering have been used and reported by many groups [98–102]. Due to the functionalize properties, ZnO is used in solar cells, transparent conductive contacts, gas sensors, thin film transistors and laser diodes [103–108]. The variability of piezoelectric properties of ZnO, make it useful also for short-wavelength light emitting diodes, optical waveguides, laser deflectors and surface acoustic wave (SAW) band-pass filters [109–111].

Nowadays, researchers are making efforts to improve the various properties of ZnO thin films by different means. Swift heavy ion (SHI) irradiation is a well-known process to modify the physical properties of materials [52,67,112–121]. The properties can be tuned by controlling the incident ion energy and fluence [122,123]. The energetic ion lose their energy after interaction with ZnO, this transferred excess energy creates the density of defects, stress and strain in the structure of ZnO [124]. The formation of self-affine nanostructure over the surface of ZnO thin films using SHI has been investigated by Agarwal *et al.* [125]. Incident ion fluence affects the shape and density of these nanostructures. The energetic ions can also be used for better understanding of phonon modes in nanostructures [126]. Thermal annealing is another way to alter the properties of ZnO thin films and renders them more useful for various applications. Thermal annealing may induce the directional growth in the thin films and also the optical quality of thin film can be improved [58]. These modifications can be used in radiation harsh environment for optoelectronic applications.

## **4.2. SHI irradiation studies of host matrix**

### **4.2.1. Experimental details**

In order to study the host matrix, pure ZnO thin films were synthesized by RF sputtering and then irradiated with 100 MeV Ag ions with different fluences.

#### *Deposition parameters*

The sputtering target of pure ZnO was prepared using ZnO powder (99.99% Alfa Aesar) by using a hydraulic press machine (HYCON Hydraulic engineers and consultants, New Delhi) with pressure approximately ~ 7 tons for the film deposition. Then, the target was sintered for 24 hours at the temperature 1200 °C by sequential steps in a programmable furnace with a continuous flow of oxygen gas during the target sintering.

Thin films of ZnO were deposited on glass and silicon substrates at room temperature by RF magnetron sputtering, using ZnO target of 2-inch diameter and 3 mm thickness in the presence of Ar gas (flow rate ~ 4 sccm) in the sputtering chamber during deposition. Before using, all the substrates were cleaned in an ultrasonic bath with a mixture of de-ionized water and trichloroethylene (TCE) and then washed with boiled acetone. A base pressure of  $10^{-6}$  mbar was achieved by using a turbo molecular pump for deposition. The sputtering was carried out at a pressure of  $5 \times 10^{-2}$  mbar during the deposition in the presence of a pure argon atmosphere (grade-I) with a target to substrate distance of 40 mm. The deposition was performed for 15 minutes at fixed RF power 150 watts, and self-bias voltage 250-280 volt during deposition.

#### *Irradiation parameters*

The films were irradiated with 100 MeV Ag ions (charge state +7) using the 15UD Pelletron accelerator facility at the Inter-University Accelerator Centre (IUAC) New Delhi in Materials Science beam line chamber. The vacuum in the irradiation chamber during the irradiation was  $\sim 6 \times 10^{-7}$  mbar. Electronic ( $S_e$ ) and nuclear ( $S_n$ ) energy losses of 100 MeV Ag ions in ZnO thin film are 20.39 and 0.122 keV/nm, respectively, and the range of Ag ions in ZnO film is  $\sim 12.15$   $\mu\text{m}$  as calculated by SRIM simulation. The ion beam was scanned over an area of  $1 \times 1$   $\text{cm}^2$  with fluence  $3 \times 10^{12}$ ,  $1 \times 10^{13}$  and  $3 \times 10^{13}$  ions/ $\text{cm}^2$  and the beam current was kept constant at 1 pA (particle nano-ampere).

### **4.2.2. Results and Discussion**

### 4.2.2.1. X-ray diffraction analysis

The crystalline behaviour of pristine and irradiated ZnO thin films was investigated by XRD analysis. **Figure 4.1** shows the XRD pattern for pristine and 100 MeV  $\text{Ag}^{7+}$  ions irradiated films at the different ion fluence  $3 \times 10^{12}$ ,  $1 \times 10^{13}$ , and  $3 \times 10^{13}$  ions/cm<sup>2</sup>. The pristine film shows the crystalline hexagonal wurtzite structure with reflections from (100), (002), and (101) planes at  $\sim 31.7^\circ$ ,  $34.4^\circ$ , and  $36.2^\circ$  respectively [JCPDS card no. 89-1397].

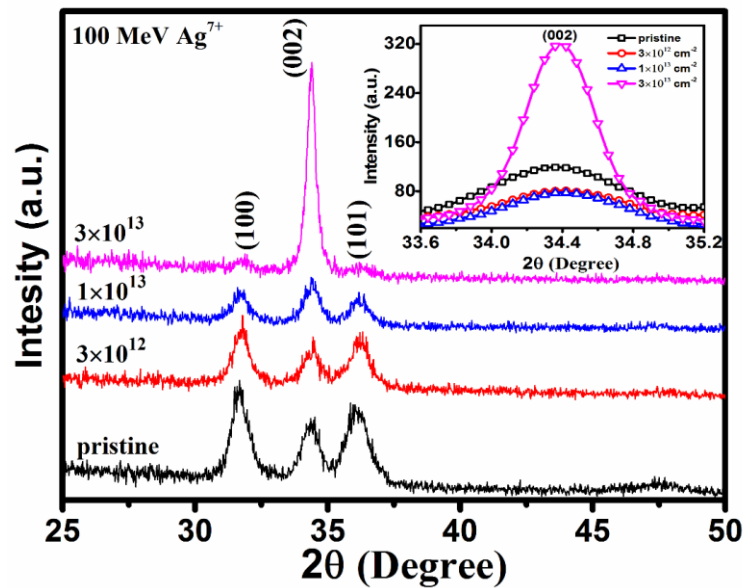


**Figure 4.1** XRD spectra of the pristine and irradiated ZnO thin films with different fluences, Inset shows the zoomed behaviour of (002) plane with ion irradiation.

Ion-irradiated ZnO thin films show the intensity of (100) and (101) planes are decreased with increasing ion fluences, which is attributed to electronic excitation due to SHI irradiation. At the higher fluence ( $3 \times 10^{13}$  ions/cm<sup>2</sup>), the ZnO thin film becomes more c-axis oriented while the other two reflection plane (100) and (101) seem to be vanish as shown in **Figure 4.1**. It is observed that at the higher irradiation fluence film releases strain which is responsible for growth in c-axis orientation because (002) plane of ZnO having the lowest surface energy according to basic crystal growth theory [127,128] as shown in **Figure 4.2**, which was estimated by using the **Equation 3.7** [129].



The average crystalline size of pristine film is  $10.8 \pm 0.7$  nm and is increased up to  $20.5 \pm 0.3$  nm with increasing the ion fluences (**Figure 4.2**) as calculated by using Debye-Scherrer's formula (**Equation 3.6**) and summarized in **Table 4.1** [130].

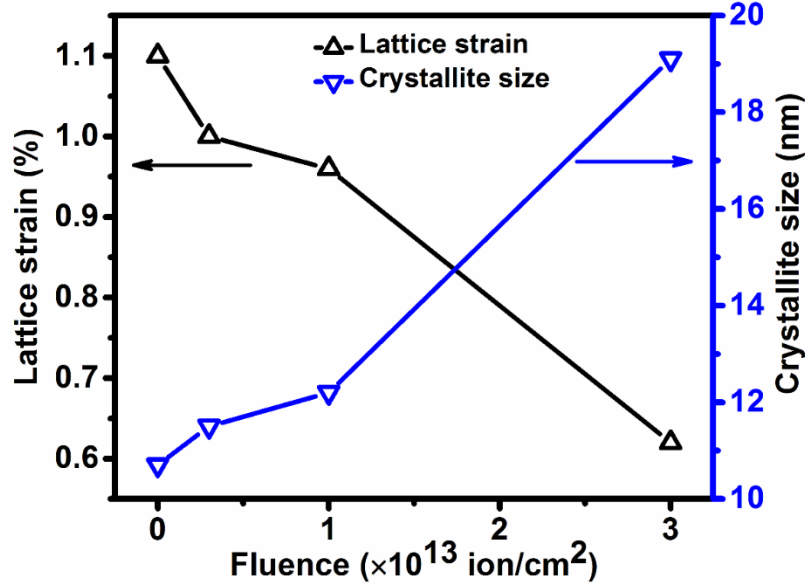


**Figure 4.2** Variation of the lattice strain and crystallite size with different ion fluences.

During swift heavy ion irradiation, incident ion transfers a large amount of energy into the target material by electronic energy loss ( $S_e$ ). This large amount of energy creates the very high-temperature zone in the target material, which is responsible for the surface modifications. In this process, film releases the strain at higher fluence which is responsible for the crystalline quality of the film and can be explained in the term of the thermal spike model [131]. Preferred c-axis oriented ZnO thin film could be suitable for piezoelectric transduction mechanism [132].

**Table 4.1** Variation of crystallite size with different ion irradiation fluences.

Sr. No.	Fluences (ionscm <sup>2</sup> )	Crystallite size (nm)
1.	Pristine	$10.8 \pm 0.7$
2.	$3 \times 10^{12}$	$12.6 \pm 0.9$
3.	$1 \times 10^{13}$	$12.7 \pm 0.6$
4.	$3 \times 10^{13}$	$20.5 \pm 0.3$

#### 4.2.2.2. UV-visible spectroscopy

Optical properties of pristine and irradiated ZnO thin films were characterized by UV-visible spectroscopy. It provides more information about the optical band gap and transmittance of pristine and irradiated thin films. ZnO thin films were deposited on a glass substrate and irradiated at three different fluences  $3 \times 10^{12}$ ,  $1 \times 10^{13}$  and  $3 \times 10^{13}$  ions/cm<sup>2</sup>. Transmission spectra of ZnO thin films are shown in **Figure 4.3**, wavelength ranging from 400 to 800 nm. It was observed from the spectra that, there is a significant change in transmittance of ZnO thin films with increasing ion fluences. The transmittance of the pristine film and irradiated film at higher fluence  $3 \times 10^{13}$  ions/cm<sup>2</sup> were calculated by transmission spectra and found to be ~ 90% and 80% respectively at 550 nm. The reduction of transmittance at higher fluence attributed to the increased electron carrier density and defect creation such as oxygen vacancies induced by swift heavy ion irradiation in ZnO thin film [133]. ZnO is a direct bandgap material, and the band gap of the pristine and irradiated ZnO thin films was determined from Tauc's relation [134] which is expressed in **Equation 3.9**.

The bandgap value is calculated by extrapolating the linear part of the spectra by plotting  $(\alpha h\nu)^2$  versus  $h\nu$  graph (inset of **Figure 4.3**). The optical band gap of the film slightly increased (from 3.28 to 3.30 eV) with ion irradiation can be explained in the term of Burstein-Moss effect (B-M effect) which depends on electron carrier concentration in the material which effected by SHI irradiation [135].

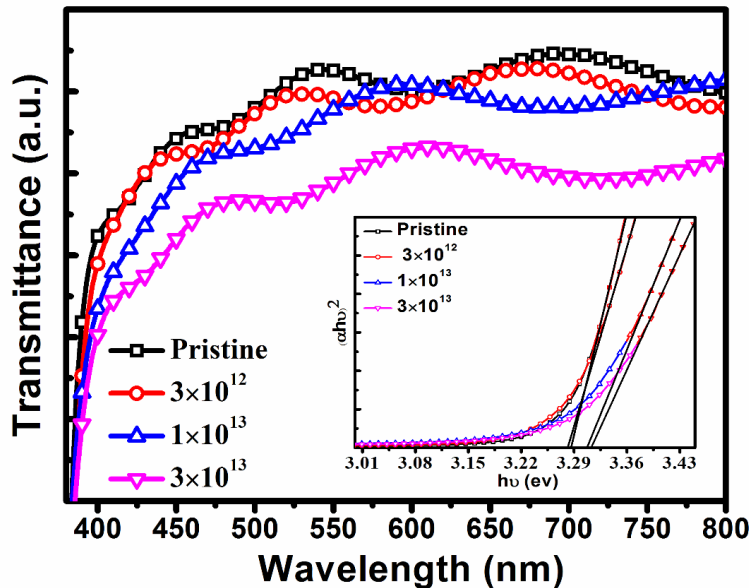


*Figure 4.3 UV-visible transmission spectra for pristine and 100 MeV Ag ion irradiated films of ZnO and the optical band gap variation of pristine and irradiated film calculated by Tau'c plot (inset).*

#### 4.2.2.3. Atomic force microscopy

The surface morphology of pristine and 100 MeV Ag<sup>7+</sup> irradiated films have been carried out by atomic force microscopy (AFM) in tapping mode. **Figure 4.4** shows the three-dimensional (5×5 μm<sup>2</sup>) micrographs of pristine and 100 MeV Ag<sup>7+</sup> irradiated ZnO thin films. It was clear from the images that ZnO grains are connected to each other and films were grown uniformly on the substrate. **Figure 4.5** shows the distribution of grain size with the Gaussian function of the pristine and irradiated ZnO thin films at different fluences.

The grain size of the thin films was increased which is attributed to the agglomeration of the ZnO grains with ion irradiation. The grain size of the pristine film was calculated to be  $\sim 198 \pm 6.8$  nm, and it increases up to  $\sim 219 \pm 2.8$  nm at the fluence of  $3 \times 10^{13}$  ion/cm<sup>2</sup> as shown in **Figure 4.5**. The discrimination in the calculated grain size from AFM and XRD is observed because the analysis of XRD spectra gives the average mean crystallite size whereas the AFM shows the agglomeration of particles which are much bigger than those observed by XRD. The observations of AFM and XRD can be correlated by the fact that smaller particles have a larger surface free energy and therefore, agglomerate faster and develop larger grains and XRD is related to smaller particles whereas AFM gives larger grains [136]. The root-mean-square roughness ( $R_{\text{rms}}$ ) of the pristine film was calculated by following relation and is estimated 10.2 nm for the pristine film.

$$R_{\text{rms}} = \left[ \frac{1}{N} \sum_{i=1}^N |Z_i - \bar{Z}|^2 \right]^{\frac{1}{2}} \quad (4.1)$$

Where N is no. of surface height data and Z is the mean height distance. The roughness of ZnO films be marginally changing with swift heavy ion irradiation and it is not much effected by swift heavy ion irradiation. Variation in the roughness and grain size with ion irradiation are shown in **Figure 4.6** and summarized in **Table 4.2**. When swift heavy ions

passes through the material, it deposited a large amount of energy into the material. If the surface energy of the film, greater than acquired energy form incident ion beam then they leads to agglomeration of the grains and formed the bigger grains due to surface diffusion process near the surface of the film. With the increase of ion fluences, surface energy of the films are also change due to total energy ( $S_e \times \phi$ ) deposited by incident ion beam. This surface diffusion process is responsible for the grain growth and change in shape and size of the grains near surface region.

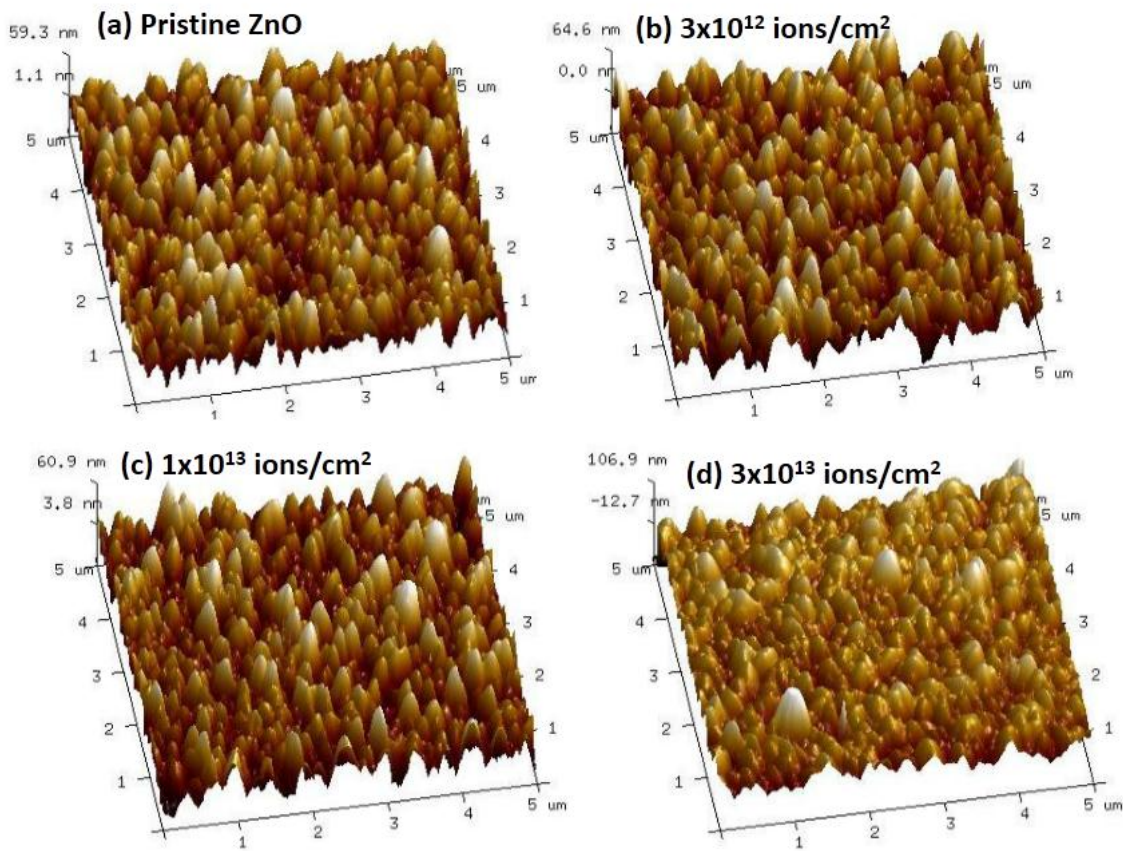


**Figure 4.4** AFM micrographs of (a) pristine (b)  $3 \times 10^{12}$  ions/cm<sup>2</sup> (c)  $1 \times 10^{13}$  ions/cm<sup>2</sup> and (d)  $3 \times 10^{13}$  ions/cm<sup>2</sup>.

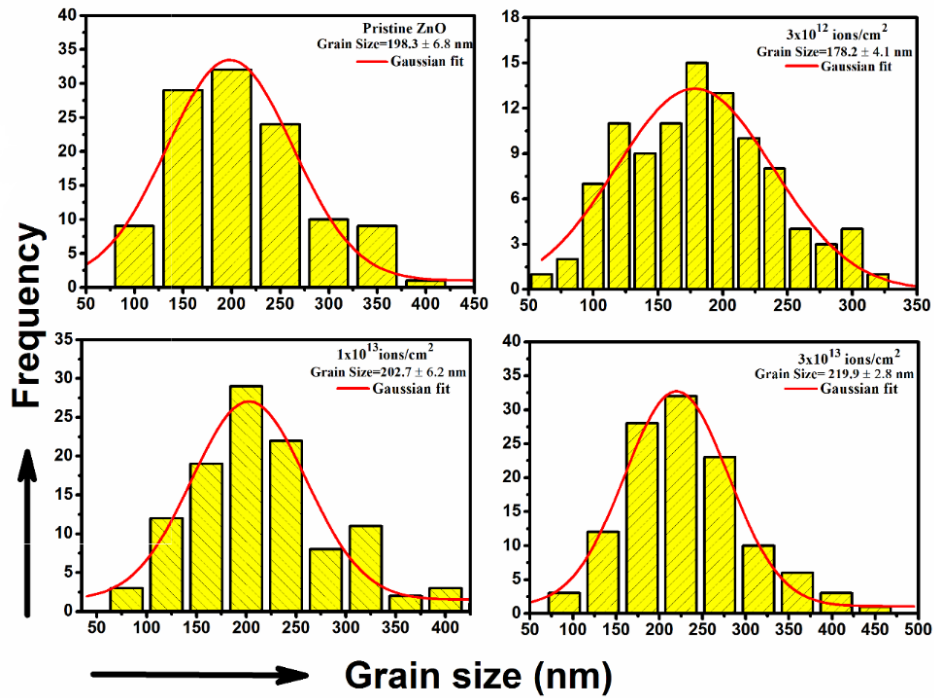


Figure 4.5 Variation of grain size with different ion fluences calculated by atomic force microscopy.

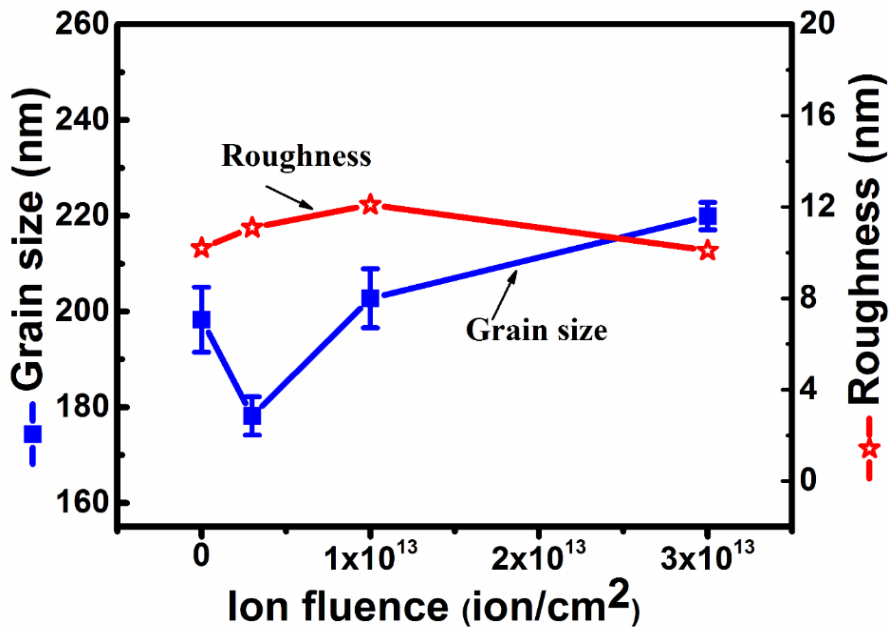


Figure 4.6 Variation of roughness and grain size with different ion irradiation fluences.

**Table 4.2** Grain size and roughness of the film with different fluences.

<b>Fluences (ions/cm<sup>2</sup>)</b>	Pristine	3×10 <sup>12</sup>	1×10 <sup>13</sup>	3×10 <sup>13</sup>
<b>Grain size (nm)</b>	198.3 ± 6.8	178.2 ± 4.1	202.7 ± 6.2	219.9 ± 2.8
<b>Roughness (nm)</b>	10.2	11.1	12.1	10.1

#### 4.2.2.4. Scanning electron microscopy

**Figure 4.7** (a)-(d) show the FESEM micrographs of the pristine and irradiated film at a fluences 3×10<sup>12</sup>, 1×10<sup>13</sup> and 3×10<sup>13</sup> ions/cm<sup>2</sup>. Agglomeration of the particle is clearly seen in the **Figure 4.7** (d) image that was irradiated at the higher fluence 3×10<sup>13</sup> ions/cm<sup>2</sup> as evidenced by AFM.

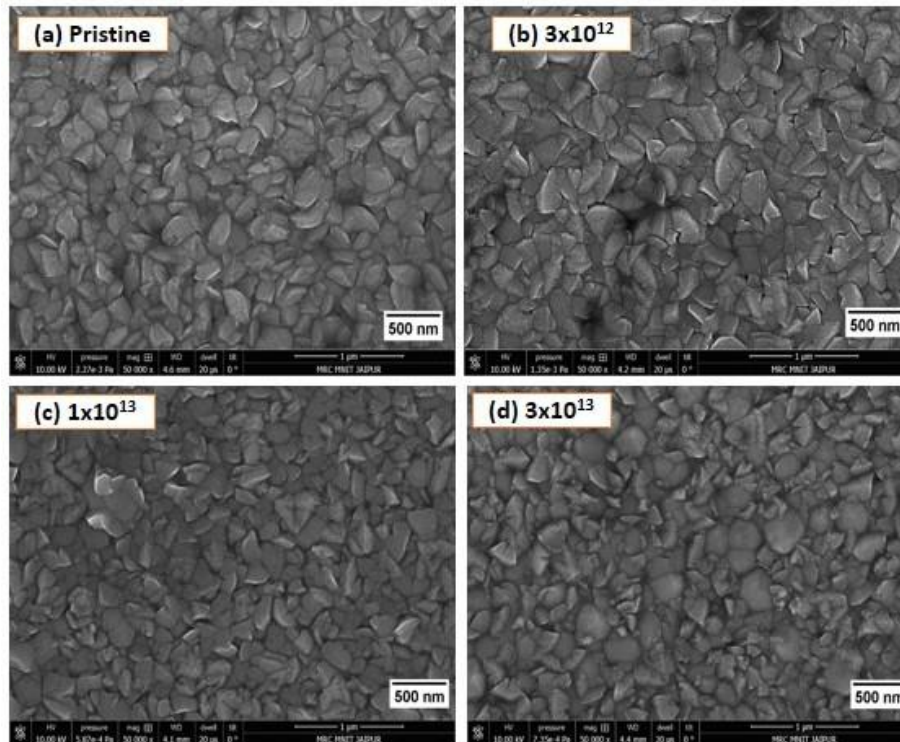


**Figure 4.7** FESEM micrographs of pristine and 100 MeV Ag ion irradiated film of ZnO at different fluences.

Agglomeration of ZnO grains in the film increases with the increasing ion fluence which is attributed to increasing the local melting temperature on the surface due to the

interaction of high energetic ion. The FESEM and AFM both showing the surface morphology of the pristine and irradiated ZnO thin film with different ion fluences. The average surface roughness is  $\sim 10.9$  nm calculated by AFM. SEM results were also showing larger grains with different size and shape on the top surface of the film. The agglomeration of the particles is also observed in SEM images at the higher fluence which is confirmed by AFM.

#### 4.2.2.5. Micro-Raman spectroscopy

The Raman active phonon modes of the wurtzite structure of ZnO as expected from the group theory are  $A_1+2E_2+E_1$  modes, where all atoms occupy  $C_{3v}$  sites [137,138]. Typical micro-Raman spectra of the ZnO thin films irradiated with fluences  $3 \times 10^{12}$ ,  $1 \times 10^{13}$  and  $3 \times 10^{13}$  ions/cm<sup>2</sup> are shown in **Figure 4.8**. The spectra reveal that pristine and irradiated films show the peaks at 280, 440, very sharp peak at 573, broad peak at 680 and peak at 780 cm<sup>-1</sup>. The weak Raman mode  $B_1$  (high) -  $B_2$  (low) and  $B_1$  (high) +  $B_1$  (low) were recorded at 280 and 780 cm<sup>-1</sup> for pristine and irradiated ZnO thin films respectively. The peak at 573 cm<sup>-1</sup> can be assigned to  $A_1$  (LO) mode, which is an agreement between the theoretical calculations [139]. Small band at 630 cm<sup>-1</sup> has been assigned to the  $E_1$  (LO) mode [140]. The  $B_1$  (high) -  $B_2$  (low) and  $B_1$  (high) +  $B_1$  (low) modes are not much affected by SHI irradiation. These modes can be considered as weak Raman modes of ZnO according to group theory. The sharp peak at 573 cm<sup>-1</sup> decreases slowly with the increase the ion fluence, while  $E_2$  (high) mode at 440 cm<sup>-1</sup>, decreases at the fluence of  $3 \times 10^{13}$  ions/cm<sup>2</sup>. The characteristic modes of ZnO,  $E_2$  (high) and  $A_1$  (LO) at 440 cm<sup>-1</sup> and 573 cm<sup>-1</sup> are attributed to the highly textured and wurtzite structure of the ZnO thin film (shown in inset). The pristine ZnO thin film seems to be oxygen deficient as indicated by the  $A_1$  (LO) mode at 573 cm<sup>-1</sup> with higher intensity. Swift heavy ion induced density of defects and disorder is subjected to loss of the translation symmetry of the lattice of the materials which leads to the invalidations of the  $k=0$  wave vector selection rule from all part of the Brillouin zone in Raman scattering. Therefore, irradiation induced  $A_1$  (LO) mode is explained in the term of surface phonon mode which is directly related to intrinsic lattice defects in the materials structure. Other Raman modes of the ZnO thin

film have been related to the formation of wurtzite structure of the ZnO according to the selection rule [124].

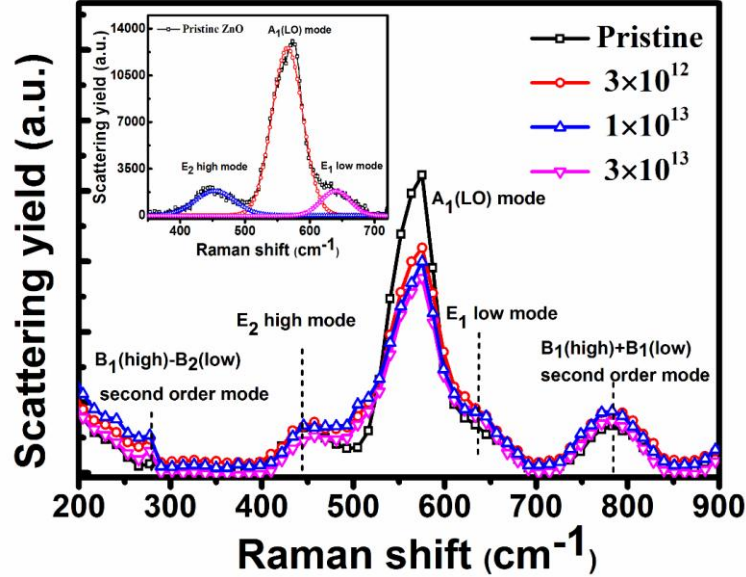


**Figure 4.8** Raman spectra of pristine and 100 MeV Ag irradiated at different fluences.

The observed decrease in the intensity corresponding to (100) and (101) planes with increasing fluences and more c-axis orientation of ZnO thin films along the (002) plane at the highest fluence reveals the better crystallinity with SHI irradiation. This improved crystallinity can be described in light of interaction of ion and material. The imparted energy from the incident high energy ions to target material is responsible for the electronic ionization/excitation and lattice vibrations along the ion path due to large amount of energy transfer. These vibrations and excitations causes to the release of strain in the film which lower the surface energy. Therefore, ZnO thin films become oriented along (002) plane as it has lowest surface energy and results in increased crystallinity due to irradiation.

Raman spectra confirmed the formation of wurtzite structure of ZnO for the present study whereas the observed A<sub>1</sub>(LO) mode is related to the intrinsic lattice defects in the structure. The decrease in the intensity of A<sub>1</sub>(LO) mode is further confirmed the increased lattice defects in the ZnO film due to high energetic ions. These ions induced defects and vacancies play a major role to tune the optical properties in the ZnO thin film.



The reduction of transmittance and at higher fluence attributed to the increased electron carrier density and defect creation such as oxygen vacancies induced by swift heavy ion irradiation in ZnO thin film. The band gap is also slightly increased (from 3.28 to 3.30 eV) with ion irradiation which might be attributed to electron carrier concentration which can be explained in the term of Burstein-Moss effect (B-M effect). These modifications in the film are subjected to change in surface energy of the films which is also responsible for grain growth and morphological features of the film with ion irradiation. Therefore, such kind of ZnO thin film can be used in radiation harsh environment and optoelectronic applications.

### **4.3. Thermal annealing studies of host matrix**

In present section, the annealing effect on the structural as well optical properties of RF sputtered ZnO thin films have been discussed.

#### **4.3.1. Experimental details**

ZnO thin films were deposited by RF-magnetron sputtering on glass and Si substrates. The substrates were cleaned ultrasonically in acetone, isopropanol and deionized water subsequently. A turbo pump coupled with rotary pump was used to achieve the  $\sim 5 \times 10^{-5}$  mbar pressure and  $3 \times 10^{-2}$  mbar during a deposition in the presence of argon (grade-1) gas. Substrate temperature during deposition is 300 °C and the experiment was performed for 30 minutes at the power of RF supply is 150 watts (self-bias voltage 250-300 volt). These ZnO thin films were annealed at temperature 400 °C and 500 °C in oxygen environment for 1 hour.

#### **4.3.2. Results and discussions**

##### **4.3.2.1. Rutherford backscattering spectroscopy**

For the evaluation of the thickness of film, RBS has been performed. RBS of as deposited ZnO thin film is shown in **Figure 4.9**. Thickness of the film was found to be 155 nm by fitting RBS spectra with SIMNRA simulation program [141]. The plateau region of the spectrum, represents the Si substrate. **Figure 4.9** showing the fitted RBS spectra of the

ZnO thin film. Black line shows the actual RBS spectra and red line shows the fitted spectra by simulation.

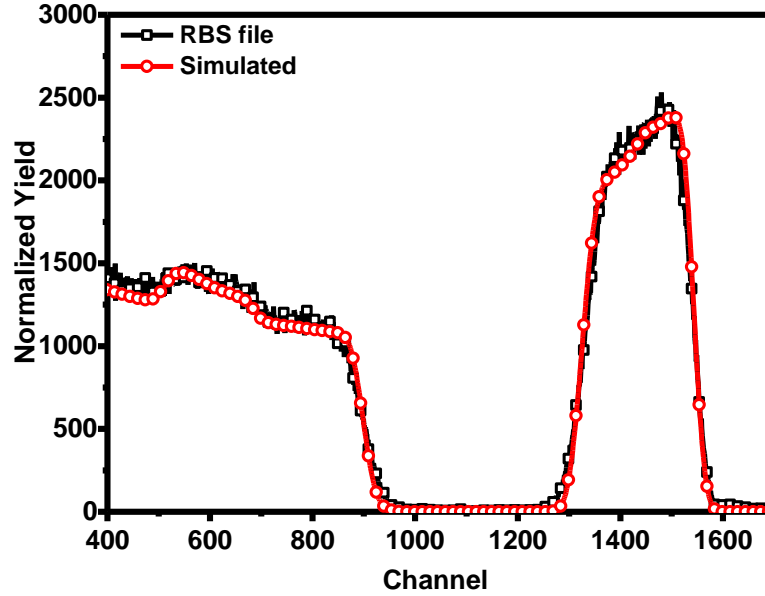


*Figure 4.9 RBS spectra of the as deposited ZnO thin film on Si substrate.*

#### 4.3.2.2. X-ray diffraction analysis

Crystallinity and structural information of as deposited ZnO thin film was estimated by X-ray diffraction analysis. **Figure 4.10** shows the XRD pattern of as deposited ZnO film and it confirms the formation of hexagonal wurtzite structure of ZnO with different phases such as (110), (002), (101), (102), (110), (103), and (112) at  $31.34^\circ$ ,  $34.12^\circ$ ,  $35.95^\circ$ ,  $47.27^\circ$ ,  $56.31^\circ$ ,  $62.49^\circ$ , and  $67.45^\circ$  respectively (JCPDS-89-1397). The higher intensity of (002) reflection plane at  $34.12^\circ$  indicates that the film is more preferential oriented along the c-axis because of lower formation energy required for the growth in c-axis. Crystallite size of as deposited ZnO film was calculated by Debye Scherer's formula (**Equation 3.6**) and it was found to be  $\sim 15$  nm.

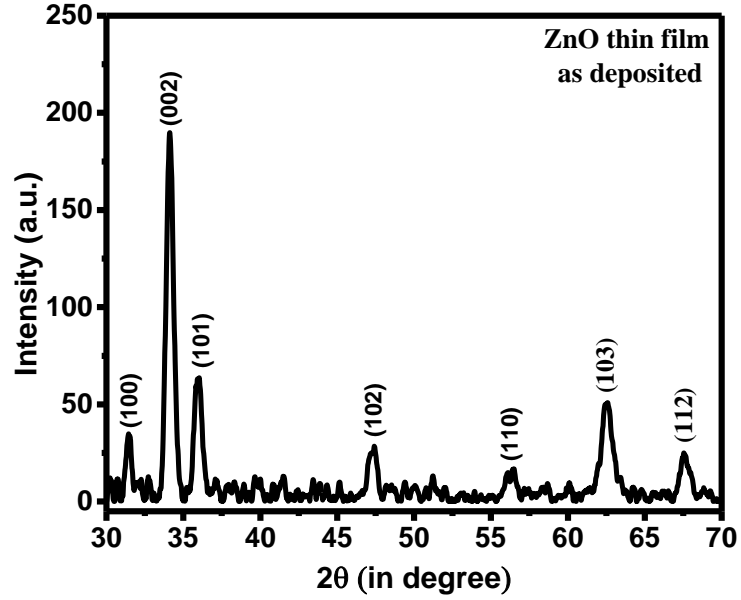


Figure 4.10 XRD pattern of as deposited ZnO thin film.

#### 4.3.2.3. UV-visible spectroscopy

The optical behaviour of the as deposited and annealed ZnO thin films were characterized by the UV-visible spectroscopy. Figure 4.11 shows the average transmittance spectra of as deposited and annealed ZnO thin films.

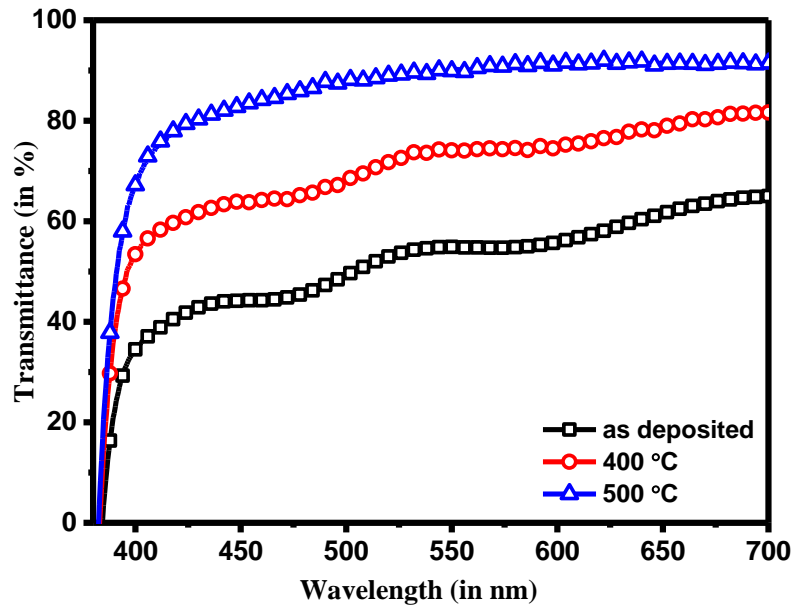
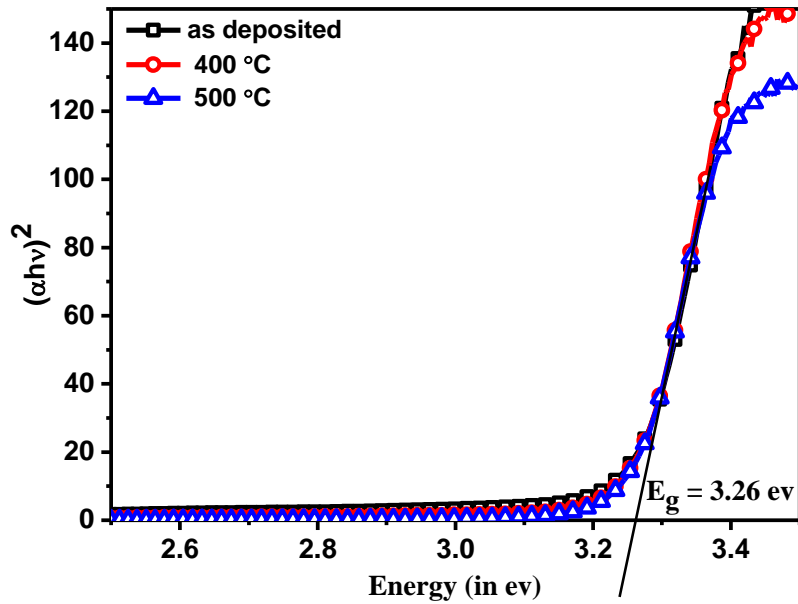


Figure 4.11 Transmittance spectra of as deposited and annealed ZnO thin films.

It is clear from figure that the average transmittance of the film increases with increasing the annealing temperature, and it has increased from 50% to 90% with annealing at 500 °C. Higher annealing temperature leads to better Crystallinity of the film, which was also confirmed by Raman spectroscopy. The crystallinity of films was improved with annealing temperature, attributed by the quantity of free charge in film decreased with temperature [142]. The transmittance of the film was increased due to the intake of oxygen in oxygen deficient ZnO film, absorbed oxygen removes the oxygen vacancies hence reducing the density of defects [143]. The optical energy band gap was also calculated by Tauc's relation (**Equation 3.9**) and it was found to be 3.26 eV for as deposited and annealed thin films. There is no significant change in the band gap of as deposited and annealed thin films of ZnO (**Figure 4.12**).



*Figure 4.12 Band gap variation of as deposited and annealed film calculated by Tauc's plot.*

#### 4.3.2.4. Micro-Raman spectroscopy

Raman spectra of as deposited and annealed ZnO thin films are shown in **Figure 4.13**. The Raman active phonon modes of the wurtzite structure of ZnO expected from the group theory are  $A_1+2E_2+E_1$  modes, where all atoms occupy  $C_{3v}$  sites. The Raman spectra of films reveal that as deposited ZnO thin film show peaks at  $276\text{ cm}^{-1}$ , which was

related to the  $B_2$  second order mode with low intensity and  $581\text{ cm}^{-1}$  which can be assigned to  $A_1$  (LO) mode. When the films were annealed at temperature  $400^\circ\text{C}$  and  $500^\circ\text{C}$ , the intensities of the  $A_1$  (LO) mode and  $B_2$  second order mode were found to increase. At the temperature  $500^\circ\text{C}$ ,  $E_2$  high mode was also appearing in annealed ZnO thin films.  $A_1$  (LO) mode and  $E_2$  high mode are expected, as the films are highly textured and the excitation light is normal to the surface [144,145]. The appearance of  $E_2$  high mode in ZnO film, which was annealed at  $500^\circ\text{C}$ , confirmed the highly textured and wurtzite structure of the ZnO thin films [56].

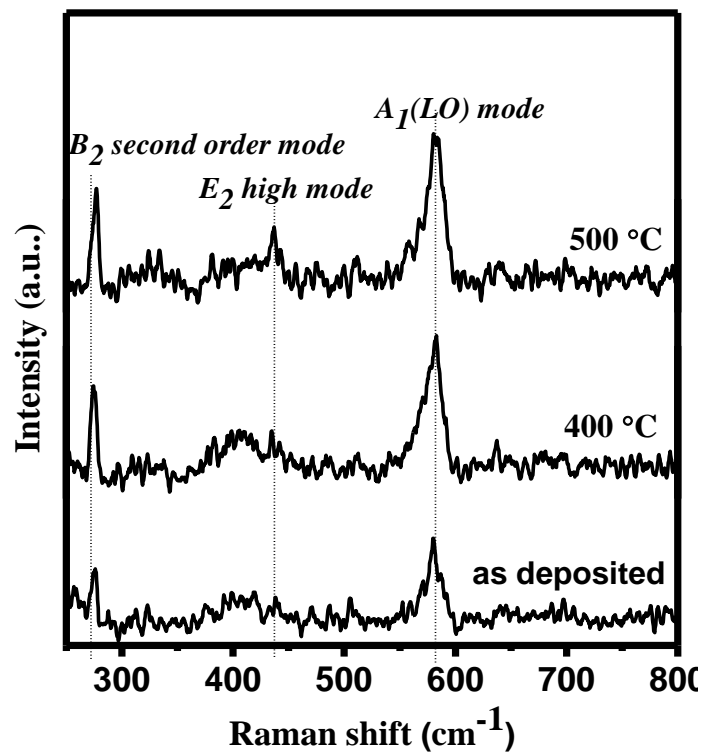


*Figure 4.13 Raman spectra of as deposited and annealed ZnO thin films.*

#### 4.4. Summary

In this chapter, the synthesis of ZnO thin films by RF sputtering have been discussed in detail. Further, the modification in the properties of ZnO thin films by SHI irradiation and thermal annealing have also been investigated. The crystallinity of the ion irradiated thin films was enhanced along the c-axis orientation due to impact of energetic ions. It was attributed to the release of strain in the thin films and having the lowest surface energy. The average crystalline size of pristine film was calculated as  $10.8 \pm 0.7\text{ nm}$  and found to

be increased up to  $20.5 \pm 0.3$  nm with increasing the ion fluences. The optical analysis confirmed that the SHI irradiation is suitable technique to tailor the optical properties of ZnO films. Transmittance of the thin films was observed to be decreasing with increasing fluences. This property can be used in transparent window materials. The dependence of surface morphology and grain size on incident ions were further confirmed by AFM and FESEM analysis and observed the increased grain size after irradiation. All the induced modifications are explained in term of energy loss of ions into the target materials. Besides, the thin films were annealed in oxygen environment and were characterized to analyze the effect of annealing. The transmittance and the optical quality of the films were observed to be improved on thermal annealing.

# Chapter 5

## Synthesis and Characterization of Ag-ZnO Nano-composites Thin Films Using Two Different Approach

---

In this chapter, synthesis of Ag-ZnO nanocomposite thin films have been discussed by two different approaches; RF-sputtering and Ag ion implantation. Higher metal concentration in ZnO matrix achieved by RF-sputtering technique. Structural and optical properties have been observed and studied in systematic manner.

## 5.1. Introduction

Zinc oxide (ZnO) has become a favorable material for the various optoelectronic devices and thin film applications and have hexagonal wurtzite crystal structure from II-VI semiconductor group [146]. Such promising properties of ZnO makes it a suitable material for potential application in divergent areas such as transparent conducting oxides, light emitting diodes, laser deflectors, gas sensors, LEDs, photo detectors and solar cells [147–154]. ZnO has become an alternate of indium tin oxide in solar cell industry for the preparation of transparent conductive electrodes with low material cost, a high degree of chemical stability, and less toxicity [155,156]. In the last few years, ZnO-based nanomaterials have attracted considerable attention because of their dimensionality and size of their structural features, electrical and optical properties and also motivate to utilize in various nano-device fabrication realm [157,158]. Indeed many researchers are struggling to improve their properties by applying different procedures for example incorporation of the metal as a dopant, ion implantation and interplay with annealing and different growth technique [159–162]. Different synthesis techniques have been used to synthesize the Ag-ZnO nanocomposite thin films such as spin coating, RF sputtering, spray pyrolysis, pulsed laser deposition, and e-beam evaporation etc. [163–166]. It was suggested that the deposition parameters and the amount of metal doping are two main key factors which are responsible for the change in the physical properties of the ZnO thin films. Furthermore, the incorporation of noble metals (Ag, Au, and Cu) in ZnO thin film are very attractive way to enhanced the structural, electrical and optical properties [167–171]. These noble metals, in the form of nanoparticles, exhibits selective surface plasmon resonance (SPR) band in visible and near infrared region. Therefore, the presence of plasmon-active nanoparticles in a matrix offered new optical properties for different plasmonic applications [116,172,173]. Among them, silver (Ag) is a more suitable element for the doping as compare to Cu and Au because it is related to IB group and have lowest transition energy with shallow acceptor level at 0.3 eV and act as an acceptor which existing on substitutional Zn sites [174,175]. Doping of silver (Ag) in ZnO matrix, creates the trivial acceptor level in the ZnO, due to the substitution of Zn sites by Ag sites during doping process because it has lower formation energy in comparison of Ag interstitial theoretically [176]. Therefore Ag is the suitable elements



for fabricating the p-type conductivity in ZnO thin film [177]. The absorption/scattering cross section of Ag nanoparticle is larger than a geometrical cross section, which leads the higher efficiency of interaction with incident light, therefore the Ag ion used for the implantation [178].

Ion implantation is a precise technique for material modifications (structural as well as optical) by doping of metal ions into target materials up to certain depth [179–183]. Nowadays, ion implantation facility has also been widely used in device fabrication because it provides the facility to introduce charge carrier for conduction into oxide semiconductors with selective area doping as well optical and electrical isolation. Depth concentration and controlled amount of selective dopant metal can be easily controlled by implantation dose and energy during implantation. The low energy (typically range ~ 10–500 keV) ion beam has been used for implantation process and range of the implantation species is (Implanted length) from few angstrom (Å) to 1 μm (also depends on the target material). This technique is also convenient for synthesizing the nanoparticles in the target materials with better control of depth and selective area. Different lattice interstitials, vacancies and planer defects are generated by the collision of incident ions with target material during implantation, which could be responsible for the structural modifications.

In the present study, a comparative study on pure ZnO and Ag-ZnO nanocomposite thin films synthesized by RF magnetron sputtering technique has been done. Effect of higher Ag doping on the electrical and structural properties of the ZnO have been demonstrated in the first study. In the next section, ZnO thin films were synthesized by RF sputtering and then 120 keV Ag ions were implanted into ZnO matrix with different implantation dose ranging from  $3 \times 10^{14}$  to  $3 \times 10^{16}$  ions/cm<sup>2</sup>. The modifications in structural, optical and electrical properties have been investigated using different characterization techniques.

## **5.2. Synthesis of Ag-ZnO nano-composite thin films using RF-magnetron sputtering**

### **5.2.1. Experimental details**

Pure ZnO and Ag-ZnO nanocomposite thin films were grown by RF magnetron co-sputtering method. A target (3 mm thick and 2 inch diameter) of ZnO powder (Alfa Aesar), was prepared by a hydraulic press machine and then it sintered at 1200 °C for 24 hours in the tubular furnace, continuous flow of oxygen gas. Some small pieces of silver (Ag) were glued on the ZnO target at the different position before deposition for synthesizing the composite thin films. Silicon (p-type 100), quartz, and glass used as the substrate during the deposition and all were cleaned by acetone and deionized water in the sequential manner. A turbo pump coupled with the rotary pump for achieving the high vacuum of the order of  $10^{-6}$  mbar in the deposition chamber before the deposition. The deposition was carried out at a vacuum  $10^{-2}$  mbar order, in the presence of pure argon gas (Grade-I) in the sputtering chamber during deposition. The target to substrate distance was ~ 50 mm measured before the deposition. The deposition was performed for 20-30 minutes at the 150 watt RF power and the substrate temperature 300 °C, measured by thermocouple gauge and controlled by using a feed-back controlled heater in gauge. The all crucial parameters which monitored during deposition are tabulated in **Table 5.1**.

*Table 5.1 The sputtering parameters for thin film deposition.*

<i>Sl. No.</i>	<i>Sputtering parameter</i>	<i>Value</i>
1.	R.F. Power	150 watt
2.	Gas used during deposition	Argon (grade-1)
3.	Pressure before deposition	$6 \times 10^{-6}$ mbar
4.	Pressure during deposition	$5 \times 10^{-2}$ mbar
5.	Substrate temperature	300 °C
6.	Target to substrate distance	5 cm

## 5.2.2. Results and Discussion

### 5.2.2.1. Rutherford backscattering spectroscopy

RBS technique is used to estimate the composition of the species with high accuracy. **Figure 5.1 (a-d)** represents the RBS spectrum of the pure ZnO and Ag-ZnO nanocomposite films. For the estimation of concentration, the obtain experimental RBS

spectra were simulated by Rutherford Universal Manipulation Simulation Program (RUMP) [184] which is shown in all figure by separated red line. The Ag atomic fraction in ZnO matrix was found to be 8 at.%, 15 at.% and 40 at.% respectively. The plateau region of the spectrum is responsible for the Si substrate. Since these films were grown on the Si substrate. From RBS spectra, it can be concluded that the Ag-ZnO composite structure is formed with different Ag doping and embedded in the ZnO matrix.

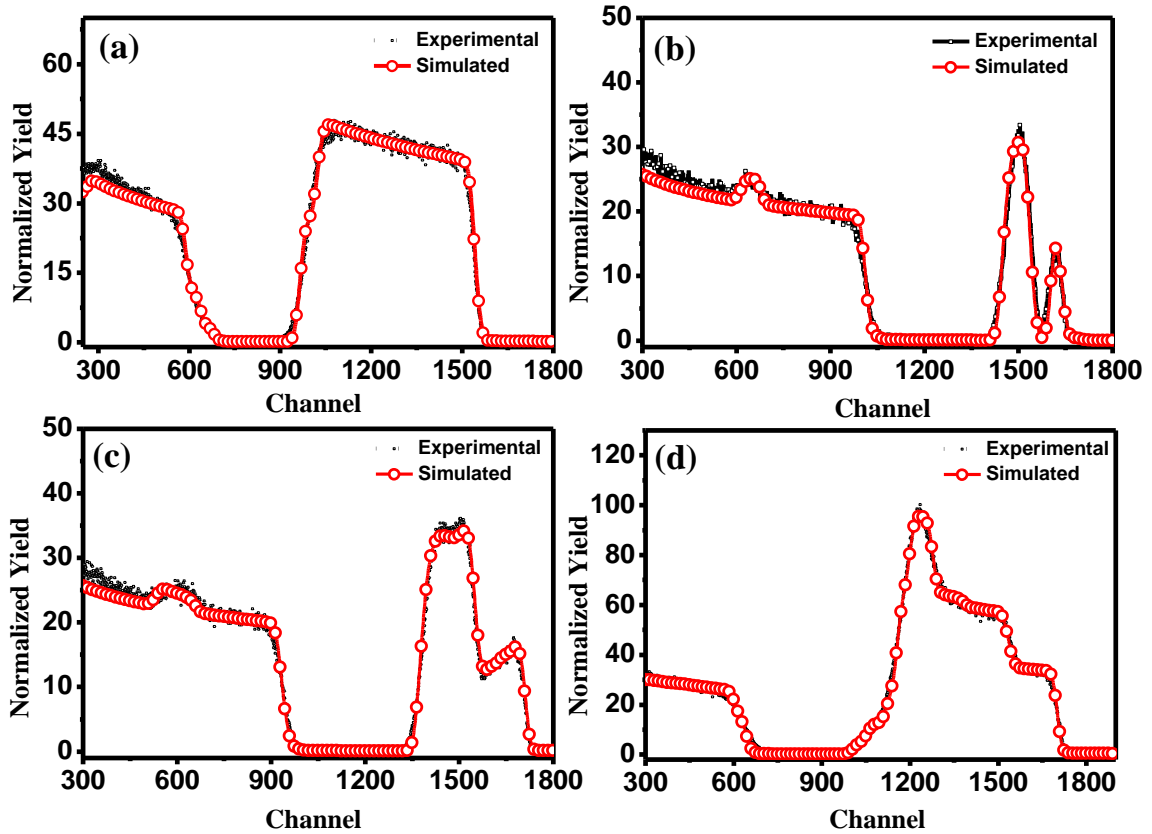


**Figure 5.1** RBS spectra for the (a) pure ZnO (b) Ag-ZnO (8%) and (c) Ag-ZnO (15%) (d) Ag-ZnO (40%) nanocomposite thin films.

### 5.2.2.2. X-ray diffraction analysis

The crystalline quality of the pure ZnO and Ag-ZnO nanocomposite thin films was investigated by XRD. **Figure 5.2** shows the XRD patterns obtained on pure ZnO and Ag-ZnO nanocomposite films with doping concentrations of 8 at.%, 15 at.% and 40 at.% respectively. For pure ZnO we identified number of peaks at the diffraction angle of  $31.79^\circ$ ,  $34.43^\circ$ ,  $36.19^\circ$  and  $46.32^\circ$ , respectively which corresponds to the planes (100), (002), (101), and (102), can be well indexed to the wurtzite hexagonal structure with

JCPDS-89-1397 card. It is also evident that the pure ZnO film has grown along preferred c-axis orientation (002) as confirmed by X-ray pattern. However, for Ag doping of 15 at.% and 40 at.% initial reflections (100), (002) of ZnO are vanished but at higher Ag doping (40%), a strong reflection (111) arises which corresponds to the silver nanocluster at 38.18°. Therefore the appearance of new peak ascribed the highly presence of silver (Ag) in ZnO thin film as confirmed by RBS. The lattice parameter of the pure and ZnO and Ag-ZnO nanocomposite films was calculated by using Bragg's law and basic crystal structure formula of the hexagonal wurtzite structure. A marginal change of the lattice parameters was observed when Ag doping was introduced in the ZnO matrix. Lattice parameters before and after doping are summarized in **Table 5.2**. Since Ag ions (radius of 1.02 Å) have a large radius as compared Zn ions (radius of 0.72 Å) to Ag ions which attributed to change in lattice parameter with Ag incorporation. The change in the lattice parameter values indicates that Ag substitute by Zn. Since it is well known that Ag doping in ZnO yield p-type semiconducting behaviour. Furthermore the stress in the pure ZnO and Ag-ZnO nanocomposite film was also calculated by the following relation [185].

$$\sigma (Pa) = -233 \left[ \frac{c-c'}{c'} \right] [GPa] \quad (5.1)$$

In equation (5.1),  $\sigma$  shows the stress of the sample,  $c$  is calculated lattice parameter for the prepared film and  $c'$  is the strain-free lattice constant of the bulk ZnO. The result of lattice parameter and stress for the thin film are tabulated in **Table 5.2**. The presence of negative sign in the stress shows the compressive nature of the stress for pure and Ag-ZnO nanocomposite thin films, it arises due to the lattice defects which was the presence of the pure ZnO and Ag doped ZnO composite thin film. The crystallite size of pure ZnO film was calculated by Scherrer's formula (**Equation 3.6**) and found to be 14.1 nm [86]. At the higher doping concentration of Ag (40%), the appearance of the Ag peak in the spectra indicates the formation of the Ag-ZnO composite in the thin film.

**Table 5.2** Lattice parameter and crystallite size for pure ZnO and Ag-ZnO nanocomposite thin film.

Sl. No.	Sample Detail	Lattice parameter		c/a ratio	Crystallite size (nm)	Stress $\sigma$ (GPa)
		a (Å)	c (Å)			
1.	Pure ZnO	3.2484	5.2057	1.6025	14.1	-0.04
2.	Ag-ZnO (8%)	3.2492	5.2103	1.6032	13.5	-0.22
3.	Ag-ZnO (15%)	3.2402	5.2486	1.6198	24.4	-1.95
4.	Ag-ZnO (40%)	3.2343	5.2078	1.6101	19.7 for ZnO 13.0 for Ag	-0.13

The crystallite size for higher doping was also calculated and yielded 19.70 nm for ZnO, and 13.0 nm for Ag-ZnO nanocomposite thin film at higher doping. This clarifies that the crystalline behaviour of the ZnO film can be control by Ag concentration as shown in X-ray pattern.

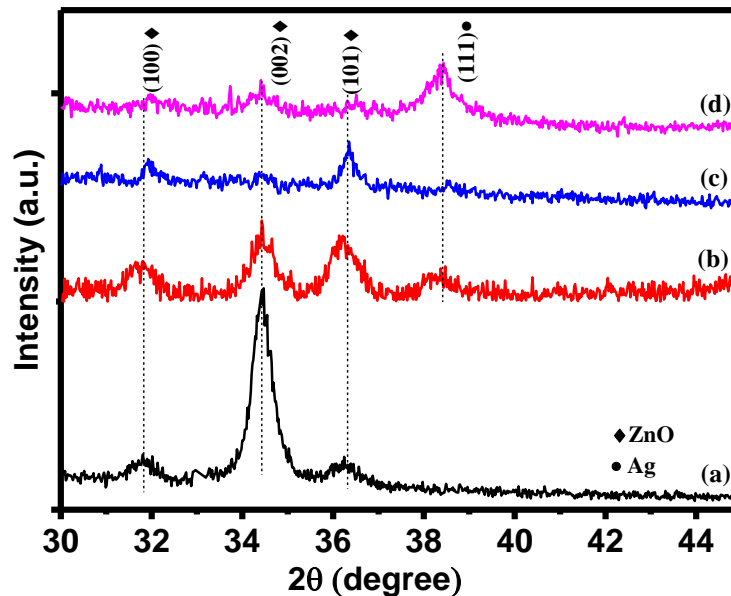


**Figure 5.2** XRD diffraction pattern for the pure (a) and Ag-ZnO nanocomposite thin film with three different doping concentration (b. 8%, c. 15% and d. 40% Ag concentration).

### 5.2.2.3. Scanning electron microscopy

Surface morphology of the top surface of the pure and composite films can be easily observed from surface electron microscopy (SEM). **Figure 5.3 (a-d)** shows the SEM images of the pure ZnO and Ag-ZnO nanocomposite thin film with three doping

concentrations of 8 at.%, 15 at.% and 40 at.% respectively. In the case of pure ZnO which shown in **Figure 5.3 (a)**, a non-uniform irregular pyramidal type sharp-blunt shape grains are observed which spread over the complete substrate. The observed grain size was found to 150-250 nm for the pure ZnO thin film. After the Ag incorporation, noticeable changes were observed in surface features of the composite thin film. For the lower doping concentration (8% and 15% both), disappearance of the pyramidal type of grains clearly observed. Pure ZnO grains shows the sharp grain boundary between the grains but as the doping of Ag increase then the grain boundary becomes disappear and agglomeration process accure there.

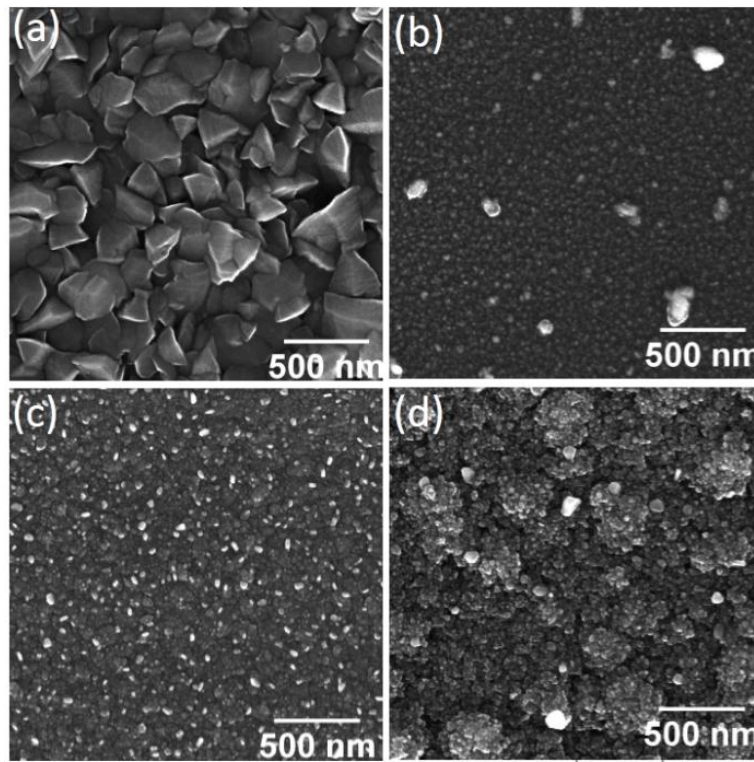


**Figure 5.3** Scanning electron micrograph for (a) pure ZnO (b) 8% Ag-ZnO (c) 15% Ag-ZnO and (d) 40% Ag-ZnO nanocomposite thin films.

At the higher doping concentration, film becomes more compact due to Ag incorporation and formed the big island of the grains on the top surface of the film. During the deposition, the films have been grown on the substrate which governs by two process, nucleation and coalescence process. Nucleation process has responsible for the formation of the island, these islands contain those nuclei which have lower formation

energy. As the doping of metal increase with further deposition, the size of these islands increase and they became come closer during deposition and formed a large bulky island. Coalescence process between smaller grains are responsible for these type of growth which can easily observe for the case of higher doping [186,187]. For the higher concentration (40%), different size of bulky islands appeared on the surface of Ag-ZnO nanocomposite thin film.

#### **5.2.2.4. Micro-Raman measurement**

Raman spectra of pure ZnO and Ag-ZnO nanocomposite thin films shown in **Figure 5.4**. Raman spectra revealed that pure ZnO film showed two different bands one at 441 and another at 575  $\text{cm}^{-1}$ . The first band appeared at 441  $\text{cm}^{-1}$  could be assigned to  $E_2$  high mode and other bands at 575  $\text{cm}^{-1}$  represent the  $A_1$  (LO) mode of the pure ZnO film. The presence of  $E_2$  high mode in the spectra confirmed the formation of wurtzite structure of the ZnO film. These results are in good agreement with result obtained by XRD measurements which showed the formation of hexagonal wurtzite structure. Doping of Ag is very much effected on the Raman spectra shows a gradual change in the variation mode when Ag doping was introduced in the ZnO matrix. A complete disappearance of the  $E_2$  high mode at the higher doping of Ag in ZnO was found, whereas some new mode arises at 495  $\text{cm}^{-1}$  at the higher concentration (40%). The appearance of this new mode at higher doping resulting in a low crystallinity of the film. The local vibrational mode at 495  $\text{cm}^{-1}$  arises due to Ag doping in ZnO thin film, and some other doping material also exhibits this mode [188]. The intensity of  $A_1$  (LO) mode increases at higher Ag (40 at.%) doping.  $A_1$  (LO) mode of the thin films is directly related to the defect density, zinc interstitials and oxygen vacancies in NCs thin film. Therefore the higher doping of Ag is mainly responsible for the lower crystallinity and defect creation in the thin films.

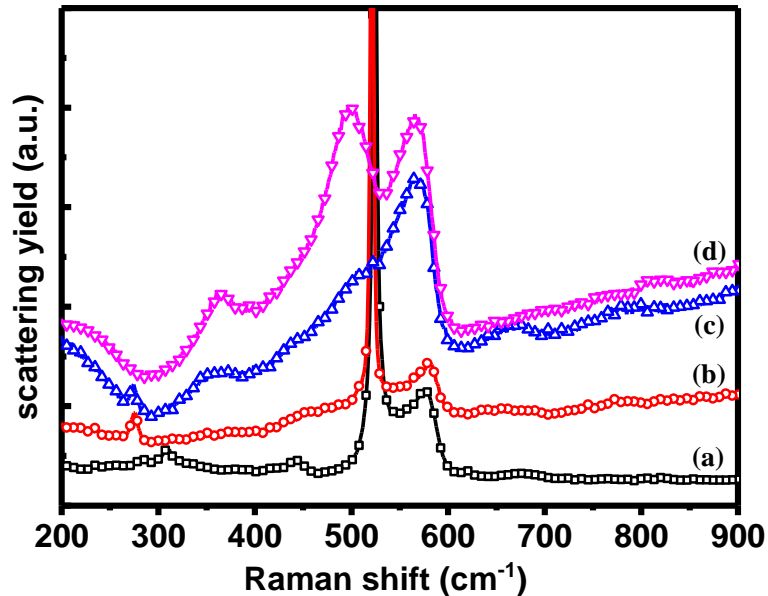


*Figure 5.4 Raman spectra for the pure (a) and Ag-ZnO nanocomposite thin film with different doping concentration (b. 8% c. 15% and d. 40% Ag concentration).*

#### 5.2.2.5. Electrical measurements

**Figure 5.5** shows the variation in current with applied voltage (I-V spectra) of the pure ZnO and Ag-ZnO NCs thin film with different Ag concentration and we calculated the resistance as well conductivity of the films from these spectra. The contacts for this purpose were made using silver paste at room temperature. These measurements were performed at room temperature using a two probe method. **Figure 5.5** shows the I-V curve of pure ZnO and Ag-ZnO nanocomposite thin films with Ag concentrations of 8 at.%, 15 at.% and 40 at.% respectively. The slope of I-V curve yielded resistance value by fitting the linear part of the graph, from this the resistivity of NCs thin film can be determined. The resistivity of the films is significantly affected by Ag doping in ZnO thin film. The conductivity of the film is also calculated with the help of resistivity of the sample. The conductivity of the film at the higher doping concentration (40 at.%) was found to be very higher and measured value are nearly comparable to the conductivity of the pure Ag. The variation of resistance and conductivity of the NCs thin films as a function of Ag concentration which is shown in **Figure 5.6**. A significant improvement in the conductivity of the Ag-ZnO nanocomposite was found and depends on the number of charge carrier. The charge carrier density is effected by the inclusion of Ag doping in the



ZnO thin film. It is apparent that Ag ions increase the majority charge carrier in ZnO thin film and as a consequence the resistance decrease of the film. The conductivity of the pure ZnO thin film was found to be  $4.32 \times 10^{-3} \text{ mho cm}^{-1}$  which is lower compared to Ag-ZnO nanocomposite particularly at higher doping concentration it reaches up to  $4.18 \times 10^4 \text{ mho cm}^{-1}$ .

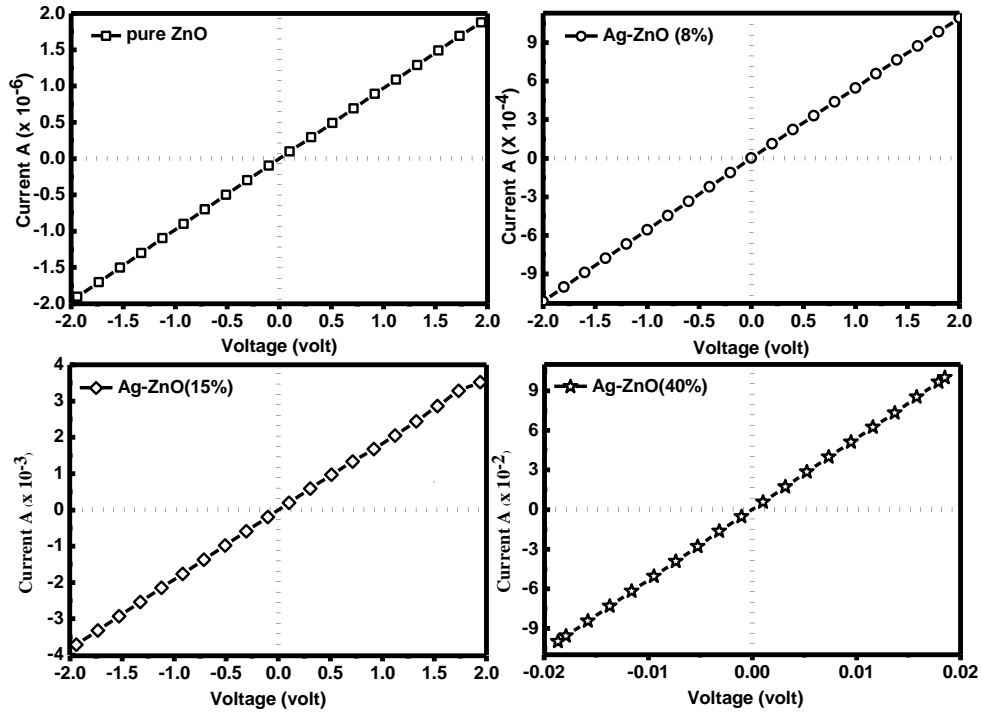


Figure 5.5 I-V spectra for the pure and Ag-ZnO nanocomposite thin films.

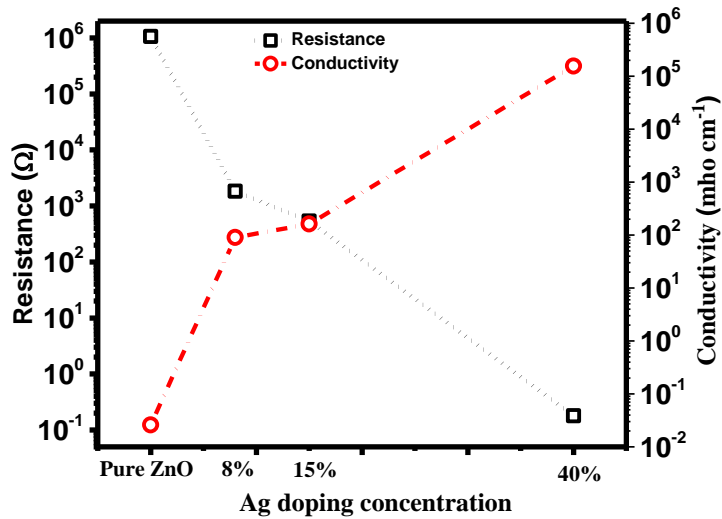


Figure 5.6 Variation of resistance and conductivity with Ag doping concentration.

**Table 5.3** The electrical parameter for pure ZnO and Ag-ZnO nanocomposite thin film.

<b>Sr. No.</b>	<b>Sample Detail</b>	<b>Carrier concentration</b>	<b>Type of majority charge carrier</b>	<b>Resistance</b>	<b>Conductivity (in mho cm<sup>-1</sup>)</b>
1.	Pure ZnO	$4.32 \times 10^{14} \text{ cm}^{-3}$	n-type	1.06 MΩ	$4.32 \times 10^{-3}$
2.	Ag-ZnO (8%)	--	--	1.86 KΩ	$9.00 \times 10^1$
3.	Ag-ZnO (15%)	$2.28 \times 10^{20} \text{ cm}^{-3}$	p-type	536 Ω	$1.71 \times 10^2$
4.	Ag-ZnO (40%)	$5.11 \times 10^{21} \text{ cm}^{-3}$	p-type	0.18 Ω	$4.18 \times 10^4$

For the confirmation of the semiconducting behaviour of NCs thin films, Hall measurements setup (ECOPIA Hall probe system) was applied at room temperature. Pure ZnO thin film showed the n-type conductivity with carrier concentration of about  $4.32 \times 10^{14} \text{ cm}^{-3}$ . While Ag doped ZnO showed the p-type conductivity because of Ag incorporation in ZnO matrix because of the Ag is good candidate for the occupation of Zn substitutional ( $\text{Ag}_{\text{Zn}}$ ) and interstitial ( $\text{Ag}_{\text{i}}$ ). Theoretically, Ag has shallow acceptor level and lowest transition energy as well as less formation energy for  $\text{Ag}_{\text{Zn}}$  in comparison of  $\text{Ag}_{\text{i}}$ . These properties of the Ag acknowledge to presenting good element in comparison of Cu and Au for p-type doping in ZnO [189–191]. The carrier concentration of the NCs thin film is tabulated in **Table 5.3**.

### **5.3. Synthesis of Ag-ZnO nano-composite thin films using negative ion implantations technique**

#### **5.3.1. Experimental details**

##### *Deposition parameters*

ZnO target (2 inch diameter and 3 mm thickness) from the ZnO powder (Merck) using hydraulic press machine (HYCON Hydraulic engineers and consultants, New Delhi) for

the film deposition by RF-magnetron sputtering. A tubular furnace was used for the prepared ZnO target sintering at the temperature 1200 °C for the duration of 24 hours. The continuous flow of oxygen gas was kept during target sintering in the furnace. Sputtering was performed in the presence of argon gas and synthesized ZnO thin film with the thickness of ~ 500 nm. The rotary pump was used for achieving the rough vacuum and it is coupled with the turbo-molecular pump for obtaining the high vacuum in the sputtering chamber. The initial vacuum in the deposition chamber before the deposition was  $5 \times 10^{-5}$  mbar and it decreased when introducing the argon gas in the chamber and measured  $3 \times 10^{-2}$  mbar pressure during the film deposition. The deposition was performed at room temperature for 30 minutes at the RF power was ~150 watts. The target to substrate distance ~ 4 cm and self-bias voltage of the sputtering unit was 250-300 volt during the deposition.

#### ***Implantation parameters***

After the film deposition, all the samples were mounted in the implantation chamber for the implantation. 120 keV Ag ion beam was used for the ion implantation in ZnO thin film using negative ion implantation facility at IUAC, New Delhi. The value of  $S_n$  and  $S_e$  are calculated by SRIM and found to be  $2.54 \times 10^2$  eV/Å and  $2.71 \times 10^1$  eV/Å respectively with the range of ~ 424 Å in ZnO material. The Ag ion beam scanned over the complete sample area ( $1 \times 1$  cm<sup>2</sup>) with five different implantation dose  $3 \times 10^{14}$ ,  $1 \times 10^{15}$ ,  $3 \times 10^{15}$ ,  $1 \times 10^{16}$  and  $3 \times 10^{16}$  ions/cm<sup>2</sup>. The constant beam current ~ 1.1 µA was stable during Ag ion implantation.

### **5.3.2. Results and discussion**

#### **5.3.2.1. Rutherford backscattering spectroscopy**

Rutherford backscattering spectroscopy (RBS) is the efficient technique to estimate the thickness and compositional parameter of the materials. RBS spectrum and depth profile of Ag implanted ZnO films (at higher fluence  $3 \times 10^{16}$  ions/cm<sup>2</sup>) are shown in **Figure 5.7 (a-d)**.

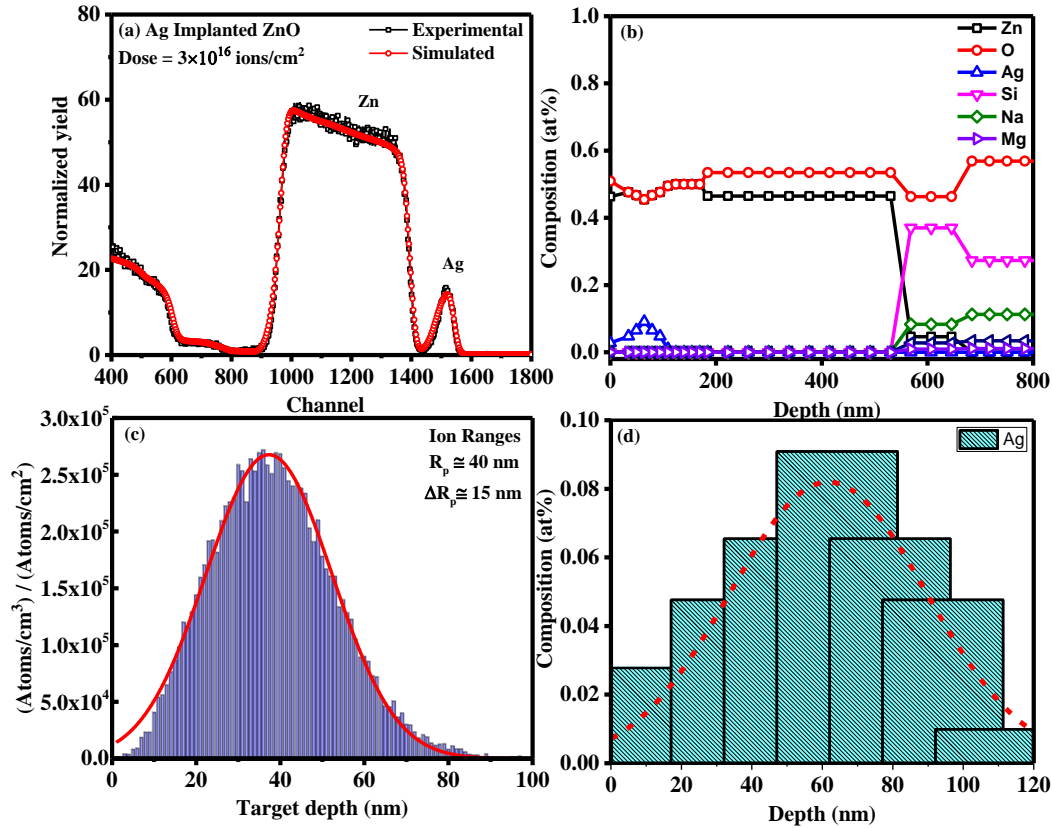


**Figure 5.7** (a) RBS spectra of the Ag implanted ZnO thin film (b) Depth profile of Ag implanted ZnO thin film and (c) Depth distribution curve of Ag ion implanted in ZnO thin film estimated by SRIM-TRIM simulation (d) Enlarge view shows the experimental distribution of Ag ions by RBS.

The experimental RBS spectra was simulated by Rutherford Universal Manipulation Program (RUMP) [192] as shown in **Figure 5.7 (a)**. The thickness and presence of Ag at the surface of the ZnO film have been estimated by the simulated spectra. The thickness of the film has been estimated and found to be  $\sim 500$  nm. The potential sputtering near to the surface take place during the ion implantation and could be responsible for a variation in the thickness [193]. The presence and asymmetric distribution of Ag ions at the surface of the ZnO film have been observed by depth profile curve (**Figure 5.7 (d)**). The depth profile of Ag implanted films showed that, the stoichiometry of the film is affected by Ag ions implantation close to the surface region. Furthermore, theoretical distribution of 20000 Ag ions (**Figure 5.7 (e)**) in ZnO film was calculated by the SRIM-TRIM simulation program [194]. The experimental distribution

of Ag in ZnO matrix is supported by the simulated depth profile of Ag implanted ZnO film (**Figure 5.7 (b)**). The marginal difference between simulated and experimental Ag distribution may be subjected to the energy deposition by incident ions which leads to the preferential sputtering as well as high dynamic annealing near the surface.

### 5.3.2.2. XRD analysis

**Figure 5.8 (a)** shows the X-ray diffraction (XRD) pattern for pure ZnO and 120 keV Ag Implanted ZnO thin films at different implantation doses from  $3 \times 10^{14}$  to  $3 \times 10^{16}$  ions/cm<sup>2</sup>. Pure ZnO film shows the crystalline nature and indicates the hexagonal wurtzite structure with (100), (002), (101), (102), and (110) reflection planes which appear at the diffraction angle  $31.7^\circ$ ,  $34.2^\circ$ ,  $36.2^\circ$ ,  $47.4^\circ$ , and  $57.1^\circ$  respectively (JCPDS Card No. 89-1397). At the higher implantation dose, all other planes are disappeared except one plane (002), which indicates the monocrystalline nature of the ZnO thin film with higher crystallinity. Grain growth along the c-axis with Ag ion implantation has been clearly observed by the spectra which can be useful for device fabrication.

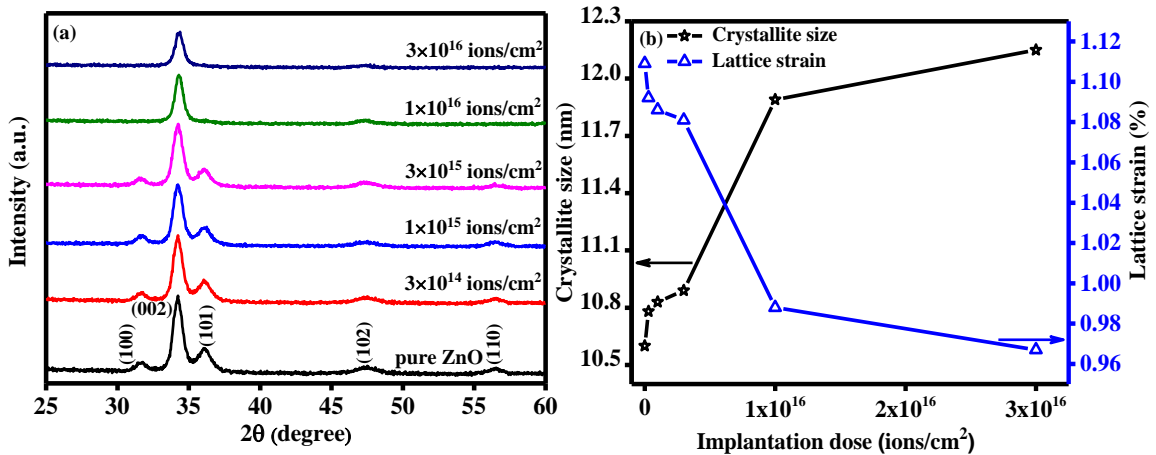


**Figure 5.8 (a)** X-ray diffraction pattern of the pure ZnO and 120 keV Ag implanted thin film with different dose (b) Variation in crystallite size and lattice strain with implantation dose.

Lattice strain of the film releases with the Ag ion implantation clearly mentioned in **Figure 5.8 (b)** and it is responsible for the growth of the film in *c*-axis. Basic crystal theory suggests that, (002) plane has the lowest surface energy for easy growth along this

plane for the ZnO. Lattice strain for the pure and Ag implanted ZnO films are calculated using **Equation 3.7** [195]. The lattice strain of the film decreases with increasing the implantation dose. The crystallite size of the pure ZnO film has been calculated and found to be  $\sim 10.6$  nm and it marginally increases up to 13.0 nm with Ag ion implantation at higher dose  $3 \times 10^{16}$  ions/cm<sup>2</sup>. The crystalline behavior of the film improves with Ag ion implantation due to realizing of strain at higher implantation dose.

### 5.3.2.3. UV-visible absorption spectroscopy

**Figure 5.9** shows UV–Visible transmittance spectra of pure ZnO and Ag implanted ZnO thin films. The range of spectrum is taken from 350 to 750 nm (visible range of electromagnetic spectrum) during the characterization. The transmittance of the film significantly decreases with Ag ion implantation. The value of transmittance is decreased from  $\sim 80\%$  to  $\sim 40\%$  for pure and Ag implanted ZnO thin film at higher dose  $3 \times 10^{16}$  ions/cm<sup>2</sup> calculated at  $\sim 550$  nm. This decrement in the transmittance may be attributed due to charge carrier density as well defects creation during Ag ion implantation in the ZnO film.

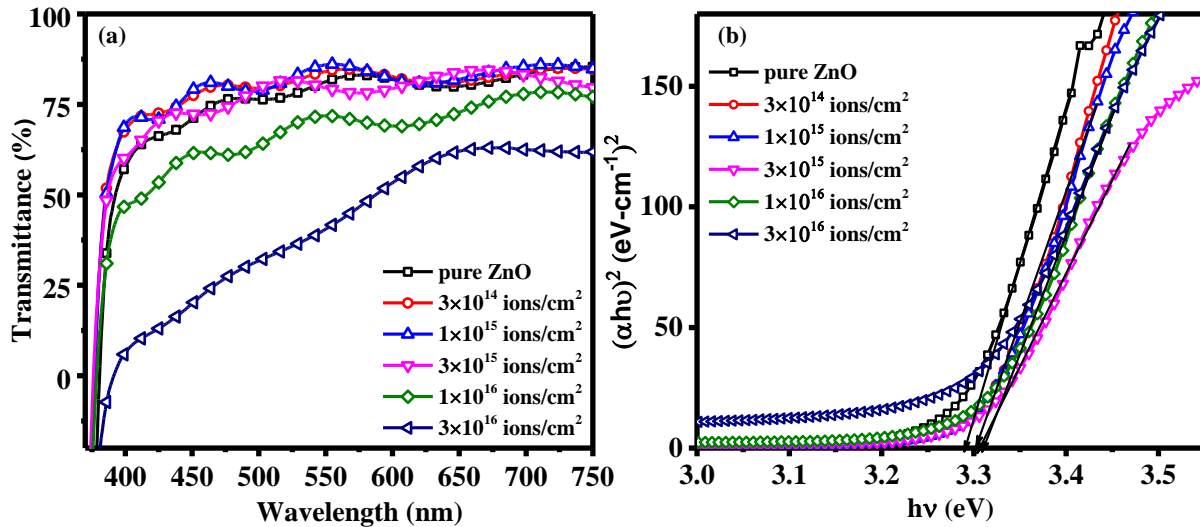


**Figure 5.9** (a) UV-visible transmittance spectra of the pure ZnO and 120 keV Ag implanted ZnO thin film with different dose (b) Variation in band gap of the pure and implanted ZnO thin films.

Surface morphology of the films also play the major role for change in optical properties of the film which is further investigated by atomic force microscopy. The band gap of pure and Ag implanted ZnO thin film has been determined using Tauc's **Equation 3.9** [196]. ZnO has direct band gap material, so the value of n for this case is taken 2 for calculating the band gap of the film. There is no significant change observed in optical band gap of pure and Ag implanted ZnO thin film at the higher implantation dose shown in **Figure 5.9 (b)**.

### 5.3.2.4. Atomic force microscopy

To observe the surface features of pure and Ag implanted ZnO thin films have been characterized by AFM in tapping mode. **Figure 5.10** shows the 2-D AFM micrograph ( $1 \times 1 \mu\text{m}^2$ ) with different implantation dose ranging from  $3 \times 10^{14}$  to  $3 \times 10^{16}$  ions/cm<sup>2</sup>. The very well inter-connected grains on the top of the surface of the film are clearly observed by AFM images. The grain size of pure ZnO film is calculated by Nano-scope image processing software and found to be  $\sim 25.28$  nm.

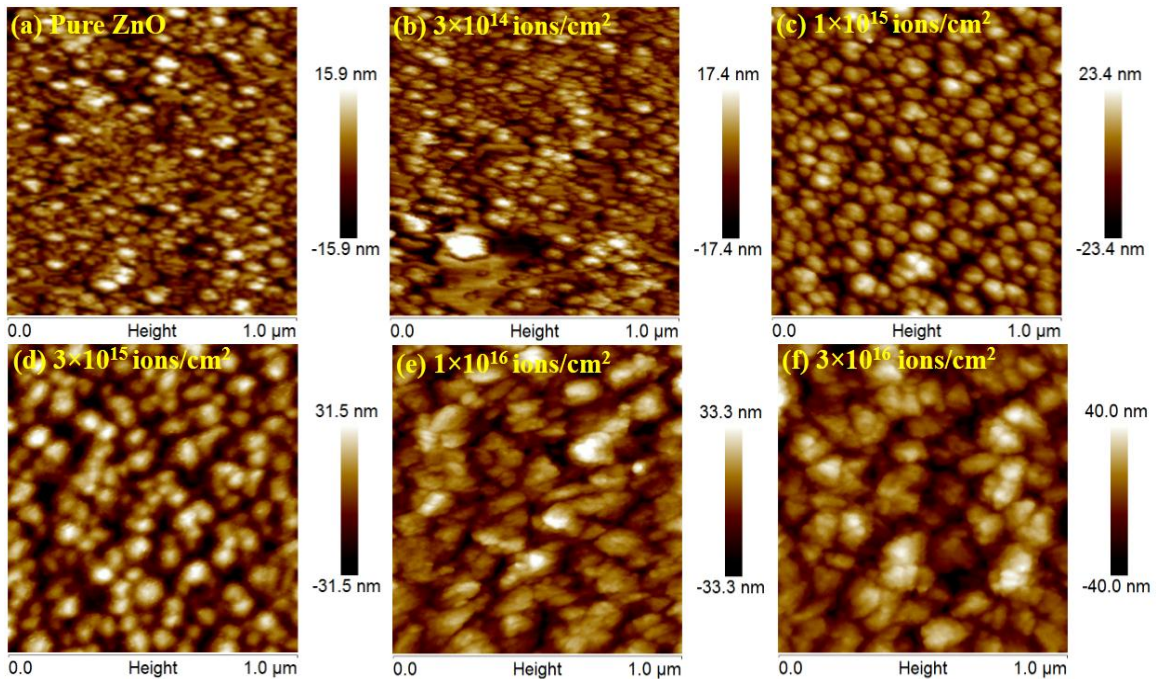


**Figure 5.10.** 3-D AFM micrographs of as-deposited and 120 keV Ag implanted ZnO thin film with different implantation dose.

The grain size of the film increased with increasing the implantation dose and it reached up to  $\sim 47.51$  nm at the higher implantation dose ( $3 \times 10^{16}$  ions/cm<sup>2</sup>). The relaxation of the strain with in crystal lattice and appearance of the high density of defects have been found due to interaction of low energy (120 keV) Ag ions with ZnO films and also high dynamic annealing near the surface region. Therefore, the formation of defects clusters accumulated at the surface and lead to agglomeration of the grains [197]. The grain size has been increased with implantation dose as confirmed by AFM and XRD. The grain size of film is larger in comparison to crystallite size as calculated by AFM, because AFM shows the agglomeration of grains however the XRD shows average crystallize size. The root-mean-square roughness ( $R_{rms}$ ) of pure and Ag implanted ZnO thin films have been estimated by **Equation 4.1**.

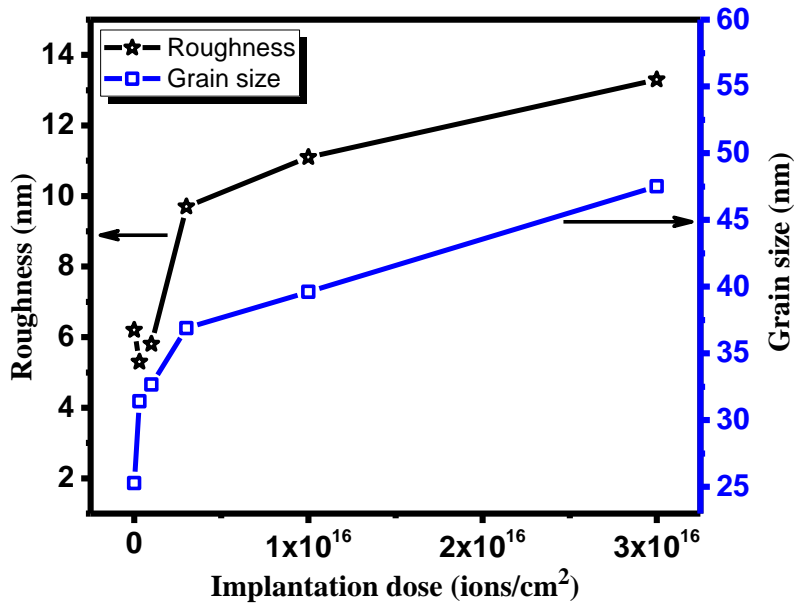


**Figure 5.11** Variation in roughness and gain size of the pure and 120 keV Ag implanted ZnO thin film with different implantation dose.

The roughness of pure ZnO thin film has been calculated by relation and found to be  $\sim 6.2$  nm. The increment in the roughness values has been observed with increasing the implantation dose. The roughness of the Ag implanted ZnO thin film at higher implantation dose ( $3 \times 10^{16}$  ions/cm<sup>2</sup>) has been found to be  $\sim 13.3$  nm. During ion implantation, potential sputtering take place near the surface of ZnO film due to high density of collision cascades induced by 120 keV Ag ions, which could be responsible for



higher surface roughness [198]. **Figure 5.11** shows the variation in the grain size and roughness of the pure and Ag implanted ZnO thin films with different implantation dose.

### 5.3.2.5. Micro-Raman spectroscopy

For the case of ZnO (hexagonal wurtzite structure) space group associated with  $C_{6v}^4$  symmetry. According to basic group theory, ZnO has eight set of phonon normal modes as  $2A_1 + 2E_1 + 2B_1 + 2E_2$  with  $A_1 + E_1$  acoustic modes and remain six modes  $A_1 + E_1 + 2B_1 + 2E_2$  are optical phonon modes at  $\Gamma$  point of the Brillouin zone [199]. Raman spectra for pure and Ag implanted ZnO thin films are shown in **Figure 5.12**.

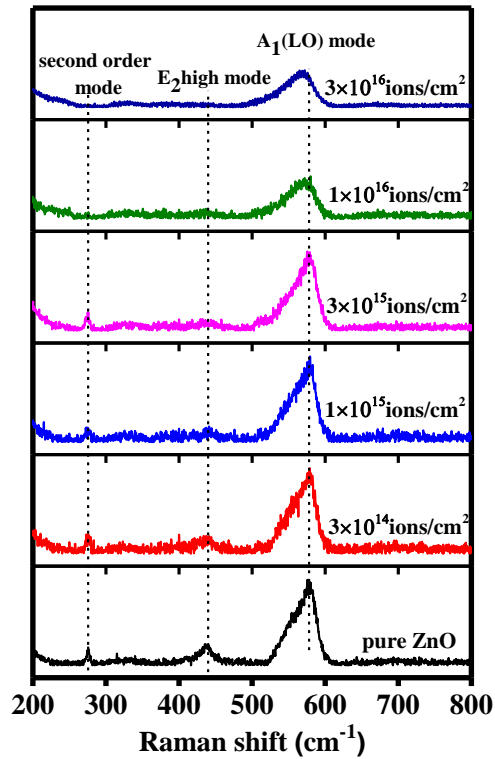


**Figure 5.12** Raman spectra of the pure ZnO and 120 keV Ag implanted ZnO thin film with different implantation dose.

The typical spectra shows three bands at  $580\text{ cm}^{-1}$ ,  $438\text{ cm}^{-1}$  and  $274\text{ cm}^{-1}$  for pure and implanted ZnO thin films. The sharp and highly intense band at  $580\text{ cm}^{-1}$  is assigned to  $A_1$  (LO) mode, which is good agreement with theoretical results. The other bands  $438\text{ cm}^{-1}$  and  $274\text{ cm}^{-1}$  are associated with the  $E_2$  (high) mode and  $B_1$  (high) –  $B_2$  (low) mode

respectively. The presence of E<sub>2</sub> (high) mode in the spectra of pure ZnO thin film confirmed the formation of the wurtzite structure. The E<sub>2</sub> (high) mode as well B<sub>1</sub> (high) – B<sub>2</sub> (low) disappears with Ag ion implantation but A<sub>1</sub> (LO) mode is not much affected at the lower implantation dose up to 3×10<sup>15</sup> ions/cm<sup>2</sup>. At the higher implantation dose (1×10<sup>16</sup> and 3×10<sup>16</sup> ions/cm<sup>2</sup>), the intensity of the A<sub>1</sub> (LO) mode decreases and observed a red shift in its position due to Ag ion implantation. The observed red shift in A<sub>1</sub> (LO) mode may be due to Ag incorporation in the ZnO matrix during implantation. The structural lattice strain of the film also responsible for observed red shift because films releasing their strain with Ag ion implantation as confirmed by X-ray diffraction pattern. A complete disappearance of the E<sub>2</sub> high mode has been found at the higher implanted dose indicating the Ag incorporation, which is responsible for lower crystallinity and defect creation in the ZnO matrix.

#### **5.2.3.6. X-ray photoelectron spectroscopy**

The presence of species and surface structure of the pure and 120 keV Ag implanted ZnO (at higher dose) thin film have been investigated by XPS analysis and obtained results are shown in **Figure 5.13**. In the case of pure ZnO, high-resolution spectra of Zn 2p region exhibits 2p<sub>3/2</sub> and 2p<sub>1/2</sub> states at the position of ~ 1022.70 eV and ~ 1045.85 eV. Oxygen shows the asymmetric behavior with two type of oxygen group. First oxygen group is associated with the Zn-O bonding, while second group confirms the existence of hydroxyl group at the binding energy of ~ 530.57 eV and ~ 531.96 eV respectively. The existence of Ag is confirmed by the peak observed in the survey scan (for the implanted film), therefore high-resolution XPS spectrum of Ag has been recorded and displayed in **Figure 5.13**. The binding energies of Ag (3d<sub>5/2</sub>) and Ag (3d<sub>3/2</sub>) are ~ 374.06 eV and ~ 368.05 eV, respectively. The energy splitting of 3d doublet is ~ 6 eV. This energy splitting reveals the metallic nature of Ag at the surface of ZnO film. The core spectrum of Ag is further deconvoluted to identify the interaction of Ag with ZnO and observed the lesser contribution of Ag<sub>2</sub>-O and Ag-Zn-O components in addition to metallic Ag. The existence of hydroxyl group in pure and implanted film is subjected to surface defects or belongs to oxygen deficient region/loosely bound oxygen on the surface [200]. The area of peak associated with hydroxyl group found higher with lesser intensity in the case of

an implanted film, which attributed to the creation of defects in the film during implantation. The decrement in intensity has been observed in core spectra of the Zn and O, which confirms the change in stoichiometry at the surface of the film and it is also supported by RBS

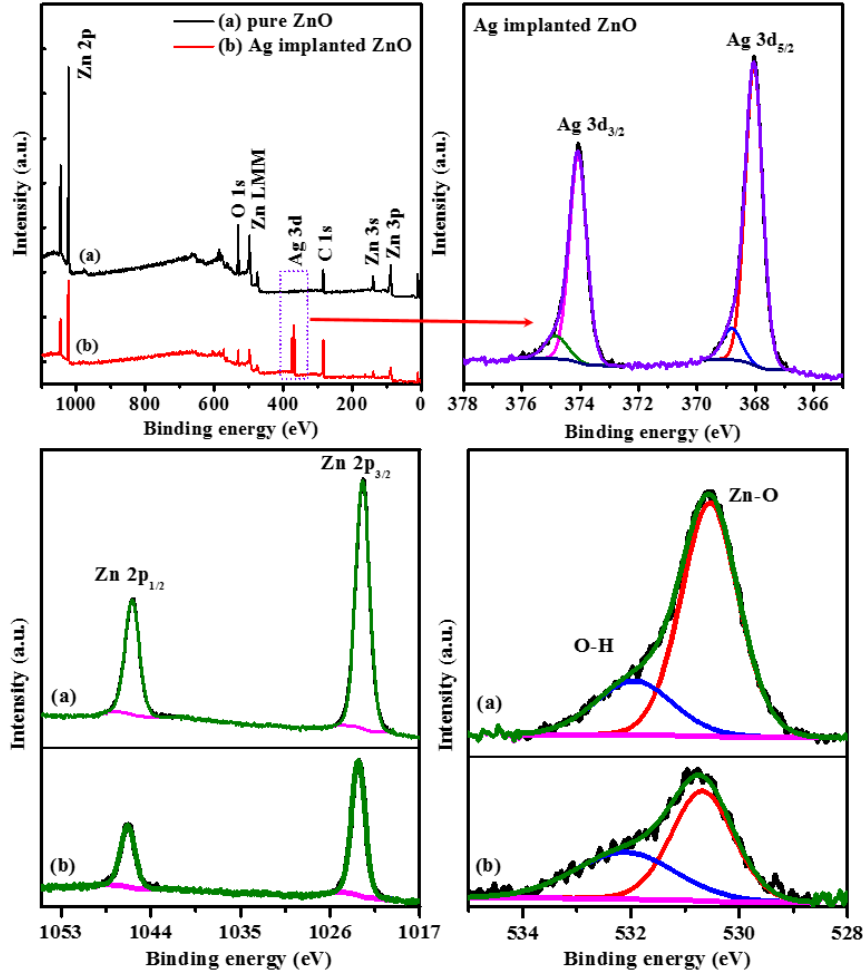


**Figure 5.13** XPS spectra of the pure ZnO and Ag implanted ZnO nanocomposite thin film at the dose  $3 \times 10^{16}$  ions/cm<sup>2</sup>.

#### 5.4. Summary

Ag-ZnO nanocomposite thin films have been synthesized by two different approaches; RF-magnetron sputtering and Ag ion implantation. To obtain higher concentration of the metal in ZnO matrix, RF- sputtering is more efficient technique. Three different metal concentration (8%, 15% and 40%) with ZnO matrix have been synthesized and then

characterized by different characterization tools to understand the structural, optical and electrical nature of the films. structural and morphological features of the pure and composite films have been observed by the XRD and SEM. In this case, very good electrical enhancement was found for the higher Ag doping. The nature of the film has been transformed from n-type to p-type with enhanced conductivity confirmed by Hall measurement. In another approach, Ag ion implantation was used to synthesize Ag nanoparticles in ZnO matrix. 120 keV Ag ion beam has been used for Ag ion implantation with different implantation dose. X-ray diffraction spectra revealed the formation of hexagonal structure with good crystallinity along c-axis. The charge carrier density has been affected by the Ag ion implantation which directly influenced the transmittance of the film. The lattice strain and transmittance of the film decrease with implantation and leads to the crystalline behaviour of the film. These types of nanocomposite films may be useful in different applications in device and sensing areas.

## Chapter 6

# SHI and Thermally Induced Modifications of Ag-ZnO Nanocomposite Thin Films

---

In this chapter, thermal and SHI irradiation induced modifications in Ag-ZnO nanocomposite thin films have been studied. 100 MeV Ag ion beam is used for irradiation with three different fluences. As deposited films have been annealed in vacuum environment at three temperatures of 300 °C, 400 °C and 500 °C. Tuning of surface plasmon band by irradiation as well as thermal treatment has been observed.

## 6.1. Introduction

The functional nanomaterial with potential technological applications is the prominent field for researcher and scientist community in the present scenario. Ag-ZnO nanocomposite provides the diverse application in the fabrication of optoelectronic devices as silver nanocomposite shows better optical properties in the visible range of electromagnetic spectrum. The photo-catalytic activity of ZnO is also effected by the presence of silver nanoparticles. In the photo-absorption process, the silver nanoparticle can trap the charge carrier and these charge carriers are responsible for restriction of the charge recombination process [201–204]. The thin film of Ag-ZnO NCs exhibits the various optical and structural properties which can directly controlled by silver dopant, thermal annealing and ion beam treatment [205,206]. Swift heavy ion irradiation technique is mostly used to modify or enhance the properties of several materials [207–209]. When energetic ions are incident on the target material, they transfer a large amount of energy and produces a high density of electronic excitation along ion path in the narrow cylindrical zone. This high amount of deposited energy leads to the high density of defects in the target material, due to the heating effect along the ion path [210]. These defects and a large amount of energy in the target material are responsible for the structural and optical modifications by SHI irradiation. The thermal annealing is also advantageous process to tune the optical and structural properties of film after the deposition. At the same time, annealing environment is also play the major role to enhance the properties of the films [211,212].

In this study, investigation on the 100 MeV  $\text{Ag}^{7+}$  ions beam induced structural and optical modifications of Ag-ZnO nanocomposite thin films which were prepared by RF magnetron sputtering and irradiated at different fluences. In the subsequent section, Ag-ZnO NCs thin films have been synthesized by RF-magnetron sputtering and then annealed in the vacuum environment (of the order of  $10^{-2}$ ) to prevent the oxidation of Ag nanoparticles at three different annealing temperatures of 300 °C, 400 °C and 500 °C. The modifications produced due to SHI irradiation and thermal annealing are compared using different characterization technique.

## 6.2. SHI irradiation studies of nano-composites thin films

## 6.2.1. Experimental details

### *Deposition parameters*

Ag-ZnO nanocomposite thin films of thickness  $\sim 55$  nm were deposited on glass and Si substrates by the RF sputtering technique. ZnO target was prepared from ZnO powder (Alfa Aesar, 99.9 %) using hydraulic press machine and was sintered at  $1200^\circ\text{C}$  in the tube furnace for 24 hours in the presence of oxygen gas. Small pieces of silver (1mm thick) were glued on the ZnO target (3 mm thickness, 2-inch diameter) at a different position during deposition. The pressure in the sputtering chamber was  $10^{-6}$  Torr before introducing the argon gas into the chamber, achieved by turbo molecular pump which was coupled with the rotary pump in the sputtering unit. The deposition was performed at a pressure  $5 \times 10^{-2}$  Torr with the presence of argon gas (grade-I) in the sputtering chamber. The target to substrate distance was calculated before deposition and found to be  $\sim 4$  cm. The substrate temperature was  $\sim 300^\circ\text{C}$ , which was measured by thermocouple gauge and controlled using a feed-back controlled heater. The deposition was performed for 30-40 minutes with RF power at 150 watts and the self-bias voltage at 250-300 volt measured by sputtering unit.

### *Irradiation parameters*

Ag-ZnO NCs thin films were irradiated with 100 MeV  $\text{Ag}^{7+}$  ion beam by using 15 UD pelletron accelerator facility at IUAC, New Delhi. The ion beam is scanned over the area  $1 \times 1 \text{ cm}^2$  with three different fluences at  $3 \times 10^{12}$ ,  $1 \times 10^{13}$  and  $3 \times 10^{13}$  ions/ $\text{cm}^2$ .

## 6.2.2. Results and discussion

### 6.2.2.1. Rutherford backscattering spectroscopy

**Figure 6.1** shows the RBS spectrum of pristine Ag-ZnO nanocomposite (NCs) thin film on Si substrate. To estimate the metal atomic fraction and thickness of thin film, the obtained experimental RBS spectrum of the film was simulated by SIMNRA program and fitted as showing in **Figure 6.1**. The Ag atomic fraction was calculated to be  $\sim 8.0$  at.%, and thickness of pristine Ag-ZnO nanocomposite thin film was  $\sim 55$  nm which was observed by SIMNRA simulation program [213]. To understand the modifications of Ag-ZnO nanocomposite thin films due to 100 MeV  $\text{Ag}^{7+}$  ion irradiatio, it is necessary to find out the dynamics of ion interaction into the nanocomposite thin film. When swift heavy

ions (SHI) traverse through the target material, it interact with the electron as well nuclei of the target material and loose huge amount of energy in two different ways: (a) direct transfer of energy to target atoms by elastic collisions, termed as nuclear energy loss ( $S_n$ ) and (b) transfer of energy of incoming ions to the electrons of target atoms, termed as electronic energy loss ( $S_e$ ). Large amount of energy deposited by incident ions is responsible for the atomic displacement along the beam path and explained by two different models; Coulomb spike model (CSM) and Thermal spike model (TSM). When 100 MeV  $Ag^{7+}$  ions pass through the nanocomposite thin film, they loss their energy by creating electronic excitation as well as ionization of the atom of the target material by an inelastic collision between the incident ion and target electrons. Localized defects and disordered region created by electronic excitation during SHI irradiation are responsible for modifications in the lattice structure, optical properties and structural properties of the target material. In this study, the value of Electronic energy loss ( $S_e$ )  $\sim$  20.39 keV/nm and nuclear energy loss ( $S_n$ )  $\sim$  0.122 keV/nm for 100 MeV  $Ag^{7+}$  with ion range in target material is 20.15  $\mu$ m, calculated by stopping and range of ions in matter (SRIM) software [37]. Electronic and nuclear energy loss depend on incident ion energy, in low energy region nuclear energy loss ( $S_n$ ) is dominant and another side in high energy region, electronic energy loss ( $S_e$ ) is dominant, which can clearly be seen in **Figure 6.2**. In present work, 100 MeV energy is taken for irradiation of nanocomposite films as for high energy region electronic energy loss will be dominant and responsible for modifications which are shown in **Figure 6.2** by a vertical dashed line.



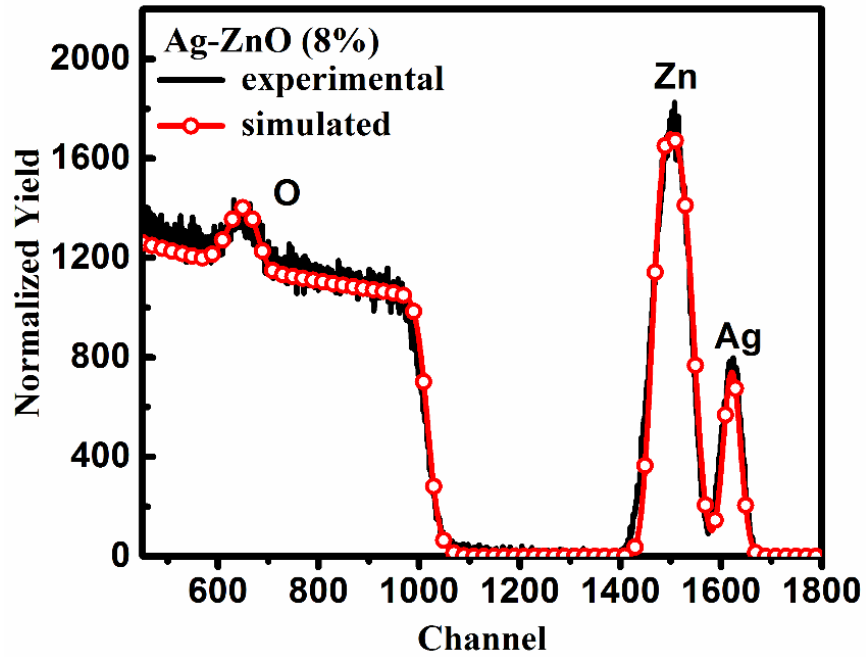


Figure 6.1 Rutherford backscattering spectrum (RBS) of Ag-ZnO nanocomposite thin film.

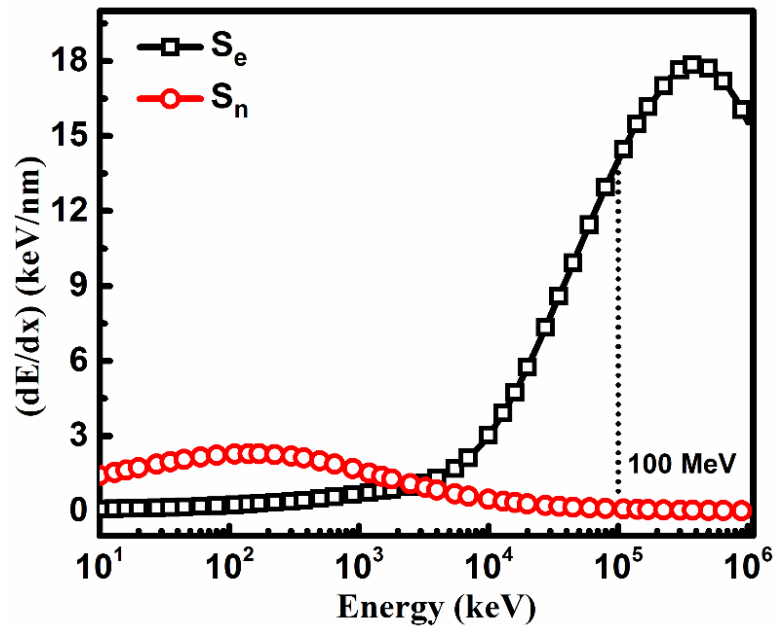


Figure 6.2 The nuclear and electronic energy losses of 100 MeV  $\text{Ag}^{7+}$  ions as the function of incident ion energy.

#### 6.2.2.2. X-ray diffraction analysis

The structural modifications of pristine and irradiated Ag-ZnO thin films at different fluences have been analyzed using XRD technique and XRD patterns are shown in **Figure 6.3**. It is clear that the pristine Ag-ZnO thin film crystallizes in hexagonal wurtzite phase with lattice planes (100), (002), and (101) at 31.34°, 34.12° and 35.95° respectively. The indexing of XRD pattern was done in accordance with the JCPDS card no. 89-1397. Crystallite plane spacing ( $d$ ) for pristine and irradiated thin film have been estimated using Bragg's formula described in **Equation 3.5**. The crystalline plane spacing ( $d$ ) is calculated for the (002) plane with first order diffraction ( $n=1$ ). The value of lattice constants have been calculated by using crystal structural formula for hexagonal wurtzite structure which described in this form [214]:

$$\frac{1}{d_{hkl}^2} = \frac{4}{3} \left( \frac{h^2+hk+k^2}{a^2} \right) + \frac{l^2}{c^2} \quad (6.1)$$

Where  $h, k, l$  shows the Miller indices for the thin film,  $d$  is the interplanar spacing and  $a, c$  are the lattice constant. Lattice parameter and  $d$  spacing for the pristine and irradiated thin film are tabulated in **Table 6.1**. Stress in the pristine and irradiated thin film is also evaluated by using the relation [215];

$$\sigma = -233 \left[ \frac{c-c'}{c'} \right] \text{ [GPa]} \quad (6.2)$$

Symbols have their usual meaning in above formula,  $\sigma$  is the stress for the sample and  $c, c'$  are the lattice constant for the Ag-ZnO composite thin film and strain free lattice constant for pure ZnO respectively. Stress variation of the pristine and irradiated thin film has been shown in **Figure 6.4** (inset) and summarized in **Table 6.1**. The presence of Ag in pristine and irradiated thin films was also confirmed by the peak obtained at 38.23° with (111) plane [JCPDS card no. 87-0720]. The crystallite size was determined by using the Scherrer's formula (**Equation 3.6**).

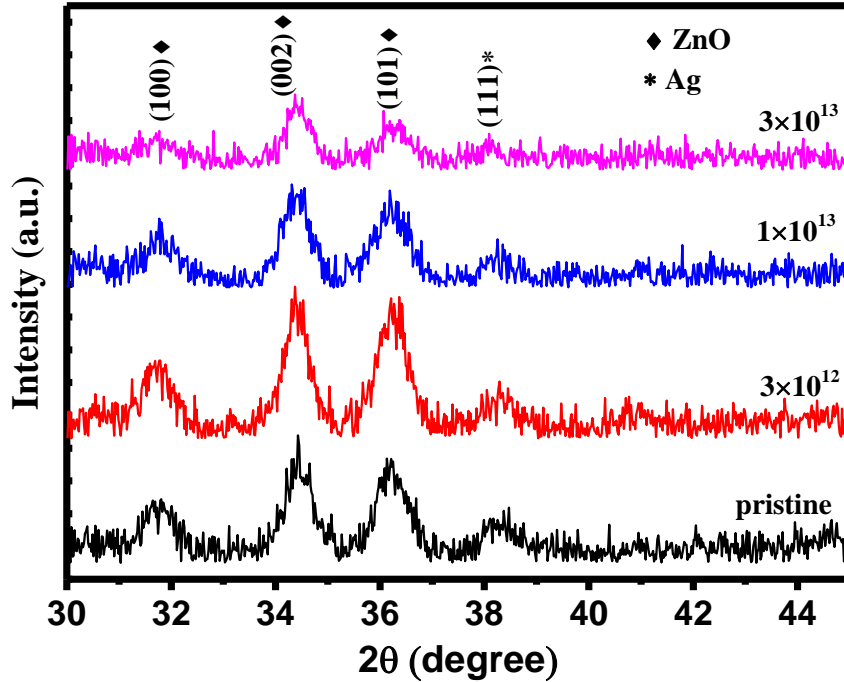


*Figure 6.3 XRD spectra of pristine and irradiated films at three different fluences.*

**Figure 6.4** shows the variation in crystallite size of the pristine and irradiated thin films with different ion fluences which was calculated from the X-ray diffraction pattern and summarized in **Table 6.1**. The changes in the crystallite size revealed that the crystalline behavior of nanocomposite film improves with ion irradiation at lower fluence, but crystallinity is decreased at higher fluence. The crystallinity of the films is effected by ion irradiation at different fluences which are related to the lattice strain between the grains of the nanocomposite thin film. The lattice strain releases between the grains at the lower fluence and it is responsible for the improvement in the crystalline behaviour of the film. But when irradiation fluence increases, more number of incident ions interact with the film attributed to the disordering inside the large grains due to overlapping of the ion tracks [216].

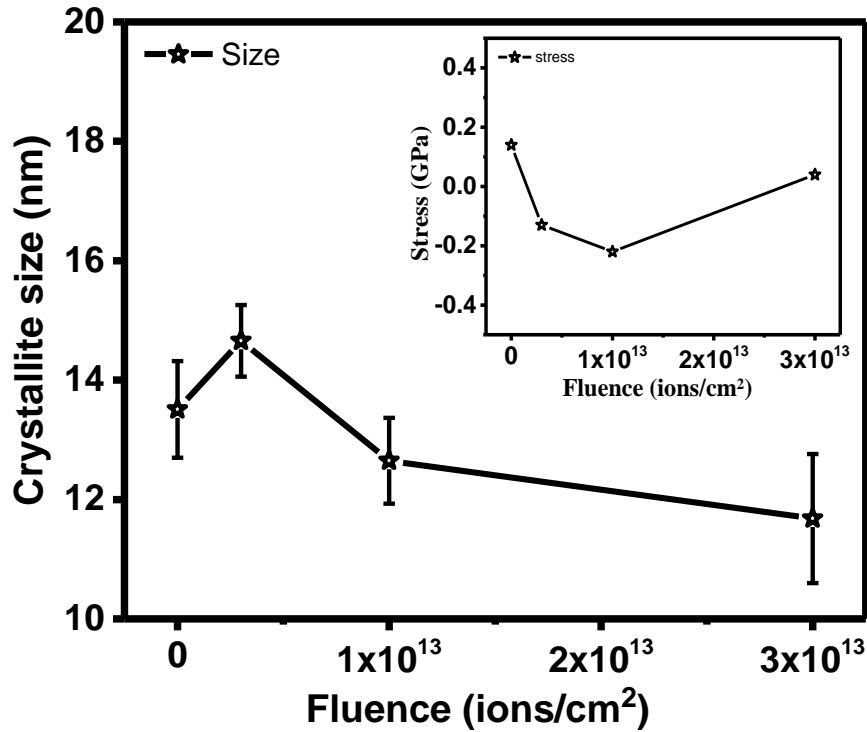


Figure 6.4 Crystallite size of pristine and 100 MeV  $\text{Ag}^{7+}$  irradiated thin film.

Table 6.1 Lattice parameters, crystallite size and stress of the pristine and irradiated thin films estimated by X-ray diffraction spectra.

Fluence (ions/cm <sup>2</sup> )	d spacing (Å) (for 002)	Lattice constant 'a' (Å)	Lattice constant 'c' (Å)	c/a ratio	Crystallite size (nm)	Stress $\sigma$ (GPa)
Pristine	2.601	3.249 ± 0.002	5.202 ± 0.002	1.601	13.51 ± 0.81	+0.14
3×10 <sup>12</sup>	2.604	3.252 ± 0.001	5.208 ± 0.001	1.602	14.66 ± 0.60	-0.13
1×10 <sup>13</sup>	2.605	3.248 ± 0.002	5.210 ± 0.002	1.604	12.65 ± 0.72	-0.22
3×10 <sup>13</sup>	2.602	3.256 ± 0.003	5.204 ± 0.003	1.598	11.68 ± 1.08	+0.04

### 6.2.2.3. UV-visible absorption spectroscopy

To study the optical modifications of pristine and 100 MeV Ag ion beam irradiated Ag-ZnO nanocomposite thin films, UV-visible absorption spectroscopy measurements were done. Figure 6.5 shows the optical absorption spectra of pristine and irradiated thin films.

For pristine Ag-ZnO thin film, a broad SPR peak was observed at  $\sim 475$  nm, when fluence is increased up to  $3 \times 10^{12}$  ions/cm<sup>2</sup>, SPR peak is shifted ( $\sim 30$  nm) towards the lower wavelength (blue shift) and found at 445 nm. The intensity of the SPR peak for the  $3 \times 10^{12}$  ions/cm<sup>2</sup> fluence is also found to be decreased in comparison to pristine film, and it is disappeared on further increasing the fluence. This shift and decreased intensity may be the result of the reduction of metal particle size with irradiation fluence [217] and also effected by the modifications in the ZnO matrix during SHI irradiation. During the high energy ion irradiation, the electronic energy loss is more dominant, so a large amount of energy transfer from an incident ion to target material which creates the high temperature zone along the incident ion path according to thermal spike model and this high temperature leads the melting of material along the ion path and responsible for the optical modifications in Ag-ZnO nanocomposite thin film by ion irradiation.

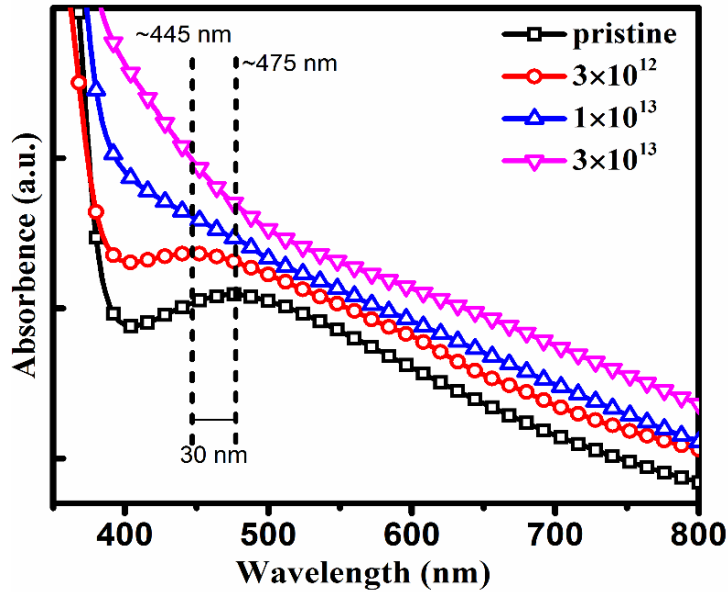


**Figure 6.5** UV- visible absorption spectra of pristine and 100 MeV  $\text{Ag}^{7+}$  irradiated films.

**Figure 6.6** shows the graph between  $(\alpha h\nu)^2$  and  $h\nu$  to measure the optical band gap. The optical band gap of Ag-ZnO nanocomposite thin films was calculated by Tau's relation described in **Equation 3.9** [134]. The optical band gap for pristine Ag-ZnO nanocomposite thin film was observed  $\sim 3.19$  eV and it is decreased up to 3.15 eV, with increasing fluence at  $3 \times 10^{13}$  ions/cm<sup>2</sup>. The variation in the optical band gap at different

fluences is summarized in **Table 6.2** under the limit of this method of calculating band gap, so this is not appreciable.

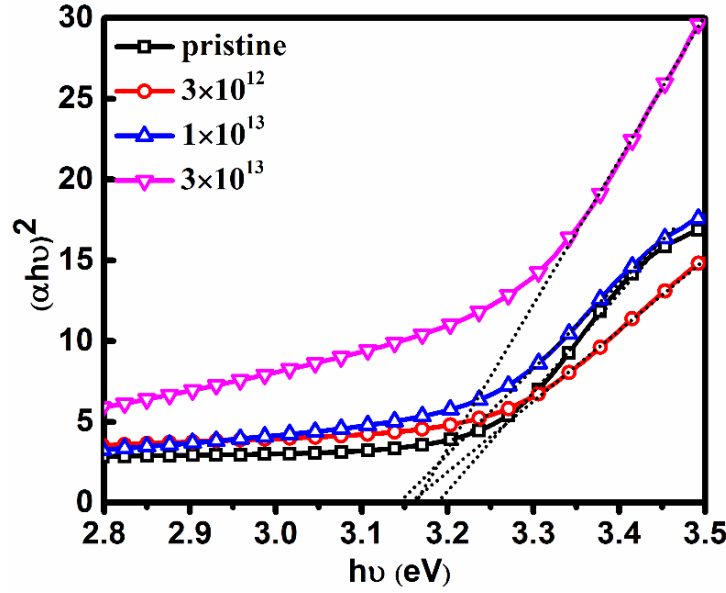


**Figure 6.6** Band gap variation of pristine and irradiated films, calculated by Tauc's relation.

**Table 6.2** Band gap, roughness and grain size of pristine and irradiated thin films.

Sl. No.	Fluence (ions/cm <sup>2</sup> )	Band gap (eV)	Roughness (nm)	Grain size (nm)
1.	Pristine	3.19 ± 0.01	11.9	52.53 ± 0.06
2.	3×10 <sup>12</sup>	3.16 ± 0.01	14.6	72.31 ± 0.08
3.	1×10 <sup>13</sup>	3.14 ± 0.01	9.6	38.19 ± 0.05
4.	3×10 <sup>13</sup>	3.15 ± 0.01	9.2	36.15 ± 0.11

#### 6.2.2.4. Atomic force microscopy

**Figure 6.7** shows the 2D AFM images of pristine and 100 MeV Ag irradiated Ag-ZnO nanocomposite thin film. The measured root-mean-square roughness ( $R_{rms}$ ) of the pristine film was ~ 11.91 nm and it increased to ~ 14.61 nm in the films irradiated with fluence of 3×10<sup>12</sup> ions/cm<sup>2</sup>. With further increase in the fluence, the roughness was decreased to ~ 9.27 nm for the fluence of 3×10<sup>13</sup> ions/cm<sup>2</sup>. The roughness variation with incident ion fluences is described in **Table 6.2**. The  $R_{rms}$  roughness of pristine and irradiated films is

calculated by the **Equation 4.1**. The increase in the surface roughness and then further decrease with increase in irradiation dose is a result of rapid annealing due to high energetic ions. The average size of the surface grains were also calculated by AFM micrographs and assuming nearly spherical grains distributed on the surface of the pristine and irradiated thin film. The calculated grain size for the pristine film is  $52.53 \pm 0.06$  nm and it increases at the fluence  $3 \times 10^{12}$  ions/cm<sup>2</sup> but further increase the fluence, the grain size is decrease and found to be  $36.15 \pm 0.11$  nm for  $3 \times 10^{13}$  ions/cm<sup>2</sup> fluence. The variation of grain size with irradiation fluence are summarized in **Table 6.2**. In the case of high energy SHI irradiation, the density of electronic excitation induced through the target material and it is responsible for the change in surface morphology of film at different ion fluences. Diffusion and fragmentation process between the target atoms with in irradiation zones during SHI Irradiation are responsible for the grain size distribution. Variation in grain size with irradiation calculated by AFM images is supported to XRD data.

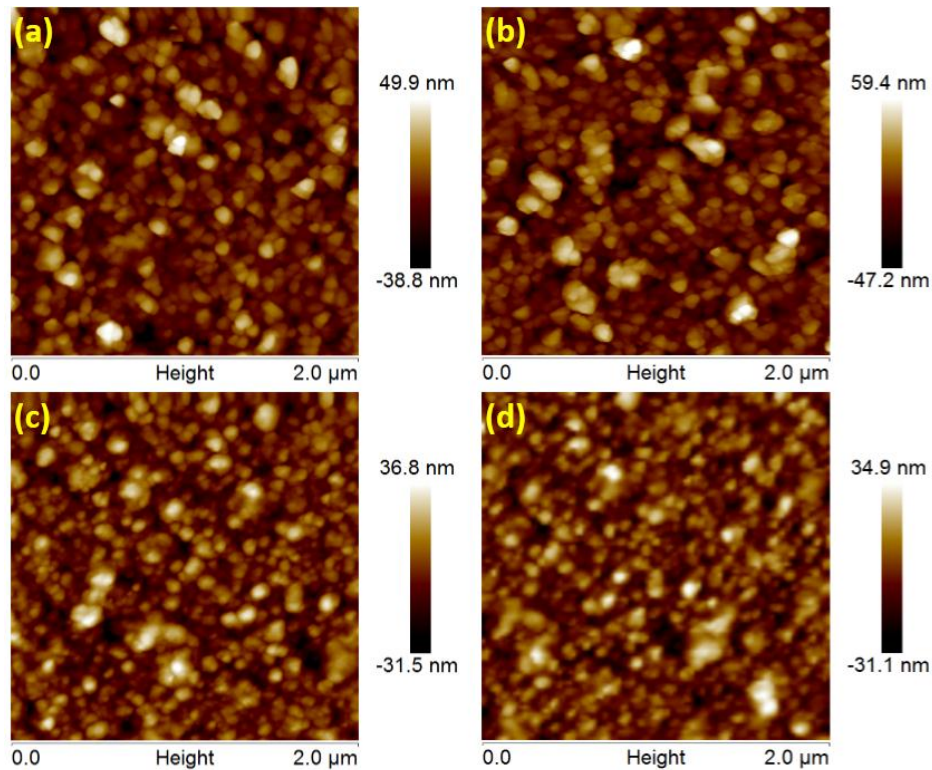


**Figure 6.7** AFM micrographs (2D) of pristine and irradiated Ag-ZnO nanocomposite thin films.

### 6.2.2.5. Micro-Raman spectroscopy

The hexagonal wurtzite ZnO structure associated to  $C_{6v}^4$  space group with two formula units per primitive cell and it have  $A_1+2E_2+E_1$  Raman active phonon modes according to the group theory, where all atoms occupy  $C_{3v}$  sites. The Raman spectra of pristine and 100 MeV Ag ion beam irradiated Ag-ZnO nanocomposite thin films at three different fluences  $3 \times 10^{12}$ ,  $1 \times 10^{13}$ , and  $3 \times 10^{13}$  ions/cm<sup>2</sup> are shown in **Figure 6.8**. The spectra depict that no sharp band exists in the pristine film, but when films were irradiated at lower fluence, the intensity of E<sub>2</sub> high mode starts increasing in comparison to pristine film. This increased intensity describes the improvement in the crystallinity at lower fluences. With further increased fluences, the E<sub>2</sub> band is completely disappeared, and the intensity of A<sub>1</sub> (LO) mode is increased very sharply. This improvement in the A<sub>1</sub> (LO) mode intensity and disappearance of E<sub>2</sub> band at the higher fluence in the nanocomposite thin film are attributed to the density of defects such the creation of oxygen vacancies due to SHI irradiation [218].

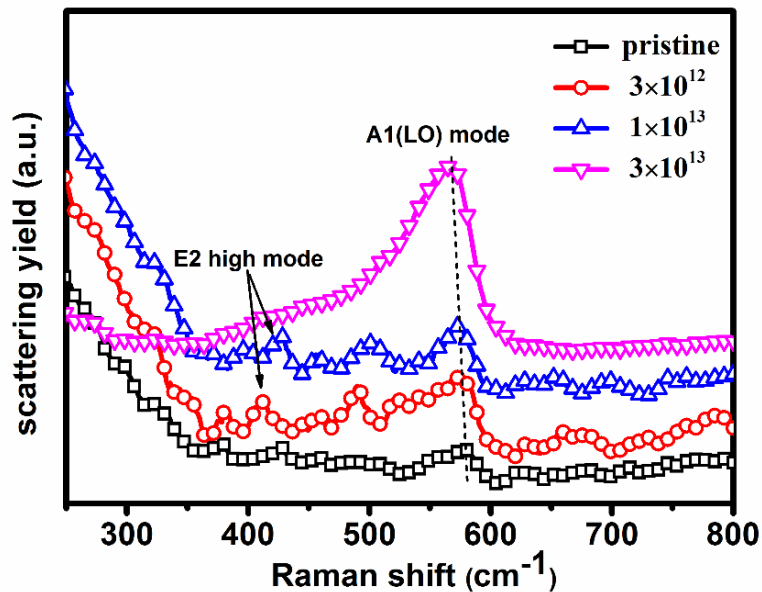


*Figure 6.8 Raman spectra of pristine and irradiated films at different fluences.*

### 6.2.2.6. Photo-luminescence measurement

**Figure 6.9** shows the PL spectra for pristine and 100 MeV Ag<sup>7+</sup> ion irradiated Ag-ZnO nanocomposite thin films at room temperature with an excitation wavelength of 325 nm



He-Cd laser. The spectra of pristine and irradiated thin films mainly consist of four emission bands at 377, 420, 445 and 467 nm respectively. A sharp peak observed at 377 nm is attributed to near band emission (NBE) and band to band transition. This may be due to deep-level defects such as zinc interstitials or oxygen vacancies in Ag-ZnO NCs thin film [52]. The peak at 445 nm is assigned to the transition of electrons from Zn interstitial to acceptor energy level of Zn valency and another peak at 467 nm is ascribed to the oxygen vacancies in the ZnO thin film [219,220]. The interface of the grain boundaries of Ag and ZnO grains prevent the radiative defects at the grain boundaries as confirmed by blue emission at 420 nm [221]. The defects formation during ion irradiation could be understood on the basis of interaction between incident ion and target material.

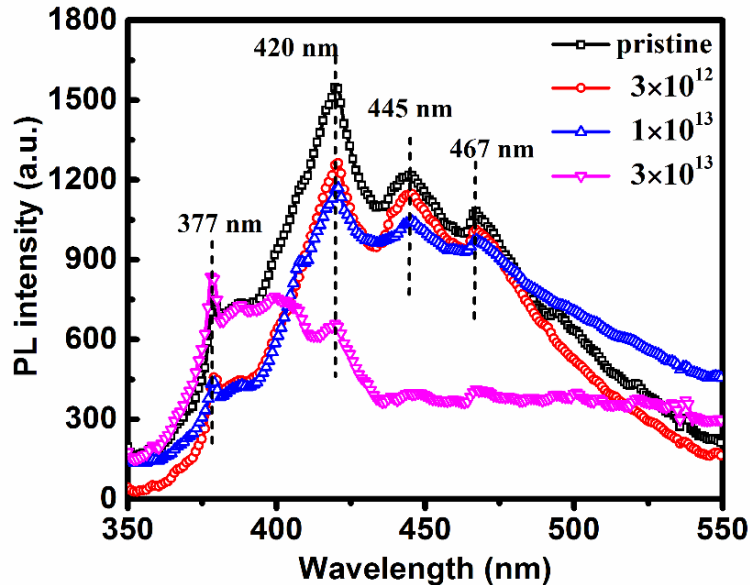


*Figure 6.9 PL spectra of pristine and irradiated films at different fluences.*

#### 6.2.2.7. X-ray photo-electron spectroscopy

To determine the different component and oxidation states of Ag-ZnO nanocomposite thin film, XPS studies of the pristine film were carried out. The spectra is given in the **Figure 6.10** where **Figure 6.10 (a)** shows the full scan spectra while **Figure 6.10 (b-d)** show the core shell spectra corresponding to the Zn 2p, O 1s and Ag 3d state of the elements. The position of peaks were matched with the standard database and it indicated the presence of Zn, O and Ag elements in the specimen. The short scan of Zn 2p region

exhibited  $Zn^{2+}$  state with binding energy  $\sim 1023.26$  eV and  $\sim 1046.37$  eV for  $2p_{3/2}$  and  $2p_{1/2}$  states respectively. The short scan for O 1s exhibited asymmetric behaviour which was contribution of two types of oxygen groups. The first peak which located at lower binding energy ( $\sim 531.23$  eV) was attributed to Zn-O bonding and other peak ( $\sim 532.87$  eV) was related to hydroxyl group which is resulted due to surface defects. Presence of this group are advantageous in photocatalytic behaviour and play a significant role for preventing the electron-hole recombination process [222]. **Figure 6.10 (d)** indicates the splitting of Ag ( $3d_{5/2}$ ) and Ag ( $3d_{3/2}$ ) were clearly seen at  $\sim 374.67$  eV and  $\sim 368.61$  eV, respectively. The spectrum was further deconvoluted to estimate a smaller contribution from  $Ag_2O$  and Ag-Zn-O components in addition to the metallic Ag. The concentration of the Ag in ZnO matrix also calculated form the spectra and found to be  $\sim 8\%$  which was in good agreement with the RBS results.

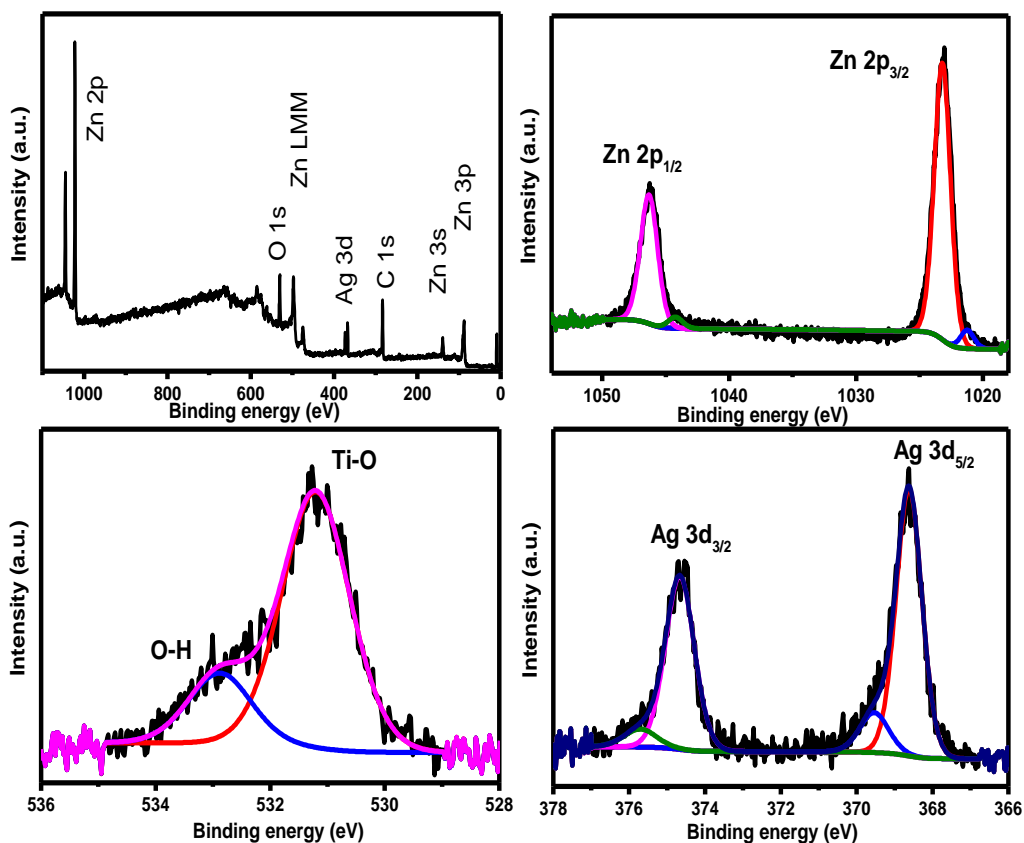


**Figure 6.10** XPS spectra of Ag-ZnO nanocomposite thin film (Survey as well as core spectra of Zn, O and Ag).

## **6.3. Thermal annealing studies of nano-composites thin films**

### **6.3.1. Experimental details**

#### *Deposition parameters*

A target of pure ZnO (2" dia.) was prepared from the ZnO powder (Merck) with the help of hydraulic press machine (HYCON, New Delhi). The prepared ZnO target was sintered in the tubular furnace at the temperature of 1200 °C for 24 hours with continuous flow of oxygen gas during sintering process. For synthesizing the Ag-ZnO NCs film, one small piece (1 mm thick) of pure Ag (Sigma Aldrich) was glued on the prepared ZnO target before the film deposition. The silicon substrates were used for film deposition and clean with RCA method before the film deposition. The pressure in the sputtering chamber was recorded  $5 \times 10^{-6}$  mbar before inserting the argon gas in the chamber. The vacuum of the chamber was decreased after introducing the gas and observed  $1.5 \times 10^{-2}$  mbar during the film deposition. The rough vacuum was created by rotary pump and it coupled with turbo-molecular pump for getting the very high vacuum. The deposition was performed for 40 minutes at the RF power ~ 60 watts at the room temperature. The thickness of the film was measured by the quartz crystal monitor and found to be ~ 80 nm at the deposition rate of 0.2 Å/second.

#### *Annealing parameters*

After the deposition, the prepared Ag-ZnO NCs films were annealed at three different temperatures of 300 °C, 400 °C and 500 °C. A rotary pump was attached with tubular furnace for achieving the vacuum. So the annealing was performed in the vacuum and the observed value of the vacuum was found to be  $\sim 1.24 \times 10^{-2}$  mbar during annealing.

### **6.3.2. Results and discussion**

#### **6.3.2.1. X-ray diffraction analysis**

The structural behavior and crystalline quality of as-deposited and annealed Ag-ZnO NCs thin films were investigated by XRD spectroscopy. **Figure 6.11** shows the X-ray patterns of as-deposited and films annealed at 300 °C, 400 °C and 500 °C temperatures. Most intense Bragg peak was identified at the diffraction angle of  $34.19^\circ$  for as-deposited as well as annealed films that corresponds to the (002) planes of the hexagonal wurtzite

structure. There is no evidence of Ag-O and Ag<sub>2</sub>O related phases in the pattern. Importantly, the intensity of the (002) peak increases with increasing the annealing temperature. Consequently, the FWHM of the films is decreasing with increasing the annealing temperature. This signifies that the crystalline quality of the films are significantly improved after the thermal annealing and is responsible for the growth along the c-axis (002 plane). Moreover, the (002) orientation of the hexagonal wurtzite structure have small surface energy which results in a higher growth rate, according to the basic crystal growth theory [223,224]. The presence of single Bragg peak in the pattern revealed the higher crystallinity of the films. The crystallite size (*D*) of as-deposited and annealed films was calculated according to Scherrer's formula [225] as shown in **Equation 3.6**.

The crystallite size was calculated and found to be 13.6 nm for as-deposited film and increases up to 28.5 nm for annealed film at the annealing temperature 500 °C. The increment in the crystallite size is the direct evidence of the improved crystalline quality of the film after the annealing treatment. The various microstructural parameters such as lattice parameter, dislocation density, stress and lattice strain have been calculated from the XRD pattern. The lattice parameters for the as-deposited and annealed film were calculated by using crystal structure formula for hexagonal wurtzite structure of ZnO which is explained using **Equation 3.5 and Equation 6.1**.

**Table 6.3** summarizes the lattice parameters of as-deposited and annealed films. In addition, the crystalline nature of the films is affected by dislocation density which depend on the thermal annealing. To account this, we have estimated the dislocation density [226] for the as-deposited and annealed films by given relation:

$$\text{Dislocation density } (\delta) = \frac{1}{D^2} \quad (6.3)$$

A high dislocation density of  $5.4 \times 10^{15}$  line/m<sup>2</sup> was observed for as-deposited film from the above relation (**Equation 6.3**). On the other hand, a low dislocation density of  $1.2 \times 10^{15}$  line/m<sup>2</sup> was found for films after annealing at higher temperature. The value of dislocation density has been decreased significantly as compared to as-deposited films which attributed to lower defects and higher crystalline quality of the films. The value of

lattice strain and stress have been also calculated for as-deposited and annealed film by **Equation 6.2** and **Equation 3.7**.

The negative sign in the stress indicates the compressive nature for as-deposited and annealed films because the (002) peak shifted towards larger angle side. The value of stress has been observed to decrease with increasing the annealing temperature and thus lead to stress relaxations between grains and overcome the difference of thermal expansion coefficient between the film and substrates. The strain could be released during the annealing which supports the higher crystallization of the films as confirmed by lattice strain calculations. All discussed micro-structural parameters have been calculated for as-deposited and annealed films and summarized in **Table 6.3**.

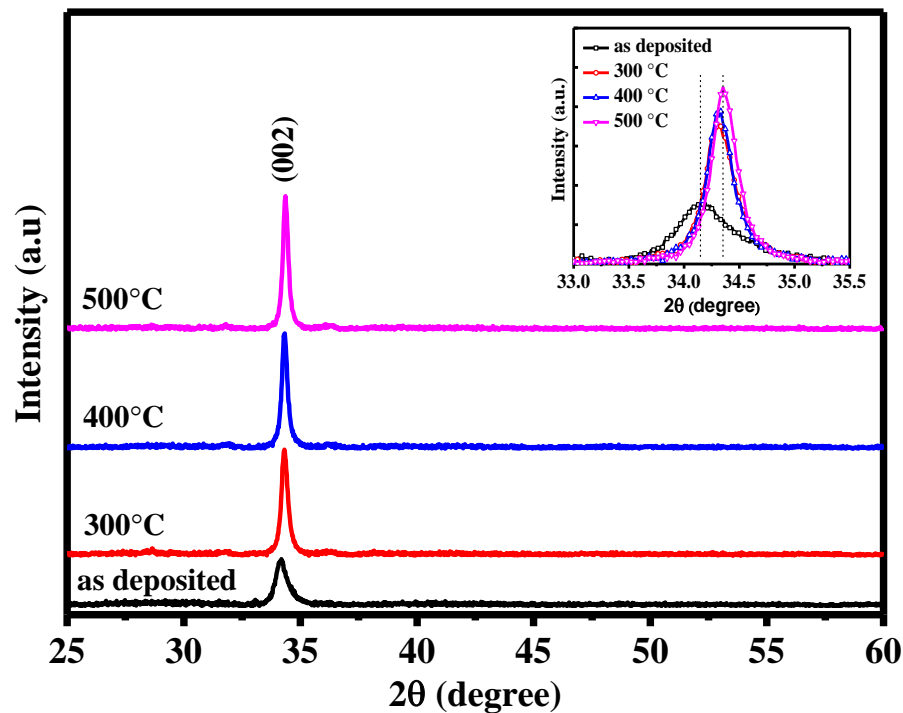


*Figure 6.11 X-ray spectra of as-deposited and annealed Ag-ZnO NCs thin film at three different temperatures of 300 °C, 400 °C and 500 °C.*

**Table 6.3** Structural parameters of as-deposited and annealed Ag-ZnO NCs thin films.

Sample detail	$2\theta$ (degree)	Lattice parameter		$d$ -spacing (Å)	Crystallite size (nm)	Dislocation density	Lattice strain %	Stress (GPa)
		a (Å)	c (Å)					
As dep.	34.19	3.0253	5.2398	2.6199	13.6	5.4	0.86	- 1.79
300 °C	34.32	3.0131	5.2186	2.6093	24.9	1.6	0.47	- 0.84
400 °C	34.33	3.0120	5.2168	2.6084	27.7	1.3	0.43	- 0.75
500 °C	34.36	3.0099	5.2132	2.6066	28.5	1.2	0.41	- 0.59

### 6.3.2.2. UV-visible spectroscopy

The optical modifications in as-deposited and annealed Ag-ZnO NCs thin film have been carried out by UV-visible spectroscopy in reflectance mode. The variation in reflectance has been observed with thermal annealing at different temperatures of 300 °C, 400 °C and 500 °C.

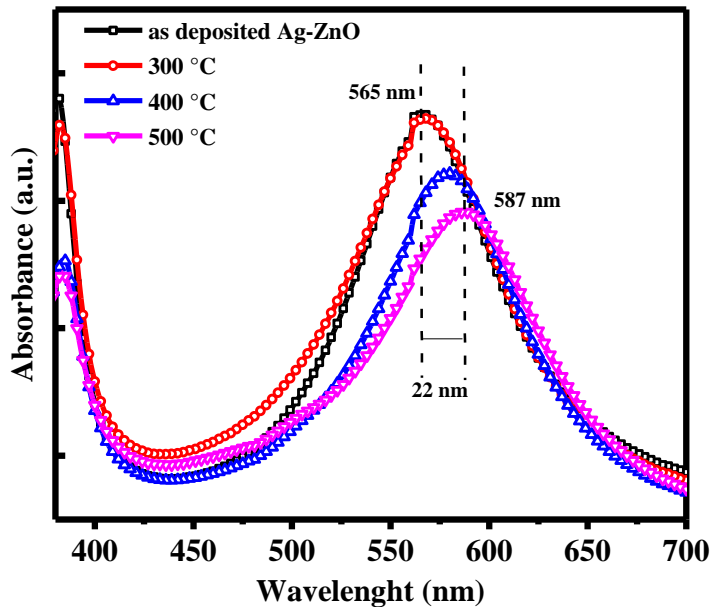


**Figure 6.12** UV-visible spectroscopy of the as-deposited and annealed Ag-ZnO thin films.

A very large deep region was found in reflection spectra which could be related to the absorbance of the nanoparticles in the wavelength range between 450 nm and 650 nm.

Therefore, the absorbance of as-deposited and annealed film have been calculated from the reflectance data and is shown in **Figure 6.12**.

A well-defined strong absorption resonance (SPR) band has been observed both in as-deposited as well as in the annealed films. The position of SPR band was found at ~ 565 nm for as-deposited film and 565 nm, 576 nm and 587 nm for the films annealed at 300 °C, 400 °C and 500 °C respectively. The prominent red shift of ~ 22 nm has been observed in the SPR band with the thermal annealing as applied in this study. The observed red shift in SPR could be linked with the growth of the nanoparticles during the thermal annealing. As the annealing temperature increases, the crystalline quality of ZnO films have improved significantly and explains the SPR shifting in the films after annealing. The SPR frequency of the nanoparticles depends on many factors such as size and shape of nanoparticles, spatial distribution and nature of the surrounding medium. The local refractive index of the medium is very sensitive for the shifting in SPR frequency of the nanoparticles. Furthermore, to study the effect of refractive index on the SPR shifting, the refractive index and other optical parameters have been calculated by the following relations [227]:

$$n = \frac{1 + \sqrt{R}}{1 - \sqrt{R}} \quad (6.4)$$

$$n = \sqrt{\frac{4R}{(1-R)^2} - k^2} + \left(\frac{1+R}{1-R}\right), \quad \text{where,} \quad k = \frac{\alpha\lambda}{4\pi} \quad (6.5)$$

In above **relations (6.4 and 6.5)**, n is the refractive index, R is the reflectance, k is the extinction coefficient and  $\alpha$  is the absorption coefficient of the film. The value of refractive index has been increases from 2.16 to 2.42 with increasing the annealing temperature. The extinction coefficient was calculated for as-deposited and annealed films and is tabulated in **Table 6.4**. The dielectric constant and absorbance of the films were calculated using given relations [228]:

$$\varepsilon_r = n^2 - k^2(\text{real part}) + nk^*(\text{imaginary part}) \quad (6.6)$$

$$\alpha = \frac{2.303}{d} A \quad (6.7)$$

The real and imaginary part of the dielectric constant has been calculated for as-deposited and annealed films for the wavelength same at SPR band from **Equation (6.6)**. The dielectric constant of the film increases with annealing temperature. The optical band gap of the as-deposited and annealed film Ag-ZnO films has been calculated by Tauc's relation **Equation 3.9**.

Generally, the band gap of pure ZnO thin film is reported  $\sim 3.30$  eV, while in the present study, the band was found to be  $\sim 3.17$  eV due to Ag incorporation in the host ZnO matrix (shown in **Figure 6.13**).

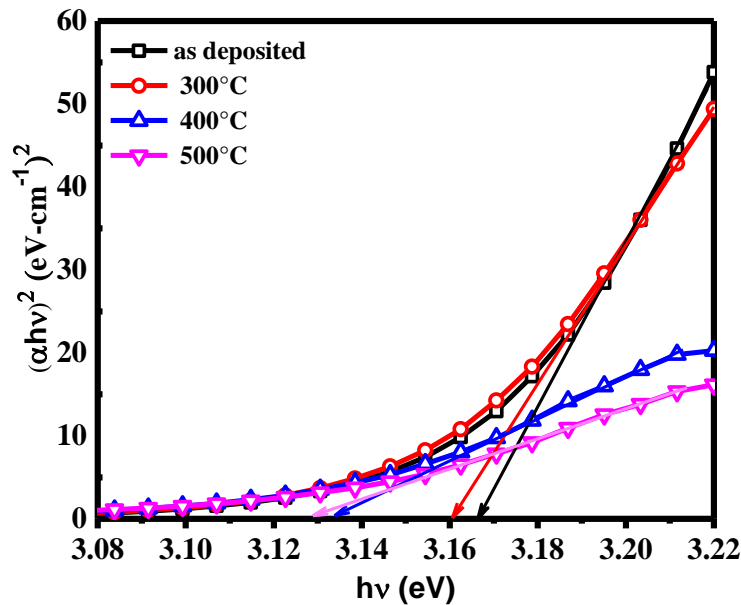


**Figure 6.13** Band gap variation of the as-deposited and annealed Ag-ZnO thin films at different temperatures.

The value of band gap decreases up to  $\sim 3.12$  eV at higher annealing temperature and might be attributed to an increase in the metal/oxygen ratio with lower defects density after the thermal annealing process. Such results are also supported by XRD analysis. At the same time, FWHM of the bands decreases with increasing annealing temperature and yields a remarkable red shift ( $\sim 22$  nm) in the SPR band. The perfect Gaussian shape of the band revealed the homogeneity, particularly the shape of nanoparticles in the ZnO matrix which will further supported by TEM particles size



analysis in the upcoming section. Thus, the size/shape of the nanoparticles and local refractive index of surrounding material might play key role in the SPR tuning. Since, the thermal annealing as shown in this study could be very effective to control over the optical properties of the surrounding matrix with a fairly control on the size and shape of the nanoparticles. This tunable nature in the optical properties of these Ag-ZnO NCs thin film make them very promising for various plasmonic applications. All calculated optical parameters are be summarized in **Table 6.4**.

*Table 6.4 Optical parameter with different annealing temperatures.*

<i>Sample detail</i>	<i>SPR band position (<math>\lambda</math>)</i>	<i>Band gap (<math>E_g</math>)</i>	<i>Refractive index (<math>n</math>)</i>	<i>Extinction coefficient (<math>k</math>)</i>	<i>Dielectric constant (<math>\epsilon_r</math>)</i>
As-deposited	565 nm	3.17 eV	2.16	0.127	4.78
300 °C	565 nm	3.16 eV	2.17	0.124	4.96
400 °C	576 nm	3.13 eV	2.31	0.085	5.52
500 °C	588 nm	3.12 eV	2.42	0.081	6.05

### **6.3.2.3. Atomic force microscopy**

The surface features of as-deposited and annealed films have been observed by the atomic force microscopy (AFM). The characterization was performed in tapping mode. 2-D figures ( $1 \times 1 \mu\text{m}^2$ ) of as-deposited and annealed Ag-ZnO NCs films are shown in **Figure 6.14**. The homogeneous distribution of the grain on the film surface observed in the images. The grains are perfectly connected that form the triangular shape. The grain growth has been observed after the thermal annealing. The grain size was calculated by AFM micrographs and found to be 60.38 nm for the as-deposited film. After the annealing treatment at 500 °C, the grain size was increased up to 79.42 nm. The agglomeration between the grains took place during the annealing process and is responsible for the grain growth. The grains achieve thermal energy during the annealing and participate in the agglomeration process.

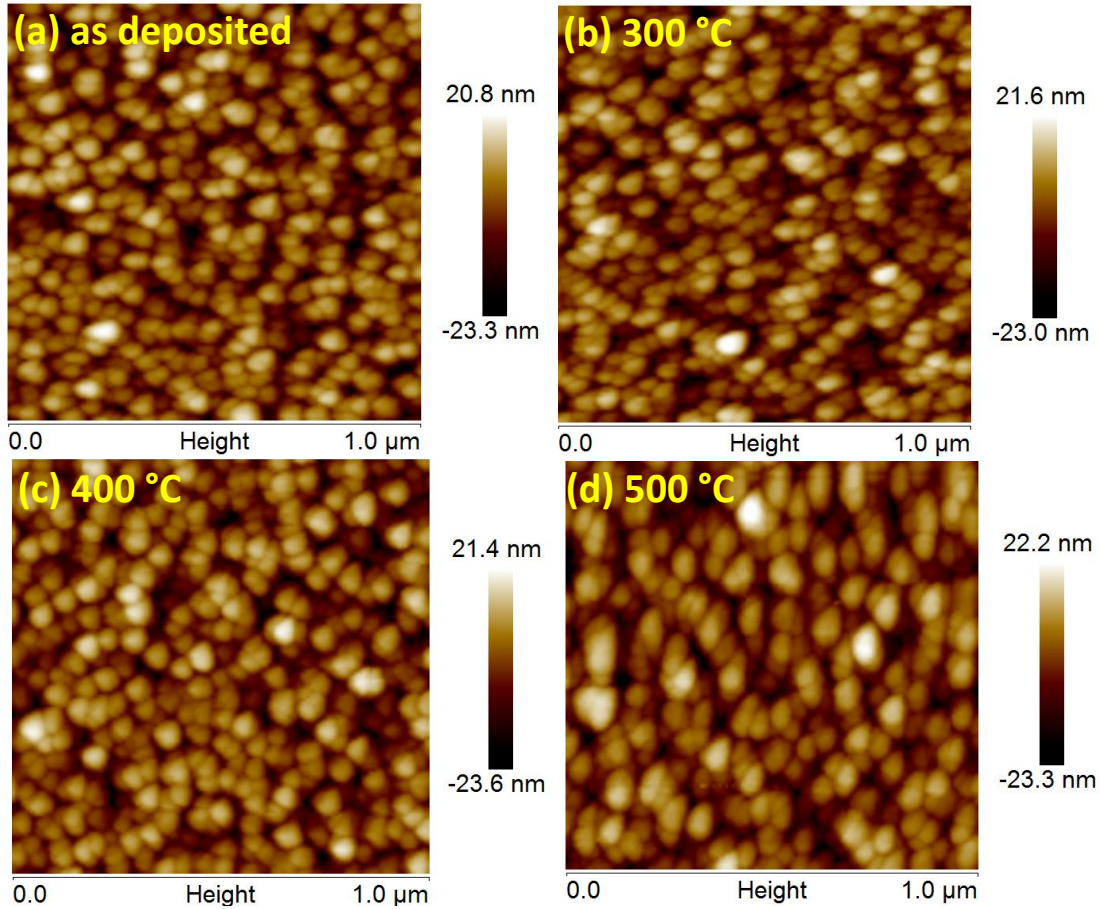


**Figure 6.14** 2D ( $1 \times 1 \mu\text{m}^2$ ) AFM micrographs of (a) as-deposited and annealed (b) 300 °C (c) 400 °C (d) 500 °C Ag-ZnO NCs thin films.

Both X-ray analysis and AFM results support the grain growth after the thermal annealing. The root-mean-square roughness ( $R_{\text{rms}}$ ) of the as-deposited and annealed films were calculated by **Equation 4.1**. Interestingly, no significant changes were observed in the surface roughness of the as-deposited and annealed Ag-ZnO NCs thin film.

**Table 6.5** Variation in roughness and grain size with annealing for the Ag-ZnO NCs thin films.

<i>Sl. No.</i>	<i>Sample detail</i>	<i>Roughness (<math>R_q</math>)</i>	<i>Grain size</i>
1.	as-deposited	6.44 nm	60.38 nm
2.	300 °C	6.57 nm	64.41 nm
3.	400 °C	6.58 nm	69.23 nm
4.	500 °C	6.69 nm	79.42 nm

### 6.3.2.4. Micro-Raman spectroscopy

The Raman active phonon modes for ZnO wurtzite structure have been observed by the Raman spectroscopy. According to group theory, there are  $A_1+2E_2+E_1$  modes which are related to wurtzite ZnO, where all atoms occupy  $C_{3v}$  sites [229,230]. **Figure 6.15** shows the micro-Raman spectra of the as-deposited and annealed Ag-ZnO NCs thin films with different annealing temperatures of 300 °C, 400 °C and 500 °C.

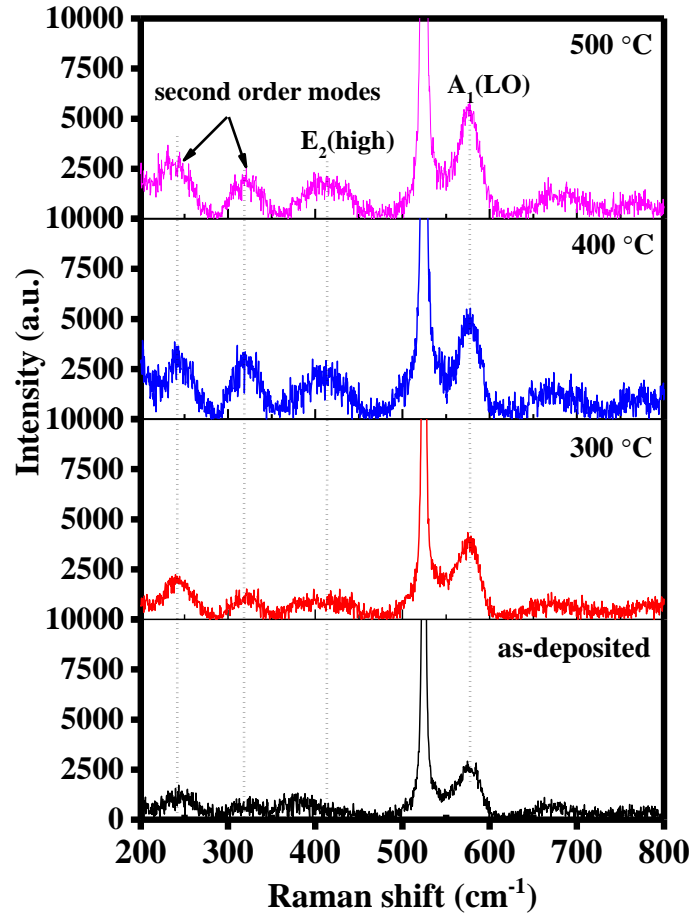


Figure 6.15: Raman spectra of as-deposited and annealed Ag-ZnO NCs thin films.

The different Raman peaks are observed in the spectra which are related to particular bands of ZnO. Raman spectra of as-deposited and annealed Ag-ZnO films show the different peaks at 239  $\text{cm}^{-1}$ , 320  $\text{cm}^{-1}$ , 414  $\text{cm}^{-1}$  and 577  $\text{cm}^{-1}$ . Silicon substrate peak was detected at 523  $\text{cm}^{-1}$  with higher intensity in as-deposited and annealed films. The first two peak are related to the second order modes of ZnO. The  $E_2$  (high mode) has been observed only in annealed Ag-ZnO films at 414  $\text{cm}^{-1}$  and another sharp peak at 577  $\text{cm}^{-1}$ . These peaks could be assigned to  $A_1$  (LO) mode of ZnO.

The intensity of bands was found to be increased with thermal annealing as confirmed by Raman spectra. The lattice defects and crystalline quality of the film can be affected by the thermal annealing which support the conclusion drawn from the XRD results. The intensity of E<sub>2</sub> (high) and A<sub>1</sub> (LO) modes of ZnO increased with thermal annealing. We expect that this increment might be due to reduction in oxygen vacancies and strain relaxation between the grains which directly corroborates the results obtained by XRD.

### 6.3.2.5. Transmission electron microscopy

**Figure 6.16** shows the TEM micrographs of as-deposited Ag-ZnO NCs thin film. **Figure 6.16 (a)** shows the top view of the film with continuous distribution of the film over the substrate. This shows that the as-deposited film is homogeneous in the nature. The presence of Ag in the form of nanoparticles are clearly seen in the TEM image and marked in the **Figure 6.16 (b)**.

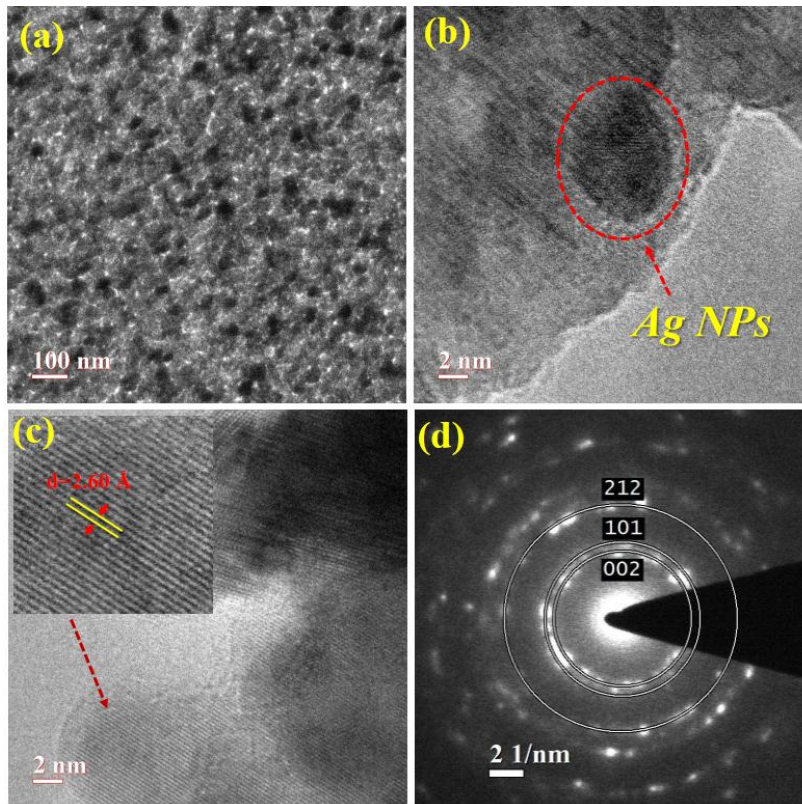


**Figure 6.16** TEM micrographs of as-deposited Ag-ZnO NCs thin film (a) surface image (b) Ag nanoparticle (c) HRTEM image with d-spacing (d) SAED pattern.

The size of Ag nanoparticles were measured from the TEM image and found that the average particle size is about  $\langle D \rangle = 8.2 \pm 0.2$  nm. The cross fringes are observed in the HRTEM image which confirms the formation of NCs with presence of Ag. The d-spacing was measured to be 2.60 Å which corresponding to (002) reflection of the wurtzite structure of ZnO (shown inset) as can be seen in **Figure 6.16 (c)**. The selected area electron diffraction pattern (SAED) of the as-deposited film is shown in **Figure 6.16 (d)**. The presence of clear rings in the SAED pattern has been observed and marked with corresponding planes in the **Figure 6.16 (d)** which is the direct confirmation about the crystallinity of the film. The presence of Ag nanoparticles has been directly confirmed by the TEM analysis which is in agreement with the XPS results which will be describing in next section.

#### **6.3.2.6. X-ray photoelectron spectroscopy**

The formation of compound and presence of elements have been successfully estimated by X-ray photoelectron spectroscopy (XPS). The survey scan with high resolution spectra of each existing elements are displayed in **Figure 6.17**. The high resolution spectra of Zn 2p region showed two peaks one at energy scale of  $\sim 1021.82$  eV and other one at  $\sim 1044.92$  eV. These peaks are related to  $2p_{3/2}$  and  $2p_{1/2}$  states of Zn 2p respectively. The presence of oxygen group is also confirmed by the two different peaks appeared in the core spectra at the binding energies of  $\sim 530.02$  eV and  $\sim 531.60$  eV. The first peak could be assigned to the first oxygen group which is associated with Zn-O bonding and the second group is due to the presence of hydroxyl group which might arise because of defects and impurities present in the as-deposited film. The presence of Ag has been clearly observed in high resolution spectra of Ag. The Ag 3d doublet scan be clearly visible in **Figure 6.17 (d)**, centered at binding energies of  $\sim 373.63$  eV and  $\sim 367.62$  eV for  $3d_{5/2}$  and  $3d_{3/2}$  respectively. Furthermore, the de-convolution of the core spectra of Ag was studied to observe the nature of interaction between Ag and ZnO. It is found that the lesser contribution comes from  $Ag_2O$  and Ag-Zn-O components therefore the formation of the nanoparticles is expected which us already shown in TEM analysis. The binding energy of the Ag  $3d_{5/2}$  peak has been shifted towards the lower energy which is attributed

to the interaction between Ag and ZnO nanostructures. Therefore, with these evidences XPS analysis has confirmed the composition and nature of interaction of the various species in the film. Note that the film contains a number of elements i.e. Zn, O and Ag as confirmed by these measurements.

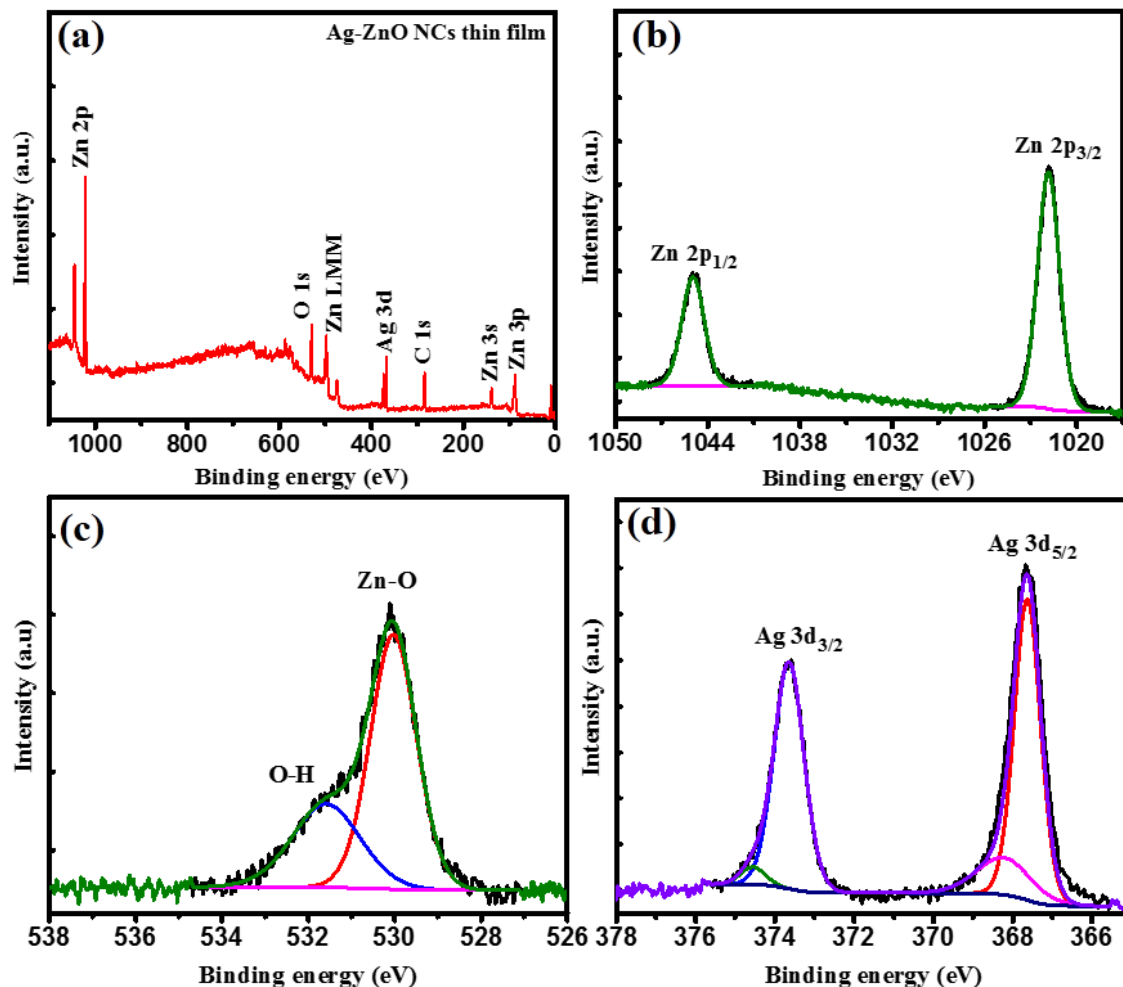


*Figure 6.17 XPS spectra of the as-deposited Ag-ZnO NCs thin film (a) survey scan (b) high resolution spectra of Zn (c) O and (d) Ag.*

## 6.4. Summary

In this chapter, SHI and thermal induced modifications in Ag-ZnO thin films have been studied in detailed. 100 MeV Ag ion beam has been taken to irradiate the Ag-ZnO

nanocomposite thin films with three different ion fluences  $3 \times 10^{12}$ ,  $1 \times 10^{13}$  and  $3 \times 10^{13}$  ions/cm<sup>2</sup>. High energy ion induced structural and optical modifications are studied by different techniques. The surface plasmon band corresponding to Ag nanoparticles has been observed at the 475 nm for the pristine film. Ion-induced SPR tuning has been observed with ion irradiation. The blue shift (30 nm) in SPR position with marginal decrement in the band gap have been confirmed by UV-visible absorption spectroscopy. The crystallinity of the film has been found to be decrease with ion irradiation confirmed by XRD. Raman spectroscopy was used to study the density of lattice defects which is found in increasing order with increasing fluence with support of Photo-luminance spectroscopy. Thermal induced modifications also observed for the Ag-ZnO nanocomposite thin films. Thin films have been annealed in vacuum environment at three different temperature of 300 C, 400 C and 500 C. The formation of the composite was confirmed by XPS and TEM analysis with significant evidence with the presence of Ag nanoparticles. The size of Ag nanoparticle has been calculated and found to be 8.2 nm. A very intense SPR band of Ag nanoparticles has been recorded at 565 nm for as deposited film, and it increase towards the higher wavelength (red shift). Thermal induced SPR tuning has been observed with annealing treatment which also support to growth off the nanoparticles in ZnO matrix. Crystalline behaviour of the films drastically increase with thermal annealing confirmed by XRD and also support to Raman measurements. This tunable properties of Ag-ZnO nanocomposite thin films could be very effective for the different plasmonic application.





# Chapter 7

## Conclusion and Future Prospects

---

This chapter summarizes the conclusion of the proposed thesis work followed by the scope for future investigations.

## 7.1. Conclusions

In the present thesis, we synthesized pure and Ag-ZnO nanocomposite thin films by RF-sputtering technique. Furthermore, thermal and SHI induced modifications in structural, morphological and optical properties have been investigated systematically. 100 MeV Ag ion beam is used for the irradiation study and 120 keV Ag ion beam was also used for the formation of Ag-ZnO nanocomposite (ion implantation). The following conclusions are drawn from the study.

- Pure ZnO thin films have been synthesized in crystalline form and the crystalline behaviour of the films were improved with SHI irradiation at higher irradiation fluence  $3 \times 10^{13}$  ions/cm<sup>2</sup>. The enhancement in the crystallinity along the c-axis orientation is due to the impact of energetic ions.
- It is observed that optical properties can be tailored by ion irradiation as transmittance decreases with increasing irradiation fluence. This property can be used in transparent window materials.
- The dependence of surface morphology and grain size on incident ions are confirmed by AFM and FESEM analysis and observed the increased grain size after irradiation. All the induced modifications are explained in terms of energy loss of incident ions into the target materials.
- Also, the optical properties were improved by thermal annealing. The thin films were annealed at two different temperatures 400 °C and 500 °C. Transmittance in the visible region and quality of films were enhanced with increasing temperature, as confirmed by UV-visible and Raman spectroscopy.
- Ag-ZnO nanocomposite (NCs) thin films were deposited using RF magnetron co-sputtering method with three different compositions and the concentration of Ag (8 at.%, 15 at.%, and 40 at.%) in ZnO was calculated by RBS. The composite nature of the thin films was also confirmed by RBS and showed the existence of Ag, Zn, and O.
- Ag-ZnO nanocomposite thin films have been characterized by various characterization techniques in order to understand the structural and electrical

behaviour of the films. Raman measurements were performed for the estimation of lattice defects and disordering induced by Ag incorporation.

- Electrical measurements revealed that the conductivity of nanocomposite thin films enhances drastically as compared to pure ZnO film and it increases with increasing Ag concentration. Furthermore, nanocomposite thin films showed a p-type conductivity due to the incorporation of Ag metal.
- Ag-ZnO nanocomposite thin films were synthesized by ion implantation of ZnO thin films using 120 keV Ag ion beam with different implantation dose from  $3 \times 10^{14}$  to  $3 \times 10^{16}$  ions/cm<sup>2</sup>. Implantation of Ag ions affects the surface stoichiometry as observed by XPS and RBS.
- X-ray diffraction spectra reveals the presence of stable hexagonal wurtzite structure with good crystalline nature along c-axis. However, the crystallinity decreases with implantation dose. At the higher dose, the film was entirely c-axis oriented which can be beneficial for device fabrication. A drastic decrement in the transmittance in visible region at higher implantation dose was also observed which could be attributed to the charge carrier density affected by Ag implantation.
- The effect of SHI irradiation on structural and optical properties of RF sputtered Ag-ZnO nanocomposite thin films have also been studied. Nanocomposite thin films were irradiated with 100 MeV Ag<sup>7+</sup> ions at three different fluences  $3 \times 10^{12}$ ,  $1 \times 10^{13}$  and  $3 \times 10^{13}$  ions/cm<sup>2</sup>. The variation in crystallite size of the film with ion irradiation was clearly observed.
- SPR of Ag nanoparticles has appeared at ~ 475 nm in the pristine thin film, which is blue shifted by ~30 nm in film irradiated at fluence of  $3 \times 10^{12}$  ions/cm<sup>2</sup> and completely disappeared in film irradiated at higher fluences,  $1 \times 10^{13}$  and  $3 \times 10^{13}$  ions/cm<sup>2</sup>. Surface roughness increases and then decreases with increase in irradiation dose and is ascribed to rapid annealing due to high energetic ions.
- SPR of in Ag-ZnO nanocomposite thin films were tuned by thermal annealing also. A red shift of ~ 22 nm was observed after the thermal treatment which confirms the presence and growth of the nanoparticles in ZnO matrix. The crystalline behavior of film enhanced with the annealing temperature. The tunable

properties of Ag-ZnO nanocomposite thin films could be very effective for the different plasmonic application.

## 7.2. Future scope

There are many possibilities and queries arise in the present study therefore, many other ways are possible to extend the study by considering following points in future:

- This study can be extended to the other dopants also such as Au, Cu, Ni, Fe etc. for the tuning of optical, electrical and structural properties of ZnO thin films.
- Incorporation of magnetic metal particles in ZnO matrix is very interesting field for the magnetic modifications by SHI irradiation.
- Various other oxide matrix such as TiO<sub>2</sub>, SnO<sub>2</sub>, HfO<sub>2</sub>, V<sub>2</sub>O<sub>5</sub> can also be investigated for formation of the different nanocomposites with different fillers for various applications.
- Effect of low energy ion beam irradiation on SPR band frequency for these types of nanocomposite can be studied in future work.
- Ion implantation for the selective species in the oxide matrix is an efficient approach for formation of different nanocomposite and can be useful for the device application also.
- Biocompatibility of metal-carbon nanocomposites makes them interesting to be explored further. Different metal-carbon nanocomposites with different metal concentration can be studied in future.
- Metal-metal oxide nanocomposites with the various nanostructures like nano-rods, nano-sheets, nano-fibers, nanotubes etc. can be useful for sensing applications.

## References:

- [1] E. Drexler, *The coming era of nanotechnology*, (1986).
- [2] G.A. Silva, *Neuroscience nanotechnology: progress, opportunities and challenges*, *Nat. Rev. Neurosci.* 7 (2006) 65–74. doi:10.1038/nrn1827.
- [3] W. Jiang, B.Y.S. Kim, J.T. Rutka, W.C.W. Chan, *Nanoparticle-mediated cellular response is size-dependent*, *Nat. Nanotechnol.* 3 (2008) 145–150. doi:10.1038/nnano.2008.30.
- [4] M. Meyer, O. Persson, *Nanotechnology-interdisciplinarity, patterns of collaboration and differences in application*, *Scientometrics.* 42 (1998) 195–205. doi:10.1007/BF02458355.
- [5] M.-C.D. and, D. Astruc\*, *Gold Nanoparticles: Assembly, Supramolecular Chemistry, Quantum-Size-Related Properties, and Applications toward Biology, Catalysis, and Nanotechnology*, (2003). doi:10.1021/CR030698+.
- [6] T. Svedberg, J.B. Nichols, *Determination of size and distribution of size of particle by centrifugal methods*, *J. Am. Chem. Soc.* 45 (1923) 2910–2917. doi:10.1021/ja01665a016.
- [7] R.M. Macnab, *How Bacteria Assemble Flagella*, *Annu. Rev. Microbiol.* 57 (2003) 77–100. doi:10.1146/annurev.micro.57.030502.090832.
- [8] C.-H. Lee, J. Yoo, Y.-J. Doh, G.-C. Yi, *ZnO/Mg<sub>0.2</sub>Zn<sub>0.8</sub>O coaxial nanorod heterostructures for high-performance electronic nanodevice applications*, *Appl. Phys. Lett.* 94 (2009) 43504. doi:10.1063/1.3075606.
- [9] D.A. Orringer, Y.E.L. Koo, T. Chen, G. Kim, H.J. Hah, H. Xu, S. Wang, R. Keep, M.A. Philbert, R. Kopelman, O. Sagher, *In vitro characterization of a targeted, dye-loaded nanodevice for intraoperative tumor delineation*, in: *Neurosurgery*, University of Michigan, Ann Arbor, 2009: pp. 965–971. doi:10.1227/01.NEU.0000344150.81021.AA.
- [10] S.-T. Yang, Y. Liu, Y.-W. Wang, A. Cao, *Biosafety and Bioapplication of Nanomaterials by Designing Protein-Nanoparticle Interactions*, *Small.* 9 (2013) 1635–1653. doi:10.1002/sml.201201492.
- [11] M. Nurunnabi, K. Parvez, M. Nafiujjaman, V. Revuri, H.A. Khan, X. Feng, Y. Lee, *Bioapplication of graphene oxide derivatives: drug/gene delivery, imaging*,

- polymeric modification, toxicology, therapeutics and challenges, *RSC Adv.* 5 (2015) 42141–42161. doi:10.1039/C5RA04756K.
- [12] Gianfranco Carotenuto, and Yie-Shein Her, E. Matijević\*, Preparation and Characterization of Nanocomposite Thin Films for Optical Devices†, (1996). doi:10.1021/IE950721K.
- [13] M.G. Manera, J. Spadavecchia, D. Buso, C. de Julián Fernández, G. Mattei, A. Martucci, P. Mulvaney, J. Pérez-Juste, R. Rella, L. Vasanelli, P. Mazzoldi, Optical gas sensing of TiO<sub>2</sub> and TiO<sub>2</sub>/Au nanocomposite thin films, *Sensors Actuators B Chem.* 132 (2008) 107–115. doi:10.1016/j.snb.2008.01.014.
- [14] Y. Yao, Y. Ohko, Y. Sekiguchi, A. Fujishima, Y. Kubota, Self-sterilization using silicone catheters coated with Ag and TiO<sub>2</sub> nanocomposite thin film, *J. Biomed. Mater. Res. Part B Appl. Biomater.* 85B (2008) 453–460. doi:10.1002/jbm.b.30965.
- [15] R. Hauert, J. Patscheider, From alloying to nanocomposites - Improved performance of hard coatings, *Adv. Eng. Mater.* 2 (2000) 247–259. doi:10.1002/(SICI)1527-2648(200005)2:5<247::AID-ADEM247>3.0.CO;2-U.
- [16] S. Paul, A. Kanwal, M. Chhowalla, Memory effect in thin films of insulating polymer and C<sub>60</sub> nanocomposites, *Nanotechnology.* 17 (2006) 145–151. doi:10.1088/0957-4484/17/1/023.
- [17] D. Ala, M. Aguiar, J.A. Freire, I.A. Hümmelgen, Organic reversible switching devices for memory applications, *Adv. Mater.* 12 (2000) 1063–1066. doi:10.1002/1521-4095(200007)12:14<1063::AID-ADMA1063>3.0.CO;2-9.
- [18] T. Minami, H. Nanto, S. Takata, Highly Conductive and Transparent Aluminum Doped Zinc Oxide Thin Films Prepared by RF Magnetron Sputtering, *Jpn. J. Appl. Phys.* 23 (1984) L280–L282. doi:10.1143/JJAP.23.L280.
- [19] H. Zhang, G. Wang, D. Chen, X. Lv, J. Li, Tuning Photoelectrochemical Performances of Ag–TiO<sub>2</sub> Nanocomposites via Reduction/Oxidation of Ag, *Chem. Mater.* 20 (2008) 6543–6549. doi:10.1021/cm801796q.
- [20] U. Schürmann, W. Hartung, H. Takele, V. Zaporojtchenko, F. Faupel, Controlled syntheses of Ag–polytetrafluoroethylene nanocomposite thin films by co-sputtering from two magnetron sources, *Nanotechnology.* 16 (2005) 1078–1082.

doi:10.1088/0957-4484/16/8/014.

- [21] R.Z. Hu, M.Q. Zeng, M. Zhu, Cyclic durable high-capacity Sn/Cu<sub>6</sub>Sn<sub>5</sub> composite thin film anodes for lithium ion batteries prepared by electron-beam evaporation deposition, *Electrochim. Acta.* 54 (2009) 2843–2850. doi:10.1016/j.electacta.2008.11.021.
- [22] K. Fukumi, A. Chayahara, K. Kadono, T. Sakaguchi, Y. Horino, M. Miya, J. Hayakawa, M. Satou, Au<sup>+</sup>-Ion-Implanted Silica Glass with Non-Linear Optical Property, *Jpn. J. Appl. Phys.* 30 (1991) L742–L744. doi:10.1143/JJAP.30.L742.
- [23] T. Marques, M. Schwarcke, C. Garrido, V. Zucolot, O. Baffa, P. Nicolucci, Gel Dosimetry Analysis of Gold Nanoparticle Application in Kilovoltage Radiation Therapy, *J. Phys. Conf. Ser.* 250 (2010) 12084. doi:10.1088/1742-6596/250/1/012084.
- [24] W. Hong, H. Bai, Y. Xu, Z. Yao, Z. Gu, G. Shi, Preparation of Gold Nanoparticle/Graphene Composites with Controlled Weight Contents and Their Application in Biosensors, *J. Phys. Chem. C.* 114 (2010) 1822–1826. doi:10.1021/jp9101724.
- [25] S. Vallejos, T. Stoycheva, P. Umek, C. Navio, R. Snyders, C. Bittencourt, E. Llobet, C. Blackman, S. Moniz, X. Correig, Au nanoparticle-functionalised WO<sub>3</sub> nanoneedles and their application in high sensitivity gas sensor devices, *Chem. Commun.* 47 (2011) 565–567. doi:10.1039/C0CC02398A.
- [26] Chemical Elements.com - Silver (Ag), (n.d). <http://www.chemicalelements.com/elements/ag.html> (accessed August 14, 2017).
- [27] P.K. Jain, X. Huang, I.H. El-Sayed, M.A. El-Sayed, Review of Some Interesting Surface Plasmon Resonance-enhanced Properties of Noble Metal Nanoparticles and Their Applications to Biosystems, *Plasmonics.* 2 (2007) 107–118. doi:10.1007/s11468-007-9031-1.
- [28] C. Klingshirn, Introduction, in: 2010: pp. 1–6. doi:10.1007/978-3-642-10577-7\_1.
- [29] I.B. Kobiakov, Elastic, piezoelectric and dielectric properties of ZnO and CdS single crystals in a wide range of temperatures, *Solid State Commun.* 35 (1980) 305–310. doi:10.1016/0038-1098(80)90502-5.
- [30] J. Müller, B. Rech, J. Springer, M. Vanecek, TCO and light trapping in silicon thin

- film solar cells, *Sol. Energy.* 77 (2004) 917–930. doi:10.1016/j.solener.2004.03.015.
- [31] N. Jones, B. Ray, K.T. Ranjit, A.C. Manna, D. M, K. J, M. KL, C. SF, W. PD, R. HJ, Antibacterial activity of ZnO nanoparticle suspensions on a broad spectrum of microorganisms, *FEMS Microbiol. Lett.* 279 (2008) 71–76. doi:10.1111/j.1574-6968.2007.01012.x.
- [32] E.G. and, J. Rochford, Hanhong Chen, and Gaurav Saraf, Y. Lu, A.H. and, G. Boschloo\*, Fast Electron Transport in Metal Organic Vapor Deposition Grown Dye-sensitized ZnO Nanorod Solar Cells, (2006). doi:10.1021/JP062865Q.
- [33] N.K. Zayer, R. Greef, K. Rogers, A.J.C. Grellier, C.N. Pannell, In situ monitoring of sputtered zinc oxide films for piezoelectric transducers, *Thin Solid Films.* 352 (1999) 179–184. doi:10.1016/S0040-6090(99)00329-6.
- [34] S.J. Jiao, Z.Z. Zhang, Y.M. Lu, D.Z. Shen, B. Yao, J.Y. Zhang, B.H. Li, D.X. Zhao, X.W. Fan, Z.K. Tang, ZnO p-n junction light-emitting diodes fabricated on sapphire substrates, *Appl. Phys. Lett.* 88 (2006) 31911. doi:10.1063/1.2166686.
- [35] P. Sharma, A. Gupta, F.J. Owens, A. Inoue, K.V. Rao, Room temperature spintronic material—Mn-doped ZnO revisited, *J. Magn. Magn. Mater.* 282 (2004) 115–121. doi:10.1016/j.jmmm.2004.04.028.
- [36] P. Mitra, A.P. Chatterjee, H.S. Maiti, Chemical deposition of ZnO films for gas sensors, *J. Mater. Sci. Mater. Electron.* 9 (1998) 441–445. doi:10.1023/A:1008993706957.
- [37] R. Bott, *Zinc Oxide From Fundamental Properties Towards Novel Applications*, Springer, 2014. doi:10.1007/s13398-014-0173-7.2.
- [38] I. Ivanov, J. Pollmann, Electronic structure of ideal and relaxed surfaces of ZnO: A prototype ionic wurtzite semiconductor and its surface properties, *Phys. Rev. B.* 24 (1981) 7275–7296. doi:10.1103/PhysRevB.24.7275.
- [39] A. Janotti, C.G. Van de Walle, Native point defects in ZnO, *Phys. Rev. B.* 76 (2007) 165202. doi:10.1103/PhysRevB.76.165202.
- [40] M.D. McCluskey, S.J. Jokela, Defects in ZnO, *J. Appl. Phys.* 106 (2009) 71101. doi:10.1063/1.3216464.
- [41] R. Singhal, D.C. Agarwal, Y.K. Mishra, F. Singh, J.C. Pivin, R. Chandra, D.K.



- Avasthi, Electronic excitation induced tuning of surface plasmon resonance of Ag nanoparticles in fullerene C<sub>70</sub> matrix, *J. Phys. D. Appl. Phys.* 42 (2009) 155103. doi:10.1088/0022-3727/42/15/155103.
- [42] R. Singhal, D.C. Agarwal, Y.K. Mishra, S. Mohapatra, D.K. Avasthi, A.K. Chawla, R. Chandra, J.C. Pivin, Swift heavy ion induced modifications of optical and microstructural properties of silver–fullerene C<sub>60</sub> nanocomposite, *Nucl. Instruments Methods Phys. Res. Sect. B Beam Interact. with Mater. Atoms.* 267 (2009) 1349–1352. doi:10.1016/j.nimb.2009.01.044.
- [43] U.B. Singh, D.C. Agarwal, S.A. Khan, M. Kumar, A. Tripathi, R. Singhal, B.K. Panigrahi, D.K. Avasthi, Engineering of hydrophilic and plasmonic properties of Ag thin film by atom beam irradiation, *Appl. Surf. Sci.* 258 (2011) 1464–1469. doi:10.1016/j.apsusc.2011.09.105.
- [44] R. Vishnoi, R. Singhal, K. Asokan, D. Kanjilal, D. Kaur, Ion irradiation induced modifications of nanostructured Ni-Mn-Sn ferromagnetic shape memory alloy thin films, in: *Thin Solid Films*, 2011: pp. 1631–1637. doi:10.1016/j.tsf.2011.08.021.
- [45] R. Vishnoi, R. Singhal, K. Asokan, D. Kanjilal, D. Kaur, Phase transformation in Ni–Mn–Sn ferromagnetic shape memory alloy thin films induced by dense ionization, *Appl. Phys. A.* 107 (2012) 925–934. doi:10.1007/s00339-012-6826-5.
- [46] B. Gervais, S. Bouffard, Simulation of the primary stage of the interaction of swift heavy ions with condensed matter, *Nucl. Instruments Methods Phys. Res. Sect. B Beam Interact. with Mater. Atoms.* 88 (1994) 355–364. doi:10.1016/0168-583X(94)95384-8.
- [47] S.K. Srivastava, D.K. Avasthi, W. Assmann, Z.G. Wang, H. Kucal, E. Jacquet, H.D. Carstanjen, M. Toulemonde, Test of the hypothesis of transient molten state diffusion for swift-heavy-ion induced mixing, *Phys. Rev. B.* 71 (2005) 193405. doi:10.1103/PhysRevB.71.193405.
- [48] B. Schattat, W. Bolse, Fast heavy ion induced interface mixing in thin-film systems, *Nucl. Instruments Methods Phys. Res. Sect. B Beam Interact. with Mater. Atoms.* 225 (2004) 105–110. doi:10.1016/j.nimb.2004.04.183.
- [49] D.C. Agarwal, A. Kumar, S.A. Khan, D. Kabiraj, F. Singh, A. Tripathi, J.C. Pivin, R.S. Chauhan, D.K. Avasthi, SHI induced modification of ZnO thin film: Optical

- and structural studies, *Nucl. Instruments Methods Phys. Res. Sect. B Beam Interact. with Mater. Atoms.* 244 (2006) 136–140. doi:10.1016/j.nimb.2005.11.077.
- [50] P.M.R. Kumar, C.S. Kartha, K.P. Vijayakumar, F. Singh, D.K. Avasthi, P.M.R. Kumar, C.S. Kartha, K.P. Vijayakumar, Modifications of ZnO thin films under dense electronic excitation *Modifications of ZnO thin films under dense electronic excitation*, 13509 (2005). doi:10.1063/1.1823574.
- [51] S. Rehman, R.G. Singh, J.C. Pivin, W. Bari, F. Singh, Structural and spectroscopic modifications of nanocrystalline zinc oxide films induced by swift heavy ions, *Vacuum.* 86 (2011) 87–90. doi:10.1016/j.vacuum.2011.04.019.
- [52] V. Kumar, F. Singh, O.M. Ntwaeaborwa, H.C. Swart, Effect of Br<sup>+6</sup> ions on the structural, morphological and luminescent properties of ZnO/Si thin films, *Appl. Surf. Sci.* 279 (2013) 472–478. doi:10.1016/j.apsusc.2013.04.145.
- [53] S. Mal, S. Nori, J. Narayan, J.T. Prater, D.K. Avasthi, Ion-irradiation-induced ferromagnetism in undoped ZnO thin films, *Acta Mater.* 61 (2013) 2763–2768. doi:10.1016/j.actamat.2012.09.071.
- [54] P. Prabukanthan, G. Harichandran, *Materials Science in Semiconductor Processing* Effect of 100 MeV O<sup>7+</sup> ion beam irradiation on radio frequency reactive magnetron sputtered ZnO thin films, *Mater. Sci. Semicond. Process.* 16 (2013) 193–199. doi:10.1016/j.mssp.2012.04.016.
- [55] D.C. Agarwal, F. Singh, D. Kabiraj, S. Sen, P.K. Kulriya, I. Sulania, S. Nozaki, R.S. Chauhan, D.K. Avasthi, Thermal and ion induced annealing of nanocrystalline ZnO thin film deposited by atom beam sputtering, *J. Phys. D. Appl. Phys.* 41 (2008) 45305. doi:10.1088/0022-3727/41/4/045305.
- [56] F. Singh, P.K. Kulriya, J.C. Pivin, Origin of swift heavy ion induced stress in textured ZnO thin films: An in situ X-ray diffraction study, 2010. doi:10.1016/j.ssc.2010.07.026.
- [57] G.P. Daniel, V.B. Justinictor, P.B. Nair, K. Joy, P. Koshy, P. V Thomas, Effect of annealing temperature on the structural and optical properties of ZnO thin films prepared by RF magnetron sputtering, *Phys. B Phys. Condens. Matter.* 405 (2010) 1782–1786. doi:10.1016/j.physb.2010.01.039.

- [58] R. Elilarassi, G. Chandrasekaran, Effect of annealing on structural and optical properties of zinc oxide films, *Mater. Chem. Phys.* 121 (2010) 378–384. doi:10.1016/j.matchemphys.2010.01.053.
- [59] B. Zhou, A. V Rogachev, Z. Liu, D.G. Piliptsov, H. Ji, X. Jiang, Applied Surface Science Effects of oxygen / argon ratio and annealing on structural and optical properties of ZnO thin films, *Appl. Surf. Sci.* 258 (2012) 5759–5764. doi:10.1016/j.apsusc.2012.02.088.
- [60] M. Jung, J. Lee, S. Park, H. Kim, J.C. Å, Investigation of the annealing effects on the structural and optical properties of sputtered ZnO thin films, 283 (2005) 384–389. doi:10.1016/j.jcrysgro.2005.06.047.
- [61] M. Garcı, Investigation of the annealing effects on the structural and optoelectronic properties of RF-sputtered ZnO films studied by the Drude – Lorentz model, (2015) 1375–1382. doi:10.1007/s00339-015-9318-6.
- [62] Y. Jeong, S. Park, Thermal stress induced band gap variation of ZnO thin films, *Curr. Appl. Phys.* 14 (2014) 30–33. doi:10.1016/j.cap.2013.10.003.
- [63] P. Murkute, H. Ghadi, S. Saha, S. Kumar, Materials Science in Semiconductor Processing Enhancement in optical characteristics of c-axis-oriented radio frequency – sputtered ZnO thin films through growth ambient and annealing temperature optimization, *Mater. Sci. Semicond. Process.* 66 (2017) 1–8. doi:10.1016/j.mssp.2017.03.026.
- [64] M.F. Al-kuhaili, S.M.A. Durrani, I.A. Bakhtiari, M. Saleem, Optical constants of vacuum annealed radio frequency ( RF ) magnetron sputtered zinc oxide thin films, *Opt. Commun.* 285 (2012) 4405–4412. doi:10.1016/j.optcom.2012.06.031.
- [65] D. Phan, G. Chung, Applied Surface Science The effect of post-annealing on surface acoustic wave devices based on ZnO thin films prepared by magnetron sputtering, *Appl. Surf. Sci.* 257 (2011) 4339–4343. doi:10.1016/j.apsusc.2010.12.053.
- [66] U. Chaitra, D. Kekuda, K.M. Rao, Effect of annealing temperature on the evolution of structural , microstructural , and optical properties of spin coated ZnO thin films, *Ceram. Int.* 43 (2017) 7115–7122. doi:10.1016/j.ceramint.2017.02.144.
- [67] S. Kumar, R. Kumar, D.P. Singh, Swift heavy ion induced modifications in cobalt

- doped ZnO thin films: Structural and optical studies, *Appl. Surf. Sci.* 255 (2009) 8014–8018. doi:10.1016/j.apsusc.2009.05.005.
- [68] V. Kumar, V. Kumar, S. Som, L.P. Purohit, O.M. Ntwaeaborwa, H.C. Swart, Role of swift heavy ions irradiation on the emission of boron doped ZnO thin films for near white light application, *J. Alloys Compd.* 594 (2014) 32–38. doi:10.1016/j.jallcom.2014.01.110.
- [69] G. Jayalakshmi, K. Saravanan, S. Balakumar, T. Balasubramanian, Swift heavy ion induced modifications in structural, optical & magnetic properties of pure and V doped ZnO films, *Vacuum*. 95 (2013) 66–70. doi:10.1016/j.vacuum.2013.02.014.
- [70] M. Hossein, H. Reza, Preparation and characterization of nanocomposite ZnO – Ag thin film containing nano-sized Ag particles: influence of preheating, annealing temperature and silver content on characteristics, (2010) 195–202. doi:10.1007/s10971-010-2177-x.
- [71] X.B. Wang, C. Song, K.W. Geng, F. Zeng, F. Pan, Luminescence and Raman scattering properties of Ag-doped ZnO films, 4992 (2006). doi:10.1088/0022-3727/39/23/014.
- [72] M. Lee, T.G. Kim, W. Kim, Y. Sung, Surface Plasmon Resonance ( SPR ) Electron and Energy Transfer in Noble Metal - Zinc Oxide Composite Nanocrystals, (2008) 10079–10082.
- [73] L.N. Wang, L.Z. Hu, H.Q. Zhang, Y. Qiu, Y. Lang, G.Q. Liu, J.Y. Ji, J.X. Ma, Z.W. Zhao, Materials Science in Semiconductor Processing Studying the Raman spectra of Ag doped ZnO films grown by PLD, 14 (2011) 274–277. doi:10.1016/j.mssp.2011.05.004.
- [74] A. Tripathi, K. Prakash, R.K. Shukla, UV enhancement in polycrystalline Ag-doped ZnO films deposited by the sol – gel method, *J. Lumin.* 149 (2014) 361–368. doi:10.1016/j.jlumin.2013.12.043.
- [75] R. Deng, B. Yao, Y.F. Li, T. Yang, B.H. Li, Z.Z. Zhang, C.X. Shan, J.Y. Zhang, D.Z. Shen, Influence of oxygen / argon ratio on structural, electrical and optical properties of Ag-doped ZnO thin films, *J. Cryst. Growth.* 312 (2010) 1813–1816. doi:10.1016/j.jcrysgr.2010.02.042.

- [76] Y. Seob, M. Soo, J. Sa, J. Lee, The effect of substrate temperature on Al-doped ZnO characteristics for organic thin film transistor applications, *Mater. Res. Bull.* 48 (2013) 5136–5140. doi:10.1016/j.materresbull.2013.06.001.
- [77] J.W. Zhang, G. He, T.S. Li, M. Liu, X.S. Chen, Y.M. Liu, Z.Q. Sun, Modulation of microstructure and optical properties of Mo-doped ZnO thin films by substrate temperature, 65 (2015) 7–13. doi:10.1016/j.materresbull.2015.01.004.
- [78] S. Lin, J. Huang, D. Lii, Effect of substrate temperature on the properties of Ti-doped ZnO films by simultaneous rf and dc magnetron sputtering, 90 (2005) 22–30. doi:10.1016/j.matchemphys.2004.08.040.
- [79] I. Li, F. Liang, C. Ximing, L.I.U. Gaobin, L.I.U. Jun, Y. Fengfan, F.U. Guangzong, ScienceDirect Effect of annealing treatment on the structural , optical , and electrical, 26 (2007) 247–253.
- [80] I.S. Kim, E. Jeong, D.Y. Kim, M. Kumar, S. Choi, Applied Surface Science Investigation of p-type behavior in Ag-doped ZnO thin films by E-beam evaporation, 255 (2009) 4011–4014. doi:10.1016/j.apsusc.2008.10.117.
- [81] H.S. Kang, B. Du Ahn, J.H. Kim, G.H. Kim, S.H. Lim, H.W. Chang, S.Y. Lee, Structural, electrical, and optical properties of p-type ZnO thin films with Ag dopant, *Appl. Phys. Lett.* 88 (2006) 10–13. doi:10.1063/1.2203952.
- [82] Y.K. Mishra, S. Mohapatra, R. Singhal, D.K. Avasthi, D.C. Agarwal, Y.K. Mishra, S. Mohapatra, R. Singhal, D.K. Avasthi, Au – ZnO : A tunable localized surface plasmonic nanocomposite, 43107 (2008). doi:10.1063/1.2838302.
- [83] C.D. Dimitrakopoulos, P.R.L. Malenfant, Organic thin film transistors for large area electronics, *Adv. Mater.* 14 (2002) 99–117. doi:10.1002/1521-4095(20020116)14:2<99::AID-ADMA99>3.0.CO;2-9.
- [84] B. Yu, K.M. Leung, Q. Guo, W.M. Lau, J. Yang, Synthesis of Ag–TiO<sub>2</sub> composite nano thin film for antimicrobial application, *Nanotechnology.* 22 (2011) 115603. doi:10.1088/0957-4484/22/11/115603.
- [85] L.R. Doolittle, Algorithms for the rapid simulation of Rutherford backscattering spectra, *Nucl. Instruments Methods Phys. Res. Sect. B Beam Interact. with Mater. Atoms.* 9 (1985) 344–351. doi:10.1016/0168-583X(85)90762-1.
- [86] B.D. Cullity, *Element of X-ray diffraction*, Addison-Wesley Publishing Company,

- Inc, 1978.
- [87] A.J. Bradley, A.H. Jay, A method for deducing accurate values of the lattice spacing from x-ray powder photographs taken by the Debye-Scherrer method, *Proc. Phys. Soc.* 44 (1932) 563–579. doi:10.1088/0959-5309/44/5/305.
- [88] C. Kumar, ed., *UV-VIS and Photoluminescence Spectroscopy for Nanomaterials Characterization*, Springer Berlin Heidelberg, Berlin, Heidelberg, 2013. doi:10.1007/978-3-642-27594-4.
- [89] J. Tauc, R. Grigorovici, A. Vancu, Optical Properties and Electronic Structure of Amorphous Germanium, *Phys. Status Solidi.* 15 (1966) 627–637. doi:10.1002/pssb.19660150224.
- [90] P.C. Braga, D. Ricci, *Atomic Force Microscopy: Biomedical Methods and Applications*, *Antibiot. Resist. Methods Protoc.* 242 (2004) 199–207. doi:10.1385/1-59259-077-2:199.
- [91] T.L. Kirk, U. Ramsperger, D. Pescia, Near field emission scanning electron microscopy, *J. Vac. Sci. Technol. B Microelectron. Nanom. Struct.* 27 (2009) 152. doi:10.1116/1.3071849.
- [92] D.B. Williams, C.B. Carter, *The Transmission Electron Microscope*, in: *Transm. Electron Microsc.*, Springer US, Boston, MA, 2009: pp. 3–22. doi:10.1007/978-0-387-76501-3\_1.
- [93] J.R. Ferraro, K. Nakamoto, C.W. Brown, *Introductory Raman spectroscopy*, Academic Press, 2003.
- [94] T. Aoki, Aoki, Takeshi, *Photoluminescence Spectroscopy*, in: *Charact. Mater.*, John Wiley & Sons, Inc., Hoboken, NJ, USA, 2012. doi:10.1002/0471266965.com058.pub2.
- [95] S. Hofmann, *Auger- and X-Ray Photoelectron Spectroscopy in Materials Science*, Springer Berlin Heidelberg, Berlin, Heidelberg, 2013. doi:10.1007/978-3-642-27381-0.
- [96] C.-S. Chen, C.-T. Kuo, T.-B. Wu, I.-N. Lin, Microstructures and Electrical Properties of  $V_{2}O_{5}$ -based Multicomponent ZnO Varistors Prepared by Microwave Sintering Process, *Jpn. J. Appl. Phys.* 36 (1997) 1169–1175. doi:10.1143/JJAP.36.1169.

- [97] J.M. Hvam, Temperature-Induced Wavelength Shift of Electron-Beam-Pumped Lasers from CdSe, CdS, and ZnO, *Phys. Rev. B.* 4 (1971) 4459–4464. doi:10.1103/PhysRevB.4.4459.
- [98] J. Hu, R.G. Gordon, Textured aluminum- doped zinc oxide thin films from atmospheric pressure chemical- vapor deposition, *J. Appl. Phys.* 71 (1992) 880–890. doi:10.1063/1.351309.
- [99] J.-H. Lee, K.-H. Ko, B.-O. Park, Electrical and optical properties of ZnO transparent conducting films by the sol–gel method, *J. Cryst. Growth.* 247 (2003) 119–125. doi:10.1016/S0022-0248(02)01907-3.
- [100] M.-M. Bagheri-Mohagheghi, M. Shokooh-Saremi, Investigations on the physical properties of the SnO<sub>2</sub>–ZnO transparent conducting binary–binary system deposited by spray pyrolysis technique, *Thin Solid Films.* 441 (2003) 238–242. doi:10.1016/S0040-6090(03)00948-9.
- [101] X.W. Sun, H.S. Kwok, Optical properties of epitaxially grown zinc oxide films on sapphire by pulsed laser deposition, *J. Appl. Phys.* 86 (1999) 408–411. doi:10.1063/1.370744.
- [102] D.C. Agarwal, D.K. Avasthi, F. Singh, D. Kabiraj, P.K. Kulariya, I. Sulania, J.C. Pivin, R.S. Chauhan, Swift heavy ion induced structural modification of atom beam sputtered ZnO thin film, *Surf. Coatings Technol.* 203 (2009) 2427–2431. doi:10.1016/j.surfcoat.2009.02.109.
- [103] J.F. Wager, Transparent Electronics, *Science* (80-. ). 300 (2003). <http://science.sciencemag.org/content/300/5623/1245> (accessed April 5, 2017).
- [104] S.J. Pearton, D.P. Norton, K. Ip, Y.W. Heo, T. Steiner, Recent progress in processing and properties of ZnO, *Prog. Mater. Sci.* 50 (2005) 293–340. doi:10.1016/j.pmatsci.2004.04.001.
- [105] M. Grätzel, Conversion of sunlight to electric power by nanocrystalline dye-sensitized solar cells, *J. Photochem. Photobiol. A Chem.* 164 (2004) 3–14. doi:10.1016/j.jphotochem.2004.02.023.
- [106] P.F. Carcia, R.S. McLean, M.H. Reilly, G. Nunes, Transparent ZnO thin-film transistor fabricated by rf magnetron sputtering, *Appl. Phys. Lett.* 82 (2003) 1117–1119. doi:10.1063/1.1553997.

- [107] D.C. Look, D.C. Reynolds, C.W. Litton, R.L. Jones, D.B. Eason, G. Cantwell, Characterization of homoepitaxial *p*-type ZnO grown by molecular beam epitaxy, *Appl. Phys. Lett.* 81 (2002) 1830–1832. doi:10.1063/1.1504875.
- [108] T. Gao, T.H. Wang, Synthesis and properties of multipod-shaped ZnO nanorods for gas-sensor applications, *Appl. Phys. A.* 80 (2005) 1451–1454. doi:10.1007/s00339-004-3075-2.
- [109] Z.W. Pan, Z.R. Dai, Z.L. Wang, Nanobelts of Semiconducting Oxides, *Science* (80-. ). 291 (2001) 1947–1949. doi:10.1126/science.1058120.
- [110] M.H. Huang, S. Mao, H. Feick, H. Yan, Y. Wu, H. Kind, E. Weber, R. Russo, P. Yang, Room-Temperature Ultraviolet Nanowire Nanolasers, *Science* (80-. ). 292 (2001) 1897–1899. doi:10.1126/science.1060367.
- [111] C.H. Liu, W.C. Yiu, F.C.K. Au, J.X. Ding, C.S. Lee, S.T. Lee, Electrical properties of zinc oxide nanowires and intramolecular p–n junctions, *Appl. Phys. Lett.* 83 (2003) 3168–3170. doi:10.1063/1.1609232.
- [112] P. Shah, S. Kumar, A. Gupta, D.K. Avasthi, Thermal properties of swift heavy ion irradiated CuO, *Nucl. Instruments Methods Phys. Res. Sect. B Beam Interact. with Mater. Atoms.* 156 (1999) 222–226. doi:10.1016/S0168-583X(99)00264-5.
- [113] R. Singhal, D.C. Agarwal, Y.K. Mishra, F. Singh, J.C. Pivin, R. Chandra, D.K. Avasthi, Electronic excitation induced tuning of surface plasmon resonance of Ag nanoparticles in fullerene C<sub>70</sub> matrix, *J. Phys. D. Appl. Phys.* 42 (2009) 155103. doi:10.1088/0022-3727/42/15/155103.
- [114] R. Singhal, A. Kumar, Y.K. Mishra, S. Mohapatra, J.C. Pivin, D.K. Avasthi, Swift heavy ion induced modifications of fullerene C<sub>70</sub> thin films, *Nucl. Instruments Methods Phys. Res. Sect. B Beam Interact. with Mater. Atoms.* 266 (2008) 3257–3262. doi:10.1016/j.nimb.2008.04.003.
- [115] R. Vishnoi, R. Singhal, K. Asokan, D. Kanjilal, D. Kaur, Ion irradiation induced modifications of nanostructured Ni–Mn–Sn ferromagnetic shape memory alloy thin films, *Thin Solid Films.* 520 (2011) 1631–1637. doi:10.1016/j.tsf.2011.08.021.
- [116] R. Singhal, D. Kabiraj, P.K. Kulriya, J.C. Pivin, R. Chandra, D.K. Avasthi, Blue-Shifted SPR of Au Nanoparticles with Ordering of Carbon by Dense Ionization



- and Thermal Treatment, *Plasmonics*. 8 (2013) 295–305. doi:10.1007/s11468-012-9389-6.
- [117] R. Singhal, J.C. Pivin, D.K. Avasthi, Ion beam irradiation-induced tuning of SPR of Au nanoparticles in fullerene C70 matrix: dependence of energy loss, *J. Nanoparticle Res.* 15 (2013) 1641. doi:10.1007/s11051-013-1641-2.
- [118] D.K. Avasthi, Y.K. Mishra, F. Singh, J.P. Stoquert, Ion tracks in silica for engineering the embedded nanoparticles, *Nucl. Instruments Methods Phys. Res. Sect. B Beam Interact. with Mater. Atoms.* 268 (2010) 3027–3034. doi:10.1016/j.nimb.2010.05.033.
- [119] Y.K. Mishra, V.S.K. Chakravadhanula, U. Schürmann, H. Kumar, D. Kabiraj, S. Ghosh, V. Zaporozhchenko, F. Faupel, Controlled reduction of size of Ag nanoparticles embedded in teflon matrix by MeV ion irradiation, *Nucl. Instruments Methods Phys. Res. Sect. B Beam Interact. with Mater. Atoms.* 266 (2008) 1804–1809. doi:10.1016/j.nimb.2008.01.040.
- [120] D.K. Avasthi, A. Kumar, R. Singhal, A. Tripathi, D.S. Misra, Studies on Carbon Nanotubes and Fullerenes Under Extreme Conditions, *J. Nanosci. Nanotechnol.* 10 (2010) 3767–3779. doi:10.1166/jnn.2010.1979.
- [121] D.K. Avasthi, G.K. Mehta, Ion Beams for Materials Engineering—An Overview, in: 2011: pp. 1–46. doi:10.1007/978-94-007-1229-4\_1.
- [122] S.K. Srivastava, D.K. Avasthi, W. Assmann, Z.G. Wang, H. Kucal, E. Jacquet, H.D. Carstanjen, M. Toulemonde, Test of the hypothesis of transient molten state diffusion for swift-heavy-ion induced mixing, *Phys. Rev. B.* 71 (2005) 193405. doi:10.1103/PhysRevB.71.193405.
- [123] W. Bolse, B. Schattat, Atomic mixing in thin film systems by swift heavy ions, *Nucl. Instruments Methods Phys. Res. Sect. B Beam Interact. with Mater. Atoms.* 190 (2002) 173–176. doi:10.1016/S0168-583X(01)01225-3.
- [124] F. Singh, R.G. Singh, V. Kumar, S.A. Khan, J.C. Pivin, Softening of phonons by lattice defects and structural strain in heavy ion irradiated nanocrystalline zinc oxide films, *J. Appl. Phys.* 110 (2011) 83520. doi:10.1063/1.3651638.
- [125] D.C. Agarwal, R.S. Chauhan, D.K. Avasthi, S.A. Khan, D. Kabiraj, I. Sulania, Formation of self-affine nanostructures on ZnO surfaces by swift heavy ions, *J.*

- Appl. Phys. 104 (2008) 24304. doi:10.1063/1.2953177.
- [126] S. Rehman, R.G. Singh, J.C. Pivin, W. Bari, F. Singh, Structural and spectroscopic modifications of nanocrystalline zinc oxide films induced by swift heavy ions, *Vacuum*. 86 (2011) 87–90. doi:10.1016/j.vacuum.2011.04.019.
- [127] N. Fujimura, T. Nishihara, S. Goto, J. Xu, T. Ito, Control of preferred orientation for ZnOx films: control of self-texture, *J. Cryst. Growth*. 130 (1993) 269–279. doi:10.1016/0022-0248(93)90861-P.
- [128] A.N. Mariano, R.E. Hanneman, Crystallographic Polarity of ZnO Crystals, *J. Appl. Phys.* 34 (1963) 384–388. doi:10.1063/1.1702617.
- [129] H.P. (Harold P. Klug, L.E. (Leroy E. Alexander, X-ray diffraction procedures for polycrystalline and amorphous materials, John Wiley & Sons, 1974.
- [130] B.D. Cullity, *Elements of X-ray diffraction*, 1978.
- [131] G. Szenes, General features of latent track formation in magnetic insulators irradiated with swift heavy ions, *Phys. Rev. B*. 51 (1995) 8026–8029. doi:10.1103/PhysRevB.51.8026.
- [132] J.G.E. Gardeniers, Z.M. Rittersma, G.J. Burger, Preferred orientation and piezoelectricity in sputtered ZnO films, *J. Appl. Phys.* 83 (1998) 7844–7854. doi:10.1063/1.367959.
- [133] P.M.R. Kumar, C.S. Kartha, K.P. Vijayakumar, F. Singh, D.K. Avasthi, T. Abe, Y. Kashiwaba, G.S. Okram, M. Kumar, S. Kumar, Modifications of ZnO thin films under dense electronic excitation, *J. Appl. Phys.* 97 (2005) 13509. doi:10.1063/1.1823574.
- [134] J. Tauc, Optical properties and electronic structure of amorphous Ge and Si, *Mater. Res. Bull.* 3 (1968) 37–46. doi:10.1016/0025-5408(68)90023-8.
- [135] Introduction, in: *Phys. Semicond.*, Springer Berlin Heidelberg, n.d.: pp. 1–12. doi:10.1007/3-540-34661-9\_1.
- [136] R. Vishnoi, D. Kaur, Size dependence of martensite transformation temperature in nanostructured Ni–Mn–Sn ferromagnetic shape memory alloy thin films, *Surf. Coatings Technol.* 204 (2010) 3773–3782. doi:10.1016/j.surfcoat.2010.04.053.
- [137] C. Bundesmann, N. Ashkenov, M. Schubert, D. Spemann, T. Butz, E.M. Kaidashev, M. Lorenz, M. Grundmann, Raman scattering in ZnO thin films doped

- with Fe, Sb, Al, Ga, and Li, *Appl. Phys. Lett.* 83 (2003) 1974–1976. doi:10.1063/1.1609251.
- [138] J.F. Scott, uv Resonant Raman Scattering in ZnO, *Phys. Rev. B.* 2 (1970) 1209–1211. doi:10.1103/PhysRevB.2.1209.
- [139] V.A. Fonoberov, A.A. Balandin, Interface and confined optical phonons in wurtzite nanocrystals, *Phys. Rev. B.* 70 (2004) 233205. doi:10.1103/PhysRevB.70.233205.
- [140] A. Zaoui, W. Sekkal, Pressure-induced softening of shear modes in wurtzite ZnO: A theoretical study, *Phys. Rev. B.* 66 (2002) 174106. doi:10.1103/PhysRevB.66.174106.
- [141] M. Mayer, SIMNRA User 's Guide, (n.d.).
- [142] A.O. Dikovska, P.A. Atanasov, C. Vasilev, I.G. Dimitrov, T.R. Stoyanchov, Thin ZnO films produced by pulsed laser deposition, *J. Optoelectron. Adv. Mater.* 7 (2005) 1329–1334.
- [143] D.C. Agarwal, R.S. Chauhan, A. Kumar, D. Kabiraj, F. Singh, S.A. Khan, D.K. Avasthi, J.C. Pivin, M. Kumar, J. Ghatak, P. V. Satyam, Synthesis and characterization of ZnO thin film grown by electron beam evaporation, *J. Appl. Phys.* 99 (2006) 123105. doi:10.1063/1.2204333.
- [144] V.A. Fonoberov, A.A. Balandin, Polar optical phonons in wurtzite spheroidal quantum dots: theory and application to ZnO and ZnO/MgZnO nanostructures, *J. Phys. Condens. Matter.* 17 (2005) 1085–1097. doi:10.1088/0953-8984/17/7/003.
- [145] K.A. Alim, V.A. Fonoberov, M. Shamsa, A.A. Balandin, Micro-Raman investigation of optical phonons in ZnO nanocrystals, *J. Appl. Phys.* 97 (2005) 1–5. doi:10.1063/1.1944222.
- [146] T.L. Yang, D.H. Zhang, J. Ma, H.L. Ma, Y. Chen, Transparent conducting ZnO:Al films deposited on organic substrates deposited by r.f. magnetron-sputtering, *Thin Solid Films.* 326 (1998) 60–62. doi:10.1016/S0040-6090(98)00763-9.
- [147] Zheng Wei Pan, Zu Rong Dai, Zhong Lin Wang, Nanobelts of semiconducting oxides, *Science* (80-. ). 291 (2001) 1947–1949. doi:10.1126/science.1058120.
- [148] R. Romero, M.C. López, D. Leinen, F. Martín, J.R. Ramos-Barrado, Electrical properties of the n-ZnO/c-Si heterojunction prepared by chemical spray pyrolysis,

- Mater. Sci. Eng. B. 110 (2004) 87–93. doi:10.1016/j.mseb.2004.03.010.
- [149] S. Sharma, C. Periasamy, A study on the electrical characteristic of n-ZnO/p-Si heterojunction diode prepared by vacuum coating technique, *Superlattices Microstruct.* 73 (2014) 12–21. doi:10.1016/j.spmi.2014.05.011.
- [150] J.C. Pivin, G. Socol, I. Mihailescu, P. Berthet, F. Singh, M.K. Patel, L. Vincent, Structure and magnetic properties of ZnO films doped with Co, Ni or Mn synthesized by pulsed laser deposition under low and high oxygen partial pressures, *Thin Solid Films.* 517 (2008) 916–922. doi:10.1016/j.tsf.2008.08.125.
- [151] G.S.T. Rao, D. Tarakarama Rao, Gas sensitivity of ZnO based thick film sensor to NH<sub>3</sub> at room temperature, *Sensors Actuators B Chem.* 55 (1999) 166–169. doi:10.1016/S0925-4005(99)00049-0.
- [152] T. Reimer, I. Paulowicz, R. Röder, S. Kaps, O. Lupan, S. Chemnitz, W. Benecke, C. Ronning, R. Adelung, Y.K. Mishra, Single Step Integration of ZnO Nano- and Microneedles in Si Trenches by Novel Flame Transport Approach: Whispering Gallery Modes and Photocatalytic Properties, *ACS Appl. Mater. Interfaces.* 6 (2014) 7806–7815. doi:10.1021/am5010877.
- [153] V. Cretu, V. Postica, A.K. Mishra, M. Hoppe, I. Tiginyanu, Y.K. Mishra, L. Chow, N.H. de Leeuw, R. Adelung, O. Lupan, V. Sontea, T. Strunskus, F. Faupel, R. Adelung, Synthesis, characterization and DFT studies of zinc-doped copper oxide nanocrystals for gas sensing applications, *J. Mater. Chem. A.* 4 (2016) 6527–6539. doi:10.1039/C6TA01355D.
- [154] Y.K. Mishra, G. Modi, V. Cretu, V. Postica, O. Lupan, T. Reimer, I. Paulowicz, V. Hrkac, W. Benecke, L. Kienle, R. Adelung, Direct Growth of Freestanding ZnO Tetrapod Networks for Multifunctional Applications in Photocatalysis, UV Photodetection, and Gas Sensing, *ACS Appl. Mater. Interfaces.* 7 (2015) 14303–14316. doi:10.1021/acsami.5b02816.
- [155] D.C. Agarwal, R.S. Chauhan, A. Kumar, D. Kabiraj, F. Singh, S.A. Khan, D.K. Avasthi, J.C. Pivin, M. Kumar, J. Ghatak, P. V. Satyam, Synthesis and characterization of ZnO thin film grown by electron beam evaporation, *J. Appl. Phys.* 99 (2006) 123105. doi:10.1063/1.2204333.
- [156] Y.K. Mishra, S. Kaps, A. Schuchardt, I. Paulowicz, X. Jin, D. Gedamu, S. Freitag,

- M. Claus, S. Wille, A. Kovalev, S.N. Gorb, R. Adelung, Fabrication of Macroscopically Flexible and Highly Porous 3D Semiconductor Networks from Interpenetrating Nanostructures by a Simple Flame Transport Approach, Part. Part. Syst. Charact. 30 (2013) 775–783. doi:10.1002/ppsc.201300197.
- [157] N. Wang, Y. Cai, R.Q. Zhang, Growth of nanowires, Mater. Sci. Eng. R Reports. 60 (2008) 1–51. doi:10.1016/j.mser.2008.01.001.
- [158] J. Gröttrup, V. Postica, N. Ababii, O. Lupan, C. Zamponi, D. Meyners, Y.K. Mishra, V. Sontea, I. Tiginyanu, R. Adelung, Size-dependent UV and gas sensing response of individual Fe<sub>2</sub>O<sub>3</sub>-ZnO:Fe micro- and nanowire based devices, J. Alloys Compd. 701 (2017) 920–925. doi:10.1016/j.jallcom.2016.12.346.
- [159] H.Q. Bian, S.Y. Ma, Z.M. Zhang, J.M. Gao, H.B. Zhu, Microstructure and Raman scattering of Ag-doping ZnO films deposited on buffer layers, J. Cryst. Growth. 394 (2014) 132–136. doi:10.1016/j.jcrysgro.2014.02.036.
- [160] S.K. Singh, H. Sharma, R. Singhal, V.V.S. Kumar, D.K. Avasthi, Synthesis and annealing study of RF sputtered ZnO thin film, in: 2016: p. 80063. doi:10.1063/1.4947941.
- [161] F. Singh, P.K. Kulriya, J.C. Pivin, Origin of swift heavy ion induced stress in textured ZnO thin films: An in situ X-ray diffraction study, 2010. doi:10.1016/j.ssc.2010.07.026.
- [162] J. Chen, X. Yan, W. Liu, Q. Xue, The ethanol sensing property of magnetron sputtered ZnO thin films modified by Ag ion implantation, 2011. doi:10.1016/j.snb.2011.08.026.
- [163] M. Liu, X.Q. Wei, Z.G. Zhang, G. Sun, C.S. Chen, C.S. Xue, H.Z. Zhuang, B.Y. Man, Effect of temperature on pulsed laser deposition of ZnO films, Appl. Surf. Sci. 252 (2006) 4321–4326. doi:10.1016/j.apsusc.2005.07.038.
- [164] W. Tang, D.C. Cameron, Aluminum-doped zinc oxide transparent conductors deposited by the sol-gel process, Thin Solid Films. 238 (1994) 83–87. doi:10.1016/0040-6090(94)90653-X.
- [165] R. Georgekutty, M.K. Seery, S.C. Pillai, A Highly Efficient Ag-ZnO Photocatalyst: Synthesis, Properties, and Mechanism, J. Phys. Chem. C. 112 (2008) 13563–13570. doi:10.1021/jp802729a.

- [166] J. Liqiang, W. Dejun, W. Baiqi, L. Shudan, X. Baifu, F. Honggang, S. Jiazhong, Effects of noble metal modification on surface oxygen composition, charge separation and photocatalytic activity of ZnO nanoparticles, *J. Mol. Catal. A Chem.* 244 (2006) 193–200. doi:10.1016/j.molcata.2005.09.020.
- [167] S.K. Singh, R. Singhal, V.V. Siva Kumar, Study on swift heavy ions induced modifications of Ag-ZnO nanocomposite thin film, *Superlattices Microstruct.* 103 (2017) 195–204. doi:10.1016/j.spmi.2017.01.032.
- [168] X.H. Wang, J. Shi, S. Dai, Y. Yang, A sol-gel method to prepare pure and gold colloid doped ZnO films, *Thin Solid Films.* 429 (2003) 102–107. doi:10.1016/S0040-6090(03)00057-9.
- [169] H.S. Kang, B. Du Ahn, J.H. Kim, G.H. Kim, S.H. Lim, H.W. Chang, S.Y. Lee, Structural, electrical, and optical properties of p-type ZnO thin films with Ag dopant, *Appl. Phys. Lett.* 88 (2006) 202108. doi:10.1063/1.2203952.
- [170] Y. Yan, M.M. Al-Jassim, S.-H. Wei, Doping of ZnO by group-IB elements, *Appl. Phys. Lett.* 89 (2006) 181912. doi:10.1063/1.2378404.
- [171] D.L. Hou, X.J. Ye, H.J. Meng, H.J. Zhou, X.L. Li, C.M. Zhen, G.D. Tang, Magnetic properties of n-type Cu-doped ZnO thin films, *Appl. Phys. Lett.* 90 (2007) 142502. doi:10.1063/1.2719034.
- [172] R. Singhal, J.C. Pivin, D.K. Avasthi, Ion beam irradiation-induced tuning of SPR of Au nanoparticles in fullerene C70 matrix: dependence of energy loss, *J. Nanoparticle Res.* 15 (2013) 1641. doi:10.1007/s11051-013-1641-2.
- [173] R. Singhal, D.C. Agarwal, S. Mohapatra, Y.K. Mishra, D. Kabiraj, F. Singh, D.K. Avasthi, A.K. Chawla, R. Chandra, G. Mattei, J.C. Pivin, Synthesis and characterizations of silver-fullerene C70 nanocomposite, *Appl. Phys. Lett.* 93 (2008) 3–5. doi:10.1063/1.2976674.
- [174] Y. Yan, S.-H. Wei, Doping asymmetry in wide-bandgap semiconductors: Origins and solutions, *Phys. Status Solidi.* 245 (2008) 641–652. doi:10.1002/pssb.200743334.
- [175] O. Volnianska, P. Boguslawski, J. Kaczkowski, P. Jakubas, A. Jezierski, E. Kaminska, Theory of doping properties of Ag acceptors in ZnO, *Phys. Rev. B.* 80 (2009) 245212. doi:10.1103/PhysRevB.80.245212.

- [176] Q. Wan, Z. Xiong, J. Dai, J. Rao, F. Jiang, First-principles study of Ag-based p-type doping difficulty in ZnO, *Opt. Mater. (Amst)*. 30 (2008) 817–821. doi:10.1016/j.optmat.2007.02.051.
- [177] A.N. Gruzintsev, V.T. Volkov, E.E. Yakimov, Photoelectric properties of ZnO films doped with Cu and Ag acceptor impurities, *Semiconductors*. 37 (2003) 259–262. doi:10.1134/1.1561514.
- [178] D. et al. Evanoff, Size-Controlled Synthesis of Nanoparticles. 2. Measurement of Extinction, Scattering, and Absorption Cross Sections, *J. Phys. Chem. B*. 108 (2004) 13957–13962. doi:10.1021/jp0475640.
- [179] M.A. Myers, M.T. Myers, M.J. General, J.H. Lee, L. Shao, H. Wang, P-type ZnO thin films achieved by N<sup>+</sup> ion implantation through dynamic annealing process, *Appl. Phys. Lett.* 101 (2012) 112101. doi:10.1063/1.4751467.
- [180] Y.W. Heo, M.P. Ivill, K. Ip, D.P. Norton, S.J. Pearton, J.G. Kelly, R. Rairigh, A.F. Hebard, T. Steiner, Effects of high-dose Mn implantation into ZnO grown on sapphire, *Appl. Phys. Lett.* 84 (2004) 2292–2294. doi:10.1063/1.1690111.
- [181] J.S. Williams, Ion implantation of semiconductors, *Mater. Sci. Eng. A Struct. Mater. Prop. Microstruct. Process.* A253 (1998) 8–15. doi:10.1049/ep.1976.0363.
- [182] T. Diaz De La Rubia, G.H. Gilmer, Structural transformations and defect production in ion implanted silicon: A molecular dynamics simulation study, *Phys. Rev. Lett.* 74 (1995) 2507–2510. doi:10.1103/Phys. Rev. Lett.74.2507.
- [183] S. Venkataraj, N. Ohashi, I. Sakaguchi, Y. Adachi, T. Ohgaki, H. Ryoken, H. Haneda, Structural and magnetic properties of Mn-ion implanted ZnO films, *J. Appl. Phys.* 102 (2007) 14905. doi:10.1063/1.2752123.
- [184] L.R. Doolittle, Algorithms for the rapid simulation of Rutherford backscattering spectra, *Nucl. Instruments Methods Phys. Res. Sect. B Beam Interact. with Mater. Atoms*. 9 (1985) 344–351. doi:10.1016/0168-583X(85)90762-1.
- [185] M. Chen, Z.L. Pei, C. Sun, L.S. Wen, X. Wang, Surface characterization of transparent conductive oxide Al-doped ZnO films, *J. Cryst. Growth*. 220 (2000) 254–262. doi:10.1016/S0022-0248(00)00834-4.
- [186] W. Lin, R. Ma, W. Shao, B. Liu, Structural, electrical and optical properties of Gd doped and undoped ZnO:Al (ZAO) thin films prepared by RF magnetron

- sputtering, *Appl. Surf. Sci.* 253 (2007) 5179–5183. doi:10.1016/j.apsusc.2006.11.032.
- [187] C.-C. Lin, H.-P. Chen, S.-Y. Chen, Synthesis and optoelectronic properties of arrayed p-type ZnO nanorods grown on ZnO film/Si wafer in aqueous solutions, *Chem. Phys. Lett.* 404 (2005) 30–34. doi:10.1016/j.cplett.2005.01.047.
- [188] H.Q. Bian, S.Y. Ma, F.M. Li, H.B. Zhu, Influence of ZnO buffer layer on microstructure and Raman scattering of ZnO:Ag film on Si substrate, *Superlattices Microstruct.* 58 (2013) 171–177. doi:10.1016/j.spmi.2013.03.017.
- [189] V.V. Siva Kumar, D. Kanjilal, Growth of p-type Ag-doped ZnO by rf sputter deposition, *J. Chinese Adv. Mater. Soc.* 2 (2014) 199–206. doi:10.1080/22243682.2014.937741.
- [190] M.A. Myers, J.H. Lee, Z. Bi, H. Wang, High quality p-type Ag-doped ZnO thin films achieved under elevated growth temperatures, *J. Phys. Condens. Matter.* 24 (2012) 145802. doi:10.1088/0953-8984/24/14/145802.
- [191] J.C. Fan, K.M. Sreekanth, Z. Xie, S.L. Chang, K.V. Rao, p-Type ZnO materials: Theory, growth, properties and devices, *Prog. Mater. Sci.* 58 (2013) 874–985. doi:10.1016/j.pmatsci.2013.03.002.
- [192] L.R. Doolittle, Algorithms for the rapid simulation of Rutherford backscattering spectra, *Nucl. Inst. Methods Phys. Res. B.* 9 (1985) 344–351. doi:10.1016/0168-583X(85)90762-1.
- [193] P.D. Townsend, Optical effects of ion implantation, *Reports Prog. Phys.* 50 (1987) 501–558. doi:10.1088/0034-4885/50/5/001.
- [194] J.F. Ziegler, J.P. Biersack, *Treatise on Heavy-Ion Science: Volume 6: Astrophysics, Chemistry, and Condensed Matter*, in: *Treatise Heavy-Ion Sci.*, Springer US, Boston, MA, 1985: pp. 93–129. doi:10.1007/978-1-4615-8103-1\_3.
- [195] B. D. Cullity, *Elements Of X Ray Diffraction* : Cullity, B. D : Free Download & Streaming : Internet Archive, 2001. <https://archive.org/details/elementsofxraydi030864mbp> (accessed March 6, 2017).
- [196] J. Tauc, Optical properties and electronic structure of amorphous Ge and Si, *Mater. Res. Bull.* 3 (1968) 37–46. doi:10.1016/0025-5408(68)90023-8.
- [197] A.Y. Azarov, A. Hallén, X.L. Du, P. Rauwel, A.Y. Kuznetsov, B.G. Svensson,



- Effect of implanted species on thermal evolution of ion-induced defects in ZnO, *J. Appl. Phys.* 115 (2014). doi:10.1063/1.4866055.
- [198] L. Hanley, S.B. Sinnott, The growth and modification of materials via ion – surface processing, *Surf. Sci.* 500 (2002) 500–522.
- [199] H. Morkoç, U. Özgür, Zinc oxide : fundamentals, materials and device technology, Wiley-VCH, 2009.
- [200] M. Chen, Z.L. Pei, X. Wang, C. Sun, L.S. Wen, Structural, electrical, and optical properties of transparent conductive oxide ZnO:Al films prepared by dc magnetron reactive sputtering, *J. Vac. Sci. Technol. A Vacuum, Surfaces, Film.* 19 (2001) 963–970. doi:10.1116/1.1368836.
- [201] L. Irimpan, V.P.N. Nampoori, P. Radhakrishnan, Spectral and nonlinear optical characteristics of nanocomposites of ZnO–Ag, *Chem. Phys. Lett.* 455 (2008) 265–269. doi:10.1016/j.cplett.2008.02.097.
- [202] Yuanhui Zheng, Lirong Zheng, Yingying Zhan, Xingyi Lin, \* and Qi Zheng, K. Wei, Ag/ZnO Heterostructure Nanocrystals: Synthesis, Characterization, and Photocatalysis, (2007). doi:10.1021/IC700688F.
- [203] R. Saravanan, E. Thirumal, V.K. Gupta, V. Narayanan, A. Stephen, The photocatalytic activity of ZnO prepared by simple thermal decomposition method at various temperatures, *J. Mol. Liq.* 177 (2013) 394–401. doi:10.1016/j.molliq.2012.10.018.
- [204] K. Schwartz, A.E. Volkov, M. V. Sorokin, C. Trautmann, K.-O. Voss, R. Neumann, M. Lang, Effect of electronic energy loss and irradiation temperature on color-center creation in LiF and NaCl crystals irradiated with swift heavy ions, *Phys. Rev. B.* 78 (2008) 24120. doi:10.1103/PhysRevB.78.024120.
- [205] S. Zhao, Y. Zhou, K. Zhao, Z. Liu, P. Han, S. Wang, W. Xiang, Z. Chen, H. Lü, B. Cheng, G. Yang, Violet luminescence emitted from Ag-nanocluster doped ZnO thin films grown on fused quartz substrates by pulsed laser deposition, *Phys. B Condens. Matter.* 373 (2006) 154–156. doi:10.1016/j.physb.2005.11.116.
- [206] H.S. Kang, B. Du Ahn, J.H. Kim, G.H. Kim, S.H. Lim, H.W. Chang, S.Y. Lee, Structural, electrical, and optical properties of p-type ZnO thin films with Ag dopant, *Appl. Phys. Lett.* 88 (2006) 202108. doi:10.1063/1.2203952.

- [207] A. Benyagoub, Mechanism of the monoclinic-to-tetragonal phase transition induced in zirconia and hafnia by swift heavy ions, *Phys. Rev. B.* 72 (2005) 94114. doi:10.1103/PhysRevB.72.094114.
- [208] R.G. Singh, F. Singh, I. Sulania, D. Kanjilal, K. Sehwat, V. Agarwal, R.M. Mehra, Electronic excitations induced modifications of structural and optical properties of ZnO–porous silicon nanocomposites, *Nucl. Instruments Methods Phys. Res. Sect. B Beam Interact. with Mater. Atoms.* 267 (2009) 2399–2402. doi:10.1016/j.nimb.2009.04.005.
- [209] M.S. Kamboj, G. Kaur, R. Thangaraj, D.K. Avasthi, Effect of heavy ion irradiation on the electrical and optical properties of amorphous chalcogenide thin films, *J. Phys. D. Appl. Phys.* 35 (2002) 477–479. doi:10.1088/0022-3727/35/5/310.
- [210] N. Itoh, A.M. Stoneham, Materials modification by electronic excitation, *Radiat. Eff. Defects Solids.* 155 (2001) 277–290. doi:10.1080/10420150108214126.
- [211] B. Du Ahn, S. Hoon Oh, C. Hee Lee, G. Hee Kim, H. Jae Kim, S. Yeol Lee, Influence of thermal annealing ambient on Ga-doped ZnO thin films, *J. Cryst. Growth.* 309 (2007) 128–133. doi:10.1016/j.jcrysgro.2007.09.014.
- [212] Y.K. Mishra, V.S.K. Chakravadhanula, V. Hrkac, S. Jebril, D.C. Agarwal, S. Mohapatra, D.K. Avasthi, L. Kienle, R. Adelung, Crystal growth behaviour in Au-ZnO nanocomposite under different annealing environments and photoswitchability, *J. Appl. Phys.* 112 (2012) 64308. doi:10.1063/1.4752469.
- [213] M. Mayer, SIMNRA User's Guide, Max-Planck-Institut Für Plasmaphys. 9 (1997) 67.
- [214] G.J. Fang, D.J. Li, B.L. Yao, Effect of vacuum annealing on the properties of transparent conductive AZO thin films prepared by DC magnetron sputtering, *Phys. Status Solidi Appl. Res.* 193 (2002) 139–152. doi:10.1002/1521-396X(200209)193:1<139::AID-PSSA139>3.0.CO;2-D.
- [215] M. Chen, Z.L. Pei, C. Sun, L.S. Wen, X. Wang, Surface characterization of transparent conductive oxide Al-doped ZnO films, *J. Cryst. Growth.* 220 (2000) 254–262. doi:10.1016/S0022-0248(00)00834-4.
- [216] D.C. Agarwal, A. Kumar, S.A. Khan, D. Kabiraj, F. Singh, A. Tripathi, J.C. Pivin, R.S. Chauhan, SHI induced modification of ZnO thin film: Optical and structural

- studies, Nucl. Instruments Methods Phys. Res. Sect. B Beam Interact. with Mater. Atoms. 244 (2006) 136–140. doi:10.1016/j.nimb.2005.11.077.
- [217] D.K. Avasthi, Y.K. Mishra, F. Singh, J.P. Stoquert, Ion tracks in silica for engineering the embedded nanoparticles, Nucl. Instruments Methods Phys. Res. Sect. B Beam Interact. with Mater. Atoms. 268 (2010) 3027–3034. doi:10.1016/j.nimb.2010.05.033.
- [218] F. Singh, P.K. Kulriya, J.C. Pivin, Origin of swift heavy ion induced stress in textured ZnO thin films: An in situ X-ray diffraction study, 2010. doi:10.1016/j.ssc.2010.07.026.
- [219] X.Q. Wei, B.Y. Man, M. Liu, C.S. Xue, H.Z. Zhuang, C. Yang, Blue luminescent centers and microstructural evaluation by XPS and Raman in ZnO thin films annealed in vacuum, N<sub>2</sub> and O<sub>2</sub>, Phys. B Condens. Matter. 388 (2007) 145–152. doi:10.1016/j.physb.2006.05.346.
- [220] L.V. Trandafilović, D.K. Božanić, S. Dimitrijević-Branković, A.S. Luyt, V. Djoković, Fabrication and antibacterial properties of ZnO–alginate nanocomposites, Carbohydr. Polym. 88 (2012) 263–269. doi:10.1016/j.carbpol.2011.12.005.
- [221] D. Lin, H. Wu, R. Zhang, W. Pan, Enhanced Photocatalysis of Electrospun Ag–ZnO Heterostructured Nanofibers, Chem. Mater. 21 (2009) 3479–3484. doi:10.1021/cm900225p.
- [222] Yuanhui Zheng, Lirong Zheng, Yingying Zhan, Xingyi Lin, \* and Qi Zheng, K. Wei, Ag/ZnO Heterostructure Nanocrystals: Synthesis, Characterization, and Photocatalysis, (2007). doi:10.1021/IC700688F.
- [223] N. Fujimura, T. Nishihara, S. Goto, J. Xu, T. Ito, Control of preferred orientation for ZnOx films: control of self-texture, J. Cryst. Growth. 130 (1993) 269–279. doi:10.1016/0022-0248(93)90861-P.
- [224] L. García-Gancedo, J. Pedrós, Z. Zhu, A.J. Flewitt, W.I. Milne, J.K. Luo, C.J.B. Ford, Room-temperature remote-plasma sputtering of c-axis oriented zinc oxide thin films, J. Appl. Phys. 112 (2012) 14907. doi:10.1063/1.4736541.
- [225] A.L. Patterson, The scherrer formula for X-ray particle size determination, Phys. Rev. 56 (1939) 978–982. doi:10.1103/PhysRev.56.978.

- [226] V. Bilgin, S. Kose, F. Atay, I. Akyuz, The effect of substrate temperature on the structural and some physical properties of ultrasonically sprayed CdS films, *Mater. Chem. Phys.* 94 (2005) 103–108. doi:10.1016/j.matchemphys.2005.04.028.
- [227] S.W. Xue, X.T. Zu, W.L. Zhou, H.X. Deng, X. Xiang, L. Zhang, H. Deng, Effects of post-thermal annealing on the optical constants of ZnO thin film, *J. Alloys Compd.* 448 (2008) 21–26. doi:10.1016/j.jallcom.2006.10.076.
- [228] X.W. Sun, H.S. Kwok, Optical properties of epitaxially grown zinc oxide films on sapphire by pulsed laser deposition, *J. Appl. Phys.* 86 (1999). doi:10.1063/1.370744.
- [229] J.F. Scott, Uv resonant Raman scattering in ZnO, *Phys. Rev. B.* 2 (1970) 1209–1211. doi:10.1103/PhysRevB.2.1209.
- [230] C. Bundesmann, N. Ashkenov, M. Schubert, D. Spemann, T. Butz, E.M. Kaidashev, M. Lorenz, M. Grundmann, Raman scattering in ZnO thin films doped with Fe, Sb, Al, Ga, and Li, *Appl. Phys. Lett.* 83 (2003) 1974–1976. doi:10.1063/1.1609251.

# **Appendix-A**

## **List of publications**



## **Research Publications:**

### **(i) Paper in refereed journals:**

1. “Swift heavy ion induced optical and structural modifications in RF sputtered nanocrystalline ZnO thin film” **S.K. Singh**, R. Singhal, R. Vishnoi, V.V. Siva Kumar and P.K. Kulriya, **Indian Journal of physics**, **91 (2017) 547-554**.
2. “Synthesis and annealing study of RF sputtered ZnO thin film” **S.K Singh**, H. Sharma, R. Singhal, V.V. Siva Kumar and D.K. Avasthi, **AIP Conference Proceeding**, **1731 (2016) 080063**.
3. “Ag-ZnO Nanocomposite Thin Film by RF-Sputtering: An Electrical and Structural Study” **S.K. Singh**, R. Singhal, **Macromolecular symposia** **376 (2017) 1600197**.
4. “Structural and Optical Investigations of 120 keV Ag Ion Implanted ZnO Thin Films” **S.K. Singh**, R. Singhal, **Thin Solid Films** **accepted (Article in press)**.
5. “Study on swift heavy ions induced modifications of Ag-ZnO nanocomposite thin film” **S.K. Singh**, R. Singhal, V.V. Siva Kumar, **Superlattices and microstructures** **103 (2017) 195-204**.
6. “Thermal-induced SPR tuning of Ag-ZnO nanocomposite thin film for plasmonic application” **S.K Singh**, R. Singhal, **Applied surface sciences** **439 (2018) 919-926**.

### **(ii) Paper not included in thesis:**

1. “Thermal annealing and SHI irradiation induced modifications in sandwiched structured Carbon-gold-Carbon (a-C/Au/a-C) nanocomposite thin film” **S.K. Singh**, R. Singhal, **Nuclear Instruments and Methods in Physics Research B** **407 (2017) 118-124**.
2. “Thermal induced structural and optical investigations of Ag-ZnO nanocomposite thin films” **S.K. Singh**, R. Singhal, **Superlattices and microstructures (minor revision received)**.
3. “Study the Effect of Substrate on Thermally Evaporated PbS Thin Film” Sat Kumar, **S.K Singh**, Rakesh Kumar and Beer Pal Singh, **Journal of Materials Science & Surface Engineering** **5 (2017) 500-503**.





# **Appendix-B**

## **Research articles**

# Swift heavy ion induced optical and structural modifications in RF sputtered nanocrystalline ZnO thin film

S K Singh<sup>1</sup>, R Singhal<sup>1\*</sup>, R Vishnoi<sup>1</sup>, V V S Kumar<sup>2</sup> and P K Kulariya<sup>2</sup>

<sup>1</sup>Department of Physics, Malaviya National Institute of Technology Jaipur, JLN Marg, Malaviya Nagar, Jaipur 302017, India

<sup>2</sup>Inter University Accelerator Centre, Aruna Asaf Ali Marg, New Delhi 110067, India

Received: 01 November 2016 / Accepted: 23 December 2016

**Abstract:** In the present study, 100 MeV Ag<sup>7+</sup> ion beam-induced structural and optical modifications of nanocrystalline ZnO thin films are investigated. The nanocrystalline ZnO thin films are grown using radio frequency magnetron sputtering and irradiated at fluences of  $3 \times 10^{12}$ ,  $1 \times 10^{13}$  and  $3 \times 10^{13}$  ions/cm<sup>2</sup>. The incident swift heavy ions induced change in the crystallinity together with the preferential growth of crystallite size along the *c* axis (002) orientation. The average crystallite size is found to be increased from  $10.8 \pm 0.7$  to  $20.5 \pm 0.3$  nm with increasing the ion fluence. The Atomic force microscopy analysis confirms the variation in the surface roughness by varying the incident ion fluences. The UV–visible spectroscopy shows the decrement in transmittance of the film with ion irradiation. The micro-Raman spectra of ZnO thin films are investigated to observe ion-induced modifications which support the increased lattice defects with higher fluence. The variation in crystallinity indicates that ZnO-based devices can be used in piezoelectric transduction mechanism.

**Keywords:** ZnO thin film; Swift heavy ions; Atomic force microscopy; X-ray diffraction

**PACS Nos.:** 77.55.hf; 96.50.Vg; 68.37.Ps

## 1. Introduction

The oxide semiconductors possess various physical properties such as transparency, conductivity, and piezoelectricity which makes them of great scientific interest for optoelectronic and piezoelectric device applications. Among all, ZnO (*n*-type) semiconductor is a very promising material of II–VI group due to its wide band gap  $\sim 3.35$  eV and large exciton binding energy of 60 meV [1, 2]. The larger band gap of ZnO in comparison to Si and Ge makes it more favourable to use at high temperature in electronic devices. The physical properties of ZnO are widely influenced by deposition conditions and parameters. To analyze the effects of deposition on film properties, many techniques such as sol–gel method, spray pyrolysis, metal organic chemical vapour deposition, pulse laser deposition and RF/DC sputtering have been used and

reported by many groups [3–7]. Due to its functionalize properties, ZnO is used in solar cells, transparent conductive contacts, gas sensors, thin film transistors and laser diodes [8–13]. The variability of piezoelectric properties of ZnO, make it useful also for short-wavelength light emitting diodes, optical waveguides, laser deflectors and surface acoustic wave (SAW) band-pass filters [14–16].

Nowadays, researchers are trying to improve the properties of different materials using swift heavy ion (SHI) irradiation. Ion irradiation is a precise technique to modify optical, structural and electrical properties of materials in the nanometer region due to its spatial selectivity [17–28]. Ion beam technique is more advantageous in comparison to other methods because of good control of incident ion energy and fluence. As the swift heavy ions (SHI) traverse through the target material, it interacts with material by losing their energy in two different way; (a) direct transfer of energy to target atoms by elastic collisions, termed as nuclear energy loss ( $S_n$ ) and (b) transfer of energy of incoming ions to the electrons of target atoms, termed as electronic energy loss ( $S_e$ ). This energy transfer leads to the

\*Corresponding author, E-mail: rahuliuc@gmail.com; rsinghal.phy@mnit.ac.in

atomic displacement in a cylindrical zone around the incident ion path of material which is explained by two established models; Coulomb spike model (CSM) and Thermal spike model (TSM). According to the CSM, a passage of high energy ions through a material produces ionized cylindrical zone for the time duration of  $\sim 10^{-17}$  s. This cylindrical zone contains higher charge region which leads to electrostatic repulsion between incident ions and target atoms and responsible for coherent radial atomic movements under Coulomb force. On the other hand, in Thermal spike model, the incident ion transfers its energy to the electronic subsystem via electron–phonon coupling (EPC) which leads to the rapidly rise in the lattice temperature of the materials above its melting point. Due to the energy dissipation by the thermal conduction, rapid quenching process takes place. This process is responsible for the modifications in the cylindrical zone around the ion path [29, 30]. Schematic diagram for ion–matter interaction is shown in Fig. 1.

The high energy ion beam has been proved very efficient tool to alter the properties of ZnO thin films. The energetic ions loss their energy after interaction with ZnO thin film and transfer excess amount of energy, which creates the density of defects, stress, and strain in the structure of ZnO. The formation of self-affine nanostructure over the surface of ZnO thin films using SHI has been investigated by Agarwal et al. [31]. They reported that the shape and density of these nanostructures depend on incident ion fluence. The effect of 120 MeV Au ion beam on ZnO thin films prepared by the sol–gel method has been investigated by Singh et al. [32] and it was observed that SHI irradiation induced disorder and high density of lattice defects causes to evolution of  $A_1$  (LO) mode. The energetic ions can also be used for better understanding of phonon modes in nanostructures. The structural and spectroscopic modifications of nanocrystalline ZnO thin films using 120 MeV

Au ion beam have been analysed by Rehman et al. [33]. They found that nanocrystals become more oriented at low fluences however at higher fluences, the release of strain and decrease in grain size was observed. These modifications could be used in radiation harsh environment for optoelectronic applications.

In present work, the structural, optical, and morphological modifications in ZnO thin film induced by 100 MeV  $\text{Ag}^{7+}$  ions have been investigated. The modifications have been analyzed using different characterization techniques such as X-ray diffraction (XRD), UV–visible spectroscopy, Atomic force microscopy (AFM), Raman spectroscopy and Scanning electron microscopy (SEM). All the modifications induced by energetic ions may be favourable in device fabrication.

## 2. Experimental details

The sputtering target of pure ZnO was prepared with ZnO powder (99.99%, Alfa-Aesar) by using a hydraulic press machine (HYCON Hydraulic engineers and consultants, New Delhi) with pressure approximately  $\sim 7$  ton. The prepared target was sintered for 24 h at the temperature 1200 °C by sequential steps in a programmable furnace with a continuous flow of oxygen gas. Thin films of ZnO were deposited on glass and silicon substrates at room temperature by radio-frequency (RF) magnetron sputtering, using ZnO target of 2-inch diameter and 3 mm thickness in the presence of Ar environment (grade-I with flow rate  $\sim 4$  sccm). A base pressure of  $\sim 10^{-6}$  mbar was achieved by using a turbo-molecular pump before deposition. The sputtering was carried out at a pressure of  $\sim 5 \times 10^{-2}$  mbar with a target to substrate distance of 40 mm. The deposition was performed for 15 min at fixed RF power 150 watts, and self-bias voltage 250–280 V. For the film deposition, substrates were cleaned in an ultrasonic bath with a mixture of de-ionized water and trichloroethylene (TCE) and then washed with boiled acetone. After deposition, ZnO thin films were irradiated with 100 MeV Ag ions (charge state +7) using the 15UD Pelletron accelerator facility at the Inter-University Accelerator Centre (IUAC), New Delhi in Materials Science beam line. The vacuum in a chamber during the irradiation was  $\sim 6 \times 10^{-7}$  mbar. The electronic ( $S_e$ ) and nuclear ( $S_n$ ) energy losses for 100 MeV Ag ions in ZnO thin film were  $\sim 20.39$  keV/nm and  $\sim 0.122$  keV/nm, respectively and the range of Ag ions in ZnO film was  $\sim 12.15$   $\mu\text{m}$  as calculated by Stopping and Range of Ions in Matter (SRIM) simulation programme. The ion beam was scanned over an area of  $1 \times 1$   $\text{cm}^2$  with fluence  $3 \times 10^{12}$ ,  $1 \times 10^{13}$  and  $3 \times 10^{13}$  ions/ $\text{cm}^2$  and the beam current was kept constant at 1 pA (particle nanoampere).

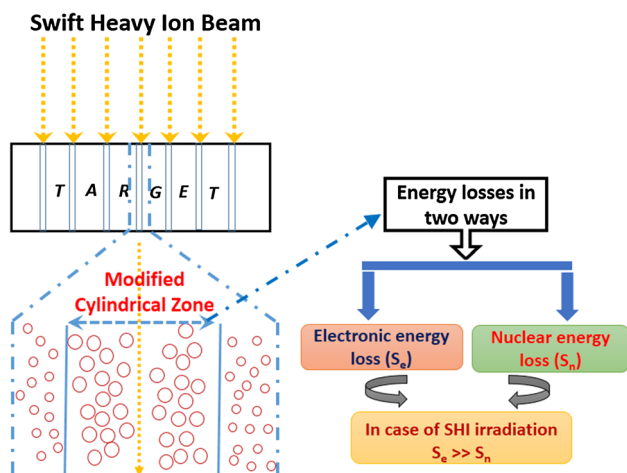


Fig. 1 Schematics diagram for ion–matter interaction

The phase formation and crystal structure of the films before as well as after irradiation were studied by Bruker X-ray diffractometer with  $\text{CuK}_\alpha$  ( $\lambda = 1.54 \text{ \AA}$ ) monochromatic radiation source. The UV–visible transmission spectra of pristine and irradiated thin films were measured by the dual beam U-3300 Hitachi Spectrometer at Inter-University Accelerator Centre (IUAC), New Delhi. The surface topography was observed by atomic force microscopy (Bruker) and scanning electron microscopy (Nova Nano FE-SEM 450 FEI). Micro-Raman spectra of pristine and irradiated ZnO thin films were obtained by using Renishaw inVia micro-Raman microscope with Ar ion laser excitation wavelength at 514.5 nm with 10 mW power.

### 3. Results and discussion

#### 3.1. XRD measurements

The structural behaviour of ZnO thin films is investigated using X-ray diffraction (XRD) pattern. Fig. 2 shows the XRD pattern for pristine, and 100 MeV  $\text{Ag}^{7+}$  ions irradiated films at the different ion fluence  $3 \times 10^{12}$ ,  $1 \times 10^{13}$ , and  $3 \times 10^{13}$  ions/cm<sup>2</sup>. The XRD pattern of pristine film confirm the presence of crystalline hexagonal wurtzite structure with reflection from (100), (002), and (101) planes at  $\sim 31.7^\circ$ ,  $34.4^\circ$ , and  $36.2^\circ$  respectively (JCPDS Card No. 89-1397). After the irradiation, the intensity of the reflections corresponding to (100) and (101) planes is observed to be decreased when the incident fluences increased. Whereas, at the highest fluence ( $3 \times 10^{13}$  ions/cm<sup>2</sup>) the intensity corresponding to (002) plane is found to be increased drastically with increased fluences which is indicating the growth of the grain along the c-axis. On the other hand, the peaks

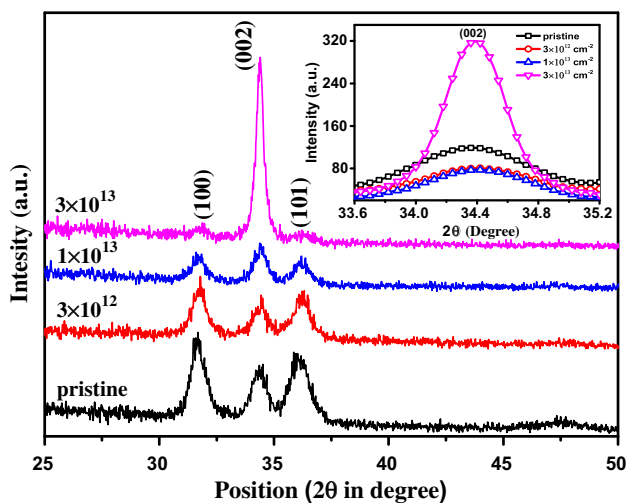


**Fig. 2** XRD spectra of the pristine and irradiated ZnO thin films with different fluences. *Inset* shows the zoomed behaviour of (002) plane with ion irradiation

associated with (100) and (101) planes are almost vanished at this highest fluence (shown in Fig. 2). The increased intensity is indicating the improved crystallinity of ZnO films. It is observed that at the higher fluences, film releases strain, which is responsible for growth in *c*-axis orientation because (002) plane of ZnO is having the lowest surface energy according to basic crystal growth theory [34, 35]. The strain can be estimated by using the following relation [36]:

$$\varepsilon = \frac{\beta \cos \theta}{4 \sin \theta} \quad (1)$$

where,  $\beta$  is full width at half maximum (FWHM) in radian and  $\theta$  is the angle of diffraction. The size of ZnO crystallite is calculated using the following Debye–Scherrer’s formula [37]:

$$D = \frac{0.9\lambda}{\beta \cos \theta} \quad (2)$$

In Eq. (2),  $\lambda$ ,  $\beta$ , and  $\theta$  are X-ray wavelength ( $\text{CuK}_\alpha = 1.54 \text{ \AA}$ ), FWHM and the Bragg diffraction angle, respectively. The calculated average crystallite size (Fig. 3) of the pristine ZnO film is  $10.8 \pm 0.7$  nm which is increased up to  $20.5 \pm 0.3$  nm with increasing the ion fluences and summarized in Table 1. During swift heavy ion irradiation, the thermal spike model is the dominant mechanism for all the structural modifications according to which incident ions transfer a large amount of energy into the target material due to electronic energy loss ( $S_e$ ). This large amount of energy creates the very high-temperature zones in the target material, which is responsible for the structural modifications. In this process, film releases the strain at higher fluence leads to the crystalline behaviour of the film [38]. The increased crystallinity along the preferred *c*-axis orientation of ZnO thin film could be suitable for piezoelectric transduction mechanism [39].

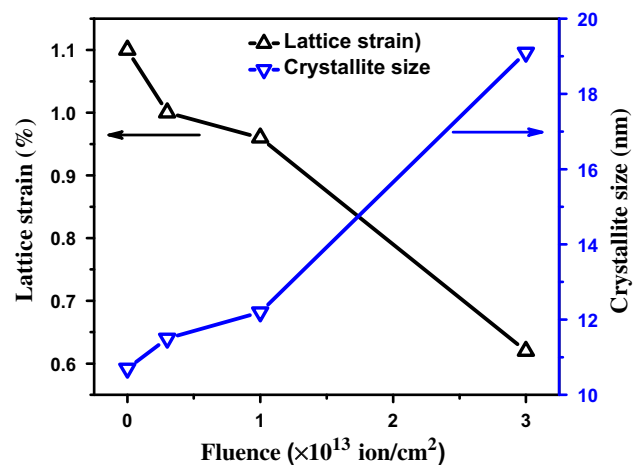


**Fig. 3** Variation of the lattice strain and crystallite size with different ion fluences

**Table 1** Variation of crystallite size with different ion irradiation fluences

Fluences (ions/cm <sup>2</sup> ) 100 MeV Ag ions	Crystallite size (in nm) with error
Pristine	10.8 ± 0.7
3 × 10 <sup>12</sup>	12.6 ± 0.9
1 × 10 <sup>13</sup>	12.7 ± 0.6
3 × 10 <sup>13</sup>	20.5 ± 0.3

### 3.2. UV–visible spectroscopy

Optical properties of pristine and irradiated ZnO thin films are analysed by UV–visible spectroscopy. The transmission spectra in the visible region of the electromagnetic spectrum of ZnO thin films are shown in Fig. 4. It is observed from spectra that there is a significant change in transmittance of ZnO thin films with increasing ion fluences. The transmittance of the pristine and irradiated film at higher fluence 3 × 10<sup>13</sup> ions/cm<sup>2</sup> are found to be ~90 and 80% respectively at 550 nm. The reduction in transmittance of the film at higher fluence is attributed to the increased electron carrier density and defect creation such as oxygen vacancies induced by SHI irradiation in ZnO thin film [40]. ZnO is a direct band gap material, and the band gap of the pristine and irradiated ZnO thin films is determined using Tauc's relation [41] which is expressed as

$$\alpha h\nu = A (h\nu - E_g)^{1/n} \quad (3)$$

In Eq. (3),  $\alpha$  is the absorption coefficient,  $h\nu$  is the incident photon energy,  $E_g$  is the optical band gap, and  $A$  is constant. The index value “ $n$ ” depends on the transition whether it is direct or indirect and allowed or forbidden. For the direct band gap, the value of  $n = 2$ . The band gap

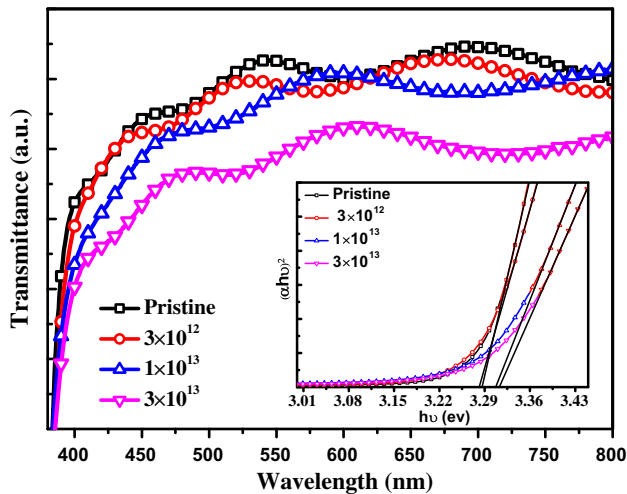


**Fig. 4** UV–visible transmission spectra for pristine and 100 MeV Ag ion irradiated films of ZnO. Band gap variation of pristine and irradiated film calculated by Tauc plot (*inset*)

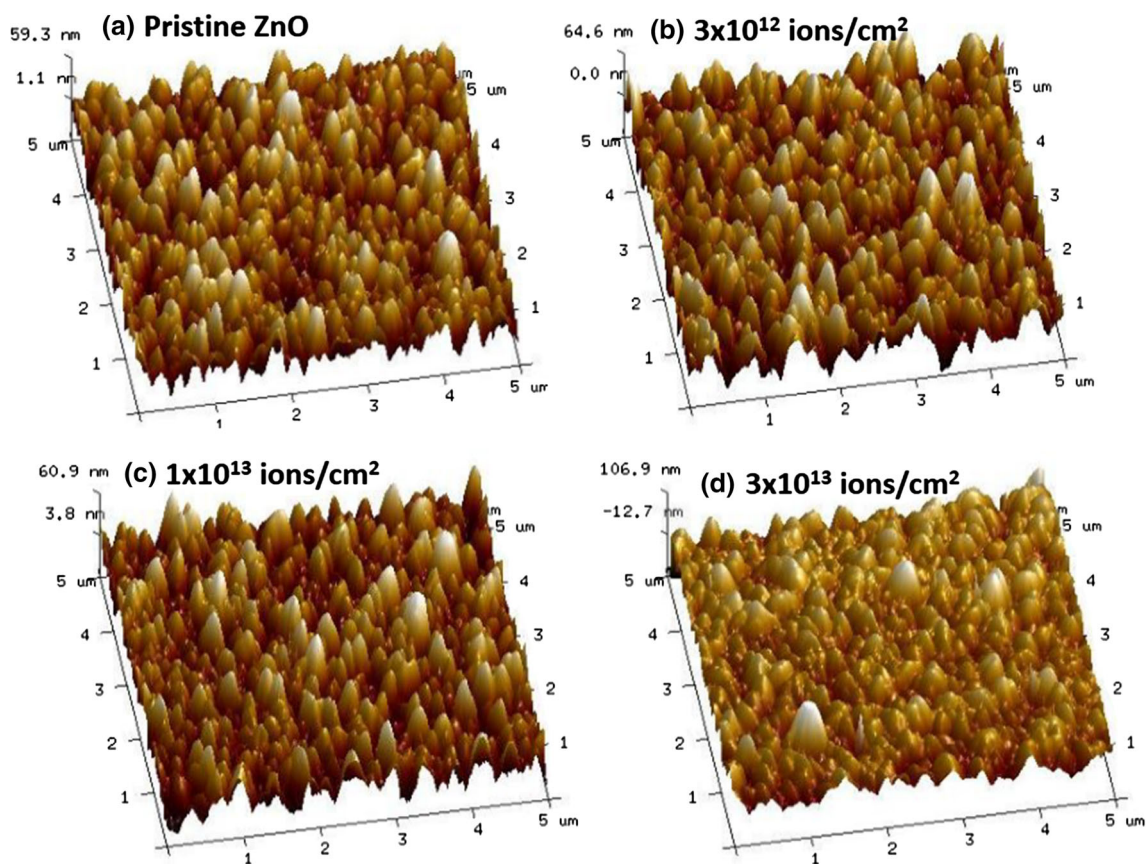
value is calculated by extrapolating the linear part of the spectra of  $(\alpha h\nu)^2$  versus  $h\nu$  plot (*inset*). It is observed that the band gap of the ZnO films is slightly increased (from 3.28 to 3.30 eV) with ion irradiation. The variation in band gap can be explained by Burstein–Moss effect (B–M effect) which depends on electron carrier concentration in the material which affected by SHI irradiation [42].

### 3.3. Atomic force microscopy

The surface morphology of pristine and irradiated ZnO thin films is observed by AFM in tapping mode. Fig. 5 shows the three-dimensional ( $5 \times 5 \mu\text{m}^2$ ) micrographs of pristine and 100 MeV Ag<sup>7+</sup> irradiated ZnO thin films. It is clear from the images that ZnO grains are connected to each other and films are grown uniformly on the substrate. Fig. 6 shows the Gaussian distribution of grain size of the pristine and irradiated ZnO thin films at different fluences. The grain size of the thin films is increased with increasing the ion fluence which is associated to the agglomeration of the ZnO grains with ion irradiation. The calculated grain size of the pristine film is around to be  $\sim 198 \pm 6.8$  nm, and it increases up to  $\sim 219 \pm 2.8$  nm at the fluence of 3 × 10<sup>13</sup> ion/cm<sup>2</sup>. The discrimination in the calculated grain size from AFM and XRD is observed because XRD pattern determines the average crystallite size whereas the AFM shows the agglomeration of particles at the surface, which are much bigger than those observed by XRD. The observations of AFM and XRD can be correlated by the fact that smaller particles have a larger surface free energy, therefore, agglomerate faster and develop larger grains and XRD is related to smaller particles whereas AFM gives larger grains [43]. The root-mean-square roughness ( $R_{\text{rms}}$ ) of the pristine and irradiated films is calculated using following relation [32];

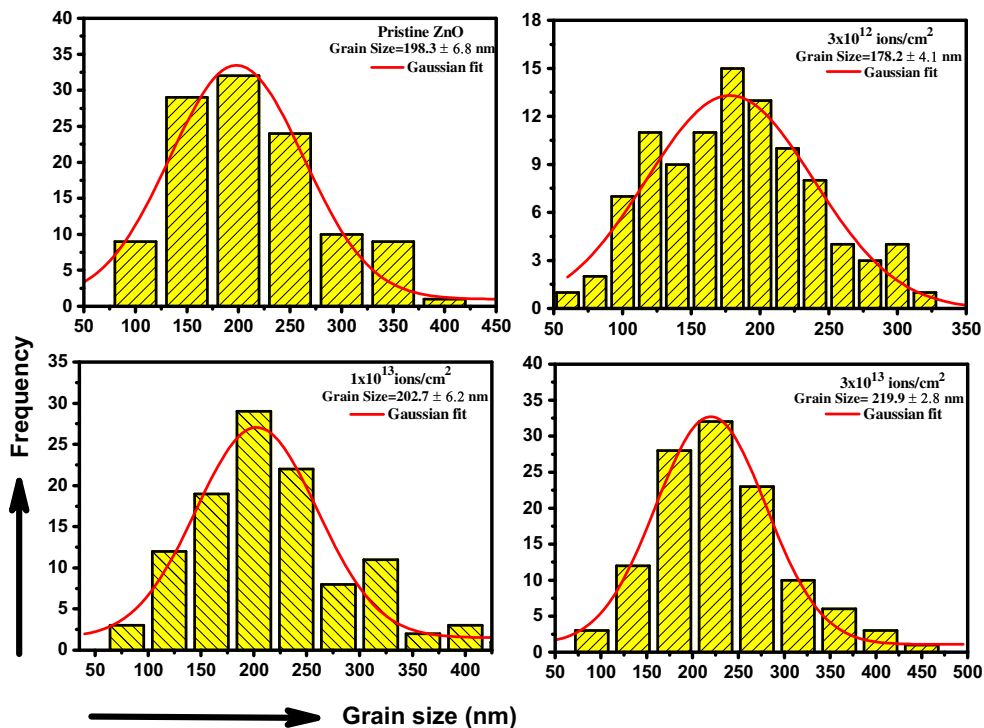
$$R_{\text{rms}} = \left[ \frac{1}{N} \sum_{i=1}^N |Z_i - \bar{Z}|^2 \right]^{1/2} \quad (4)$$

where  $N$  is a number of surface height data, and  $Z$  is the mean height distance. The estimated roughness of the pristine ZnO films is 10.2 nm and varied marginally with incident fluences shown in Fig. 7. The variation in grain size and roughness of the film have been summarized in Table 2. When swift heavy ions pass through the material, transfers a large amount of energy into the material. If the surface energy of the film is greater than acquired energy from incident ions, then it leads to agglomeration of the grains and formed the bigger grains due to surface diffusion process near the top surface of the thin film. With the increase of ion fluences, the surface energy of the film changes due to total energy ( $S_e \times \phi$ ) deposited by incident ions. This surface diffusion process is responsible for the



**Fig. 5** AFM micrographs of (a) Pristine (b)  $3 \times 10^{12}$  ion/cm<sup>2</sup> (c)  $1 \times 10^{13}$  ion/cm<sup>2</sup> and (d)  $3 \times 10^{13}$  ion/cm<sup>2</sup>

**Fig. 6** Variation of grain size with different ion fluences calculated by atomic force microscopy



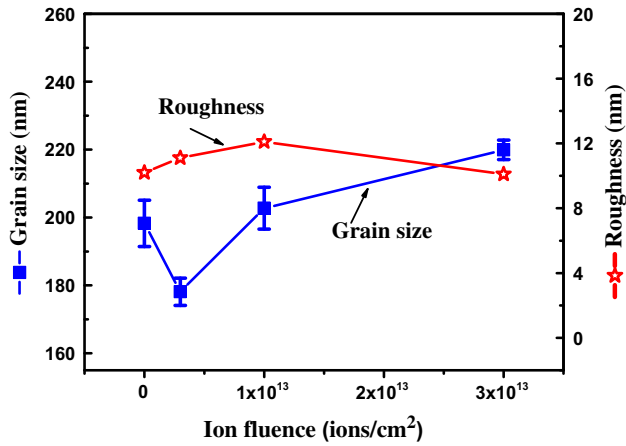


**Fig. 7** Variation of roughness and grain size with different ion irradiation fluences

**Table 2** Grain size and roughness of the film with different fluences

Fluence (ions/cm <sup>2</sup> ) 100 MeV Ag ions	Grain size (nm) with error	Roughness (nm)
Pristine	198.3 ± 6.8	10.2
3 × 10 <sup>12</sup>	178.2 ± 4.1	11.1
1 × 10 <sup>13</sup>	202.7 ± 6.2	12.1
3 × 10 <sup>13</sup>	219.9 ± 2.8	10.1

grain growth and change in shape and size of the grains near surface region [31].

### 3.4. Field emission scanning electron microscopy

Figure 8(a)–(d) shows the FESEM micrographs of the pristine and irradiated films at fluence of  $3 \times 10^{12}$ ,  $1 \times 10^{13}$  and  $3 \times 10^{13}$  ions/cm<sup>2</sup>. The thin film irradiated at higher fluence ( $3 \times 10^{13}$  ions/cm<sup>2</sup>) is showing the agglomeration of the particles over the surface (Fig. 8(d)) which is further supported the AFM study. Agglomeration of ZnO particles in the film increases with increasing the ion fluence, which is attributed to rising the local melting temperature on the surface due to the interaction of high energetic ions. FESEM results are showing larger grains with different size and shape on the top surface of the film. The agglomeration of the particles is also observed in SEM images at the higher fluence which has already mentioned above in AFM analysis.

### 3.5. Micro-Raman spectroscopy

The Raman active phonon modes of the wurtzite structure of ZnO as expected from the group theory are  $A_1 + 2E_2 + E_1$  modes, where all atoms occupy  $C_{3v}$  sites [44, 45]. Typical micro-Raman spectra of the ZnO thin

films irradiated with fluences  $3 \times 10^{12}$ ,  $1 \times 10^{13}$  and  $3 \times 10^{13}$  ions/cm<sup>2</sup> are shown in Fig. 9. The spectra confirm the presence of the peaks at 280, 440 cm<sup>-1</sup>, very sharp peak at 573 cm<sup>-1</sup>, broad peak at 630 and 780 cm<sup>-1</sup> for the pristine as well irradiated ZnO thin films. The weak Raman mode  $B_1$  (high) –  $B_2$  (low) and  $B_1$  (high) +  $B_1$  (low) are recorded at 280 and 780 cm<sup>-1</sup>. The peak at 573 cm<sup>-1</sup> can be assigned to  $A_1$  (LO) mode, which is in good agreement with the theoretical calculations [46]. Small band at 630 cm<sup>-1</sup> is assigned to the  $E_1$  (LO) mode [47]. The  $B_1$  (high) –  $B_2$  (low) and  $B_1$  (high) +  $B_1$  (low) modes are not much affected by SHI irradiation. The intensity of the peak at 573 cm<sup>-1</sup> decreases slowly with the increase the ion fluences, while  $E_2$  (high) mode at 440 cm<sup>-1</sup> decreases at the fluence of  $3 \times 10^{13}$  ions/cm<sup>2</sup>. The characteristic modes of ZnO,  $E_2$  (high) and  $A_1$  (LO) at 440 and 573 cm<sup>-1</sup> respectively are associated to the highly textured and wurtzite structure of the ZnO thin film (inset). The pristine ZnO thin film seems to be oxygen deficient as indicated by the  $A_1$  (LO) mode at 573 cm<sup>-1</sup> with higher intensity. Swift heavy ion induced density of defects and disorder is subjected to loss of the translation symmetry of the lattice of the material, which leads to the invalidations of the  $k = 0$  wave vector selection rule from all part of the Brillouin zone in Raman scattering. Therefore Irradiation-induced  $A_1$  (LO) mode is explained in the term of surface phonon mode which is directly related to intrinsic lattice defects in the material structure. Other Raman modes of the ZnO thin film have been related to the formation of wurtzite structure of the ZnO according to the selection rule [32].

The decrement in the intensity corresponding to (100) and (101) planes with increasing fluence and enhanced  $c$ -axis orientation of ZnO thin films along the (002) plane at the highest fluence are observed. The improvement in crystallinity can be described in light of interaction of ion and materials. The imparted energy from the incident high energy ions to target material is responsible for the electronic ionizations/excitations and lattice vibrations along the ion path. These vibrations and excitations cause to the releases of strain in the film which lowers the surface energy. Therefore, ZnO thin film become oriented along (002) plane as it has lower surface energy and resulted in increased crystallinity after irradiation. Raman spectra confirm the formation of wurtzite structure of ZnO films. In the present study the observed  $A_1$  (LO) mode at 573 cm<sup>-1</sup> is related to the intrinsic lattice defects in the ZnO structure. The decrease in the intensity of  $A_1$  (LO) mode further confirms the increase lattice defects in the ZnO film due to high energetic ions. These ion-induced defects and vacancies play a major role to tune the optical properties of ZnO thin films. The reduction of transmittance at higher fluence attributed to the increased electron carrier density and defect creation such as oxygen vacancies induced by

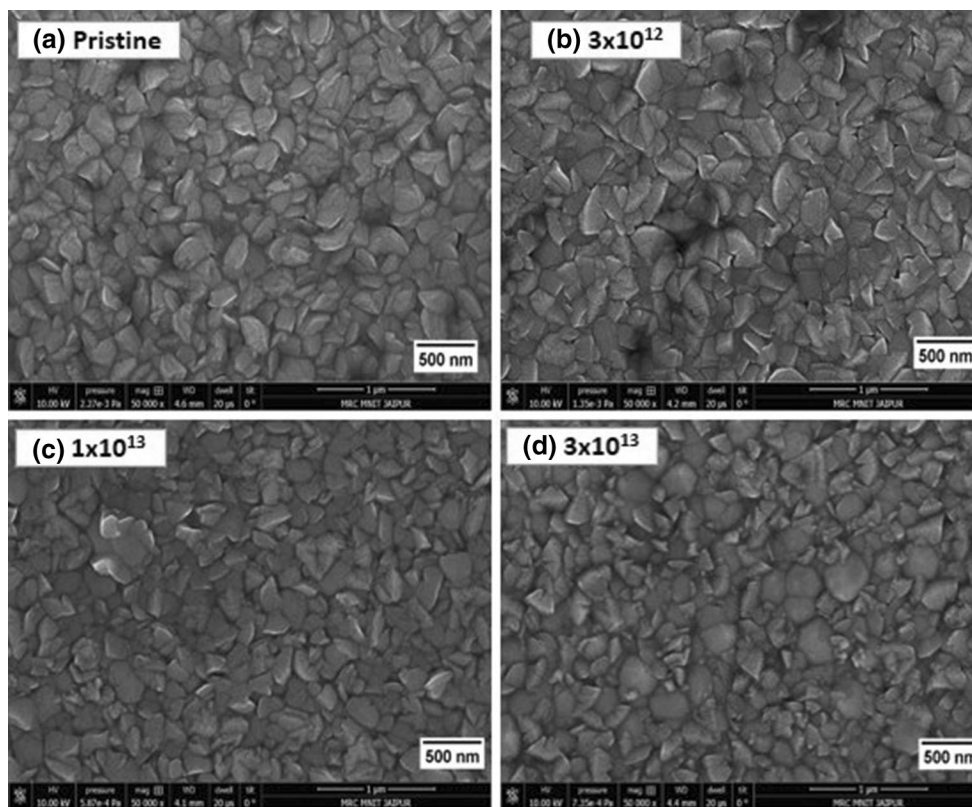


Fig. 8 FESEM micrographs of pristine and 100 MeV Ag ion irradiated film of ZnO at different fluences

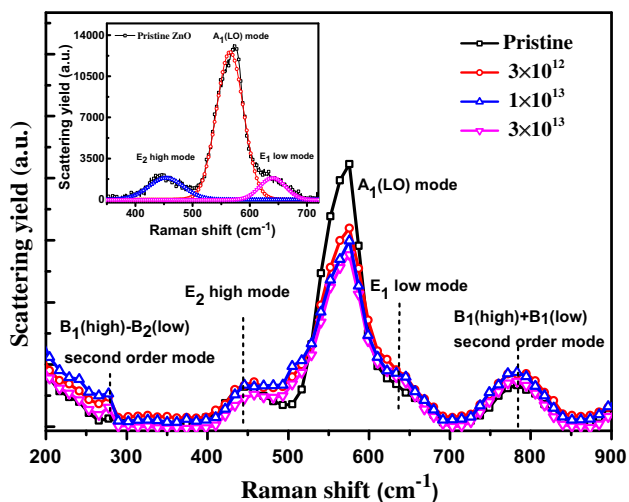


Fig. 9 Raman spectra of pristine and 100 MeV Ag irradiated at different fluences

SHI irradiation in ZnO thin film. The band gap is also slightly increased (from 3.28 to 3.30 eV) with ion irradiation and it might be attributed to electron carrier concentration which can be explained in the term of Burstein-Moss effect (B-M effect). These modifications in the films are subjected to change in surface energy of the films which is also responsible for grain growth and

morphological features of the film with ion irradiation. Therefore such kind of ZnO thin film can be used in radiation harsh environment and optoelectronic applications.

#### 4. Conclusions

In summary, the structural, optical and morphological modifications of ZnO thin films are investigated by using SHI irradiation. The enhancement in the crystallinity along the *c*-axis orientation due to the impact of energetic ions is confirmed by XRD analysis. It is observed that optical properties can be tailored by ion irradiation as transmittance decreases with higher irradiation fluence. This property can be used in transparent window materials. The dependence of surface morphology and grain size on incident ions are further confirmed by AFM and FESEM analysis and observed the increased grain size after irradiation. All the induced modifications are explained in terms of energy loss of ions into the target materials.

**Acknowledgements** One of the authors (Shushant Kumar Singh) is thankful to the Technical Education Quality Improvement Programme (TEQIP), MNIT Jaipur for providing the financial assistantship. The authors would like to thank Inter-University Accelerator Centre (IUAC) New Delhi for providing the necessary synthesis and



experimental facilities and highly grateful to pelletron group for providing the stable beam during swift heavy ion irradiation experiment. The authors are also thankful to the Materials Research Centre, MNIT Jaipur for providing characterization techniques (AFM and FESEM). One of the authors (R. Singhal) highly acknowledges the financial support provided by DST New Delhi DST FAST young scientist Project (SR/FTP/PS-081/2011), DST INSPIRE Faculty Project (IFA11PH-01) and UGC New Delhi (P.F. No. DRC-14/59/2013/10/169/00036). R. Vishnoi is greatly thankful to DST New Delhi for financial help under DST FAST Young Scientist Project (SR/FTP/PS-029/2012).

## References

- [1] C S Chen, C T Kuo, T B Wu and I N Lin, *J. Appl. Phys.* **36**, 1169 (1997)
- [2] J M Hvam *Phys. Rev. B*, **4**, 4459 (1971)
- [3] J H Lee, K H Ko and B.D. Park, *J. Cryst. Growth*, **247**, 119 (2003)
- [4] M M Bagheri-Mohagheghi and M Shokooh-Saremi, *Thin Solid Films*, **441**, 238 (2003)
- [5] J Hu and R G Gordon, *J. Appl. Phys.* **71**, 238 (1992)
- [6] X W Sun and H S Kwok, *J. Appl. Phys.* **86**, 408 (1999)
- [7] D C Agarwal *et al. Surf. Coat. Technol.* **203**, 2427 (2009)
- [8] J F Wager, *Science*, **300**, 1245 (2003)
- [9] S J Pearton, D P Norton, K Ip, Y W Heo and T Steiner, *Prog. Mater. Sci.* **50**, 293 (2005)
- [10] M J Gratzel, *Photochem. Photobiol. A*, **3**, 164 (2004)
- [11] P F Carcia, R S Melean, M H Reilly and G Nunes, *Appl. Phys. Lett.* **82**, 1117 (2003)
- [12] D C Look, D C Reynolds, C W Letton, R L Jones, D B Eason and G Cantwell, *Appl. Phys. Lett.* **81**, 1830 (2002)
- [13] T Gao and T H Wang, *Appl. Phys. A*, **80**, 1451 (2005)
- [14] Z W Pang, Z R Dai and Z L Wang, *Science*, **291**, 1947 (2001)
- [15] M H Huang, Y Y Wu, H Feick, N Tran, E Weber and P D Yang, *Science*, **292**, 1897 (2001)
- [16] C H Liu, W C Yiu, F C K Au, J K Ding, C S Lee and S T Lee, *Appl. Phys. Lett.* **83**, 3168 (2003)
- [17] P Shah, S Kumar, A Gupta, R Thangaraj and D K Avasthi, *Nucl. Instrum. Methods Phys. Res. B*, **156**, 222 (1999)
- [18] R Singhal *et al. J. Phys. D: Appl. Phys.* **42**, 155103 (2009)
- [19] R Singhal, A Kumar, Y K Mishra, S Mohapatra, J C Pivin and D K Avasthi, *Nucl. Instrum. Methods B*, **266**, 3257 (2008)
- [20] R Vishnoi, R Singhal, K Asokan, D Kanjilal and D Kaur, *Thin Solid Films*, **520**, 1631 (2011)
- [21] R Singhal, D Kabiraj, P K Kulriya, J C Pivin, R Chandra and D K Avasthi, *Plasmonics*, **8**, 295 (2013)
- [22] R Singhal, J C Pivin and D K Avasthi, *J. Nanopart. Res.* **15**, 1641 (2013)
- [23] D K Avasthi, Y K Mishra, F Singh and J P Stoquert, *Nucl. Instr. Meth. B*, **268**, 3027 (2010)
- [24] Y K Mishra *et al. Nucl. Instrum. Methods B*, **266**, 1804 (2008)
- [25] V Kumar, F Singh, O M Ntwaeaborwa and H.C. Swart, *Appl. Surf. Sci.*, **279**, 472 (2013)
- [26] S Kumar, R Kumar and D P Singh, *Appl. Surf. Sci.*, **255**, 8014 (2009)
- [27] D K Avasthi, A Kumar, R Singhal, A Tripathi and D S Mishra, *J. Nanosci. Nanotechnol.* **10**, 3767 (2010)
- [28] D K Avasthi and G K Mehta, *Swift heavy ions for materials engineering and nanostructuring*, Springer, Netherland (2011)
- [29] S K Srivastava *et al. Phys. Rev. B*, **71**, 193405 (2005)
- [30] W Bolse and B Schattat, *Nucl. Instrum. Methods Phys. Res. B*, **190**, 173 (2002)
- [31] D C Agrawal, R S Chauhan, D K Avasthi, S A Khan, D Kabiraj and I Sulaniya, *J. Appl. Phys.* **104**, 024304 (2008)
- [32] F Singh, R G Singh, V Singh, S A Khan and J C Pivin, *J. Appl. Phys.* **110**, 083520 (2011)
- [33] S Rehman, R G Singh, J C Pivin, Waseem Bari and F Singh, *Vacuum*, **86**, 87 (2011)
- [34] N Fujimura, T Nishinara, S Goto, J Xu and T Ito, *J. Cryst. Growth*, **130**, 269 (1993)
- [35] A N Mariano and R E Hanneman, *J. Appl. Phys.* **34**, 384 (1963)
- [36] H P Klug and L E Alexander, *X-ray Diffraction Procedures for Polycrystalline and Amorphous Materials*. Wiley, New York (1974)
- [37] B D Cullity, *Elements of X-ray diffraction*, Addison-Wesley, Reading (1970)
- [38] G. Szenes, *Phys. Rev. B*, **51**, 8026 (1995)
- [39] J G E Gardeniers, Z M Rittersma and G J Burger, *J. Appl. Phys.* **83**, 12 (1998)
- [40] P M R Kumar *et al. J. Appl. Phys.*, **97**, 013509 (2005)
- [41] J Tauc, *Mater. Res. Bull.*, **3**, 37 (1968)
- [42] Marius Grundmann, *The Physics of Semiconductors*, New York: Springer (2006)
- [43] R Vishnoi and D Kaur, *Surf. Coat. Technol.*, **204**, 3773 (2010)
- [44] J F Scott, *Phys. Rev. B*, **2**, 1209 (1970)
- [45] C Bundesmann *et al. Appl. Phys. Lett.* **83**, 1974 (2003)
- [46] V A Fonoberov and A A Balandin, *Phys. Rev. B*, **70**, 233205 (2004)
- [47] A Zaoui and W Sekkal, *Phys. Rev. B*, **66**, 174106 (2002)



## **Synthesis and annealing study of RF sputtered ZnO thin film**

Shushant Kumar Singh, Himanshu Sharma, R. Singhal, V. V. Siva Kumar, and D. K. Avasthi

Citation: [AIP Conference Proceedings](#) **1731**, 080063 (2016); doi: 10.1063/1.4947941

View online: <http://dx.doi.org/10.1063/1.4947941>

View Table of Contents: <http://scitation.aip.org/content/aip/proceeding/aipcp/1731?ver=pdfcov>

Published by the [AIP Publishing](#)

---

### **Articles you may be interested in**

[Resistive switching behavior of RF magnetron sputtered ZnO thin films](#)

*AIP Conf. Proc.* **1665**, 080051 (2015); 10.1063/1.4917955

[Compositional study of vacuum annealed Al doped ZnO thin films obtained by RF magnetron sputtering](#)

*J. Vac. Sci. Technol. A* **29**, 051514 (2011); 10.1116/1.3624787

[Photoluminescence Characterization of ZnO Thin Films Grown by RF- Sputtering](#)

*AIP Conf. Proc.* **1328**, 245 (2011); 10.1063/1.3573743

[Structural and optical properties of ZnO thin films by rf magnetron sputtering with rapid thermal annealing](#)

*Appl. Phys. Lett.* **92**, 141911 (2008); 10.1063/1.2896642

[Postdeposition annealing behavior of rf sputtered ZnO films](#)

*J. Vac. Sci. Technol.* **17**, 808 (1980); 10.1116/1.570565

---

# Synthesis and Annealing Study of RF Sputtered ZnO Thin Film

Shushant Kumar Singh<sup>a\*</sup>, Himanshu Sharma<sup>a</sup>, R. Singhal<sup>b</sup>, V. V. Siva Kumar<sup>c</sup>,  
D.K. Avasthi<sup>c</sup>

<sup>a</sup>Department of Physics, Malaviya National Institute of Technology, Jaipur, JLN Marg, Malaviya Nagar, Jaipur-302017, India

<sup>b</sup>Department of Physics and Materials Research Centre, Malaviya National Institute of Technology Jaipur, JLN Marg, Malaviya Nagar, Jaipur-302017, India

<sup>c</sup>Inter-University Accelerator Centre, Aruna Asaf Ali Marg, New Delhi-110067, India

\*E-mail: [singhshushant86@gmail.com](mailto:singhshushant86@gmail.com)

**Abstract.** In this paper, we have investigated the annealing effect on optical and structural properties of ZnO thin films, synthesized by RF magnetron sputtering. ZnO thin films were deposited on glass and silicon substrates simultaneously at a substrate temperature of 300 °C using Argon gas in sputtering chamber. Thickness of as deposited ZnO thin film was found to be ~155 nm, calculated by Rutherford backscattering spectroscopy (RBS). These films were annealed at 400 °C and 500 °C temperature in the continuous flow of oxygen gas for 1 hour in tube furnace. X-ray diffraction analysis confirmed the formation of hexagonal wurtzite structure of ZnO thin film along the c-axis (002) orientation. Transmittance of thin films was increased with increasing the annealing temperature estimated by UV-visible transmission spectroscopy. Quality and texture of the thin films were improved with annealing temperature, estimated by Raman spectroscopy.

**Keywords:** RF sputtering, Raman spectroscopy, UV-visible spectroscopy.

**PACS:** 81.15 Cd, 78.30 Fs and 07.60.Rd.

## INTRODUCTION

It is found that nanocrystalline materials significantly enhance various material properties. The development of plasmonic integrated devices (ICs) governed by manipulating light in nanoscale region. ZnO seems to be promising material of II-VI semiconductor group having a wide band gap (3.3 eV) with hexagonal wurtzite structure. ZnO thin films, exhibits excellent material properties such as wide band gap, transparent conducting material and piezoelectric properties; which makes its potential application for light emitting, surface acoustic waves (SAW), band pass filter, optoelectronic devices, data storage and gas sensors [1-5]. ZnO replaces widely used indium doped tin oxide (ITO) as transparent electrodes due to its lower absorption in the ultraviolet region. It is also economical in comparison of ITO as per cost concern. It has higher availability and lack of toxicity as well [6]. The properties of growing ZnO thin films having influence on deposition parameter as well as deposition process significantly. In the present

work, ZnO thin films were synthesized on glass and silicon substrates using an RF magnetron sputtering technique which is a physical vapour deposition technique (PVD). Tuning of film properties can be achieved by transmuting deposition parameter such as RF power, Gas flow rate, substrate temperature and nature of gas.

## EXPERIMENTAL

ZnO thin films were deposited on glass and silicon substrates by RF sputtering technique, using ZnO target of 2 inch diameter and 3 mm thickness, in the presence of argon atmosphere in sputtering chamber. ZnO target was prepared from ZnO powder (Alfa Aesar) using hydraulic press machine and sintered the target at 1200 °C in the tube furnace for 24 hours in the continuous flow of oxygen gas. The substrates glass and silicon were cleaned ultrasonically in acetone, isopropanol and deionized water subsequently. A turbo pump coupled with rotary pump was used to achieve the  $\sim 5 \times 10^{-5}$  mbar pressure and  $3 \times 10^{-2}$  mbar during a deposition in the presence of argon (grade-1) gas. Substrate temperature during

deposition is 300 °C and the experiment was performed for 30 minutes at the power of RF supply is 150 watts (self bias voltage 250-300 volt). Films were annealed at temperature 400 °C and 500 °C in the presence of an oxygen gas environment for 1 hour and then characterized by different characterization tools.

The thickness and metal atomic fraction of thin film, deposited on a Si substrate were measured by the Rutherford backscattered spectroscopy (RBS) at Inter University Accelerator Centre (IUAC) New Delhi. The XRD spectra of the films were recorded with Panalytical Xpert pro diffractometer using Cu K<sub>α</sub> at MNIT Jaipur. UV- visible spectra of the films were recorded using a dual beam U-3300 Hitachi spectrometer at IUAC. Raman measurements of as deposited and annealed thin films were performed using AIRIX STR 500 Raman microscope with laser excitation at 532 nm and at very low power to avoid any heating effect.

## RESULTS AND DISCUSSION

Rutherford backscattering spectroscopy (RBS) of as deposited ZnO thin film was shown in figure 1. Thickness of the film was found to be 155 nm by fitting RBS spectra with SIMNRA simulation program [7]. The plateau region of the spectrum, represents the Si substrate (Fig. 1).

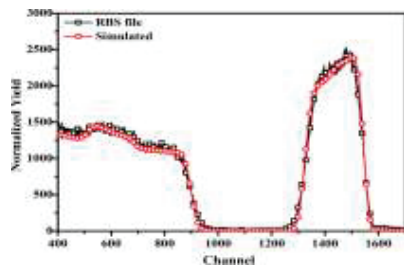


**Figure 1.** RBS spectra of the as deposited ZnO thin film on Si substrate.

Crystallinity and structural information of as deposited ZnO thin film was estimated by X-ray diffraction analysis. Figure 2 shows the XRD pattern of as deposited ZnO film and It confirms the formation of hexagonal wurtzite structure of ZnO with different phases such as (110), (002), (101), (102), (110), (103), and (112) at 31.34°, 34.12°, 35.95°, 47.27°, 56.31°, 62.49°, and 67.45° respectively (JCPDS-89-1397). Spectra of film indicated the higher intensity of (002) reflection plane at 34.12° which confirms the film is more preferential oriented along the c-axis. Crystallite

size of as deposited ZnO film was calculated by Debye Scherer's formula and it was found to be 15 nm.

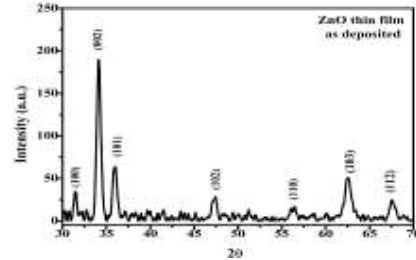


**Figure 2.** XRD pattern of as deposited ZnO thin film.

Figure 3 shows the average transmittance of as deposited and annealed ZnO thin films, confirmed by the UV-visible spectroscopy. The figure shows the average transmittance of the film increases with increasing the annealing temperature, and increase from 50% to 90% with annealing at 500 °C, increases the annealing temperature leads to better Crystallinity of the film, which was also confirmed by Raman spectroscopy. The quality of films was increased with annealing temperature, attributed by the quantity of free charge in film decrease with temperature [8] and transmittance of the film was increased due to the intake of oxygen in oxygen deficient ZnO film, absorbed oxygen remove the oxygen vacancies hence reducing the density of defects [6].

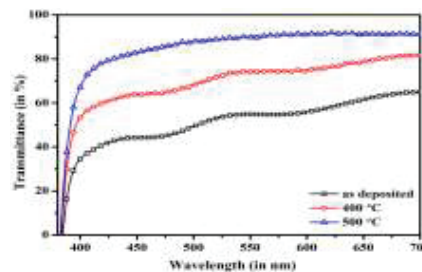


**Figure 3.** Transmittance spectra of as deposited and annealed ZnO thin films.

The band gap of films, calculated by assuming the direct band gap between valence bands to conduction band which holds by the Tauc's relation:

$$\alpha h\nu = A (h\nu - E_g)^{1/2}$$

Where,  $h\nu$  is photon energy,  $A$  is constant and  $E_g$  is the optical band gap and it band gap is determined by the extrapolating of the linear part of the  $\alpha^2$  curve towards the  $h\nu$  axis and it found

to be 3.26 eV for as deposited and annealed thin films. There is no significant change in the band gap of as deposited and annealed thin films of ZnO.

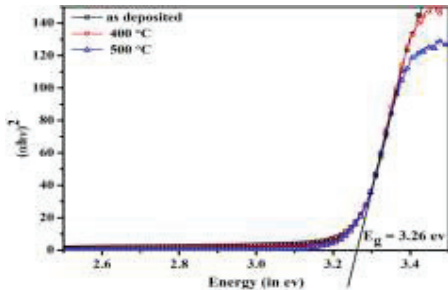


**Figure 4.** Band gap variation of as deposited and annealed film calculated by  $\tau^c$  plot.

Raman spectra of as deposited and annealed ZnO thin films are shown in figure 5. The Raman active phonon modes of the wurtzite structure of ZnO expected from the group theory are  $A_1+2E_2+E_1$  modes, where all atoms occupy  $C_{30}$  sites. The Raman spectra of films reveal that as deposited ZnO thin film show peaks at  $276\text{ cm}^{-1}$ , which was related to the B2 second order mode with low intensity and  $581\text{ cm}^{-1}$  which can be assigned to  $A_1$  (LO) mode. When films were annealed in an oxygen environment at temperature  $400^\circ\text{C}$  and  $500^\circ\text{C}$  for 1 hour, the intensity of the  $A_1$  (LO) mode and second order mode were increases. At the temperature  $500^\circ\text{C}$ ,  $E_2$  high mode was also appearing in annealed ZnO thin films.  $A_1$  (LO) mode and  $E_2$  high mode are expected, as the films are highly textured and the excitation light is normal to the surface [9-10]. The appearance of  $E_2$  high mode in ZnO film, which was annealed at  $500^\circ\text{C}$ , confirmed the highly textured and wurtzite structure of the ZnO thin films [11].

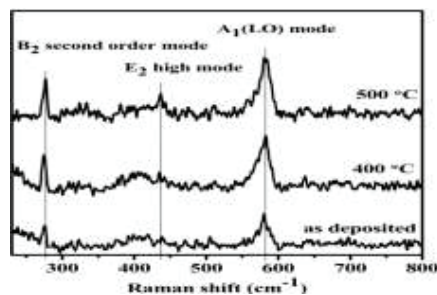


**Figure 5.** Raman spectra of as deposited and annealed ZnO thin films.

## CONCLUSION

ZnO thin films were synthesized by RF magnetron sputtering technique and annealed at different temperatures. XRD confirms the formation of ZnO thin film with a wurtzite hexagonal structure. Transmittance and film quality of films improve with increasing temperature, as confirmed by UV-visible and Raman spectroscopy.

## ACKNOWLEDGEMENTS

The author is thankful to the Technical Education Quality Improvement Program (TEQIP), MNIT Jaipur for providing the financial assistantship. The author would like to thank the Inter University Accelerator Centre (IUAC) New Delhi and Materials Research Centre, Jaipur for providing the necessary synthesis and experimental facilities. One of the authors (R. Singhal) highly acknowledges the financial support provided by DST New Delhi (DST INSPIRE Faculty Project IFA11PH-01).

## REFERENCES

1. Z.W. Pang, Z.R. Dai, Z.L. Wang, *Science* 291, 1947 (2001).
2. M. Rajalakshmi, Akhilesh, K. Arora, B.S. Bendre, Shailaja Mahamuni, *J. Appl. Phys.* 87, 2445–2448 (2000).
3. M.H. Huang, Y.Y. Wu, H. Feick, N. Tran, E. Weber, P.D. Yang, *Science* 292, 1897 (2001).
4. T. Dietl, H. Ohno, F. Matsukura, J. Cibert, D. Ferrand, *Science* 287, 1019 (2000).
5. G.S. Trivikrama Rao, D. Tarakarama Rao, *Sensors Actuators B Chem.* 55, 166 (1999).
6. D.C. Agrawal, R.S. Chauhan, Amit Kumar, D. Kabiraj, F. Singh, S. A. Khan, D.K. Avasthi, J.C. Pivin, M. Kumar, J. Ghatak, P.V. Stayam, *J. Appl. Phys.* 99, 123105 (2006)
7. M. Mayer, SIMNRA User's guide, Technical Report IPP 9/113, Max Plank Institute of fur Plasmaphysik, Garching, Germany (1997).
8. A. Og. Dikovska, P. A. Atanasov, C. Vasileva, I. G. Dimitrov, T. R. Stoyanchov, *Journal of Optoelectronics and Advanced Materials* 7, 1329-1335 (2005).
9. V.A. Fonoberov, A.A. Baladin, *J. Phys.: Condens. Matter* 17, 1085-1097 (2005).
10. K.A. Alim, V.A. Fonoberov, M. Shamsa, A.A. Baladin, *J. Appl. Phys.* 97, 124313-124315 (2005).
11. Fouran Singh, P.K. Kulriya, J.C. Pivin, *Solid State Communications* 150, 1751-1754 (2010).



# Ag-ZnO Nanocomposite Thin Film by RF-Sputtering: An Electrical and Structural Study

S. K. Singh,\* R. Singhal, and V. V. Siva Kumar

In the present study, pure ZnO and Ag-ZnO nanocomposite (NCs) thin films with three different compositions were grown by RF magnetron co-sputtering technique at substrate temperature 300 °C. The composite nature of the thin films was confirmed by Rutherford backscattering spectroscopy (RBS) and showed the existence of Ag, Zn, and O. The Ag fraction was found to be 8 at.%, 15 at.%, and 40 at.% in ZnO matrix. X-ray diffraction analysis of the pure and composite thin films confirms the formation and structure of the film and reveal the hexagonal wurtzite structure of the pure ZnO thin film. Structural modifications in pure and composite thin films were observed by scanning electron microscopy (SEM). Raman measurements of the pure and Ag-ZnO nanocomposite thin film were performed for the estimation of lattice defect and disordering which were induced by Ag incorporation. Electrical measurements revealed that the conductivity of nanocomposite thin film enhance drastically as compared to pure ZnO film and it increases with increasing Ag concentration. Furthermore, nanocomposite thin films showed a p-type conductivity due to the incorporation of Ag metal, confirmed by Hall measurements.

nano-device fabrication realm.<sup>[12,13]</sup> Indeed many researchers are struggling to improve their properties by applying different procedures for example incorporation of the metal as a dopant, ion implantation and interplay with annealing and different growth technique.<sup>[14–17]</sup> Different synthesis techniques have been used to synthesize the Ag-ZnO nanocomposite thin films such as spin coating, RF sputtering, spray pyrolysis, pulsed laser deposition, and e-beam evaporation etc.<sup>[18–21]</sup> It was suggested that the deposition parameters and the amount of metal doping are two main key factors which are responsible for the change in the physical properties of the ZnO thin films. Among them, silver (Ag) is a more suitable element for the doping as compare to Cu and Au because it is related to IB group and have lowest transition energy with shallow acceptor level at 0.3 eV and act as an acceptor which existing on substitutional

## 1. Introduction

In the present scenario, zinc oxide (ZnO) has become a favorable material for the various optoelectronic devices and thin film applications, due to its direct wide band gap (3.37 eV at room temperature 300 K) and large exciton binding energy (60 meV).<sup>[1]</sup> Such promising properties of ZnO makes it a suitable material for potential application in divergent areas such as transparent conducting oxides, light emitting diodes, laser deflectors, gas sensors, LEDs, photo detectors and solar cells.<sup>[2–9]</sup> ZnO has become an alternate of indium tin oxide in solar cell industry for the preparation of transparent conductive electrodes with low material cost, a high degree of chemical stability, and less toxicity.<sup>[10,11]</sup> In the last few years, ZnO-based nanomaterials have attracted considerable attention because of their dimensionality and size of their structural features, electrical and optical properties and also motivate to utilize in various

Zn sites.<sup>[22,23]</sup> Doping of silver (Ag) in ZnO matrix, creates the trivial acceptor level in the ZnO, due to the substitution of Zn sites by Ag sites during doping process because it has lower formation energy in comparison of Ag interstitial theoretically.<sup>[24]</sup> Therefore Ag is the suitable elements for fabricating the p-type conductivity in ZnO thin film which modifies the material behavior and responsible for the modifications in structural and electrical properties of ZnO.<sup>[25]</sup>

In this work, we presented a comparative study on pure ZnO and Ag-ZnO nanocomposite thin films synthesized by RF magnetron sputtering technique. Effect of higher Ag doping on the electrical and structural properties of the ZnO have been demonstrated and confirmed by various characterization tools. Scanning electron microscopy and I–V measurements have been performed to understand the modifications in structural and electrical properties of the ZnO before and after Ag doping. Hall measurements confirmed the p-type conductivity of Ag-ZnO nanocomposite at higher doping concentration. With this approach, a clear understanding of a structure-property correlation between microstructural and electrical data of Ag-ZnO nanocomposite is then established.

S. K. Singh, R. Singhal  
Department of Physics  
Malaviya National Institute of Technology Jaipur  
Rajasthan-302017, India  
E-mail: singhshushant86@gmail.com

V. V. Siva Kumar  
Inter University Accelerator Center  
Aruna Asaf Ali Marg, New Delhi-110067, India

DOI: 10.1002/masy.201600197

## 2. Experimental Section

For this study, pure ZnO and Ag-ZnO nanocomposite thin films were grown by RF magnetron co-sputtering method. A target

**Table 1.** The sputtering parameters for thin film deposition.

Sl. no.	Sputtering parameter	Value
1.	R.F. Power	150 watt
2.	Gas used during deposition	Argon (grade-1)
3.	Pressure before deposition	$6 \times 10^{-6}$ mbar
4.	Pressure during deposition	$5 \times 10^{-2}$ mbar
5.	Substrate temperature	300 °C
6.	Target to substrate distance	5 cm

(3 mm thick and 2 inch diameter) of ZnO powder (Alfa Aesar), was prepared by a hydraulic press machine and then it sintered at 1200 °C for 24 hours in the tubular furnace, continuous flow of oxygen gas. Some small pieces of silver (Ag) were glued on the ZnO target at the different position before deposition for synthesizing the composite thin films. Silicon (p-type 100), quartz, and glass used as the substrate during the deposition and all were cleaned by acetone and deionized water in the sequential manner. A turbo pump coupled with the rotary pump for achieving the high vacuum of the order of  $10^{-6}$  mbar in the deposition chamber before the deposition. The deposition was carried out at a vacuum  $10^{-2}$  mbar order, in the presence of pure argon gas (Grade-I) in the sputtering chamber during deposition. The target to substrate distance was  $\sim 50$  mm measured before the deposition. The deposition was performed for 20–30 minutes at the 150 watt RF power and the substrate temperature 300 °C, measured by thermocouple gauge and controlled by using a feed-back controlled heater in gauge. The all crucial parameters which monitored during deposition are tabulated in **Table 1**.

The composition of thin films was estimated by Rutherford backscattering spectrometry (RBS) by using PARAS facility (2 MeV He ions beam) at Inter University Accelerator Center (IUAC) New Delhi. The structural information of the thin films was analyzed by X-ray diffraction spectroscopy with Bruker D8 Advance diffractometer with Cu-K $\alpha$  radiation source of the wavelength of 1.54 Å at UGC-DAE CSR Indore. Surface morphology of the thin films recorded by MIRA II LMH Field Emission Scanning Electron Microscope (TESCAN make) at IUAC, New Delhi. Raman measurements of the composited thin films were analyzed by using Raman microscope (the AIRIX STR 500) with 532 nm laser excitation beam. Electrical measurement of the thin films was estimated by Kiethely Source meter (Model No. 2410) at the optical material laboratory, MNIT Jaipur. Four probe Hall measurements were performed on pure ZnO and Ag-doped nanocomposite thin films using ECOPIA Hall probe system (HMS-300) at IUAC, New Delhi.

### 3. Results and Discussion

#### 3.1. Rutherford Backscattering Spectroscopy

RBS technique is used to estimate the composition of the species with high accuracy. **Figure 1** (a–d) represents the RBS spectrum of the pure ZnO and Ag-ZnO nanocomposite films. For the estimation of concentration, the obtain experimental RBS spectra were simulated by Rutherford Universal Manipulation Simulation Program (RUMP)<sup>[26]</sup> which is shown in all figure by separated red line. The Ag atomic fraction in ZnO matrix was found to be 8 at.%, 15 at.% and 40 at.% respectively. The plateau region of the spectrum is responsible for the Si substrate. Since

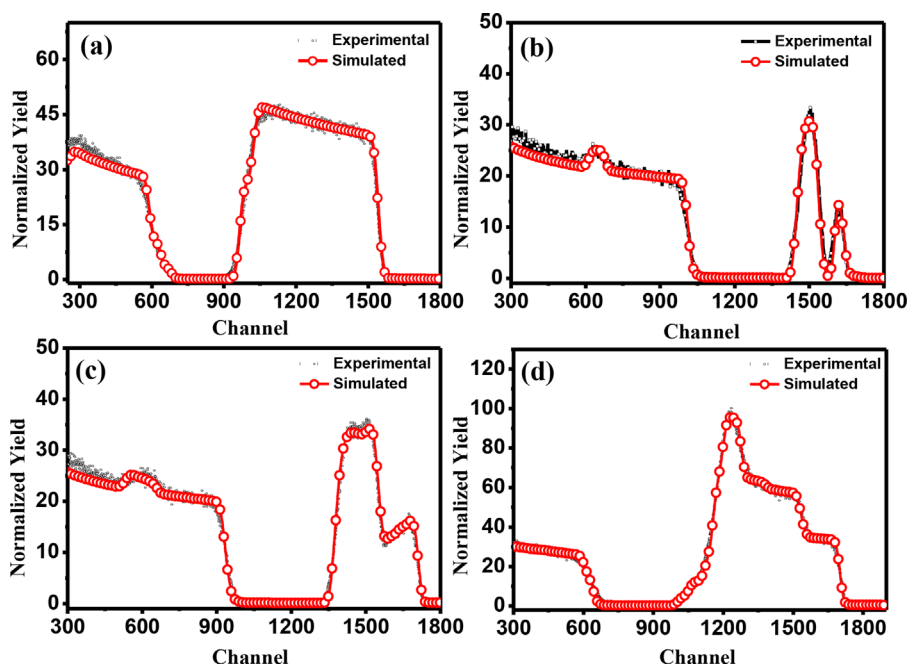


**Figure 1.** RBS spectra for the (a) pure ZnO (b) Ag-ZnO (8%) and (c) Ag-ZnO (15%) (d) Ag-ZnO (40%) nanocomposite thin films.

these films were grown on the Si substrate. From RBS spectra it can be concluded that the Ag-ZnO composite structure is formed with different Ag doping which embedded in the ZnO matrix.

### 3.2. Scanning Electron Microscopy

Surface morphology of the top surface of the pure and composite films can be easily observed from surface electron microscopy (SEM). **Figure 2(a–d)** shows the SEM images of the pure ZnO and Ag-ZnO nanocomposite thin film with three doping concentrations of 8 at.%, 15 at.% and 40 at.% respectively. In the case of pure ZnO which shown in **Figure 2(a)**, a non-uniform irregular pyramidal type sharp-blunt shape grains are observed which spread over the complete substrate. The observed grain size was found to 150–250 nm for the pure ZnO thin film. After the Ag incorporation, noticeable changes were observed in surface features of the composite thin film. For the lower doping concentration (8% and 15% both), disappearance of the pyramidal type of grains clearly observed. Pure ZnO grains shows the sharp grain boundary between the grains but as the doping of Ag increase then the grain boundary becomes disappear and agglomeration process occur there. At the higher doping concentration, film becomes more compact due to Ag incorporation and formed the big island of the grains on the

top surface of the film. During the deposition film have grown on the substrate which governs by two process, nucleation and coalescence process. Nucleation process has responsible for the formation of the island, these islands contain those nuclei which have lower formation energy. As the doping of metal increase with further deposition, the size of these islands increase and they become come closer during deposition and formed a large bulky island. Coalescence process between smaller grains are responsible for these type of growth which can easily observe for the case of higher doping.<sup>[27,28]</sup> For the higher concentration (40%), different size of bulky islands appeared on the surface of Ag-ZnO nanocomposite thin film.

### 3.3. X-Ray Diffraction Study

The crystalline quality of the pure ZnO and Ag-ZnO nanocomposite thin films was investigated by X-ray diffraction. **Figure 3** shows the X-ray patterns obtain on pure ZnO and Ag-ZnO nanocomposite films with doping concentrations of 8 at.%, 15 at.% and 40 at.% respectively. For pure ZnO we identified number of peaks at the diffraction angle of 31.79°, 34.43°, 36.19° and 46.32°, respectively which corresponds to the planes (100), (002), (101), and (102), can be well indexed to the wurtzite hexagonal structure with JCPDS-89-1397 card. It is also evident

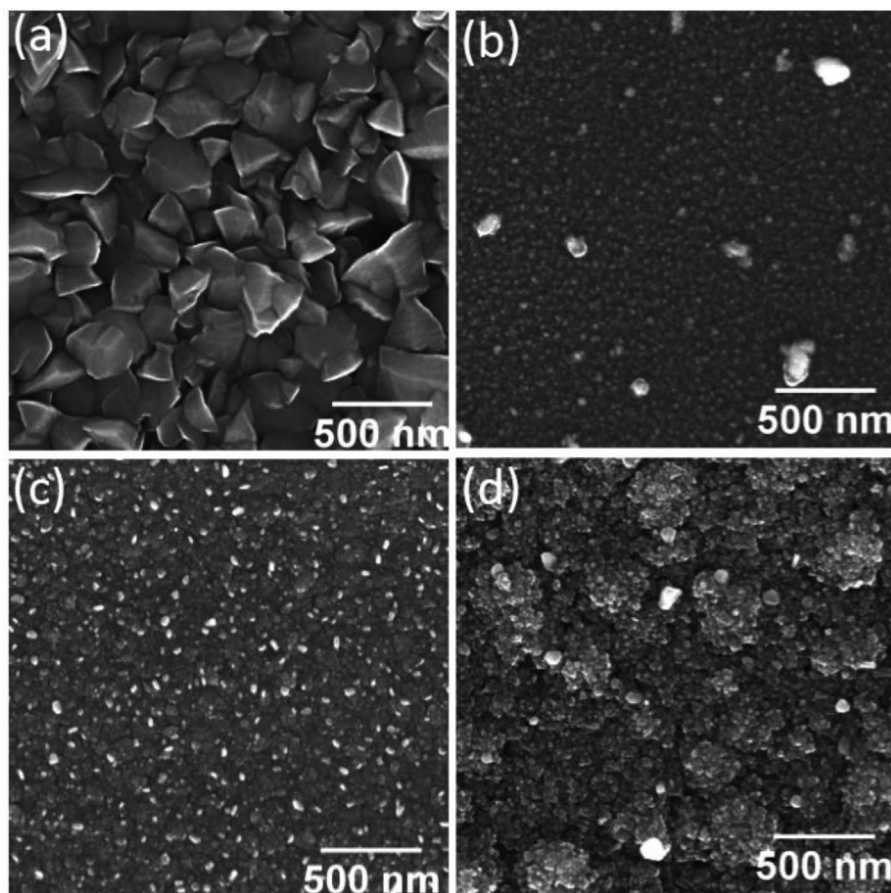


**Figure 2.** Scanning electron micrograph for (a) pure ZnO (b) 8% Ag-ZnO (c) 15% Ag-ZnO and (d) 40% Ag-ZnO nanocomposite thin films.



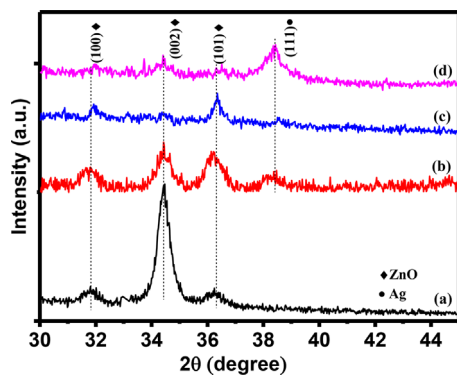


**Figure 3.** XRD diffraction pattern for the pure (a) and Ag-ZnO nanocomposite thin film with three different doping concentration (b. 8%, c. 15% and d. 40% Ag concentration).

that the pure ZnO film has grown along preferred c-axis orientation (002) as confirmed by X-ray pattern. However, for Ag doping of 15 at.% and 40 at.% initial reflections (100), (002) of ZnO are vanished but at higher Ag doping (40%), a strong reflection (111) arises which corresponds to the silver nanocluster at 38.18°. Therefore the appearance of new peak ascribed the highly presence of silver (Ag) in ZnO thin film as confirmed by RBS. The lattice parameter of the pure and ZnO and Ag-ZnO nanocomposite films was calculated by using Bragg's law and basic crystal structure formula of the hexagonal wurtzite structure. A marginal change of the lattice parameters was observed when Ag doping was introduced in the ZnO matrix. Lattice parameters before and after doping are summarized in **Table 2**. Since Ag ions (radius of 1.02 Å) have a large radius as compared Zn ions (radius of 0.72 Å) to Ag ions which attributed to change in lattice parameter with Ag incorporation. The change in the lattice parameter values indicates that Ag substitute by Zn. Since it is well known that Ag doping in ZnO yield p-type semiconducting behaviour. Furthermore the stress in the pure ZnO and Ag-ZnO nanocomposite film was also calculated by the following relation.<sup>[29]</sup>

$$\sigma(\text{Pa}) = -233 \left[ \frac{c - c'}{c'} \right] [\text{GPa}] \quad (1)$$

In Eq. (1),  $\sigma$  shows the stress of the sample,  $c$  is calculated lattice parameter for the prepared film and  $c'$  is the strain-free lattice constant of the bulk ZnO. The result of lattice parameter

and stress for the thin film are tabulated in Table 2. The presence of negative sign in the stress shows the compressive nature of the stress for pure and Ag-ZnO nanocomposite thin films, it arises due to the lattice defects which was the presence of the pure ZnO and Ag doped ZnO composite thin film.

The crystallite size of pure ZnO film was calculated by Scherrer's formula and found to be 14.1 nm<sup>[30]</sup>:

$$D = \frac{0.9\lambda}{\beta \cos\theta} \quad (2)$$

In Eq. (2),  $\lambda$  is wavelength (Cu-K $\alpha$  = 1.54 Å),  $\beta$  is full width at half maxima (FWHM) and  $\theta$  is the Bragg diffraction angle. At the higher doping concentration of Ag (40%), the appearance of the Ag peak in the spectra indicates the formation of the Ag-ZnO composite in the thin film. The crystallite size for higher doping was also calculated and yielded 19.70 nm for ZnO, and 13.0 nm for Ag-ZnO nanocomposite thin film at higher doping. This clarifies that the crystalline behavior of the ZnO film can be control by Ag concentration as shown in X-ray pattern.

### 3.4. Raman Measurements

Raman spectra of pure ZnO and Ag-ZnO nanocomposite thin films shown in **Figure 4**. Raman spectra revealed that pure ZnO film showed two different bands one at 441 and another at 575 cm<sup>-1</sup>. The first band appeared at 441 cm<sup>-1</sup> could be assigned to E<sub>2</sub> high mode and other bands at 575 cm<sup>-1</sup> represent the A<sub>1</sub> (LO) mode of the pure ZnO film. The presence of E<sub>2</sub> high mode in the spectra confirmed the formation of wurtzite structure of the ZnO film. These results are in good agreement with result obtained by XRD measurements which showed the formation of hexagonal wurtzite structure. Doping of Ag is very much effected on the Raman spectra shows a gradual change in the variation mode when Ag doping was introduced in the ZnO matrix. A complete disappearance of the E<sub>2</sub> high mode at the higher doping of Ag in ZnO was found, whereas some new mode arises at 495 cm<sup>-1</sup> at the higher concentration (40%). The appearance of this new mode at higher doping resulting in a low crystallinity of the film. The local vibrational mode at 495 cm<sup>-1</sup> arises due to Ag doping in ZnO thin film, and some other doping material also exhibits this mode.<sup>[31]</sup> The intensity of A<sub>1</sub> (LO) mode increases at higher Ag (40 at.%) doping. A<sub>1</sub> (LO) mode of the thin films is directly related to the defect density, zinc interstitials and oxygen vacancies in NCs thin film. Therefore the higher doping

**Table 2.** Lattice parameter and crystallite size for pure ZnO and Ag-ZnO nanocomposite thin film.

Sl. no.	Sample detail	Lattice parameter		c/a ratio	Crystallite size (nm)	Stress $\sigma$ (GPa)
		a (Å)	c (Å)			
1.	Pure ZnO	3.2484	5.2057	1.6025	14.1	-0.04
2.	Ag-ZnO (8%)	3.2492	5.2103	1.6032	13.5	-0.22
3.	Ag-ZnO (15%)	3.2402	5.2486	1.6198	24.4	-1.95
4.	Ag-ZnO (40%)	3.2343	5.2078	1.6101	19.7 for ZnO 13.0 for Ag	-0.13

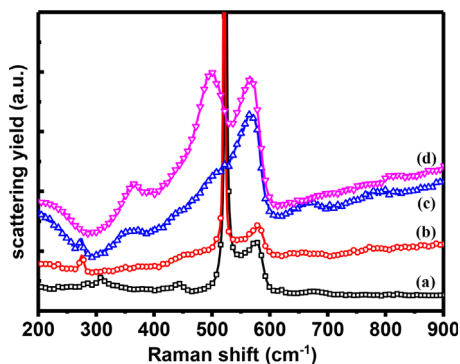


**Figure 4.** Raman spectra for the pure (a) and Ag-ZnO nanocomposite thin film with different doping concentration (b. 8% c. 15% and d. 40% Ag concentration).

of Ag is mainly responsible for the lower crystallinity and defect creation in the thin films.

### 3.5. I–V and Hall Measurements

**Figure 5** shows the variation in current with applied voltage (I–V spectra) of the pure ZnO and Ag-ZnO NCs thin film with different Ag concentration and we calculated the resistance as well conductivity of the films from these spectra. The contacts for this purpose were made using silver paste at room temperature. These measurements were performed at room temperature using a two probe method. **Figure 5** shows the I–V curve of pure ZnO and Ag-ZnO nanocomposite thin films with Ag concentrations of 8 at.%, 15 at.% and 40 at.% respectively. The slope of I–V curve yielded resistance value by fitting the

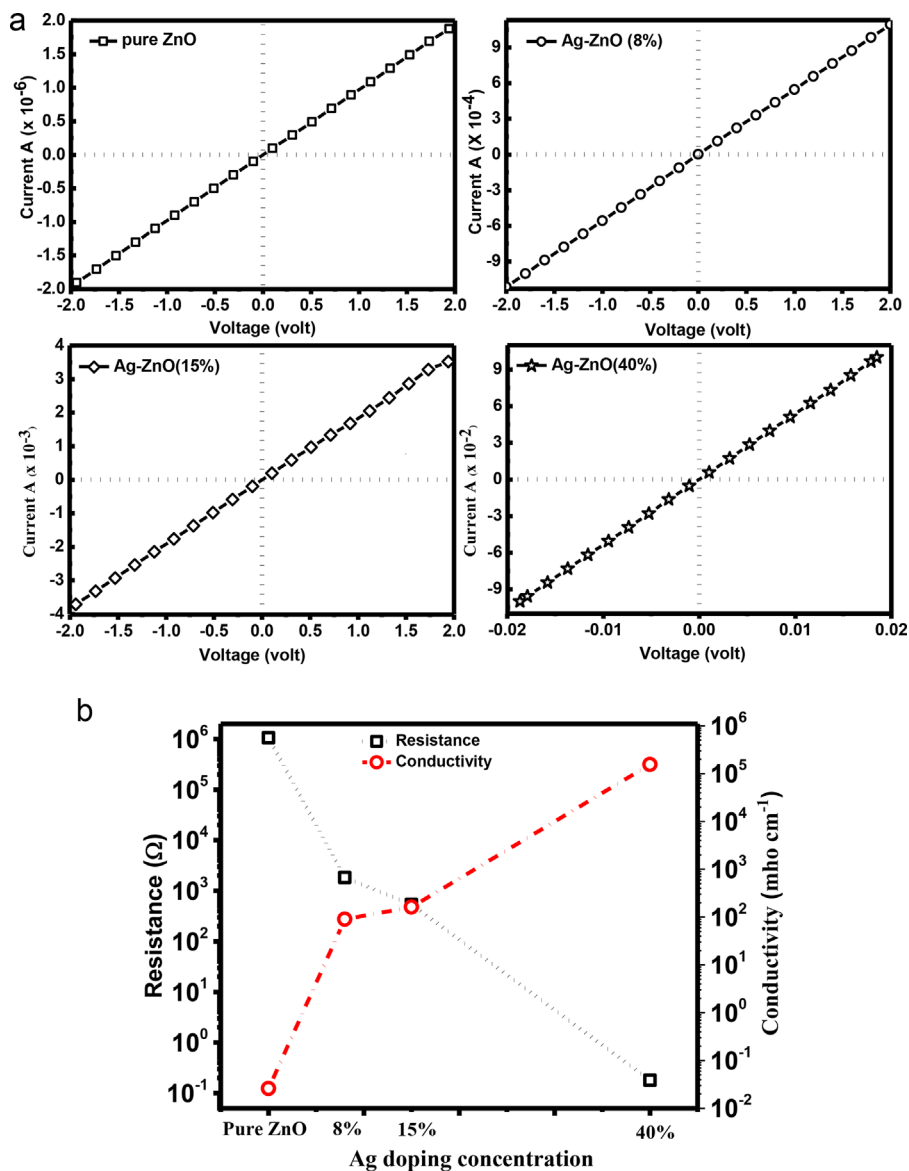


**Figure 5.** a) I–V spectra for the pure and Ag-ZnO nanocomposite thin films. b) Variation of resistance and conductivity with Ag doping concentration.

**Table 3.** The electrical parameter for pure ZnO and Ag-ZnO nanocomposite thin film.

Sl. no.	Sample detail	Carrier concentration	Type of majority charge carrier	Resistance	Conductivity
1.	Pure ZnO	$4.32 \times 10^{14} \text{ cm}^{-3}$	n-type	1.06 M $\Omega$	$4.32 \times 10^{-3} \text{ mho cm}^{-1}$
2.	Ag-ZnO (8%)	–	–	1.86 K $\Omega$	$9.00 \times 10^1 \text{ mho cm}^{-1}$
3.	Ag-ZnO (15%)	$2.28 \times 10^{20} \text{ cm}^{-3}$	p-type	536 $\Omega$	$1.71 \times 10^2 \text{ mho cm}^{-1}$
4.	Ag-ZnO (40%)	$5.11 \times 10^{21} \text{ cm}^{-3}$	p-type	0.18 $\Omega$	$4.18 \times 10^4 \text{ mho cm}^{-1}$

linear part of the graph, from this the resistivity of NCs thin film can be determined. The resistivity of the films is significantly affected by Ag doping in ZnO thin film. The conductivity of the film also calculated with the help of resistivity of the sample. The conductivity of the film at the higher doping concentration (40 at.%) was found to be very higher and measured value are nearly comparable to the conductivity of the pure Ag. The variation of resistance and conductivity of the NCs thin films as a function of Ag concentration which is shown in Figure 5(b). A significant improvement in the conductivity of the Ag-ZnO nanocomposite was found and depends on the number of charge carrier. The charge carrier density is effected by the inclusion of Ag doping in the ZnO thin film. It is apparent that Ag ions increase the majority charge carrier in ZnO thin film and as a consequence the resistance decrease of the film. The conductivity of the pure ZnO thin film was found to be  $4.32 \times 10^{-3} \text{ mho cm}^{-1}$  which is lower compared to Ag-ZnO nanocomposite particularly at higher doping concentration it reaches up to  $4.18 \times 10^4 \text{ mho cm}^{-1}$ .

For the confirmation of the semiconducting behavior of NCs thin films, Hall measurements setup (ECOPIA Hall probe system) was applied at room temperature. Pure ZnO thin film showed the n-type conductivity with carrier concentration of about  $4.32 \times 10^{14} \text{ cm}^{-3}$ . While Ag doped ZnO showed the p-type conductivity because of Ag incorporation in ZnO matrix because of the Ag is good candidate for the occupation of Zn substitutional ( $\text{Ag}_{\text{Zn}}$ ) and interstitial ( $\text{Ag}_i$ ). Theoretically, Ag has shallow acceptor level and lowest transition energy as well as less formation energy for  $\text{Ag}_{\text{Zn}}$  in comparison of  $\text{Ag}_i$ . These properties of the Ag acknowledge to presenting good element in comparison of Cu and Au for p-type doping in ZnO.<sup>[32–34]</sup> The carrier concentration of the NCs thin film is tabulated in Table 3.

#### 4. Conclusion

Pure ZnO and Ag-ZnO nanocomposite thin films have been synthesized by RF sputtering technique and characterized by various characterization technique in order to understand the structural and electrical behaviour of the films. XRD and SEM analysis confirm the structural and morphological features of the thin film. From electrical measurements, it was observed that the higher value of conductivity and p-type behaviour of the nanocomposite films at higher doping concentration. This indicates that it may be used in various device fabrication area and showed p-type conductivity which was confirmed by Hall measurements.

#### Acknowledgements

The author (S.K. Singh) is grateful to the Technical Education Quality Improvement Programme (TEQIP), MNIT Jaipur for providing the financial assistantship during research work and also thankful to Inter-University Accelerator Centre (IUAC) New Delhi for providing the necessary synthesis and characterizations facility. The author would like to thank my lab colleges for help during I–V measurements. One of the authors (R. Singhal) highly acknowledges the financial support UGC New Delhi project in the term of IUAC New Delhi P.F. No. DRC-14/59/2013/10/169/00036.

#### Keywords

I–V measurements, nanocomposite thin films, RF sputtering, Rutherford backscattering spectroscopy

- [1] T. L. Yang, D. H. Zhang, J. Ma, H. L. Ma, Y. Chen, *Thin Solid Films* **1998**, 326, 60.
- [2] Z. W. Pang, Z. R. Dai, Z. L. Wang, *Science* **2001**, 291, 1947.
- [3] R. Romero, M. C. Lopez, D. Leinen, F. Martin, J. R. Ramos-Barrado, *Mater. Sci. Eng. B* **2004**, 110, 87.
- [4] S. Sharma, C. Pariasamy, *Supperlatt. Microstructures* **2014**, 73, 12.
- [5] J. C. Pivin, G. Socol, I. Mihailescu, P. Berthet, F. Singh, M. K. Patel, L. Vincent, *Thin Solid Films* **2008**, 517, 916.
- [6] G. S. Trivikrama Rao, D. Tarakarama Rao, *Sensors Actuat. B Chem.* **1999**, 55, 166.
- [7] T. Reimer, I. Paulowicz, R. Roder, S. Kaps, O. Lupan, S. Chemnitz, W. Benecke, C. Ronning, R. Adelung, Y. K. Mishra, *ACS Appl. Mater. Interfaces* **2017**, 9, 4084.
- [8] V. Cretu, V. Postica, A. K. Mishra, M. Hoppe, I. Tiginyanu, Y. K. Mishra, L. Chow, N. H. De Leeuw, R. Adelung, O. Lupan, *J. Mater. Chem. A* **2016**, 4, 6527.
- [9] Y. K. Mishra, G. Modi, V. Cretu, V. Postica, O. Lupan, T. Reimer, I. Paulowicz, F. Hrkac, W. Benecke, L. Kienle, R. Adelung, *ACS Appl. Mater. Interfaces* **2015**, 7, 14303.
- [10] D. C. Agrawal, R. S. Chauhan, A. Kumar, D. Kabiraj, F. Singh, S. A. Khan, D. K. Avasthi, J. C. Pivin, M. Kumar, J. Ghatak, P. V. Stayam, *J. Appl. Phys.* **2006**, 99, 123105.
- [11] Y. K. Mishra, S. Kaps, A. Schuchardt, I. Paulowicz, X. Jin, D. Gedamu, S. Freitag, M. Claus, S. Wille, A. Kovalev, S. N. Gorb, R. Adelung, *Particle Particle Syst. Charact.* **2013**, 30, 775.
- [12] N. Wang, Y. Cai, R. Q. Zhang, *Mater. Sci. Eng. R* **2008**, 1, 60.
- [13] J. Grottrup, V. Postica, N. Ababii, O. Lupan, C. Zamponi, D. Meyners, Y. K. Mishra, V. Sontea, I. Tiginyanu, R. Adelung, *J. Alloys Compd.* **2017**, 701, 920.
- [14] H. Q. Bian, S. Y. Man, Z. M. Zhang, J. M. Gao, H. B. Zhu, *J. Cryst. Growth* **2014**, 394, 132.



- [15] J. Chen, X. Yan, W. Liu, Q. Xue, *Sensors Actuat. B* **2011**, *160*, 1499.
- [16] S. K. Singh, H. Sharma, R. Singhal, V. V. Siva Kumar, D. K. Avasthi, *AIP Conf. Proc.* **2016**, *1731*, 080063.
- [17] F. Singh, P. K. Kuliya, J. C. Pivin, *Solid State Commun.* **2010**, *150*, 1751.
- [18] W. Tang, D. C. Cameron, *Thin Solid Films* **1994**, *83*, 238.
- [19] M. Liu, X. Q. Wei, Z. G. Zhang, G. Sun, C. S. Chen, C. S. Xue, H. Z. Zhuzng, B. Y. Man, *Appl. Surf. Sci.* **2006**, *252*, 4321.
- [20] R. Georgekutty, M. K. Seery, S. C. Pillai, *J. Phys. Chem. C* **2008**, *112*, 13563.
- [21] J. Liqiang, W. Dejun, W. Baiqi, L. Shudan, X. Baifu, F. Honggang, S. Jiazhong, *J. Mol. Catal. A* **2006**, *244*, 193.
- [22] Y. Yan, S. H. Wei, *Phys. Status Solidi B* **2008**, *245*, 641.
- [23] O. Vlonianska, P. Boguslawski, J. Kaczkowski, P. Jakubas, A. Jezierski, E. Kaminska, *Phys. Rev. B* **2009**, *80*, 245212.
- [24] Q. Wan, Z. Xiong, J. Dai, J. Rao, F. F. Jiang, *Opt. Mater.* **2008**, *30*, 817.
- [25] A. N. Gruzintsev, V. T. Volkov, E. E. Yakimov, *Semiconductors* **2003**, *37*, 259.
- [26] Doolittle, R. Lawrence, *Nucl. Instrum. Methods Phys. Res. B* **1985**, *9*, 344.
- [27] W. Lin, R. Ma, W. Shao, B. Liu, *Appl. Surf. Sci.* **2007**, *253*, 5179.
- [28] C. C. Lin, H. P. Chen, S. Y. Chen, *Chem. Phys. Lett.* **2005**, *404*, 30.
- [29] M. Chen, Z. L. Pei, C. Sun, L. S. Wen, Z. Wang, *J. Cryst. Growth* **2000**, *220*, 254.
- [30] B. D. Cullity, *Elements of X-Ray Diffraction*. Addison-wesely, **1978**, p. 284.
- [31] H. Q. Bian, S. Y. Ma, F. M. Li, H. B. Zhu, *Superlatt. Microstructures* **2013**, *58*, 171.
- [32] V. V. Siva Kumar, D. Kanjilal, *J. Chin. Adv. Soc.* **2014**, *2*, 199.
- [33] M. A. Myers, J. H. Lee, Z. Bi, H. Wang, *J. Phys.: Condens. Matter* **2012**, *24*, 145802.
- [34] J. C. Fan, K. M. Sreekanth, Z. Xie, S. L. Chang, K. V. Rao, *Prog. Mater. Sci.* **2013**, *58*, 874.



# Structural and optical investigations of 120 keV Ag ion implanted ZnO thin films



S.K. Singh\*, R. Singhal

Department of Physics, Malaviya National Institute of Technology Jaipur, JLN Marg, Malaviya Nagar, Jaipur 302017, India

## ARTICLE INFO

### Keywords:

Ion implantation  
Rutherford backscattering spectroscopy  
Raman spectroscopy  
Zinc oxide  
Thin films  
Sputtering  
X-ray diffraction

## ABSTRACT

Structural as well as optical modifications in zinc oxide (ZnO) thin film with Ag ion implantation were carried out in the present study. The pure ZnO thin films were synthesized by RF-magnetron sputtering technique at room temperature. 120 keV Ag ion beam was used for Ag ion implantation with different implantation dose from  $3 \times 10^{14}$  to  $3 \times 10^{16}$  ions/cm<sup>2</sup> by negative ion implantation facility. The thickness and composition of pure ZnO and Ag implanted film at higher dose  $3 \times 10^{16}$  ions/cm<sup>2</sup> were estimated by Rutherford backscattering spectroscopy. The change in surface stoichiometry was estimated by using X-ray photoelectron spectroscopy with Ag ion implantation. The modifications in structural features with Ag ion implantation in ZnO films were observed by X-ray diffraction technique (XRD). The pure ZnO thin film was preferentially grown in c-axis direction with crystallite size  $\sim 10.6$  nm confirmed by XRD. Surface morphology of the pure and Ag implanted ZnO thin films was estimated by atomic force microscopy and revealed the roughness and grain size were increased with increasing the implantation dose. The transmittance of the films was decreased drastically at higher implantation dose as corroborated by UV–visible spectroscopy. Raman spectroscopy of the films was used to understand the lattice defects and disordering during Ag ion implantation. At the higher dose, the film was entirely oriented in c-axis confirmed by X-ray pattern, which can be beneficial for device fabrication.

## 1. Introduction

Oxide semiconductors are attracting to researchers due to their excellent physical properties which promote to utilize these semiconductor in device fabrications [1–3]. Among of these, ZnO is a very promising material having direct band gap about  $\sim 3.37$  eV and hexagonal wurtzite crystal structure from II–VI semiconductor group [4]. ZnO is used for high-temperature device fabrications due to its large band gap in comparison to Si/Ge based semiconducting devices [5,6]. It has also been used for potential applications such as transparent electrodes [7], optoelectronics [8], light-emitting diodes [9], solar cells [10], photo-detectors [11] and gas sensors [12] due to its functionality of the physical properties which can be easily tuned by different methods. The nanocrystalline thin film of a material offers, its importance in the different application with tunable physical properties which is difficult with the bulk material [13–17]. There are many synthesis techniques such as pulsed laser deposition [18], sol-gel method [19], spray pyrolysis [20], chemical vapor deposition [21], molecular beam epitaxial growth technique [22], DC/RF magnetron sputtering [23] and atom beam sputtering [24] used to synthesize ZnO thin films. Deposition techniques and parameters are responsible for

growth and stoichiometry of the film. Furthermore, the incorporation of noble metals (Ag, Au, and Cu) in ZnO thin film are very attractive way to enhanced the structural, electrical and optical properties [25–29]. These noble metals, in the form of nanoparticles, exhibits selective surface plasmon resonance (SPR) band in visible and near infrared region. Therefore, the presence of plasmon-active nanoparticles in a matrix offered new optical properties for different plasmonic applications [30–32]. Although intrinsic defects like zinc interstitials and oxygen vacancies are also responsible for the modifications in these properties [33].

Ion implantation is a precise technique for material modifications (structural as well as optical) by doping of metal ions into target materials up to certain depth [34–38]. Nowadays, ion implantation facility has also been widely used in device fabrication because it provides the facility to introduce charge carrier for conduction into oxide semiconductors with selective area doping as well optical and electrical isolation. Depth concentration and controlled amount of selective dopant metal can be easily controlled by implantation dose and energy during implantation. The low energy (typically range  $\sim 10$ –500 keV) ion beam has been used for implantation process and range of the implantation species is (implanted length) from few angstrom (Å) to 1  $\mu$ m

\* Corresponding author.

E-mail address: [singhshushant86@gmail.com](mailto:singhshushant86@gmail.com) (S.K. Singh).

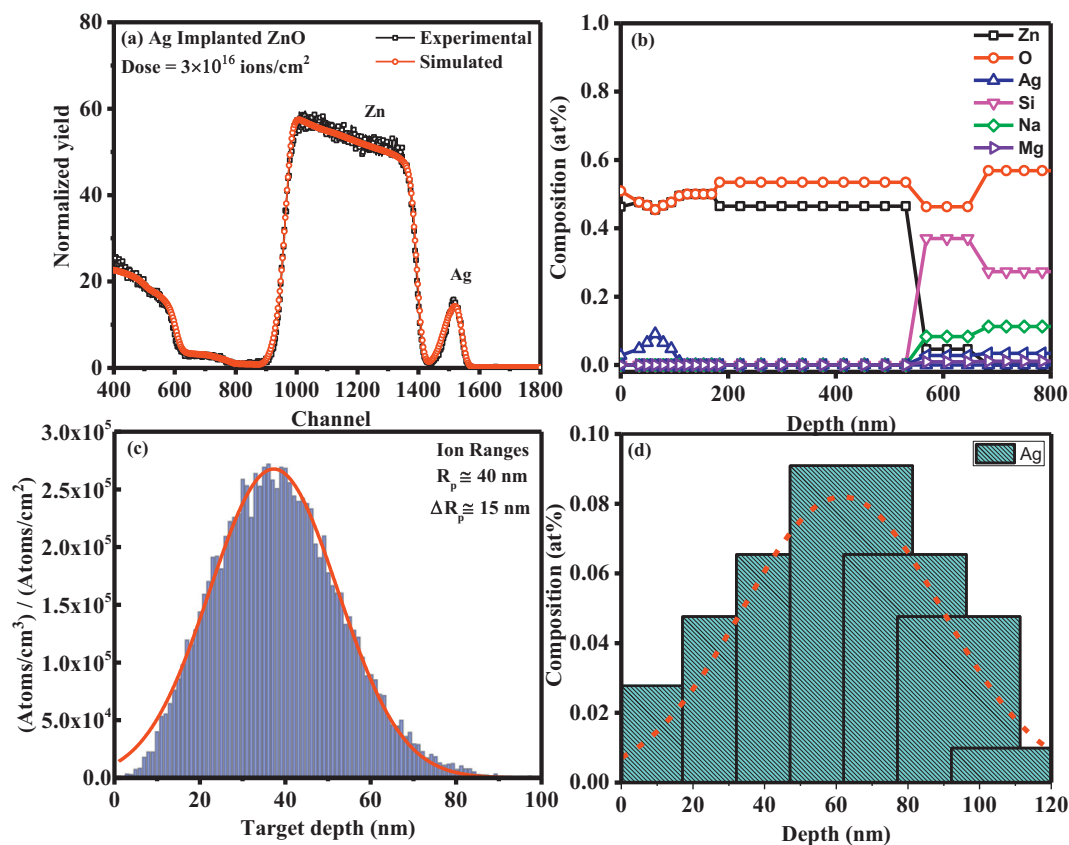


Fig. 1. (a) RBS spectra of Ag implanted ZnO thin film, (b) depth profile of Ag implanted ZnO thin film, (c) depth distribution curve of Ag ion implanted in ZnO thin film estimated by SRIM-TRIM simulation and (d) enlarge view shows the experimental distribution of Ag ions by RBS.

(also depends on the target material). This technique is also convenient for synthesized the nanoparticles in the target materials with better control of depth and selective area. Different lattice interstitials, vacancies and planer defects are generated by the collision of incident ions with target material during implantation, which could be responsible for the structural modifications. The absorption/scattering cross section of Ag nanoparticle is larger than a geometrical cross section, which leads the higher efficiency of interaction with incident light, therefore the Ag ion used for the implantation [39]. Such effects produced by Ag ion implantation in ZnO matrix are responsible to enhance their structural and optical properties. In the present study, ZnO thin films were synthesized by RF-magnetron sputtering and then 120 keV Ag ions were implanted into ZnO matrix with different implantation dose ranging from  $3 \times 10^{14}$  to  $3 \times 10^{16}$  ions/cm<sup>2</sup> for present experiment. The modifications in structural and optical properties with Ag ion implantation were estimated by different characterization techniques such as X-ray diffraction, UV-visible spectroscopy, Atomic force microscopy, X-ray photoelectron spectroscopy and Raman spectroscopy.

## 2. Experimental plan

First, we prepared a ZnO target (2 inch diameter and 3 mm thickness) from the ZnO powder (Merck) using hydraulic press machine (HYCON Hydraulic engineers and consultants, New Delhi) for the film deposition by RF-magnetron sputtering. A tubular furnace was used for the prepared ZnO target sintering at the temperature 1200 °C for the duration of 24 h. The continuous flow of oxygen gas was kept during target sintering in the furnace. The silicon and glass substrates were cleaned ultrasonically in acetone, isopropanol and deionized water subsequently before the film deposition and mounted in the deposition chamber. Sputtering was performed in the presence of argon gas and synthesized ZnO thin film with the thickness of ~500 nm. The rotary

pump was used for achieving the rough vacuum and it coupled with the turbo-molecular pump for obtaining the high vacuum in the sputtering chamber. The initial vacuum in the deposition chamber before the deposition was  $5 \times 10^{-5}$  mbar and it decreased when introducing the argon gas in the chamber and measured  $3 \times 10^{-2}$  mbar pressure during the film deposition. The deposition was performed at room temperature for 30 min at the RF power was ~150 W. The target to substrate distance ~4 cm and self-bias voltage of the sputtering unit was 250–300 V during the deposition. After the film deposition, all the samples were mounted in the implantation chamber for the implantation. 120 keV Ag ion beam was used for the ion implantation in ZnO thin film using negative ion implantation facility at Inter University Accelerator Center (IUAC), New Delhi. The nuclear energy loss ( $S_n$ ) is dominant for the lower energy range and it determined by Stopping and Range of Ion in Matter (SRIM) simulation program [40]. The value of nuclear and electronic energy loss ( $S_n$  and  $S_e$ ) are calculated by SRIM and found to be  $2.54 \times 10^2$  eV/Å and  $2.71 \times 10^1$  eV/Å respectively with the range of ~424 Å in ZnO material. The Ag ion beam scanned over the complete sample area ( $1 \times 1$  cm<sup>2</sup>) with five different implantation doses  $3 \times 10^{14}$ ,  $1 \times 10^{15}$ ,  $3 \times 10^{15}$ ,  $1 \times 10^{16}$  and  $3 \times 10^{16}$  ions/cm<sup>2</sup>. The constant beam current ~1.1 μA was stable during Ag ion implantation.

The thickness and metal distribution of pure ZnO and Ag implanted ZnO thin film were estimated by the Rutherford backscattered spectroscopy at IUAC, New Delhi. The structural change with ion implantation in ZnO thin film was estimated by X-ray diffraction spectra with Panalytical X-Pert pro diffractometer using Cu K<sub>α</sub> beam (1.54 Å) at Material Research Center (MRC), MNIT Jaipur. Chemical composition and surface analysis were carried out by X-ray photo-electron spectroscopy. UV-visible spectra of pure and implanted ZnO films were recorded using a dual beam U-3300 Hitachi spectrometer at IUAC, New Delhi. Raman measurement of as-deposited and implanted thin films was performed using Raman microscope (AIRIX-STR 500) with 532 nm

laser excitation and at low power to avoid any heating effect. Surface morphology of the pure and Ag implanted ZnO thin films were studied by atomic force microscopy (Bruker).

### 3. Results and discussion

#### 3.1. Rutherford backscattering spectroscopy

Rutherford backscattering spectroscopy (RBS) is the efficient technique to estimate the thickness and compositional parameter of the materials. RBS spectrum and depth profile of Ag implanted ZnO films (at higher fluence  $3 \times 10^{16}$  ions/cm<sup>2</sup>) are shown in Fig. 1(a–b). The experimental RBS spectra was simulated by Rutherford Universal Manipulation Program (RUMP) [41] as shown in Fig. 1(a). The thickness and presence of Ag at the surface of the ZnO film have been estimated by the simulated spectra. The thickness of the film has been estimated and found to be ~500 nm. The potential sputtering near to the surface take place during the ion implantation as confirmed by depth profile shown in Fig. 1(b) [42]. The presence and asymmetric distribution of Ag ions at the surface of the ZnO film have been observed and supported by depth profile curve. The depth profile of Ag implanted film shows that, the elemental composition of the film affected by Ag ions implantation close to the surface region. Furthermore, theoretical distribution of 20,000 Ag ions (Fig. 1(c)) in ZnO film was calculated by the SRIM-TRIM simulation program [40]. The experimental distribution of Ag in ZnO matrix is supported by the simulated depth profile of Ag implanted ZnO film (Fig. 1(c–d)). The marginal difference between simulated and experimental Ag distribution may be subjected to the energy deposition by incident ions which leads to the preferential sputtering as well as high dynamic annealing near the surface.

#### 3.2. X-ray diffraction analysis

Fig. 2(a) shows the X-ray diffraction (XRD) pattern for pure ZnO and 120 keV Ag implanted ZnO thin films at different implantation doses from  $3 \times 10^{14}$  to  $3 \times 10^{16}$  ions/cm<sup>2</sup>. Pure ZnO film shows the crystalline nature and indicates the hexagonal wurtzite structure with (100), (002), (101), (102), and (110) reflection planes which appear at the diffraction angle 31.7°, 34.2°, 36.2°, 47.4°, and 57.1° respectively (JCPDS Card No. 89-1397). At the higher implantation dose, all other planes are disappeared except one plane (002), which indicates the monocrystalline nature of the ZnO thin film with higher crystallinity. Grain growth along the c-axis with Ag ion implantation has been clearly observed by the spectra which can be useful for device fabrication. Lattice strain of the film releases with the Ag ion implantation clearly mentioned in Fig. 2(b) and it is responsible for the growth of the film in c-axis. Basic crystal theory suggests that, (002) plane has the lowest

surface energy for easy growth along this plane for the ZnO. Lattice strain for the pure and Ag implanted ZnO films are calculated by following equation [43]:

$$\text{Lattice strain } (\varepsilon) = \frac{\beta \cot \theta}{4} \quad (1)$$

where,  $\theta$  is the angle of diffraction and  $\beta$  is the full width at half maxima (FWHM). The lattice strain of the film decrease with increasing the implantation dose. The crystallite size of the pure ZnO film has been calculated and found to be ~10.6 nm and it marginally increases up to 13.0 nm with Ag ion implantation at higher dose  $3 \times 10^{16}$  ions/cm<sup>2</sup>. Crystallite size of the films is estimated by well-known Debye–Scherrer's relation as [44]:

$$\text{Crystallite size } (D) = \frac{0.9 \lambda}{\beta \cos \theta} \quad (2)$$

where, symbols have their usual meaning,  $\lambda$  is the wave length of the incident beam ( $\text{CuK}\alpha = 1.54 \text{ \AA}$ ),  $\theta$  is the diffraction angle, and  $\beta$  is FWHM. The crystalline behavior of the film improves with Ag ion implantation due to realizing of strain at higher implantation dose.

#### 3.3. X-ray photoelectron spectroscopy

The presence of species and surface structure of the pure and 120 keV Ag implanted ZnO (at higher dose) thin film have been investigated by X-ray photoelectron spectroscopy (XPS) analysis and obtained results are shown in Fig. 3. In the case of pure ZnO, high-resolution spectra of Zn 2p region exhibits 2p<sub>3/2</sub> and 2p<sub>1/2</sub> states at the position of ~1022.70 eV and ~1045.85 eV. Oxygen shows the asymmetric behavior with two type of oxygen group. First oxygen group is associated with the Zn–O bonding, while second group confirms the existence of hydroxyl group at the binding energy of ~530.57 eV and ~531.96 eV respectively. The existence of Ag is confirmed by the peak observed in the survey scan (for the implanted film), therefore high-resolution XPS spectrum of Ag has been recorded and displayed in Fig. 3.

The binding energies of Ag (3d<sub>5/2</sub>) and Ag (3d<sub>3/2</sub>) are ~374.06 eV and ~368.05 eV, respectively. The energy splitting of 3d doublet is ~6 eV. This energy splitting reveals the metallic nature of Ag at the surface of ZnO film. The core spectrum of Ag is further deconvoluted to identify the interaction of Ag with ZnO and observed the lesser contribution of Ag<sub>2</sub>–O and Ag–Zn–O components in addition to metallic Ag. The existence of hydroxyl group in pure and implanted film is subjected to surface defects or belongs to oxygen deficient region/loosely bound oxygen on the surface [45]. The area of peak associated with hydroxyl group found higher with lesser intensity in the case of an implanted film, which attributed to the creation of defects in the film

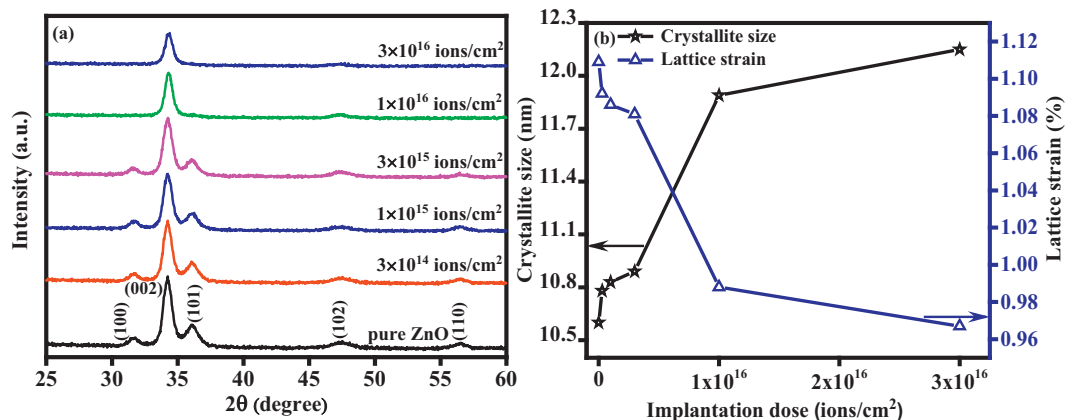


Fig. 2. (a) X-ray diffraction pattern of the pure ZnO and 120 keV Ag implanted thin film with different dose. (b) Variation in crystallite size and lattice strain with implantation dose.

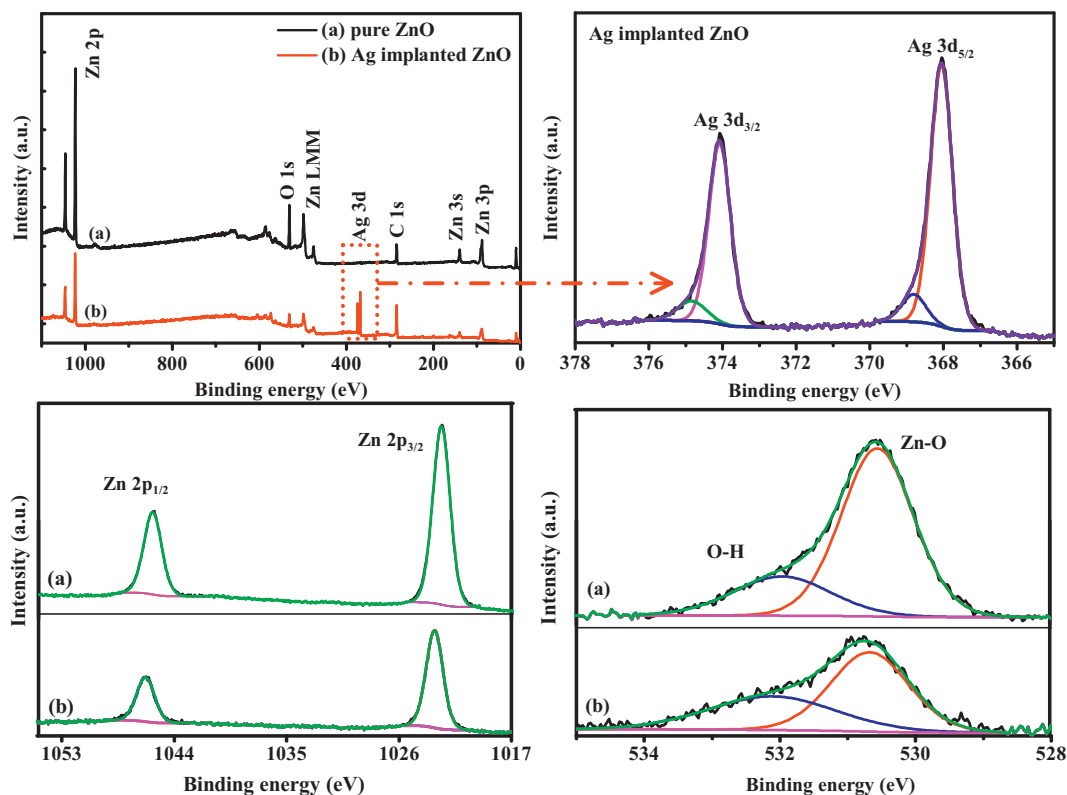


Fig. 3. XPS spectra of the pure ZnO and Ag implanted ZnO nanocomposite thin film at the dose  $3 \times 10^{16}$  ions/cm<sup>2</sup>.

during implantation. The decrement in intensity has been observed in core spectra of the Zn and O, which confirms the change in stoichiometry at the surface of the film and it is also supported by RBS.

### 3.4. UV-visible spectroscopy

Fig. 4 shows UV-Visible transmittance spectra of pure ZnO and Ag implanted ZnO thin films. The range of spectrum is taken from 350 to 750 nm (visible range of electromagnetic spectrum) during the characterization. The transmittance of the film significantly decreases with Ag ion implantation. The value of transmittance is decreased from ~80% to ~40% for pure and Ag implanted ZnO thin film at higher dose  $3 \times 10^{16}$  ions/cm<sup>2</sup> calculated at ~550 nm. This decrement in the transmittance may be attributed due to charge carrier density as well

defects creation during Ag ion implantation in the ZnO film. Surface morphology of the films also play the major role for change in optical properties of the film which is further investigated by atomic force microscopy. The band gap of pure and Ag implanted ZnO thin film has been determined by the help of Tauc's equation [46]:

$$\alpha h\nu = A(h\nu - E_g)^{1/n} \tag{3}$$

where  $\alpha$  is the coefficient of absorption,  $E_g$  is the optical band gap of material and  $\nu$  is the frequency of the incident photon. The index value "n" depends on the nature of the transition (direct, indirect, allowed and forbidden) for the material. For this case, ZnO has direct band gap material, so the value of n for this case is 2 for calculating the band gap of the film. There is no significant change observed in optical band gap of pure and Ag implanted ZnO thin film at the higher implantation dose

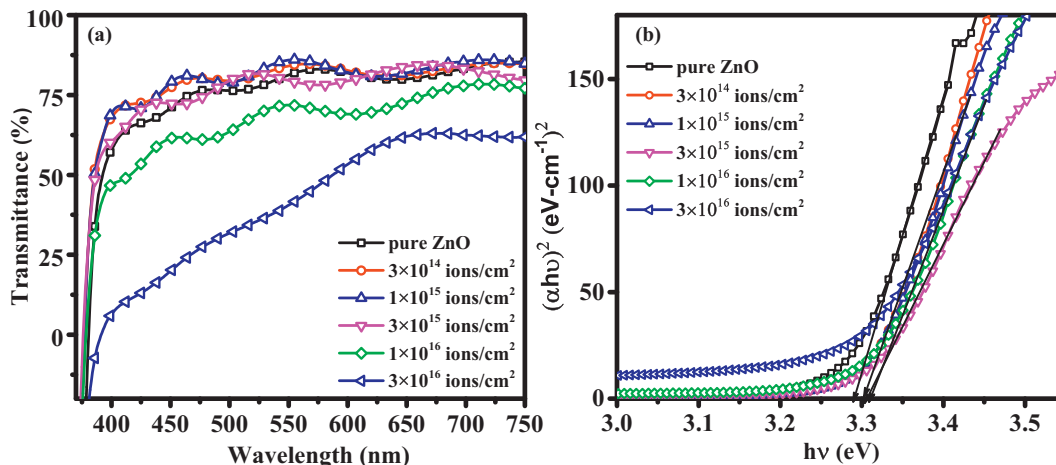


Fig. 4. (a) UV-visible transmittance spectra of the pure ZnO and 120 keV Ag implanted ZnO thin film with different dose. (b) Variation in band gap of the pure and implanted ZnO thin films.



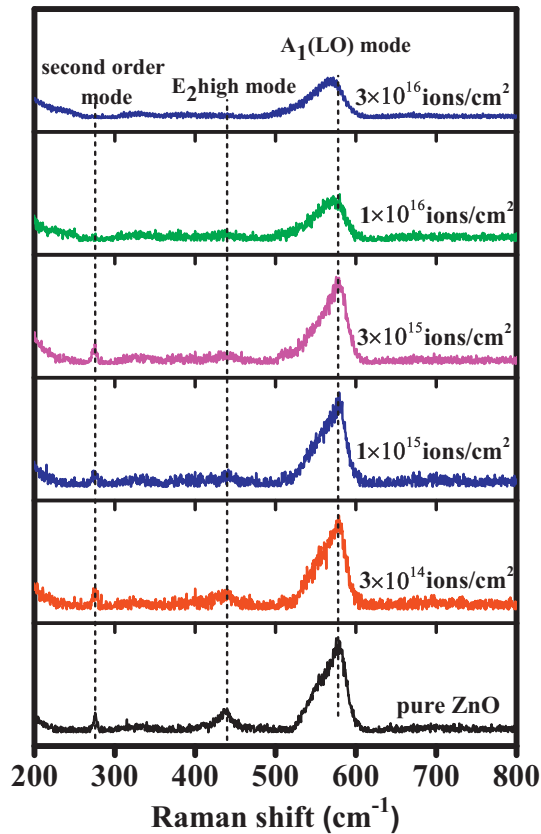


Fig. 5. Raman spectra of the pure ZnO and 120 keV Ag implanted ZnO thin film with different implantation dose.

shown in Fig. 4(b).

### 3.5. Raman spectroscopy

For the case of ZnO (hexagonal wurtzite structure) space group associated with  $C_{6v}^4$  symmetry. According to basic group theory, ZnO

has eight set of phonon normal modes as  $2A_1 + 2E_1 + 2B_1 + 2E_2$  with  $A_1 + E_1$  acoustic modes and remain six modes  $A_1 + E_1 + 2B_1 + 2E_2$  are optical phonon modes at  $\Gamma$  point of the Brillouin zone [47]. Raman spectra for pure and Ag implanted ZnO thin films are shown in Fig. 5. The typical spectra show three bands at  $580\text{ cm}^{-1}$ ,  $438\text{ cm}^{-1}$  and  $274\text{ cm}^{-1}$  for pure and implanted ZnO thin films.

The sharp and highly intense band at  $580\text{ cm}^{-1}$  is assigned to  $A_1$  (LO) mode, which is good agreement with theoretical results. The other bands  $438\text{ cm}^{-1}$  and  $274\text{ cm}^{-1}$  are associated with the  $E_2$  (high) mode and  $B_1$  (high)– $B_2$  (low) mode respectively. The presence of  $E_2$  (high) mode in the spectra of pure ZnO thin film confirmed the formation of the wurtzite structure. The  $E_2$  (high) mode as well  $B_1$  (high)– $B_2$  (low) disappears with Ag ion implantation but  $A_1$  (LO) mode is not much affected at the lower implantation dose up to  $3 \times 10^{15}\text{ ions/cm}^2$ . At the higher implantation dose ( $1 \times 10^{16}$  and  $3 \times 10^{16}\text{ ions/cm}^2$ ), the intensity of the  $A_1$  (LO) mode decreases and observed a red shift in its position due to Ag ion implantation. The observed red shift in  $A_1$  (LO) mode may be due to Ag incorporation in the ZnO matrix during implantation. The structural lattice strain of the film also responsible for observed red shift because films releasing their strain with Ag ion implantation as confirmed by X-ray diffraction pattern. A complete disappearance of the  $E_2$  high mode has been found at the higher implanted dose indicating the Ag incorporation, which is responsible for lower crystallinity and defect creation in the ZnO matrix.

### 3.6. Atomic force microscopy

To observe the surface morphology of pure and Ag implanted ZnO thin films have been characterized by atomic force microscopy (AFM) in tapping mode. Fig. 6 shows the 2-D AFM micrograph ( $1 \times 1\ \mu\text{m}^2$ ) with different implantation dose ranging from  $3 \times 10^{14}$  to  $3 \times 10^{16}\text{ ions/cm}^2$ . The very well inter-connected grains on the top of the surface of the film are clearly observed by AFM images. The grain size of pure ZnO film is calculated and found to be  $\sim 25.28\text{ nm}$  for pure ZnO thin film. The grain size of the film increased with increasing the implantation dose and it reached up to  $\sim 47.51\text{ nm}$  at the higher implantation dose ( $3 \times 10^{16}\text{ ions/cm}^2$ ). The relaxation of the strain with in crystal lattice and appearance of the high density of defects have been found due to interaction of low energy (120 keV) Ag ions with ZnO films and also high dynamic annealing near the surface region.

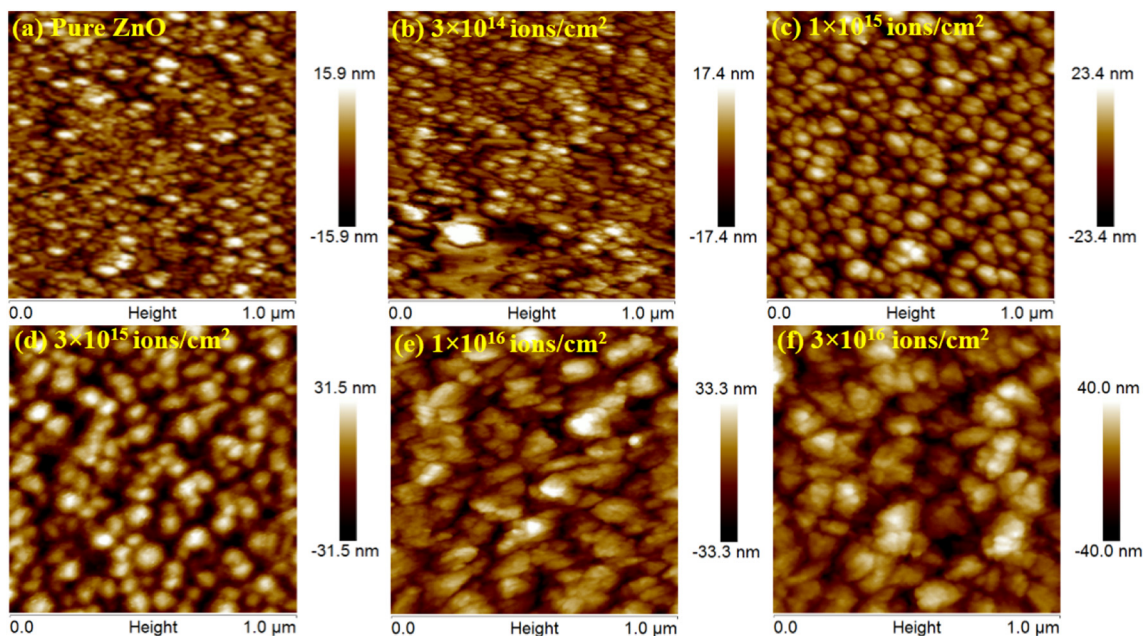


Fig. 6. 2-D AFM micrographs of as-deposited and 120 keV Ag implanted ZnO thin film with different implantation dose.

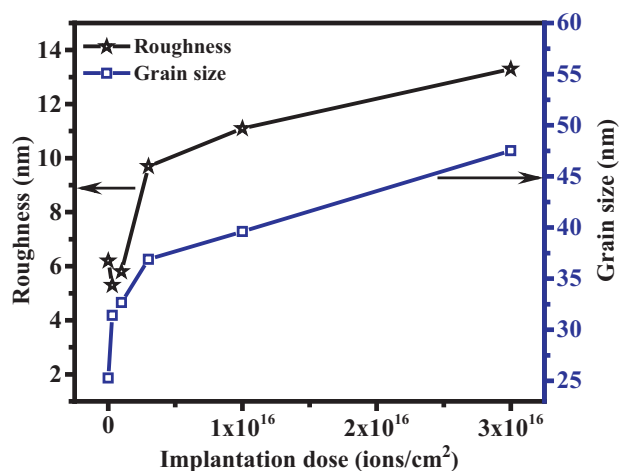


Fig. 7. Variation in roughness and gain size of the pure and 120 keV Ag implanted ZnO thin film with different implantation dose.

Therefore, the formation of defects clusters accumulated at the surface and lead to agglomeration of the grains [48]. The grain size has been increased with implantation as confirmed by AFM and XRD. The grain size of film is larger in comparison to crystallite size as calculated by AFM, because AFM shows the agglomeration of grains however the XRD shows average crystallite size. The root-mean-square roughness ( $R_{\text{rms}}$ ) of pure and Ag implanted ZnO thin films have been estimated by following relation:

$$R_{\text{rms}} = \left[ \frac{1}{N} \sum_{i=1}^N |Z_i - \bar{Z}|^2 \right]^{\frac{1}{2}} \quad (4)$$

where,  $Z$  is mean height distance and  $N$  is number of surface height data points. The roughness of pure ZnO thin film has been calculated by above relation and found to be  $\sim 6.2$  nm. The increment in the roughness values has been observed with increasing the implantation dose. The roughness of the Ag implanted ZnO thin film at higher implantation dose ( $3 \times 10^{16}$  ions/cm<sup>2</sup>) has been found to be  $\sim 13.3$  nm. During ion implantation, potential sputtering take place near the surface of ZnO film due to high density of collision cascades induced by 120 keV Ag ions, which could be responsible for higher surface roughness [49]. Fig. 7 shows the variation in the grain size and roughness of the pure and Ag implanted ZnO thin films with different implantation dose.

#### 4. Conclusions

In present study, structural and optical modifications in ZnO thin films have been investigated with 120 keV Ag ion implantation with different implantation dose. Pure ZnO thin films were successfully synthesized by RF-magnetron sputtering technique. X-ray diffraction spectra reveal the formation of hexagonal wurtzite structure with good crystalline nature along  $c$ -axis. The decrement in the transmittance of the films could be attributed to the charge carrier density which effected by Ag implantation. Surface features of the films observed by AFM and found to be significant changes in roughness and grain size. The lattice strain of the film released with ion implantation and it responsible for the modified crystalline nature of the film with single crystalline behavior. The  $c$ -axis oriented ZnO films are immense technological importance for various optoelectronic device fabrication.

#### Acknowledgement

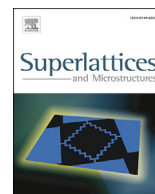
The author (SK Singh) very much thankful to “Technical Education Quality Improvement Programme (TEQIP)” MNIT, Jaipur for providing the financial assistantship during research work. The authors are highly

grateful to the Inter-University Accelerator Centre (IUAC) New Delhi for providing synthesis facility and negative implantation facility for Ag ion implantation. One of the authors (R. Singhal) highly acknowledges the financial support UGC New Delhi project in the term of IUAC New Delhi P.F. No. DRC-14/59/2013/10/169/00036.

#### References

- [1] K. Nomura, H. Ohta, K. Ueda, T. Kamiya, M. Hirano, H. Hosono, Thin-film transistor fabricated in single-crystalline transparent oxide semiconductor, *Science* 300 (2003) 1269–1272, <http://dx.doi.org/10.1126/science.1083212>.
- [2] K. Nomura, H. Ohta, A. Takagi, T. Kamiya, M. Hirano, H. Hosono, Room-temperature fabrication of transparent flexible thin-film transistors using amorphous oxide semiconductors, *Nature* 432 (2004) 488–492, <http://dx.doi.org/10.1038/nature03090>.
- [3] Z. Zang, A. Nakamura, J. Temmyo, Single cuprous oxide films synthesized by radical oxidation at low temperature for PV application, *Opt. Express* 21 (2013) 11448, <http://dx.doi.org/10.1364/OE.21.011448>.
- [4] C. Jagadish, S.J. Pearton, Zinc Oxide Bulk, Thin Films and Nanostructures: Processing, Properties, and Applications, Elsevier, 2011, <http://dx.doi.org/10.1016/b978-008044722-3/50000-2>.
- [5] W. Il Park, J.S. Kim, G.C. Yi, M.H. Bae, H.J. Lee, Fabrication and electrical characteristics of high-performance ZnO nanorod field-effect transistors, *Appl. Phys. Lett.* 85 (2004) 5052–5054, <http://dx.doi.org/10.1063/1.1821648>.
- [6] E.M.C. Fortunato, P.M.C. Barquinha, A.C.M.B.G. Pimentel, A.M.F. Gonçalves, A.J.S. Marques, R.F.P. Martins, L.M.N. Pereira, Wide-bandgap high-mobility ZnO thin-film transistors produced at room temperature, *Appl. Phys. Lett.* 85 (2004) 2541–2543, <http://dx.doi.org/10.1063/1.1790587>.
- [7] G.A. Hirata, J. McKittrick, T. Cheeks, J.M. Siqueiros, J.A. Diaz, O. Contreras, O.A. Lopez, Synthesis and optoelectronic characterization of gallium doped zinc oxide transparent electrodes, *Thin Solid Films* 288 (1996) 29–31, [http://dx.doi.org/10.1016/S0040-6090\(96\)08862-1](http://dx.doi.org/10.1016/S0040-6090(96)08862-1).
- [8] M. Willander, O. Nur, Q.X. Zhao, L.L. Yang, M. Lorenz, B.Q. Cao, J. Zúñiga Pérez, C. Czekalla, G. Zimmermann, M. Grundmann, A. Bakin, A. Behrends, M. Al-Suleiman, A. El-Shaer, A. Che Mofo, B. Postels, A. Waag, N. Boukos, A. Travlos, H.S. Kwack, J. Guinard, D. Le Si Dang, Zinc oxide nanorod based photonic devices: recent progress in growth, light emitting diodes and lasers, *Nanotechnology* 20 (2009) 332001, <http://dx.doi.org/10.1088/0957-4484/20/33/332001>.
- [9] Z. Zang, X. Zeng, J. Du, M. Wang, X. Tang, Femtosecond laser direct writing of microholes on roughened ZnO for output power enhancement of InGaN light-emitting diodes, *Opt. Lett.* 41 (2016) 3463, <http://dx.doi.org/10.1364/OL.41.003463>.
- [10] F.C. Krebs, Y. Thomann, R. Thomann, J.W. Andreasen, A simple nanostructured polymer/ZnO hybrid solar cell—preparation and operation in air, *Nanotechnology* 19 (2008) 424013, <http://dx.doi.org/10.1088/0957-4484/19/42/424013>.
- [11] C. Li, C. Han, Y. Zhang, Z. Zang, M. Wang, X. Tang, J. Du, Enhanced photoresponse of self-powered perovskite photodetector based on ZnO nanoparticles decorated CsPbBr<sub>3</sub> films, *Sol. Energy Mater. Sol. Cells* 172 (2017) 341–346, <http://dx.doi.org/10.1016/j.solmat.2017.08.014>.
- [12] M.-W. Ahn, K.-S. Park, J.-H. Heo, J.-G. Park, D.-W. Kim, K.J. Choi, J.-H. Lee, S.-H. Hong, Gas sensing properties of defect-controlled ZnO-nanowire gas sensor, *Appl. Phys. Lett.* 93 (2008) 263103, <http://dx.doi.org/10.1063/1.3046726>.
- [13] R. Singhal, D.C. Agarwal, Y.K. Mishra, D. Kabiraj, G. Mattei, J.C. Pivin, R. Chandra, D.K. Avasthi, Synthesis, characterizations, and thermal induced structural transformation of silver-fullerene C60 nanocomposite thin films for applications in optical devices, *J. Appl. Phys.* 107 (2010) 103504, <http://dx.doi.org/10.1063/1.3366709>.
- [14] K. Akimoto, S. Ishizuka, M. Yanagita, Y. Nawa, G.K. Paul, T. Sakurai, Thin film deposition of Cu<sub>2</sub>O and application for solar cells, *Sol. Energy* 80 (2006) 715–722, <http://dx.doi.org/10.1016/j.solener.2005.10.012>.
- [15] S.K. Singh, R. Singhal, R. Vishnoi, V.V.S. Kumar, P.K. Kulariya, Swift heavy ion induced optical and structural modifications in RF sputtered nanocrystalline ZnO thin film, *Indian J. Phys.* 91 (2017) 547–554, <http://dx.doi.org/10.1007/s12648-016-0950-6>.
- [16] R. Vishnoi, R. Singhal, K. Asokan, D. Kanjilal, D. Kaur, Ion irradiation induced modifications of nanostructured Ni-Mn-Sn ferromagnetic shape memory alloy thin films, *Thin Solid Films* 520 (2011) 1631–1637, <http://dx.doi.org/10.1016/j.tsf.2011.08.021>.
- [17] R. Singhal, A. Kumar, Y.K. Mishra, S. Mohapatra, J.C. Pivin, D.K. Avasthi, Swift heavy ion induced modifications of fullerene C70 thin films, *Nucl. Instrum. Methods Phys. Res., Sect. B* 266 (2008) 3257–3262, <http://dx.doi.org/10.1016/j.nimb.2008.04.003>.
- [18] B.J. Jin, S. Im, S.Y. Lee, Violet and UV luminescence emitted from ZnO thin films grown on sapphire by pulsed laser deposition, *Thin Solid Films* 366 (2000) 107–110, [http://dx.doi.org/10.1016/S0040-6090\(00\)00746-X](http://dx.doi.org/10.1016/S0040-6090(00)00746-X).
- [19] M. Wang, J. Wang, W. Chen, Y. Cui, L. Wang, Effect of preheating and annealing temperatures on quality characteristics of ZnO thin film prepared by sol-gel method, *Mater. Chem. Phys.* 97 (2006) 219–225, <http://dx.doi.org/10.1016/j.matchemphys.2005.07.072>.
- [20] F.D. Paraguay, W.L. Estrada, D.R.N. Acosta, E. Andrade, M. Miki-Yoshida, Growth, structure and optical characterization of high quality ZnO thin films obtained by spray pyrolysis, *Thin Solid Films* 350 (1999) 192–202, [http://dx.doi.org/10.1016/S0040-6090\(99\)00050-4](http://dx.doi.org/10.1016/S0040-6090(99)00050-4).

- [21] W.W. Wenas, A. Yamada, M. Konagai, K. Takahashi, Textured ZnO thin films for solar cells grown by metalorganic chemical vapor deposition, *Jpn. J. Appl. Phys.* 30 (1991) L441–L443, <http://dx.doi.org/10.1143/JJAP.30.L441>.
- [22] Y. Segawa, A. Ohtomo, M. Kawasaki, H. Koinuma, Z.K. Tang, P. Yu, G.K.L. Wong, Growth of ZnO thin film by laser MBE: lasing of exciton at room temperature, *Phys. Status Solidi* 202 (1997) 669–672, [http://dx.doi.org/10.1002/1521-3951\(199708\)202:2<669::AID-PSSB669>3.0.CO;2-T](http://dx.doi.org/10.1002/1521-3951(199708)202:2<669::AID-PSSB669>3.0.CO;2-T).
- [23] C.-C. Lin, S.-Y. Chen, S.-Y. Cheng, H.-Y. Lee, Properties of nitrogen-implanted p-type ZnO films grown on Si<sub>3</sub>N<sub>4</sub>/Si by radio-frequency magnetron sputtering, *Appl. Phys. Lett.* 84 (2004) 5040–5042, <http://dx.doi.org/10.1063/1.1763640>.
- [24] D.C. Agarwal, F. Singh, D. Kabiraj, S. Sen, P.K. Kulriya, I. Sulania, S. Nozaki, R.S. Chauhan, D.K. Avasthi, Thermal and ion induced annealing of nanocrystalline ZnO thin film deposited by atom beam sputtering, *J. Phys. D. Appl. Phys.* 41 (2008) 45305, <http://dx.doi.org/10.1088/0022-3727/41/4/045305>.
- [25] S.K. Singh, R. Singhal, V.V. Siva Kumar, Study on swift heavy ions induced modifications of Ag-ZnO nanocomposite thin film, *Superlattice. Microst.* 103 (2017) 195–204, <http://dx.doi.org/10.1016/j.spmi.2017.01.032>.
- [26] X.H. Wang, J. Shi, S. Dai, Y. Yang, A sol-gel method to prepare pure and gold colloid doped ZnO films, *Thin Solid Films* 429 (2003) 102–107, [http://dx.doi.org/10.1016/S0040-6090\(03\)00057-9](http://dx.doi.org/10.1016/S0040-6090(03)00057-9).
- [27] H.S. Kang, B. Du Ahn, J.H. Kim, G.H. Kim, S.H. Lim, H.W. Chang, S.Y. Lee, Structural, electrical, and optical properties of p-type ZnO thin films with Ag dopant, *Appl. Phys. Lett.* 88 (2006) 202108, <http://dx.doi.org/10.1063/1.2203952>.
- [28] Y. Yan, M.M. Al-Jassim, S.-H. Wei, Doping of ZnO by group-IB elements, *Appl. Phys. Lett.* 89 (2006) 181912, <http://dx.doi.org/10.1063/1.2378404>.
- [29] D.L. Hou, X.J. Ye, H.J. Meng, H.J. Zhou, X.L. Li, C.M. Zhen, G.D. Tang, Magnetic properties of n-type Cu-doped ZnO thin films, *Appl. Phys. Lett.* 90 (2007) 142502, <http://dx.doi.org/10.1063/1.2719034>.
- [30] R. Singhal, J.C. Pivin, D.K. Avasthi, Ion beam irradiation-induced tuning of SPR of Au nanoparticles in fullerene C70 matrix: dependence of energy loss, *J. Nanopart. Res.* 15 (2013) 1641, <http://dx.doi.org/10.1007/s11051-013-1641-2>.
- [31] R. Singhal, D.C. Agarwal, S. Mohapatra, Y.K. Mishra, D. Kabiraj, F. Singh, D.K. Avasthi, A.K. Chawla, R. Chandra, G. Mattei, J.C. Pivin, Synthesis and characterizations of silver-fullerene C70 nanocomposite, *Appl. Phys. Lett.* 93 (2008) 3–5, <http://dx.doi.org/10.1063/1.2976674>.
- [32] R. Singhal, D. Kabiraj, P.K. Kulriya, J.C. Pivin, R. Chandra, D.K. Avasthi, Blue-shifted SPR of Au nanoparticles with ordering of carbon by dense ionization and thermal treatment, *Plasmonics* 8 (2013) 295–305, <http://dx.doi.org/10.1007/s11468-012-9389-6>.
- [33] Q. Wang, Q. Sun, G. Chen, Y. Kawazoe, P. Jena, Vacancy-induced magnetism in ZnO thin films and nanowires, *Phys. Rev. B Condens. Matter Mater. Phys.* 77 (2008) 205411, <http://dx.doi.org/10.1103/PhysRevB.77.205411>.
- [34] M.A. Myers, M.T. Myers, M.J. General, J.H. Lee, L. Shao, H. Wang, P-type ZnO thin films achieved by N<sup>+</sup> ion implantation through dynamic annealing process, *Appl. Phys. Lett.* 101 (2012) 112101, <http://dx.doi.org/10.1063/1.4751467>.
- [35] Y.W. Heo, M.P. Ivill, K. Ip, D.P. Norton, S.J. Pearton, J.G. Kelly, R. Rairigh, A.F. Hebard, T. Steiner, Effects of high-dose Mn implantation into ZnO grown on sapphire, *Appl. Phys. Lett.* 84 (2004) 2292–2294, <http://dx.doi.org/10.1063/1.1690111>.
- [36] J.S. Williams, Ion implantation of semiconductors, *Mater. Sci. Eng. A* A253 (1998) 8–15, <http://dx.doi.org/10.1049/ep.1976.0363>.
- [37] T. Diaz De La Rubia, G.H. Gilmer, Structural transformations and defect production in ion implanted silicon: a molecular dynamics simulation study, *Phys. Rev. Lett.* 74 (1995) 2507–2510, <http://dx.doi.org/10.1103/PhysRevLett.74.2507>.
- [38] S. Venkataraj, N. Ohashi, I. Sakaguchi, Y. Adachi, T. Ohgaki, H. Ryoken, H. Haneda, Structural and magnetic properties of Mn-ion implanted ZnO films, *J. Appl. Phys.* 102 (2007) 14905, <http://dx.doi.org/10.1063/1.2752123>.
- [39] D. Evanoff, et al., Size-controlled synthesis of nanoparticles. 2. Measurement of extinction, scattering, and absorption cross sections, *J. Phys. Chem. B* 108 (2004) 13957–13962, <http://dx.doi.org/10.1021/jp0475640>.
- [40] J.F. Ziegler, J.P. Biersack, *Treatise on heavy-ion science: volume 6: astrophysics, chemistry, and condensed matter, Treatise Heavy-Ion Sci.* Springer US, Boston, MA, 1985, pp. 93–129, [http://dx.doi.org/10.1007/978-1-4615-8103-1\\_3](http://dx.doi.org/10.1007/978-1-4615-8103-1_3).
- [41] L.R. Doolittle, Algorithms for the rapid simulation of Rutherford backscattering spectra, *Nucl. Inst. Methods Phys. Res. B* 9 (1985) 344–351, [http://dx.doi.org/10.1016/0168-583X\(85\)90762-1](http://dx.doi.org/10.1016/0168-583X(85)90762-1).
- [42] P.D. Townsend, Optical effects of ion implantation, *Rep. Prog. Phys.* 50 (1987) 501–558, <http://dx.doi.org/10.1088/0034-4885/50/5/001>.
- [43] B.D. Cullity, *Element of X-ray Diffraction*, Addison-Wesley Publishing Company, Inc., 1978.
- [44] A.L. Patterson, The Scherrer formula for X-ray particle size determination, *Phys. Rev.* 56 (1939) 978–982, <http://dx.doi.org/10.1103/PhysRev.56.978>.
- [45] M. Chen, Z.L. Pei, X. Wang, C. Sun, L.S. Wen, Structural, electrical, and optical properties of transparent conductive oxide ZnO:Al films prepared by dc magnetron reactive sputtering, *J. Vac. Sci. Technol. A* 19 (2001) 963–970, <http://dx.doi.org/10.1116/1.1368836>.
- [46] J. Tauc, Optical properties and electronic structure of amorphous Ge and Si, *Mater. Res. Bull.* 3 (1968) 37–46, [http://dx.doi.org/10.1016/0025-5408\(68\)90023-8](http://dx.doi.org/10.1016/0025-5408(68)90023-8).
- [47] H. Morkoç, U. Özgür, *Zinc Oxide: Fundamentals, Materials and Device Technology*, Wiley-VCH, 2009.
- [48] A.Y. Azarov, A. Hallén, X.L. Du, P. Rauwel, A.Y. Kuznetsov, B.G. Svensson, Effect of implanted species on thermal evolution of ion-induced defects in ZnO, *J. Appl. Phys.* 115 (2014), <http://dx.doi.org/10.1063/1.4866055>.
- [49] L. Hanley, S.B. Sinnott, The growth and modification of materials via ion — surface processing, *Surf. Sci.* 500 (2002) 500–522.



# Study on swift heavy ions induced modifications of Ag-ZnO nanocomposite thin film



S.K. Singh <sup>a,\*</sup>, R. Singhal <sup>a</sup>, V.V. Siva Kumar <sup>b</sup>

<sup>a</sup> Department of Physics, Malaviya National Institute of Technology Jaipur, JLN Marg, Malaviya Nagar, Jaipur 302017, India

<sup>b</sup> Inter-University Accelerator Centre, Aruna Asaf Ali Marg, New Delhi 110067, India

## ARTICLE INFO

### Article history:

Received 1 July 2016

Received in revised form 19 January 2017

Accepted 20 January 2017

Available online 24 January 2017

### Keywords:

Ag-ZnO nanocomposite thin film

Ion irradiation

Atomic force microscopy

X-ray diffraction

## ABSTRACT

In the present work, swift heavy ion (SHI) irradiation induced modifications in structural and optical properties of Ag-ZnO nanocomposite thin films have been investigated. Ag-ZnO nanocomposite (NCs) thin films were synthesized by RF magnetron sputtering technique and irradiated with 100 MeV Ag<sup>7+</sup> ions at three different fluences  $3 \times 10^{12}$ ,  $1 \times 10^{13}$  and  $3 \times 10^{13}$  ions/cm<sup>2</sup>. Rutherford Backscattering Spectrometry revealed Ag concentration to be ~8.0 at.%, and measured thickness of the films was ~55 nm. Structural properties of pristine and irradiated films have been analyzed by X-ray diffraction analysis and found that variation in crystallite size of the film with ion irradiation. X-ray photoelectron spectroscopy (XPS) indicates the formation of Ag-ZnO nanocomposite thin film with presence of Ag, Zn and O elements. Oxidation state of Ag and Zn also estimated by XPS analysis. Surface plasmon resonance (SPR) of Ag nanoparticle has appeared at ~475 nm in the pristine thin film, which is blue shifted by ~30 nm in film irradiated at fluence of  $3 \times 10^{12}$  ions/cm<sup>2</sup> and completely disappeared in film irradiated at higher fluences,  $1 \times 10^{13}$  and  $3 \times 10^{13}$  ions/cm<sup>2</sup>. A marginal change in the optical band gap of Ag-ZnO nanocomposite thin film is also found with increasing ion fluence. Surface morphology of pristine and irradiated films have been studied using Atomic Force Microscopy (AFM). Raman and Photo-luminescence (PL) spectra of nanocomposite thin films have been investigated to understand the ion induced modifications such as lattice defects and disordering in the nanocomposite thin film.

© 2017 Elsevier Ltd. All rights reserved.

## 1. Introduction

The functional nanomaterial with potential technological applications is the prominent field for researcher and scientist community in the present scenario. ZnO is a multi-functional material of II-VI group with the optical band gap of 3.3 eV at room temperature and having hexagonal wurtzite crystal structure [1]. In recent years, ZnO is very encouraging material that is utilized in multiple fields such as solar cells, transparent conductive contacts, light emitting devices, spintronic devices, laser deflectors, paints, antibacterial activity, bio-sensors, piezoelectric transducers and gas sensors [2–12] and many efforts have been done to modify the properties of ZnO such as doping, ion irradiation, etc. so that it can be used more widely in research fields. The physical properties of ZnO thin films also depend on the deposition parameters and different deposition

\* Corresponding author.

E-mail address: [singhshushant86@gmail.com](mailto:singhshushant86@gmail.com) (S.K. Singh).

techniques. Sputtering [13], spin coating technique [14], spray pyrolysis [15], sol-gel method [16], chemical vapour deposition [17], pulsed laser deposition [18] are the various methods for growing the ZnO thin films for the different applications. Doping of novel metal in ZnO matrix offers the effective tool for improving the structural and optical properties of the thin film [19,20]. The modifications of optical and structural properties in Ag-fullerene, Ag-TiO<sub>2</sub> and Ag-SiO<sub>2</sub> nanocomposite thin films due to SHI irradiation have also been reported by many groups [21–27]. Swift heavy ion irradiation technique is mostly used to modify or enhance the properties of several materials [28–30]. When energetic ions are incident on the target material, they transfer a large amount of energy and produces a high density of electronic excitation along ion path in the narrow cylindrical zone. This high amount of deposited energy leads to the high density of defects in the target material, due to the heating effect along the ion path [31]. These defects and a large amount of energy in the target material are responsible for the structural and optical modifications by SHI irradiation. Ag-ZnO nanocomposite provides the diverse application in the fabrication of optoelectronic devices as silver nanocomposite shows better optical properties in the visible range of electromagnetic spectrum. The photo-catalytic activity of ZnO is also effected by the presence of silver nanoparticles. In the photo-absorption process, the silver nanoparticle can trap the charge carrier and these charge carriers are responsible for restriction of the charge recombination process [32–35].

In this paper, we have investigated the 100 MeV Ag<sup>7+</sup> ions beam induced structural and optical modifications of Ag-ZnO nanocomposite thin films which were prepared by RF magnetron sputtering and irradiated at three different fluences at  $3 \times 10^{12}$ ,  $1 \times 10^{13}$  and  $3 \times 10^{13}$  ions/cm<sup>2</sup>. Ion-induced structural modifications in the film are estimated by atomic force microscopy (AFM) and X-ray diffraction analysis. The photocatalytic behaviour of the film is estimated by photo-luminescence spectra of the Ag-ZnO nanocomposite thin films.

## 2. Experimental plan

Ag-ZnO nanocomposite thin films of thickness ~55 nm were deposited on glass and silicon substrates by the RF sputtering technique. ZnO target was prepared from ZnO powder (Alfa Aesar, 99.9%) using hydraulic press machine and was sintered at 1200 °C in the tube furnace for 24 h in the presence of oxygen gas. Small pieces of silver (1 mm thick) were glued on the ZnO target (3 mm thickness, 2-inch diameter) at a different position during deposition. The substrates were cleaned in acetone using ultra-sonication and rinsed in deionized water. The pressure in the sputtering chamber was  $10^{-6}$  Torr before introducing the argon gas into the chamber, achieved by turbo molecular pump which was coupled with the rotary pump in the sputtering unit. The deposition was performed at a pressure  $5 \times 10^{-2}$  Torr with the presence of argon gas (grade-I) in the sputtering chamber. The target to substrate distance was calculated before deposition and found to be ~4 cm. The substrate temperature was ~300 °C, which was measured by thermocouple gauge and controlled using a feed-back controlled heater. The deposition was performed for 30–40 min with RF power at 150 W and the self-bias voltage at 250–300 V measured by sputtering unit. Ag-ZnO NCs thin films were irradiated with 100 MeV Ag<sup>7+</sup> ion beam by using 15 UD pelletron accelerator facility at Inter University Accelerator Centre, New Delhi. The ion beam is scanned over the area  $1 \times 1$  cm<sup>2</sup> with three different fluence at  $3 \times 10^{12}$ ,  $1 \times 10^{13}$  and  $3 \times 10^{13}$  ions/cm<sup>2</sup>.

The thickness and actual metal atomic fraction of nanocomposite thin films, deposited on Si substrate were measured by the Rutherford backscattered spectroscopy (RBS) by using PARAS facility at Inter University Accelerator Centre (IUAC) New Delhi. The XRD spectra of films were recorded with Panalytical Xpert Pro diffractometer using Cu-K<sub>α</sub> at Material Research Centre (MRC) Jaipur. UV–visible absorption spectra of films was recorded using a dual beam Lambda 900 (Perkin Elmer) spectrometer at MRC Jaipur. Surface morphology was estimated by atomic force microscopy (Bruker) MRC Jaipur. Raman measurements of nanocomposite thin films were performed using AIRIX STR 500 Raman microscope with laser excitation at 532 nm and photo-luminescence (PL) spectra of thin films also recorded by the same instrument with 325 nm excitation wavelength of He-Cd laser at room temperature.

## 3. Results and discussion

### 3.1. Rutherford backscattering spectroscopy

Fig. 1 shows the RBS spectrum of pristine Ag-ZnO nanocomposite (NCs) thin film on Si substrate. To estimate the metal atomic fraction and thickness of thin film, the obtained experimental RBS spectrum of the film was simulated by SIMNRA program and fitted as showing in Fig. 1. The Ag atomic fraction was calculated to be ~8.0 at.%, and thickness of pristine Ag-ZnO nanocomposite thin film was ~55 nm which was observed by SIMNRA simulation program [36]. To understand the modifications of Ag-ZnO nanocomposite thin films due to 100 MeV Ag<sup>7+</sup> ion beam, it is necessary to find out the dynamics of ion interaction into the nanocomposite thin film. When swift heavy ions (SHI) traverse through the target material, it interact with the electron as well nuclei of the target material and loose huge amount of energy in two different ways: (a) direct transfer of energy to target atoms by elastic collisions, termed as nuclear energy loss ( $S_n$ ) and (b) transfer of energy of incoming ions to the electrons of target atoms, termed as electronic energy loss ( $S_e$ ). Large amount of energy deposited by incident ions is responsible for the atomic displacement along the beam path and explained by two different models; Coulomb spike model (CSM) and Thermal spike model (TSM). When 100 MeV Ag<sup>7+</sup> ions pass through the nanocomposite thin film, they loss their energy by creating electronic excitation as well as ionization of the atom of the target material by an inelastic collision between the incident ion and target electrons. Localized defects and disordered region created by electronic

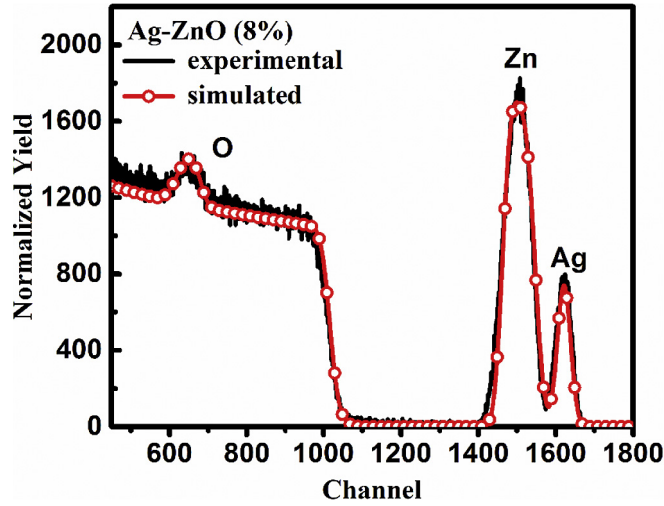


Fig. 1. Rutherford backscattering spectrum (RBS) of Ag-ZnO nanocomposite thin film.

excitation during SHI irradiation are responsible for modifications in the lattice structure, optical properties and structural properties of the target material. In this study, the value of Electronic energy loss ( $S_e$ )  $\sim 20.39$  keV/nm and nuclear energy loss ( $S_n$ )  $\sim 0.122$  keV/nm for 100 MeV  $\text{Ag}^{7+}$  with ion range in target material is 20.15  $\mu\text{m}$ , calculated by stopping and range of ions in matter (SRIM) software [37]. Electronic and nuclear energy loss depend on incident ion energy, in low energy region nuclear energy loss ( $S_n$ ) is dominant and another side in high energy region, electronic energy loss ( $S_e$ ) is dominant, which can clearly be seen in Fig. 2. In present work, 100 MeV energy is taken for irradiation of nanocomposite films as for high energy region electronic energy loss will be dominant and responsible for modifications which are shown in Fig. 2 by a vertical dashed line.

### 3.2. XRD measurements

The structural modifications of pristine and irradiated Ag-ZnO thin films at different fluences have been analyzed using X-ray diffraction (XRD) technique and XRD patterns are shown in Fig. 3. It is clear that the pristine Ag-ZnO thin film crystallizes in hexagonal wurtzite phase with lattice planes (100), (002), and (101) at  $31.34^\circ$ ,  $34.12^\circ$  and  $35.95^\circ$  respectively. The indexing of XRD pattern was done in accordance with the JCPDS card no. 89-1397. Crystallite plane spacing ( $d$ ) for pristine and irradiated thin film have been estimated by using Bragg's formula:

$$n\lambda = 2d \sin\theta$$

Where  $n$  is the order of diffraction,  $\lambda$  is wavelength (1.54  $\text{\AA}$ ) and  $d$  denotes the inter planer spacing of indices ( $h k l$ ) and  $\theta$  is the angle of diffraction. The crystalline plane spacing ( $d$ ) is calculated for the (002) plane with first order diffraction ( $n = 1$ ). The value of lattice constants have been calculated by using crystal structural formula for hexagonal wurtzite structure which described in this form [38]:

$$\frac{1}{d_{hkl}^2} = \frac{4}{3} \left( \frac{h^2 + hk + k^2}{a^2} \right) + \frac{l^2}{c^2}$$

Where  $h, k, l$  shows the Miller indices for the thin film,  $d$  is the interplanar spacing and  $a, c$  are the lattice constant. Lattice parameter and  $d$  spacing for the pristine and irradiated thin film are tabulated in Table 1. Stress in the pristine and irradiated thin film is also evaluated by using the relation [39]:

$$\sigma = -233 \left[ \frac{c - c'}{c'} \right] \text{ [GPa]}$$

Symbols have their usual meaning in above formula,  $\sigma$  is the stress for the sample and  $c, c'$  are the lattice constant for the Ag-ZnO composite thin film and strain free lattice constant for pure ZnO respectively. Stress variation of the pristine and irradiated thin film has been shown in Fig. 4 (inset) and summarized in Table 1. The presence of Ag in pristine and irradiated thin films was also confirmed by the peak obtained at  $38.23^\circ$  with (111) plane [JCPDS card no. 87-0720]. The crystallite size was determined by using the Scherrer's formula:

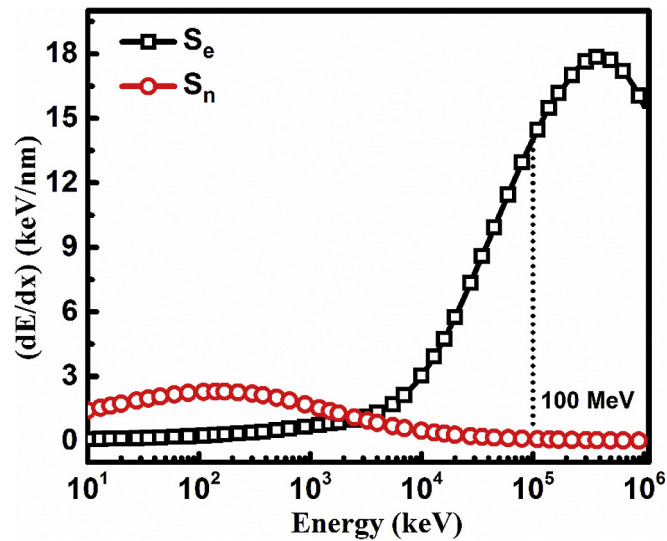


Fig. 2. The nuclear and electronic energy losses of 100 MeV  $\text{Ag}^{7+}$  ions as the function of incident ion energy.

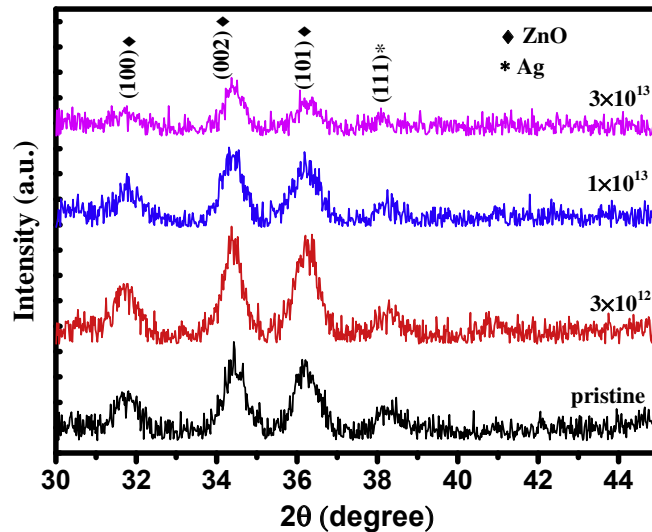


Fig. 3. XRD spectra of pristine and irradiated films at three different fluences.

**Table 1**

Lattice parameters, crystallite size and stress of the pristine and irradiated thin films estimated by X-ray diffraction spectra.

Sl. No.	Fluence (ions/cm <sup>2</sup> )	d spacing (Å) (for 002)	Lattice constant 'a' (Å)	Lattice constant 'c' (Å)	c/a ratio	Crystallite size (nm)	Stress $\sigma$ (GPa)
1.	Pristine	2.601	$3.249 \pm 0.002$	$5.202 \pm 0.002$	1.601	$13.51 \pm 0.81$	+0.14
2.	$3 \times 10^{12}$	2.604	$3.252 \pm 0.001$	$5.208 \pm 0.001$	1.602	$14.66 \pm 0.60$	-0.13
3.	$1 \times 10^{13}$	2.605	$3.248 \pm 0.002$	$5.210 \pm 0.002$	1.604	$12.65 \pm 0.72$	-0.22
4.	$3 \times 10^{13}$	2.602	$3.256 \pm 0.003$	$5.204 \pm 0.003$	1.598	$11.68 \pm 1.08$	+0.04

$$D = \frac{0.9\lambda}{\beta \cos\theta}$$

Where  $\lambda$  is wavelength ( $\text{CuK}\alpha = 1.54 \text{ \AA}$ ),  $\theta$  is the Bragg diffraction angle and  $\beta$  is full width at half maxima (FWHM). Fig. 4 shows the variation in crystallite size of the pristine and irradiated thin films with different ion fluence which was calculated from the x-ray diffraction pattern and summarized in Table 1. The changes in the crystallite size revealed that the

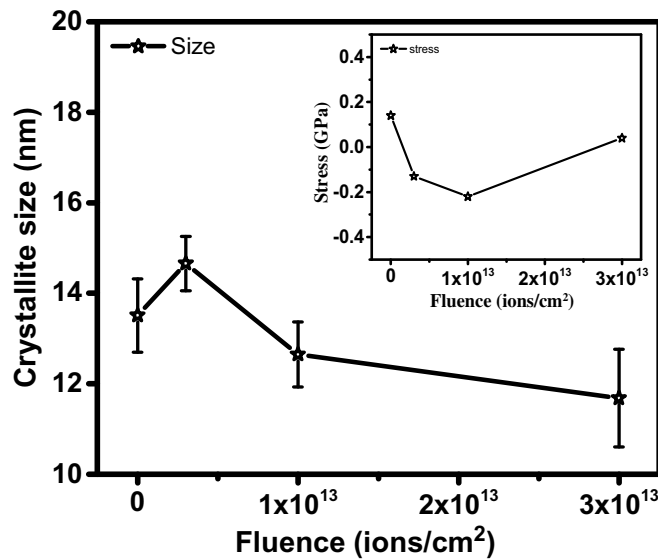


Fig. 4. Crystallite size of pristine and 100 MeV Ag<sup>7+</sup> irradiated thin film.

crystalline behaviour of nanocomposite film improves with ion irradiation at lower fluence, but crystallinity is decreased at higher fluence. The crystallinity of the films is effected by ion irradiation at different fluences which are related to the lattice strain between the grains of the nanocomposite thin film, at the lower fluence lattice strain releases between the grains and it is responsible for the improvement in the crystalline behaviour of the film. But when irradiation fluence increases, more number of incident ions interact with the film attributed to the disordering inside the large grains due to overlapping of the ion tracks [40].

### 3.3. XPS analysis

To determine the different component and oxidation states of Ag-ZnO nanocomposite thin film, XPS studies of the pristine film were carried out. The spectra is given in Fig. 5 where in (a) shows the full scan spectra while (b-d) show the core shell spectra corresponding to the Zn 2p, O 1s and Ag 3d state of the elements. The position of peaks were matched with the standard database and it indicated the presence of Zn, O and Ag elements in the specimen. The short scan of Zn 2p region exhibited Zn<sup>2+</sup> state with binding energy ~1023.26 eV and ~1046.37 eV for 2p<sub>3/2</sub> and 2p<sub>1/2</sub> states respectively. The short scan for O 1s exhibited asymmetric behaviour which was contribution of two types of oxygen groups. The first peak which located at lower binding energy (~531.23 eV) was attributed to Zn–O bonding and other peak (~532.87 eV) was related to hydroxyl group which is resulted due to surface defects. Presence of this group are advantageous in photocatalytic behaviour and play a significant role for preventing the electron-hole recombination process [41]. Fig. 5 (d) indicates the splitting of Ag (3d<sub>5/2</sub>) and Ag (3d<sub>3/2</sub>) were clearly seen at ~374.67 eV and ~368.61 eV, respectively. The spectrum was further deconvoluted to estimate a smaller contribution from Ag<sub>2</sub>O and Ag-Zn-O components in addition to the metallic Ag. The concentration of the Ag in ZnO matrix also calculated form the spectra and found to be ~8% which was in good agreement with the RBS results.

### 3.4. UV–visible absorption spectroscopy

To study the optical modifications of pristine and 100 MeV Ag ion beam irradiated Ag-ZnO nanocomposite thin films, UV–visible absorption spectroscopy measurement was done. Fig. 6 shows the optical absorption spectra of pristine and irradiated thin films. For pristine Ag-ZnO thin film, a broad SPR peak was observed at ~475 nm, when fluence is increased up to  $3 \times 10^{12}$  ions/cm<sup>2</sup>, SPR peak is shifted (~30 nm) towards the lower wavelength (blue shift) and found at 445 nm. The intensity of the SPR peak for the  $3 \times 10^{12}$  ions/cm<sup>2</sup> fluence is also found to be decreased in comparison to pristine film, and it is disappeared on further increasing the fluence. This shift and decreased intensity may be the result of the reduction of metal particle size with irradiation fluence [42] and also effected by the modifications in the ZnO matrix during SHI irradiation. During the high energy ion irradiation electronic energy loss is more dominant, so a large amount of energy transfer from an incident ion to target material which creates the high temperature zone along the incident ion path according to thermal spike model and this high temperature leads the melting of material along the ion path and responsible for the optical modifications in Ag-ZnO nanocomposite thin film by ion irradiation. Fig. 7 shows the graph between  $(\alpha h\nu)^2$



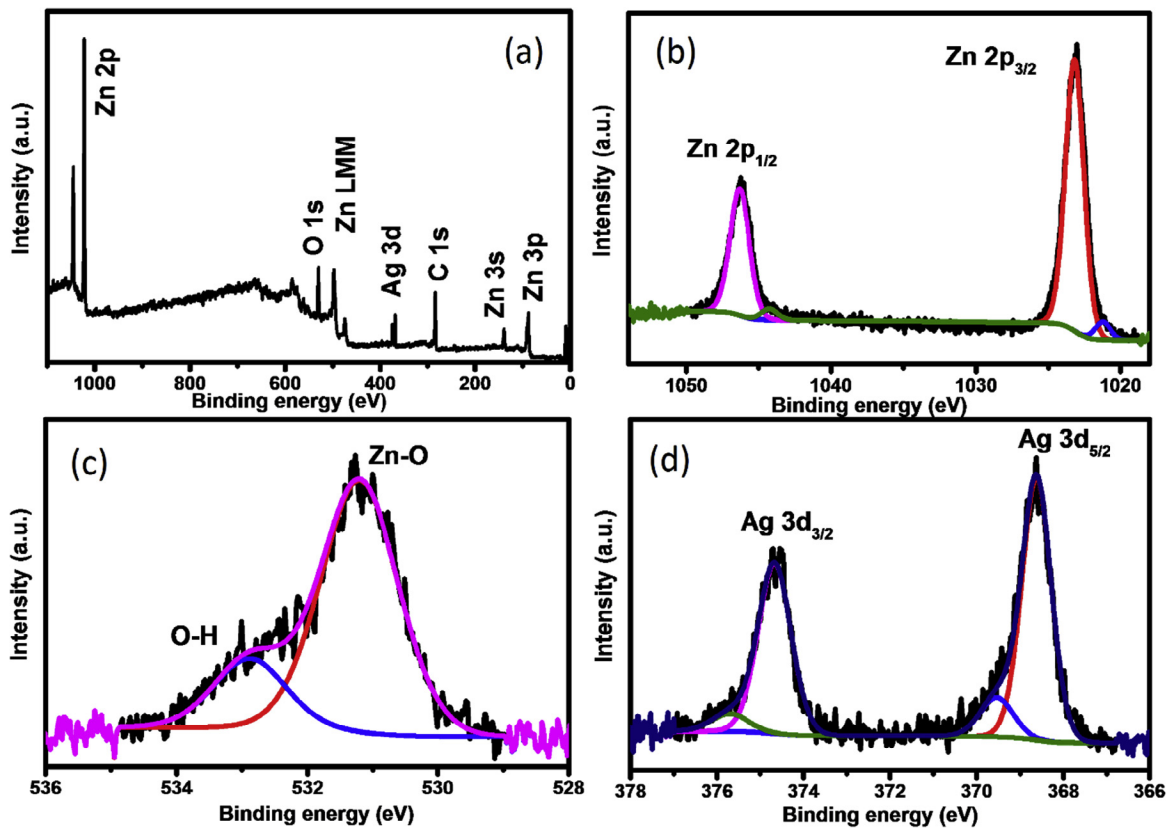


Fig. 5. XPS spectra of Ag-ZnO nanocomposite thin film (Survey as well as core spectra of Zn, O and Ag).

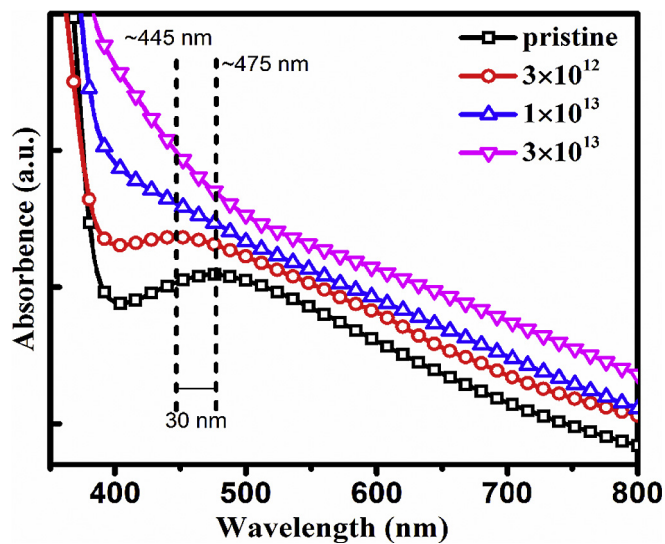


Fig. 6. UV– visible absorption spectra of pristine and 100 MeV  $\text{Ag}^{7+}$  irradiated films.

and  $h\nu$  to measure the optical band gap. The optical band gap of Ag-ZnO nanocomposite thin films were calculated by Tau's relation [43]:

$$\alpha h\nu = A(h\nu - E_g)^n$$

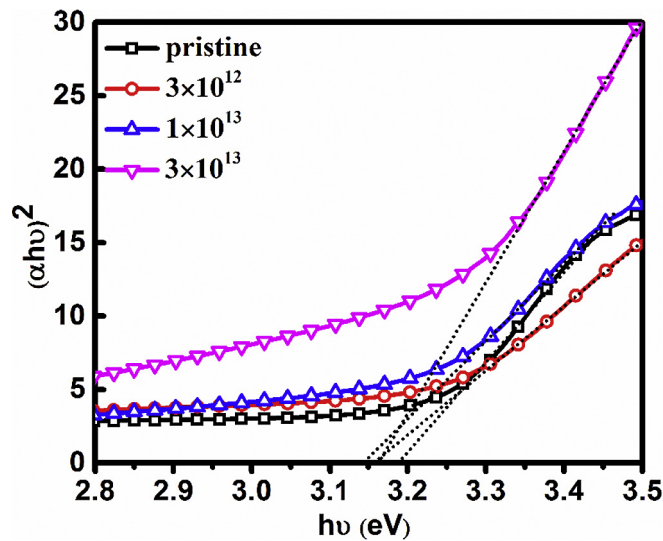


Fig. 7. Band gap variation of pristine and irradiated films, calculated by Tauc's relation.

Table 2

Band gap, roughness and grain size of pristine and irradiated thin films.

Sl. No.	Fluence (ions/cm <sup>2</sup> )	Band gap (eV)	Roughness (nm)	Grain size (nm)
1.	Pristine	3.19 ± 0.01	11.9	52.53 ± 0.06
2.	3 × 10 <sup>12</sup>	3.16 ± 0.01	14.6	72.31 ± 0.08
3.	1 × 10 <sup>13</sup>	3.14 ± 0.01	9.6	38.19 ± 0.05
4.	3 × 10 <sup>13</sup>	3.15 ± 0.01	9.2	36.15 ± 0.11

Where  $h\nu$  is the incident photon energy,  $A$  is constant,  $\alpha$  is the absorption coefficient and  $E_g$  is the optical band gap. The index value “ $n$ ” influenced by the transition between valence bands to conduction band whether it is allowed or forbidden and direct or indirect. For the present study, the value of  $n$  is  $\frac{1}{2}$ . The optical band gap for pristine Ag-ZnO nanocomposite thin film was observed  $\sim 3.19$  eV and it is decreased up to 3.15 eV, with increasing fluence at  $3 \times 10^{13}$  ions/cm<sup>2</sup>. The variation in the optical band gap at different fluences is summarized in Table 2 under the limit of this method of calculating band gap, so this is not appreciable.

### 3.5. AFM measurements

Fig. 8 shows the 2D AFM images of pristine and 100 MeV Ag irradiated Ag-ZnO nanocomposite thin film. The measured root-mean-square roughness ( $R_{rms}$ ) of the pristine film was  $\sim 11.91$  nm and it increased to  $\sim 14.61$  nm in the films irradiated with fluence of  $3 \times 10^{12}$  ions/cm<sup>2</sup>. With further increase in the fluence, the roughness was decreased to  $\sim 9.27$  nm for the fluence of  $3 \times 10^{13}$  ions/cm<sup>2</sup>. The roughness variation with incident ion fluences is described in Table 2. The  $R_{rms}$  roughness of pristine and irradiated films is calculated by the relation:

$$R_{rms} = \left[ \frac{1}{N} \sum_{i=1}^N |Z_i - \bar{Z}|^2 \right]^{1/2}$$

Symbol  $Z$  represent the mean height distance and  $N$  is no. of surface height data points in given relation. The increase in the surface roughness and then further decrease with increase in irradiation dose is a result of rapid annealing due to high energetic ions. The average size of the surface grains were also calculated by AFM micrographs and assuming nearly spherical grains distributed on the surface of the pristine and irradiated thin film. The calculated grain size for the pristine film is  $52.53 \pm 0.06$  nm and it increases at the fluence  $3 \times 10^{12}$  ions/cm<sup>2</sup> but further increase the fluence, the grain size is decrease and found to be  $36.15 \pm 0.11$  nm for  $3 \times 10^{13}$  ions/cm<sup>2</sup> fluence. The variation of grain size with irradiation fluence are summarized in Table 2. In the case of high energy SHI irradiation, the density of electronic excitation induced through the target material and it is responsible for the change in surface morphology of film at different ion fluences. Diffusion and fragmentation process between the target atoms with in irradiation zones during SHI Irradiation are responsible for the grain size distribution. Variation in grain size with irradiation calculated by AFM images is supported to XRD data.

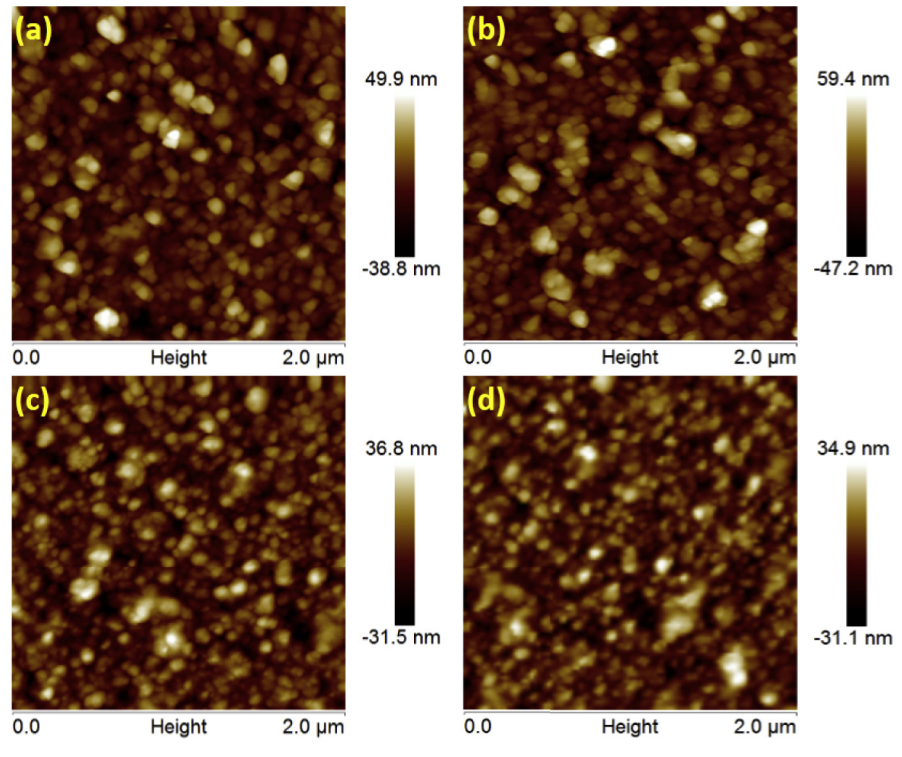


Fig. 8. AFM micrographs (2D) of pristine and irradiated Ag-ZnO nanocomposite thin films.

### 3.6. Raman spectroscopy

The hexagonal wurtzite ZnO structure associated to  $C_{6v}^4$  space group with two formula units per primitive cell and it have  $A_1+2E_2+E_1$  Raman active phonon modes according to the group theory, where all atoms occupy  $C_{3v}$  sites. The Raman spectra of pristine and 100 MeV Ag ion beam irradiated Ag-ZnO nanocomposite thin films at three different fluences  $3 \times 10^{12}$ ,  $1 \times 10^{13}$ , and  $3 \times 10^{13}$  ions/cm<sup>2</sup> are shown in Fig. 9. The spectra depict that no sharp band exists in the pristine film, but when films were irradiated at lower fluence, the intensity of  $E_2$  high mode starts increasing in comparison to pristine film. This increased intensity describes the improvement in the crystallinity at lower fluences. With further increased fluences, the  $E_2$  band is

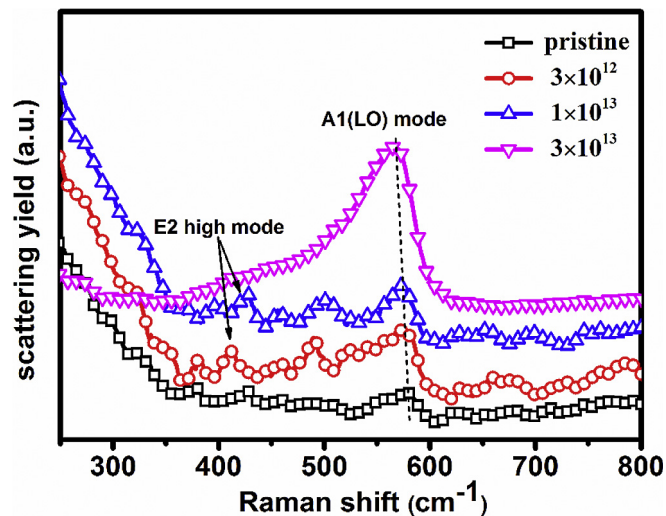


Fig. 9. Raman spectra of pristine and irradiated films at different fluences.

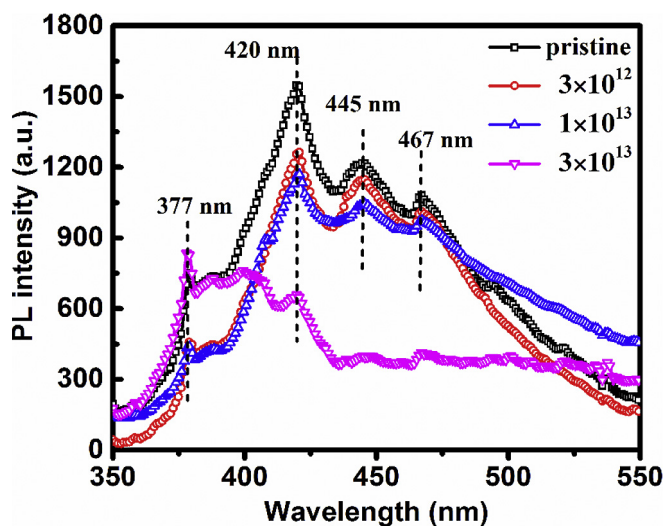


Fig. 10. PL spectra of pristine and irradiated films at different fluences.

completely disappeared, and the intensity of  $A_1$  (LO) mode is increased very sharply. This improvement in the  $A_1$  (LO) mode intensity and disappearance of  $E_2$  band at the higher fluence in the nanocomposite thin film are attributed to the density of defects such the creation of oxygen vacancies due to SHI irradiation [44].

### 3.7. Photoluminescence (PL) studies

Fig. 10 shows the PL spectra for pristine and 100 MeV  $Ag^{7+}$  ion irradiated Ag-ZnO nanocomposite thin films at room temperature with an excitation wavelength of 325 nm He-Cd laser. The spectra of pristine and irradiated thin films mainly consist of four emission bands at 377, 420, 445 and 467 nm respectively. A sharp peak observed at 377 nm is attributed to near band emission (NBE), and band to band transition. This may be due to deep-level defects such as zinc interstitials or oxygen vacancies in Ag-ZnO NCs thin film [45]. The peak at 445 nm is assigned to the transition of electrons from Zn interstitial to acceptor energy level of Zn valency and another peak at 467 nm is ascribed to the oxygen vacancies in the ZnO thin film [46,47]. The interface of the grain boundaries of Ag and ZnO grains prevent the radiative defects at the grain boundaries as confirmed by blue emission at 420 nm [48]. The defects formation during ion irradiation could be understand on the basis of interaction between incident ion and target material.

## 4. Conclusion

In summary, Ag-ZnO nanocomposite thin films were synthesized by RF sputtering method and irradiated with 100 MeV Ag ions at different fluences. We have studied the high energy ion induced modifications in structural and optical properties by different characterization techniques. The blue shift in the SPR band was observed at low fluences of the ion beam, and the band gap of the film was decreased with increasing ion fluence. The crystallinity of the film is decreased with increasing ion fluence which was analyzed by X-ray diffraction spectra. The surface morphology of the film was not very much affected by SHI irradiation, and change in roughness was marginal. Raman spectroscopy was used to study the density of lattice defects which is found in increasing order with increasing fluence with support of Photo-luminance spectroscopy.

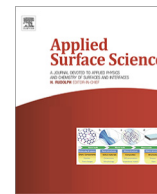
## Acknowledgements

The authors are grateful to the pelletron group of the IUAC, New Delhi for providing the thin film synthesis facility and stable beam during SHI irradiation experiment. The author Shushant Kumar Singh is very thankful to the Technical Education Quality Improvement Programme (TEQIP), MNIT Jaipur for providing the financial assistantship. Authors are also thankful to Material Research Centre, MNIT Jaipur for giving the different characterization facility. One of the authors (R. Singhal) highly acknowledges the financial support assigned by DST New Delhi (DST INSPIRE Faculty project IFA-PS-01/2011) and UGC New Delhi project in the term of IUAC New Delhi P.F. No. DRC-14/59/2013/10/169/00036.

## References

- [1] T. Kryshchab, V.S. Khomchenko, V.B. Khachatryan, N.N. Roshchina, J.A. Andracaadame, O.S. Lytvyn, V.I. Kushnirenko, *J. Mater. Sci. Mater. Electron.* **18** (2007) 1115.

- [2] D.P. Norton, Y.W. Heo, M.P. Ivill, K. Ip, S.J. Pearton, M.F. Chisholm, T. Steiner, *Mater. Today* (2004) 34.
- [3] S.J. Pearton, D.P. Norton, K. Ip, Y.W. Heo, T. Steiner, *Prog. Mater. Sci.* 50 (2005) 293.
- [4] M.J. Gratzel, *Photochem. Photobiol. A* 3 (2004) 164.
- [5] J.C. Pivin, G. Socol, I. Mihailescu, P. Berthet, F. Singh, M.K. Patel, L. Vincent, *Thin Solid Films* 517 (2008) 916–922.
- [6] F.S. Mahmood, R.D. Gould, M.H. Salih, D.C. properties of ZnO thin films prepared by R.F. magnetron sputtering, *Thin Solid Films* 270 (1995) 376.
- [7] G.S. Trivikrama Rao, D. Tarakarama Rao, *Sens. Actuators B Chem.* 55 (1999) 166.
- [8] R. Saravanan, Mohammad Mansoob Khan, V.K. Gupta, E. Mosquera, F. Gracia, V. Narayanan, A. Stephen, *RSC Adv.* 5 (2015) 34645–34651.
- [9] D.V. Parikh, T. Fink, K. Rajasekharan, N.D. Sachinvala, A.P.S. Sawhney, T.A. Calamari, A.D. Parikh, *Text. Res. J.* 75 (2005) 134–138.
- [10] G. Gosheger, J. Hardes, H. Ahrens, A. Streitburger, H. Buerger, M. Erren, A. Günsel, F.H. Kemper, W. Winkelmann, C.V. Eiff, *Biomaterials* 25 (2004) 5547–5556.
- [11] Syeda Arooj, Samina Nazir, Akhtar Nadhman, Nafees Ahmad, Bakhtiar Muhammad, Ishaq Ahmad, Kehkashan Mazhar, Rashda Abbasi, *Beilstein J. Nanotechnol.* 6 (2015) 570–582.
- [12] R. Saravanan, Mohammad Mansoob Khan, F. Gracia, Jiaqian Qin, Vinod Kumar Gupta, A. Stephen, *Sci. Rep.* 6 (2016) 31641, <http://dx.doi.org/10.1038/srep31641>.
- [13] S.S. Lin, J.L. Huang, *Surf. Coat. Technol.* 185 (2004) 222.
- [14] M. Berber, V. Bulto, R. Kilb, H. Hahn, *Scr. Mater.* 53 (2005) 547.
- [15] Y. Lee, H. Kim, Y. Roh, *Jpn. J. Appl. Phys.* 40 (2001) 2423.
- [16] W. Tang, D.C. Cameron, *Thin Solid Films* 83 (1994) 238.
- [17] Y. Natsume, H. Sakata, T. Hirayama, H. Yanagida, *J. Appl. Phys.* 72 (1992) 4203.
- [18] M. Liu, X.Q. Wei, Z.G. Zhang, G. Sun, C.S. Chen, C.S. Xue, H.Z. Zhuang, B.Y. Man, *Appl. Surf. Sci.* 252 (2006) 4321.
- [19] N. Venugopal, A. Mitra, *Opt. Mater.* 35 (2013) 1467–1476.
- [20] R. Saravanan, N. Karthikeyan, V.K. Gupta, E. Thirumal, P. Thangadurai, V. Narayanan, A. Stephen, *Mater. Sci. Eng. C* 33 (2013) 2235–2244.
- [21] R. Singhal, D.C. Agarwal, S. Mohapatra, Y.K. Mishra, D. Kabiraj, F. Singh, D.K. Avasthi, A.K. Chawla, R. Chandra, G. Mattei, J.C. Pivin, *Appl. Phys. Lett.* 93 (2008) 103114.
- [22] R. Singhal, D.C. Agarwal, Y.K. Mishra, F. Singh, J.C. Pivin, R. Chandra, D.K. Avasthi, *J. Appl. Phys. D.* 42 (2009) 155103.
- [23] R. Singhal, J.C. Pivin, R. Chandra, D.K. Avasthi, *Surf. Coat. Technol.* 229 (2013) 50–54.
- [24] R. Singhal, D.C. Agarwal, Y.K. Mishra, S. Mohapatra, D.K. Avasthi, A.K. Chawla, R. Chandra, J.C. Pivin, *Nucl. Instr. Meth. B* 267 (2009) 1349–1352.
- [25] V.S.K. Chakravadhanula, Y.K. Mishra, V.G. Kotnur, D.K. Avasthi, T. Strunskus, V. Zaporotchenko, D. Fink, L. Kienle, F. Faupel, *Beilstein J. Nanotechnol.* 5 (2014) 1419–1431.
- [26] Y.K. Mishra, F. Singh, D.K. Avasthi, J.C. Pivin, D. Malinowska, E. Pippel, *Phys. Lett.* 91 (2007) 063103.
- [27] Y.K. Mishra, D.K. Avasthi, P.K. Kulriya, F. Singh, D. Kabiraj, A. Tripathi, J.C. Pivin, I.S. Bayer, A. Biswas, *Appl. Phys. Lett.* 90 (2007) 073110.
- [28] Abdenacer Benyagoub, *Phys. Rev. B* 72 (2005) 094114–094117.
- [29] R.G. Singh, Fouran Singh, I. Sulaniya, D. Kanjilal, K. Sehwat, V. Agrawal, R.M. Mehra, *Nucl. Instrum. Methods* 267 (2009) 2399–2402.
- [30] M.S. Comboj, G. Kaur, R. Thangaraj, D.K. Avasthi, *J. Phys. D.* 35 (2002) 477.
- [31] N. Itoh, M. Stoneham, *Material Modification by Electronic Excitation*, Cambridge University Press, 2000.
- [32] L. Irimpan, V.P.N. Nampoori, P. Radhakrishnan, *Chem. Phys. Lett.* 455 (4) (2008) 265–269.
- [33] Y.H. Zheng, L.R. Zheng, Y.Y. Zhan, X.Y. Lin, Q. Zheng, K.M. Wei, *Inorg. Chem.* 46 (2007) 6980–6986.
- [34] R. Saravanan, E. Thirumal, V.K. Gupta, V. Narayanan, A. Stephen, *J. Mol. Liq.* 177 (2013) 394–401.
- [35] K. Schwartz, A.E. Volkov, M.V. Sorokin, C. Trautman, K.O. Voss, R. Neumann, M. Lang, *Phys. Rev. B* 78 (2008) 024120/1.
- [36] M. Mayer, *SIMNRA User's Guide*, Technical Report IPP 9/113, Max Plank Institute of fur Plasmaphysik, Garching, Germany, 1997.
- [37] J.F. Ziegler, J.P. Biersack, V. Littmark, *The Stopping and Range of Ions in Solids*, 1985. New York, Pergamon.
- [38] G.J. Fang, D.J. Li, B.L. Yao, *Phys. Status Solidi (A)* 193 (2002) 139.
- [39] M. Chen, Z.L. Pei, C. Sun, L.S. Wen, Z. Wang, *J. Cryst. Growth* 220 (2000) 254–262.
- [40] D.C. Agrawal, Amit Kumar, S.A. Khan, D. Kabiraj, F. Singh, A. Tripathi, J.C. Pivin, R.S. Chauhan, D.K. Avasthi, *Nucl. Instr. Meth. B* 244 (2006) 136–140.
- [41] Y. Zheng, L. Zheng, Y. Zhan, X. Lin, Q. Zheng, K. Wei, *Inorg. Chem.* 46 (2007) 6980–6986.
- [42] D.K. Avasthi, Y.K. Mishra, Fouran Singh, J.P. Stoquert, *Nucl. Instr. Meth. B* 268 (2010) 3027–3034.
- [43] J. Tauc, *Optical Properties of Solids*, 1972. North-Holland.
- [44] Fouran Singh, P.K. Kulriya, J.C. Pivin, *Solid State Commun.* 150 (2010) 1751–1754.
- [45] Vinod Kumara, Fouran Singh, O.M. Ntwaeaborwa, H.C. Swarta, *Appl. Surf. Sci.* 279 (2013) 472–478.
- [46] X.Q. Wei, B.Y. Man, M. Liu, C.S. Xue, H.Z. Zhuang, C. Yang, *Phys. B Condens. Matter* 60 (2007) 145–152.
- [47] L.V. Trandafilovic, D.K. Bozanic, S. Dimitrijevic-Brankovic, A.S. Luyt, V. Djokovic, *Carbohydr. Polym.* 88 (2012) 263–269.
- [48] D.D. Lin, H. Wu, R. Zhang, W. Pan, *Chem. Mater.* 21 (2009) 3479–3484.



## Full Length Article

## Thermal-induced SPR tuning of Ag-ZnO nanocomposite thin film for plasmonic applications

S.K. Singh\*, R. Singhal

Department of Physics, Malaviya National Institute of Technology Jaipur, JLN Marg, Jaipur 302017, Rajasthan, India



## ARTICLE INFO

## Article history:

Received 13 November 2017

Revised 7 January 2018

Accepted 10 January 2018

Available online 11 January 2018

## Keywords:

Nanocomposite thin films

Thermal annealing

Surface plasmon resonance

X-ray photoelectron spectroscopy

## ABSTRACT

The formation of silver (Ag) nanoparticles in a ZnO matrix were successfully synthesized by RF-magnetron sputtering at room temperature. As prepared Ag-ZnO nanocomposite (NCs) thin films were annealed in vacuum at three different temperatures of 300 °C, 400 °C and 500 °C, respectively. The structural modifications for as-deposited and annealed films were estimated by X-ray diffraction and TEM techniques. The crystalline behavior preferably along the c-axis of the hexagonal wurtzite structure was observed in as-deposited Ag-ZnO film and improved significantly with increasing the annealing temperature. The crystallite size of as-deposited film was measured to be 13.6 nm, and increases up to 28.5 nm at higher temperatures. The chemical composition and surface structure of the as-deposited films were estimated by X-ray photoelectron spectroscopy. The presence of Ag nanoparticles with average size of  $8.2 \pm 0.2$  nm, was confirmed by transmission electron microscopy. The strong surface plasmon resonance (SPR) band was observed at the wavelength of  $\sim 565$  nm for as-deposited film and a remarkable red shift of  $\sim 22$  nm was recorded after the annealing treatment as confirmed by UV-visible spectroscopy. Atomic force microscopy confirmed the grain growth from 60.38 nm to 79.42 nm for as-deposited and higher temperature annealed film respectively, with no significant change in the surface roughness. Thermal induced modifications such as disordering and lattice defects in Ag-ZnO NCs thin films were carried out by Raman spectroscopy. High quality Ag-ZnO NCs thin films with minimum strain and tunable optical properties could be useful in various plasmonic applications.

© 2018 Elsevier B.V. All rights reserved.

## 1. Introduction

Semiconductor based nanocomposites (NCs) have been widely used in diverse research field due to its applicability in potential fields such as plasmonic [1], photo-catalysis [2], nanodevices [3] and gas sensors [4]. Specially, ZnO based NCs are very interesting because of their wide band gap  $\sim 3.34$  eV, large exciton binding energy (60 meV) and belongs to II-VI group of semiconductors [5]. These metal-ZnO NCs have been extensively used in various field such as transparent electrodes [6], solar cell [7], photocatalytic activity [8], plasmonic [9], optoelectronic devices [10] and thin film transistors [11]. The physical properties of such NCs are strongly influenced by the deposition method, deposition parameter, doping of metal and post-deposition treatments like thermal annealing/ion beam irradiation [12–16]. The thin film of any material offer new properties which is not appear in the bulk material due to its large surface volume ratio, comparing to bulk [17–20]. There are many technique to synthesize these NCs in the form of

thin film such as physical-vapour deposition [21], sol-gel method [17], pulsed laser deposition [22], molecular beam epitaxial growth [23], chemical vapour deposition [24], DC/RF sputtering method [25] etc. Among of them, magnetron sputtering is much more advantageous technique to synthesize the NCs films, having high crystalline quality, good adhesion and packing density with the amorphous substrates also [26]. The thin film of Ag-ZnO NCs exhibits the various optical and structural properties which can directly controlled by silver dopant and thermal annealing/ion beam treatment [27,28]. The thermal annealing is also advantageous process to tune the optical and structural properties of film after the deposition. At the same time, annealing environment is also play the major role to enhance the properties of the films [29,30].

In the present experiment, Ag-ZnO NCs thin films have been synthesized by RF-magnetron sputtering and then annealed in the vacuum environment (of the order of  $10^{-2}$ ) to prevent the oxidation of Ag nanoparticles at three different annealing temperatures of 300 °C, 400 °C and 500 °C. As-deposited and annealed Ag-ZnO NCs thin films have been characterized by different characterization tools like X-ray diffraction, X-ray photoelectron spectroscopy, transmission electron microscopy, atomic force

\* Corresponding author.

E-mail address: [singhshushant86@gmail.com](mailto:singhshushant86@gmail.com) (S.K. Singh).

microscopy and Raman spectroscopy, to study the optical and structural enhancement by thermal annealing. A remarkable red shift ( $\sim 22$  nm) has been found in present experiment with monocrystalline behaviour during thermal annealing as confirmed by UV-visible and X-ray diffraction spectroscopy. These monocrystalline Ag-ZnO NCs thin film with tunable optical properties could be very useful in plasmonic applications.

## 2. Experimental plan

A target of pure ZnO (2" dia.) was prepared from the ZnO powder (Merck) with the help of hydraulic press machine (HYCON, New Delhi). The prepared ZnO target was sintered in the tubular furnace at the temperature of 1200 °C for 24 h with continuous flow of oxygen gas during sintering process. For synthesizing the Ag-ZnO NCs film, one small piece (1 mm thick) of pure Ag (Sigma Aldrich) was glued on the prepared ZnO target before the film deposition. The silicon substrates were used for film deposition and clean with RCA method before the film deposition. The pressure in the sputtering chamber was recorded  $5 \times 10^{-6}$  mbar before inserting the argon gas in the chamber. The vacuum of the chamber was decreased after introducing the gas and observed  $1.5 \times 10^{-2}$  during the film deposition. The rough vacuum was created by rotary pump and it coupled with turbo-molecular pump for getting the very high vacuum. The deposition was performed for 40 min at the RF power  $\sim 60$  watts at the room temperature. The thickness of the film was measured by the quartz crystal monitor and found to be  $\sim 80$  nm at the deposition rate of 0.2 Å/s. After the deposition, the prepared Ag-ZnO NCs films were annealed at three different temperatures of 300 °C, 400 °C and 500 °C. A rotary pump was attached with tubular furnace for achieving the vacuum. So the annealing was performed in the vacuum and the observed value of the vacuum was found to be  $\sim 1.24 \times 10^{-2}$  mbar during annealing.

The structural information of the NCs films have been estimated by X-ray diffraction spectroscopy (Cu  $K_{\alpha}$  beam at the wavelength of 1.54 Å) and surface features have been observed by the Atomic force microscopy (Bruker). The composition and surface analysis have been confirmed by X-ray photoelectron spectroscopy (XPS). The formation and size of Ag nanoparticle have been calculated by Transmission electron microscopy (Tecnai G<sup>2</sup> 20-FEI). The UV-visible spectroscopy (Perkin Elmer) has performed to observe the optical properties of the films. The Raman spectra of as-deposited and annealed films have been characterized by using Raman microscope (AIRIX-STR 500) with 532 nm laser beam at low power. All synthesis and characterization facility were used in Material Research Center (MRC) at Malaviya National Institute of Technology Jaipur.

## 3. Result and discussion

### 3.1. X-ray diffraction analysis

The structural behavior and crystalline quality of as-deposited and annealed Ag-ZnO NCs thin films were investigated by X-ray diffraction spectroscopy (XRD). Fig. 1 shows the X-ray patterns of as-deposited and films annealed at 300 °C, 400 °C and 500 °C temperatures. Most intense Bragg peak was identified at the diffraction angle of 34.19° for as-deposited as well as annealed films that corresponds to the (0 0 2) planes of the hexagonal wurtzite structure. There is no evidence of Ag-O and Ag<sub>2</sub>O related phases in the pattern. Importantly, the intensity of the (0 0 2) peak increases with increasing the annealing temperature. Consequently, the FWHM of the films decreasing with increasing the annealing temperature. This signifies that the crystalline quality of the films are significantly improved after the thermal annealing and is responsible

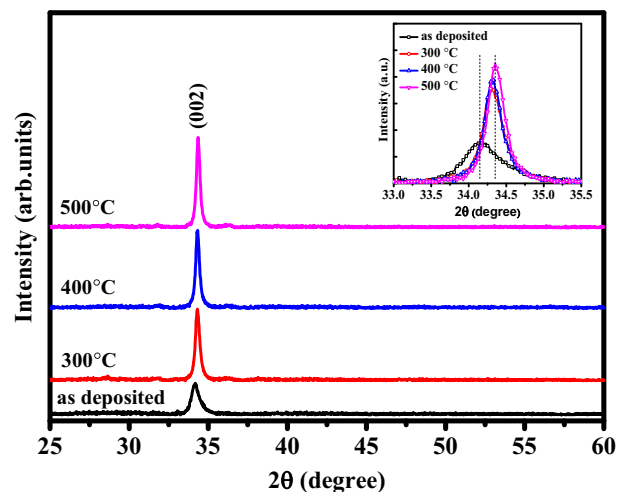


Fig. 1. X-ray spectra of as-deposited and annealed Ag-ZnO NCs thin film at three different temperatures of 300 °C, 400 °C and 500 °C.

for the growth along the c-axis (0 0 2 plane). Moreover, the (0 0 2) orientation of the hexagonal wurtzite structure have small surface energy which results in a higher growth rate, according to the basic crystal growth theory [31,32].

The presence of single Bragg peak in the pattern revealed the higher crystallinity of the films. The crystallite size ( $D$ ) of as-deposited and annealed films was calculated according to Scherrer's formula [33] as shown in equation 1:

$$D = \frac{0.9\lambda}{\beta \cos \theta} \quad (1)$$

In above Eq. (1),  $\lambda$  is the wavelength of the incident X-ray beam (Cu  $K_{\alpha} = 1.54$  Å),  $\beta$  is the full width at half maxima and  $\theta$  is the Bragg diffraction angle. The crystallite size was calculated from above relation and found to be 13.6 nm for as-deposited film and increases up to 28.5 nm for annealed film at the annealing temperature 500 °C. The increment in the crystallite size is direct evidence of the improved crystalline quality of the film after the annealing treatment. The various microstructural parameters such as lattice parameter, dislocation density, lattice strain and stress have been calculated from the XRD pattern. The lattice parameters for the as-deposited and annealed film were calculated by using crystal structure formula for hexagonal wurtzite structure of ZnO which is explain in given form [34]:

$$n\lambda = 2d \sin \theta \quad (2)$$

and

$$\frac{1}{d^2} = \frac{4}{3} \left( \frac{h^2 + hk + k^2}{a^2} \right) + \frac{l^2}{c^2} \quad (3)$$

In Eqs. (2) and (3),  $h, k, l$  are the Miller indices,  $d$  is the interplaner spacing and  $a, c$  are the lattice constant of the film. Table 1 summarizes the lattice parameters of as-deposited and annealed films. In addition, the crystalline quality of the films is affected by dislocation density which depend on the thermal annealing. To account this we have estimated the dislocation density [35] for the as-deposited and annealed films by given relation:

$$\text{Dislocation density } (\delta) = \frac{1}{D^2} \quad (4)$$

A high dislocation density of  $5.4 \times 10^{15}$  line/m<sup>2</sup> was observed for as-deposited film from the above relation (Eq. (4)). On the other hand, a low dislocation density of  $1.2 \times 10^{15}$  line/m<sup>2</sup> was found for films after annealing at higher temperature. The value of disloca-

**Table 1**  
Structural parameters of as-deposited and annealed Ag-ZnO NCs thin films.

Sample detail	2θ (°)	Lattice parameter		d-spacing (Å)	Crystallite size (nm)	Dislocation density	Lattice strain%	Stress (GPa)
		a (Å)	c (Å)					
As grown	34.19	3.0253	5.2398	2.6199	13.6	5.4	0.86	-1.79
300 °C	34.32	3.0131	5.2186	2.6093	24.9	1.6	0.47	-0.84
400 °C	34.33	3.0120	5.2168	2.6084	27.7	1.3	0.43	-0.75
500 °C	34.36	3.0099	5.2132	2.6066	28.5	1.2	0.41	-0.59

**Table 2**  
Variation in roughness and grain size with annealing for the Ag-ZnO NCs thin films.

Sl. No.	Sample detail	Roughness (R <sub>q</sub> ) (nm)	Grain size (nm)
1.	As-deposited	6.44	60.38
2.	300 °C	6.57	64.41
3.	400 °C	6.58	69.23
4.	500 °C	6.69	79.42

tion density has been decreased significantly as compared to as-deposited films which attributed to lower defects and higher crystalline quality of the films. The value of lattice strain and stress have been also calculated for as-deposited and annealed film by given relations [36]:

$$\text{Residual stress } (\sigma) = -233 \left[ \frac{c - c_0}{c_0} \right] [\text{GPa}] \quad (5)$$

and

$$\text{Lattice strain } (\varepsilon) = \frac{\beta \cos \theta}{4 \sin \theta} \quad (6)$$

In above relation (5) and (6),  $c_0$  is the strain free lattice constant for the bulk ZnO ( $c_0 = 5.2 \text{ \AA}$ ). The negative sign in the stress indicates the compressive nature for as-deposited and annealed films because the (0 0 2) peak shifted towards larger angle side. The value of stress has been observed to decrease with increasing the annealing temperature and thus lead to stress relaxations between grains and overcome the difference of thermal expansion coefficient between the film and substrates. The strain could be released during the annealing which supports the higher crystallization of the films as confirmed by lattice strain calculations. All discussed micro-structural parameters have been calculated for as-deposited and annealed films and summarized in Table 2.

### 3.2. X-ray photoelectron spectroscopy

The formation of compound and presence of elements have been successfully estimated by X-ray photoelectron spectroscopy (XPS). The survey scan with high resolution spectra of each existing elements are displayed in Fig. 2. The high resolution spectra of Zn 2p region showed two peaks one at energy scale of  $\sim 1021.82 \text{ eV}$  and other one at  $\sim 1044.92 \text{ eV}$ . These peaks are related to  $2p_{3/2}$

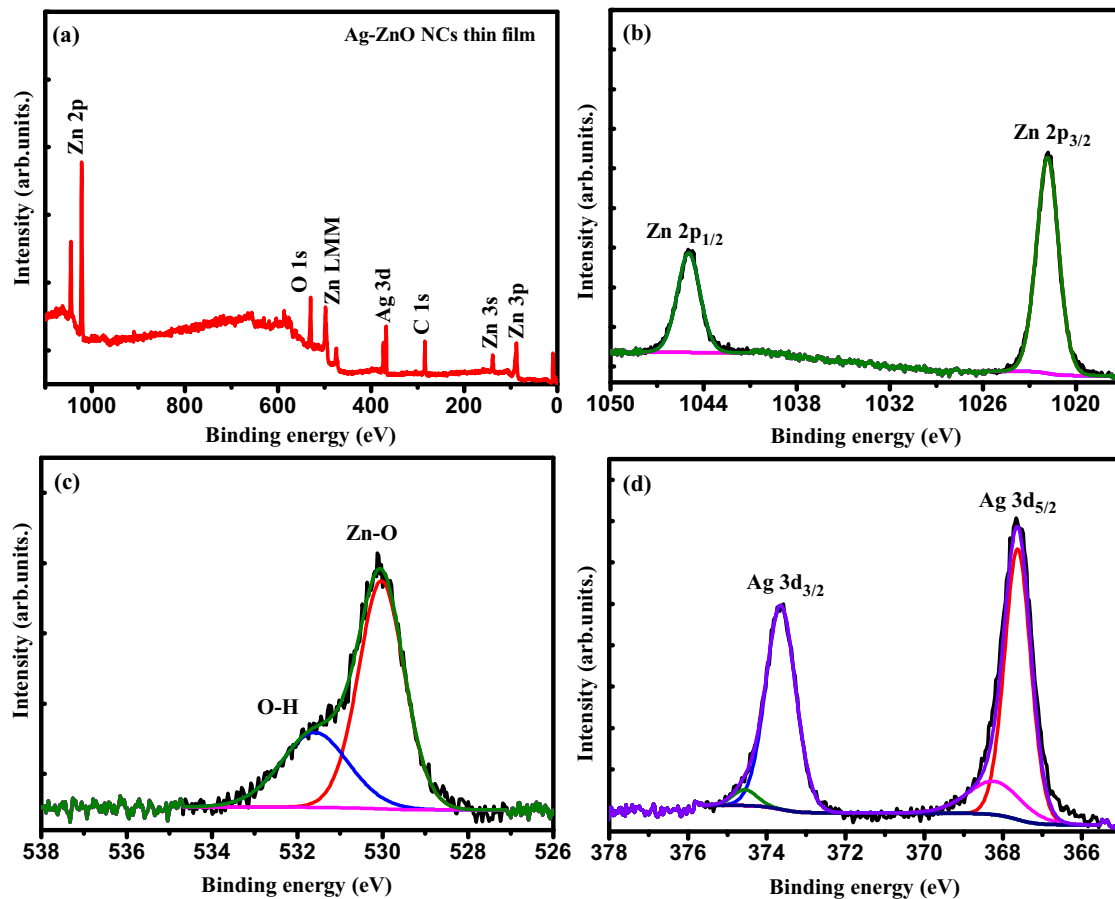


**Fig. 2.** XPS spectra of the as-deposited Ag-ZnO NCs thin film (a) survey scan, (b) high resolution spectra of Zn, (c) O and (d) Ag.



and  $2p_{1/2}$  states of Zn 2p respectively. The presence of oxygen group is also confirmed by the two different peaks appeared in the core spectra at the binding energies of  $\sim 530.02$  eV and  $\sim 531.60$  eV. The first peak could be assigned to the first oxygen group which is associated with Zn-O bonding and the second group is due to the presence of hydroxyl group which might arise because of defects and impurities present in the as-deposited film.

The presence of Ag has been clearly observed in high resolution spectra of Ag. The Ag 3d doublet scan can be clearly visible in Fig. 2(d), centered at binding energies of  $\sim 373.63$  eV and  $\sim 367.62$  eV for  $3d_{5/2}$  and  $3d_{3/2}$  respectively. Furthermore, the de-convolution of the core spectra of Ag was studied to observe the nature of interaction between Ag and ZnO. It is found that the lesser contribution comes from  $Ag_2O$  and  $Ag-ZnO$  components therefore the formation of the nanoparticles is expected and will be investigated in the next section by TEM. The binding energy of the Ag  $3d_{5/2}$  peak has been shifted towards the lower energy which is attributed to the interaction between Ag and ZnO nanostructures. Therefore, with these evidences XPS analysis confirmed the composition and nature of interaction of the various species in the film. Note that the film contains a number of elements i.e. Zn, O and Ag as confirmed by these measurements.

### 3.3. Transmission electron microscopy

Fig. 3 shows the TEM micrographs of as-deposited Ag-ZnO NCs thin film. In the figures, first (a) show the top view of the film with continuous distribution of the film over the substrate. This shows

that the as-deposited film is homogeneous in the nature. The presence of Ag in the form of nanoparticles are clearly seen in the TEM image and marked in the Fig. 3(b). The size of Ag nanoparticles were measured from the TEM image and found that the average particle size is about  $(D) = 8.2 \pm 0.2$  nm. The cross fringes are observed in the HRTEM image which confirms the formation of NCs with presence of Ag. The d-spacing was measured to be  $2.60 \text{ \AA}$  which corresponding to (002) reflection of the wurtzite structure of ZnO (shown inset) as can be seen in Fig. 3(c). The selected area electron diffraction pattern (SAED) of the as-deposited film is shown in Fig. 3(d). The presence of clear rings in the SAED pattern has been observed and marked with corresponding planes in the Fig. 3(d) which is the direct confirmation about the crystallinity of the film. The presence of Ag nanoparticles has been directly confirmed by the TEM analysis which is in agreement with the XPS results.

### 3.4. Atomic force microscopy

The surface features of as-deposited and annealed films have been observed by the atomic force microscopy (AFM). The characterization was performed in tapping mode. 2-D figures ( $1 \times 1 \mu\text{m}^2$ ) of as-deposited and annealed Ag-ZnO NCs films are shown in Fig. 4.

The homogeneous distribution of the grain on the film surface observed in the images. The grains are perfectly connected that form the triangular shape. The grain growth has been observed after the thermal annealing. The grain size was calculated by AFM micrographs and found to be  $60.38$  nm for the as-deposited

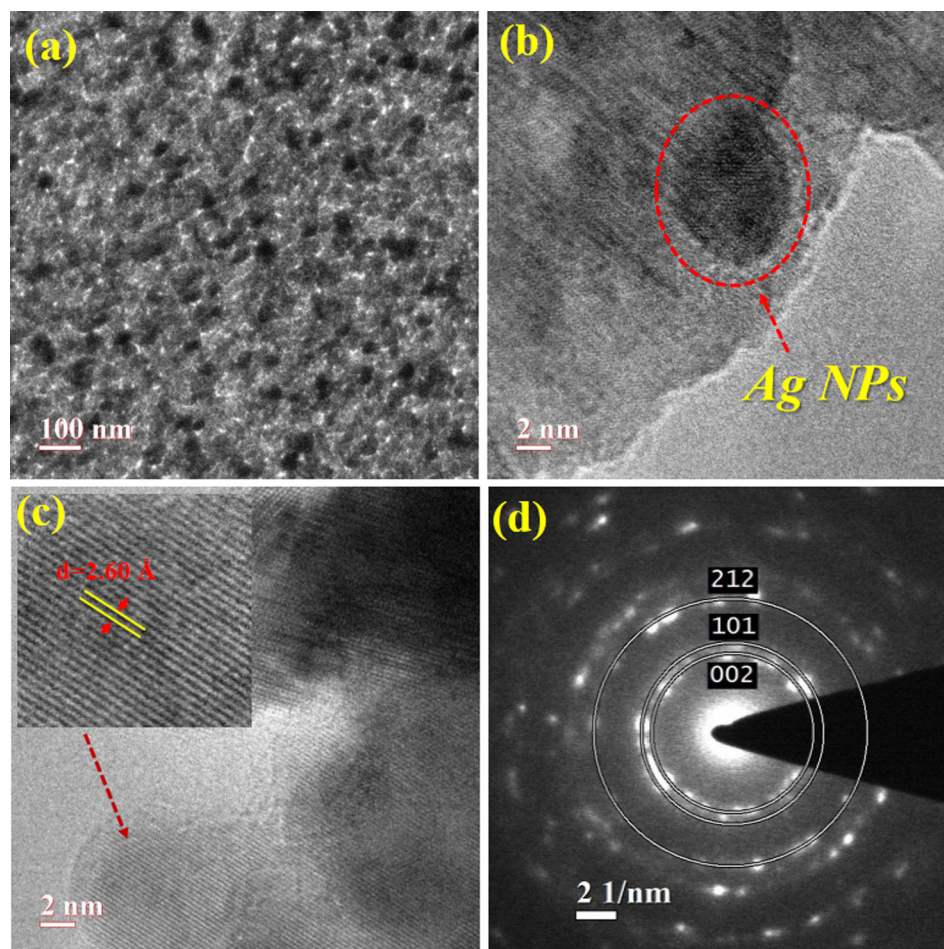


Fig. 3. TEM micrographs of as-deposited Ag-ZnO NCs thin film (a) surface image, (b) Ag nanoparticle, (c) HRTEM image with d-spacing and (d) SAED pattern.

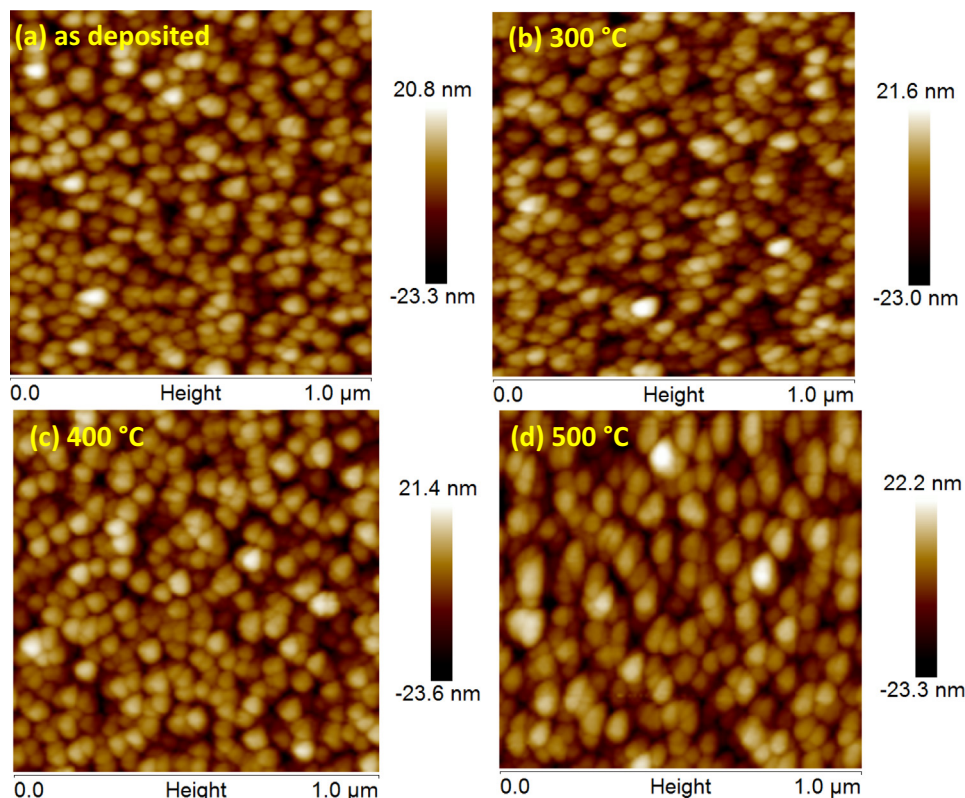


Fig. 4. 2D ( $1 \times 1 \mu\text{m}^2$ ) AFM micrographs of (a) as-deposited and annealed, (b) 300 °C, (c) 400 °C and (d) 500 °C Ag-ZnO NCs thin films.

film. After the annealing treatment at 500 °C, the grain size was increased up to 79.42 nm. The agglomeration between the grains took place during the annealing process and is responsible for the grain growth. The grains achieve thermal energy during the annealing and participate in the agglomeration process. Both X-ray analysis and AFM results support the grain growth after the thermal annealing. The root-mean-square roughness ( $R_{\text{rms}}$ ) of the as-deposited and annealed films were calculated by following relation [37]:

$$R_{\text{rms}} = \left[ \frac{1}{N} \sum_{i=1}^N |Z_i - Z|^{-2} \right]^{\frac{1}{2}} \quad (7)$$

In above relation (7),  $N$  and  $Z$  are the surface height and mean height distance, respectively. Interestingly, no significant changes were observed in the surface roughness of the as-deposited and annealed Ag-ZnO NCs thin film.

### 3.5. UV-Visible spectroscopy

The optical modifications in as-deposited and annealed Ag-ZnO NCs thin film have been carried out by UV-visible spectroscopy in reflectance mode. The variation in reflectance has been observed with thermal annealing at different temperatures of 300 °C, 400 °C and 500 °C. A very large deep region was found in reflection spectra which could be related to the absorbance of the nanoparticles in the wavelength range between 450 nm and 650 nm. Therefore, the absorbance of as-deposited and annealed film have been calculated from the reflectance data and is shown in Fig. 5. A well-defined strong absorption resonance (SPR) band has been observed both in as-deposited as well as in the annealed films. The position of SPR band was found at  $\sim 565$  nm for as-deposited film and 565 nm, 576 nm and 587 nm for the films annealed at 300 °C, 400 °C and 500 °C respectively. The prominent red shift of

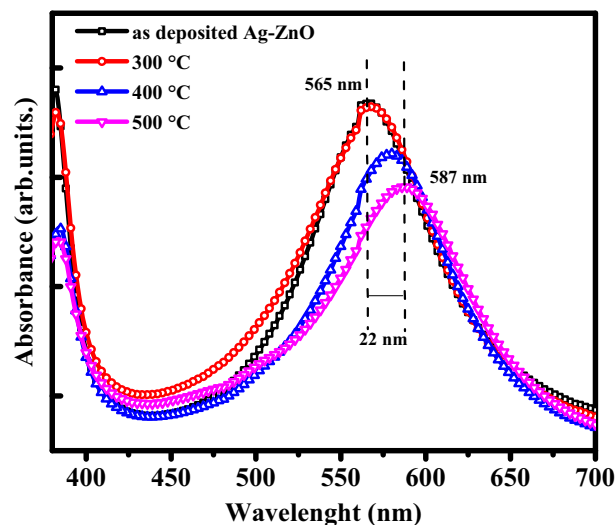


Fig. 5. UV-visible spectroscopy of the as-deposited and annealed Ag-ZnO thin films.

$\sim 22$  nm has been observed in the SPR band with the thermal annealing as applied in this study. The observed red shift in SPR could be linked with the growth of the nanoparticles during the thermal annealing. As the annealing temperature increases, the crystalline quality of ZnO films have improved significantly and explains the SPR shifting in the films after annealing.

The SPR frequency of the nanoparticles depends on many factors such as size and shape of nanoparticles, spatial distribution and nature of the surrounding medium. The local refractive index of the medium is very sensitive for the shifting in SPR frequency of the nanoparticles. Furthermore, to study the effect of refractive

index on the SPR shifting, the refractive index and other optical parameters have been calculated by the following relations [38]:

$$n = \frac{1 + \sqrt{R}}{1 - \sqrt{R}} \quad (8)$$

$$n = \sqrt{\frac{4R}{(1-R)^2} - k^2} + \left(\frac{1+R}{1-R}\right), \quad \text{where, } k = \frac{\alpha\lambda}{4\pi} \quad (9)$$

In above relations (8) and (9),  $n$  is the refractive index,  $R$  is the reflectance,  $k$  is the extinction coefficient and  $\alpha$  is the absorption coefficient of the film. The value of refractive index has been increases from 2.16 to 2.42 with increasing the annealing temperature. The extinction coefficient was calculated for as-deposited and annealed films and is tabulated in Table 3. The dielectric constant and absorbance of the films were calculated using given relations [39]:

$$\varepsilon_r = n^2 - k^2 (\text{real part}) + nk^2 (\text{imaginary part}) \quad (10)$$

$$\alpha = \frac{2.303}{d} A \quad (11)$$

The real and imaginary part of the dielectric constant has been calculated for as-deposited and annealed films for the wavelength same at SPR band from Eq. (10). The dielectric constant of the film increases with increasing the annealing temperature. The optical band gap of the as-deposited and annealed film Ag-ZnO films has been calculated by Tau's relation in given manner [40]:

$$\alpha h\nu = A(h\nu - E_g)^{1/2} \quad (12)$$

In the above Eq. (12),  $h\nu$  is the incident photon energy and  $E_g$  is the band gap of the material. Generally, the band gap of pure ZnO thin film is reported  $\sim 3.30$  eV, while in the present study, the band was found to be  $\sim 3.17$  eV due to Ag incorporation in the host ZnO matrix (shown in Fig. 6). The value of band gap decreases up to  $\sim 3.12$  eV at higher annealing temperature and might be attributed to an increase in the metal/oxygen ratio with lower defects density after the thermal annealing process. Such results are also supported by XRD analysis.

At the same time, FWHM of the bands decreases with increasing annealing temperature and yielded a remarkable red shift ( $\sim 22$  nm) in the SPR band. The perfect Gaussian shape of the band revealed the homogeneity, particularly the shape of nanoparticles in the ZnO matrix which was supported by TEM particles size analysis. Thus, the size/shape of the nanoparticles and local refractive index of surrounding material might play key role in the SPR tuning. Since, the thermal annealing as shown in this study could be very effective to control over the optical properties of the surrounding matrix with a fairly control on the size and shape of the nanoparticles. This tunable nature in the optical properties of these Ag-ZnO NCs thin film make them very promising for various plasmonic applications. All calculated optical parameters are summarized in Table 3.

**Table 3**  
Optical parameter with different annealing temperatures.

Sample detail	SPR band position ( $\lambda$ ) (nm)	Band gap ( $E_g$ ) (eV)	Refractive index ( $n$ )	Extinction coefficient ( $k$ )	Dielectric constant ( $\varepsilon_r$ )
As-deposited	565	3.17	2.16	0.127	4.78
300 °C	565	3.16	2.17	0.124	4.96
400 °C	576	3.13	2.31	0.085	5.52
500 °C	587	3.12	2.42	0.081	6.05

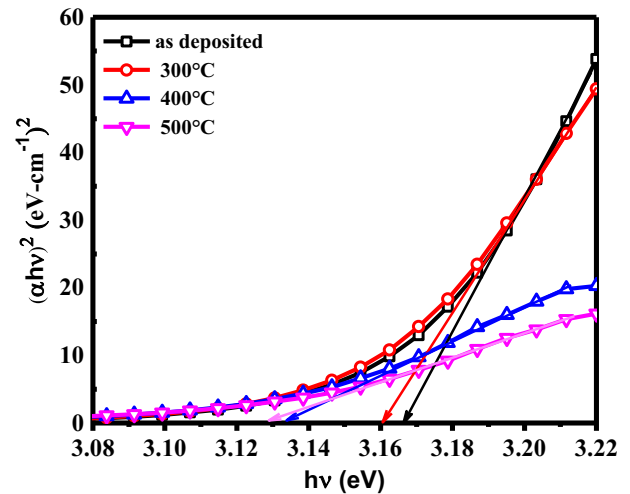


**Fig. 6.** Band gap variation of the as-deposited and annealed Ag-ZnO thin films at different temperatures.

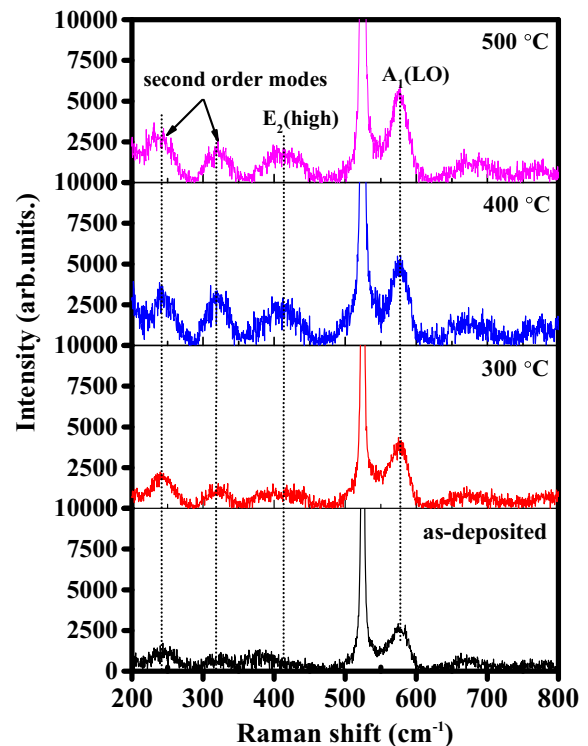


**Fig. 7.** Raman spectra of as-deposited and annealed Ag-ZnO NCs thin films.

### 3.6. Raman spectroscopy

The Raman active phonon modes for ZnO wurtzite structure have been observed by the Raman spectroscopy. According to

group theory, there are  $A_1+2E_2+E_1$  modes which are related to wurtzite ZnO, where all atoms occupy  $C_{3v}$  sites [41,42]. Fig. 7 shows the micro-Raman spectra of the as-deposited and annealed Ag-ZnO NCs thin films with different annealing temperatures of 300 °C, 400 °C and 500 °C. The different Raman peaks are observed in the spectra which are related to particular bands of ZnO. Raman spectra of as-deposited and annealed Ag-ZnO films show the different peaks at 239  $\text{cm}^{-1}$ , 320  $\text{cm}^{-1}$ , 414  $\text{cm}^{-1}$  and 577  $\text{cm}^{-1}$ . Silicon substrate peak was detected at 523  $\text{cm}^{-1}$  with higher intensity in as-deposited and annealed films. The first two peak are related to the second order modes of ZnO. The  $E_2$  (high mode) has been observed only in annealed Ag-ZnO films at 414  $\text{cm}^{-1}$  and another sharp peak at 577  $\text{cm}^{-1}$ . These peaks could be assigned to  $A_1$  (LO) mode of ZnO. The intensity of bands was found to be increased with thermal annealing as confirmed by Raman spectra. The lattice defects and crystalline quality of the film can be affected by the thermal annealing which support the conclusion drawn from the XRD results. The intensity of  $E_2$  (high) and  $A_1$  (LO) modes of ZnO increased with thermal annealing. We expect that this increment might be due to reduction in oxygen vacancies and strain relaxation between the grains which directly corroborates the results obtained by XRD.

#### 4. Conclusions

The Ag-ZnO NCs thin films were successfully synthesized by the RF-magnetron sputtering technique. The formation of the composite was confirmed by XPS and TEM analysis with significant evidence with the presence of Ag nanoparticles. The thermal induced structural and optical modifications were observed in the present case by different characterization techniques. The crystalline nature of film grown by RF-sputtering and has been increased with the thermal annealing. These results are very advantageous for the different device fabrication area. The thermal induced SPR tuning was successfully presented in this study. We observed a  $\sim 22$  nm red shift after the thermal treatment which confirms the presence and growth of the nanoparticles in ZnO matrix. This tunable properties of Ag-ZnO NCs thin films could be very effective for the different plasmonic application.

#### Acknowledgment

The author S.K. Singh grateful to “Technical Education Quality Improvement Programme (TEQIP)” MNIT, Jaipur for supporting the financial assistantship during research work. The author would like to thank Material Research Center (MRC), Malaviya National Institute of Technology Jaipur for providing the synthesis technique and all characterization facility which are used in present experiment. This work is also supported under the Project (UFR-54302) by IUAC New Delhi.

#### References

- [1] D.K. Avasthi, Y.K. Mishra, D. Kabiraj, N.P. Lalla, J.C. Pivin, Synthesis of metal-polymer NCs for optical applications, *Nanotechnology* 18 (2007) 125604, <https://doi.org/10.1088/0957-4484/18/12/125604>.
- [2] J. Yu, J. Xiong, B. Cheng, S. Liu, Fabrication and characterization of Ag-TiO<sub>2</sub> multiphase NCs thin films with enhanced photocatalytic activity, *Appl. Catal. B Environ.* 60 (2005) 211–221, <https://doi.org/10.1016/j.apcatb.2005.03.009>.
- [3] D.B. Strukov, J.L. Borghetti, R. Stanley Williams, Coupled ionic and electronic transport model of thin-film semiconductor memristive behavior, *Small* 5 (2009) 1058–1063, <https://doi.org/10.1002/sml.200801323>.
- [4] H. Tai, Y. Jiang, G. Xie, J. Yu, X. Chen, Fabrication and gas sensitivity of polyaniline-titanium dioxide NCs thin film, *Sens. Actuators B Chem.* 125 (2007) 644–650, <https://doi.org/10.1016/j.snb.2007.03.013>.
- [5] C.F. Klingshirn, B.K. Meyer, A. Waag, A. Hoffmann, J. Geurts, Zinc Oxide From Fundamental Properties Towards Novel Applications, Springer (2010), <https://doi.org/10.1007/978-3-642-10577-7>.
- [6] G.A. Hirata, J. McKittrick, T. Cheeks, J.M. Siqueiros, J.A. Diaz, O. Contreras, O.A. Lopez, Synthesis and optoelectronic characterization of gallium doped zinc oxide transparent electrodes, *Thin Solid Films* 288 (1996) 29–31, [https://doi.org/10.1016/S0040-6090\(96\)08862-1](https://doi.org/10.1016/S0040-6090(96)08862-1).
- [7] E. Galoppini, J. Rochford, H. Chen, G. Saraf, Y. Lu, A. Hagfeldt, G. Boschloo, Fast electron transport in metal organic vapor deposition grown dye-sensitized ZnO nanorod solar cells, *J. Phys. Chem. B* 110 (2006) 16139–16161, <https://doi.org/10.1021/jp062865q>.
- [8] W. Lu, S. Gao, J. Wang, One-pot synthesis of Ag/ZnO self-assembled 3D hollow microspheres with enhanced photocatalytic performance, *J. Phys. Chem. C* 112 (2008) 16792–16800, <https://doi.org/10.1021/jp803654k>.
- [9] H. Tan, R. Santbergen, A.H.M. Smets, M. Zeman, Plasmonic light trapping in thin-film silicon solar cells with improved self-assembled silver nanoparticles, *Nano Lett.* 12 (2012) 4070–4076, <https://doi.org/10.1021/nl301521z>.
- [10] K.J. Chen, F.Y. Hung, S.J. Chang, S.J. Young, Optoelectronic characteristics of UV photodetector based on ZnO nanowire thin films, *J. Alloys Compd.* 479 (2009) 674–677, <https://doi.org/10.1016/j.jallcom.2009.01.026>.
- [11] P.F. Garcia, R.S. McLean, M.H. Reilly, G. Nunes, Transparent ZnO thin-film transistor fabricated by rf magnetron sputtering, *Appl. Phys. Lett.* 82 (2003) 1117–1119, <https://doi.org/10.1063/1.1553997>.
- [12] J. Mass, P. Bhattacharya, R. Katiyar, Effect of high substrate temperature on Al-doped ZnO thin films grown by pulsed laser deposition, *Mater. Sci. Eng. B* 103 (2003) 9–15, [https://doi.org/10.1016/S0921-5107\(03\)00127-2](https://doi.org/10.1016/S0921-5107(03)00127-2).
- [13] S.K. Singh, R. Singhal, V.V. Siva Kumar, Study on swift heavy ions induced modifications of Ag-ZnO NCs thin film, *Superlattices Microstruct.* 103 (2017) 195–204, <https://doi.org/10.1016/j.spmi.2017.01.032>.
- [14] A. Kim, Y. Won, K. Woo, C.H. Kim, J. Moon, Highly transparent low resistance ZnO/Ag nanowire/ZnO composite electrode for thin film solar cells, *ACS Nano* 7 (2013) 1081–1091, <https://doi.org/10.1021/nn305491x>.
- [15] S.K. Singh, R. Singhal, R. Vishnoi, V.V.S. Kumar, P.K. Kulriya, Swift heavy ion induced optical and structural modifications in RF sputtered nanocrystalline ZnO thin film, *Indian J. Phys.* 91 (2017) 547–554, <https://doi.org/10.1007/s12648-016-0950-6>.
- [16] R. Vishnoi, R. Singhal, K. Asokan, D. Kanjilal, D. Kaur, Ion irradiation induced modifications of nanostructured Ni-Mn-Sn ferromagnetic shape memory alloy thin films, *Thin Solid Films* (2011) 1631–1637, <https://doi.org/10.1016/j.tsf.2011.08.021>.
- [17] D. Bao, H. Gu, A. Kuang, Sol-gel-derived c-axis oriented ZnO thin films, *Thin Solid Films* 312 (1998) 37–39, [https://doi.org/10.1016/S0040-6090\(97\)00302-7](https://doi.org/10.1016/S0040-6090(97)00302-7).
- [18] R. Singhal, D.C. Agarwal, S. Mohapatra, Y.K. Mishra, D. Kabiraj, F. Singh, D.K. Avasthi, A.K. Chawla, R. Chandra, G. Mattei, J.C. Pivin, Synthesis and characterizations of silver-fullerene C70 NCs, *Appl. Phys. Lett.* 93 (2008) 3–5, <https://doi.org/10.1063/1.2976674>.
- [19] R. Singhal, D. Kabiraj, P.K. Kulriya, J.C. Pivin, R. Chandra, D.K. Avasthi, Blue-shifted SPR of Au nanoparticles with ordering of carbon by dense ionization and thermal treatment, *Plasmonics* 8 (2013) 295–305, <https://doi.org/10.1007/s11468-012-9389-6>.
- [20] R. Singhal, J.C. Pivin, R. Chandra, D.K. Avasthi, Ion irradiation studies of silver/amorphous carbon NCs thin film, *Surf. Coatings Technol.* 229 (2013) 50–54, <https://doi.org/10.1016/j.surfcoat.2012.05.131>.
- [21] S. Fa, U. Kroll, C. Bucher, E. Vallat-Sauvain, A. Shah, Low pressure chemical vapour deposition of ZnO layers for thin-film solar cells: Temperature-induced morphological changes, *Sol. Energy Mater. Sol. Cells.* 86 (2005) 385–397, <https://doi.org/10.1016/j.solmat.2004.08.002>.
- [22] X.M. Fan, J.S. Lian, Z.X. Guo, H.J. Lu, Microstructure and photoluminescence properties of ZnO thin films grown by PLD on Si(1 1 1) substrates, *Appl. Surf. Sci.* 239 (2005) 176–181, <https://doi.org/10.1016/j.apsusc.2004.05.144>.
- [23] Y. Chen, D.M. Bagnall, Z. Zhu, T. Sekiuchi, K. Park, K. Hiraga, T. Yao, S. Koyama, M.Y. Shen, T. Goto, Growth of ZnO single crystal thin films on c-plane (0 0 0 1) sapphire by plasma enhanced molecular beam epitaxy, *J. Cryst. Growth* 181 (1997) 165–169, [https://doi.org/10.1016/S0022-0248\(97\)00286-8](https://doi.org/10.1016/S0022-0248(97)00286-8).
- [24] W.W. Wenas, A. Yamada, K. Takahashi, M. Yoshino, M. Konagai, Electrical and optical properties of boron-doped ZnO thin films for solar cells grown by metalorganic chemical vapor deposition, *J. Appl. Phys.* 70 (1991) 7119–7123, <https://doi.org/10.1063/1.349794>.
- [25] T. Minami, H. Nanto, S. Takata, Highly conductive and transparent aluminum doped zinc oxide thin films prepared by RF magnetron sputtering, *Jpn. J. Appl. Phys.* 23 (1984) L280–L282, <https://doi.org/10.1143/JJAP.23.L280>.
- [26] R. Ondo-Ndong, G. Ferblantier, M. Al Kalfioui, A. Boyer, A. Foucaran, Properties of RF magnetron sputtered zinc oxide thin films, *J. Cryst. Growth.* 255 (2003) 130–135, [https://doi.org/10.1016/S0022-0248\(03\)01243-0](https://doi.org/10.1016/S0022-0248(03)01243-0).
- [27] S. Zhao, Y. Zhou, K. Zhao, Z. Liu, P. Han, S. Wang, W. Xiang, Z. Chen, H. Lü, B. Cheng, G. Yang, Violet luminescence emitted from Ag-nanocluster doped ZnO thin films grown on fused quartz substrates by pulsed laser deposition, *Phys. B Condens. Matter.* 373 (2006) 154–156, <https://doi.org/10.1016/j.physb.2005.11.116>.
- [28] H.S. Kang, B. Du Ahn, J.H. Kim, G.H. Kim, S.H. Lim, H.W. Chang, S.Y. Lee, Structural, electrical, and optical properties of p-type ZnO thin films with Ag dopant, *Appl. Phys. Lett.* 88 (2006) 202108, <https://doi.org/10.1063/1.2203952>.
- [29] B. Du Ahn, S. Hoon Oh, C. Hee Lee, G. Hee Kim, H. Jae Kim, S. Yeol Lee, Influence of thermal annealing ambient on Ga-doped ZnO thin films, *J. Cryst. Growth.* 309 (2007) 128–133, <https://doi.org/10.1016/j.jcrysgro.2007.09.014>.
- [30] Y.K. Mishra, V.S.K. Chakravadhanula, V. Hrkac, S. Jebril, D.C. Agarwal, S. Mohapatra, D.K. Avasthi, L. Kienle, R. Adelung, Crystal growth behaviour in Au-

- ZnO NCs under different annealing environments and photoswitchability, *J. Appl. Phys.* 112 (2012) 64308, <https://doi.org/10.1063/1.4752469>.
- [31] N. Fujimura, T. Nishihara, S. Goto, J. Xu, T. Ito, Control of preferred orientation for ZnO films: control of self-texture, *J. Cryst. Growth.* 130 (1993) 269–279, [https://doi.org/10.1016/0022-0248\(93\)90861-P](https://doi.org/10.1016/0022-0248(93)90861-P).
- [32] L. García-Gancedo, J. Pedrós, Z. Zhu, A.J. Flewitt, W.I. Milne, J.K. Luo, C.J.B. Ford, Room-temperature remote-plasma sputtering of c-axis oriented zinc oxide thin films, *J. Appl. Phys.* 112 (2012) 14907, <https://doi.org/10.1063/1.4736541>.
- [33] A.L. Patterson, The scherrer formula for X-ray particle size determination, *Phys. Rev.* 56 (1939) 978–982, <https://doi.org/10.1103/PhysRev.56.978>.
- [34] A. Janotti, C.G. Van de Walle, Fundamentals of zinc oxide as a semiconductor, *Reports Prog. Phys.* 72 (2009) 126501, <https://doi.org/10.1088/0034-4885/72/12/126501>.
- [35] V. Bilgin, S. Kose, F. Atay, I. Akyuz, The effect of substrate temperature on the structural and some physical properties of ultrasonically sprayed CdS films, *Mater. Chem. Phys.* 94 (2005) 103–108, <https://doi.org/10.1016/j.matchemphys.2005.04.028>.
- [36] A. Kavokin, M. Zamfirescu, B. Gil, G. Malpuech, ZnO as a material mostly adapted for realisation of room-temperature polariton lasers, *Phys. Status Solidi a – Appl. Mater. Sci.* 192 (2002) 212–217, [https://doi.org/10.1002/1521-396X\(200207\)192:1](https://doi.org/10.1002/1521-396X(200207)192:1).
- [37] C. Ruppe, A. Duparré, Roughness analysis of optical films and substrates by atomic force microscopy, *Thin Solid Films* 288 (1996) 8–13, [https://doi.org/10.1016/S0040-6090\(96\)08807-4](https://doi.org/10.1016/S0040-6090(96)08807-4).
- [38] S.W. Xue, X.T. Zu, W.L. Zhou, H.X. Deng, X. Xiang, L. Zhang, H. Deng, Effects of post-thermal annealing on the optical constants of ZnO thin film, *J. Alloys Compd.* 448 (2008) 21–26, <https://doi.org/10.1016/j.jallcom.2006.10.076>.
- [39] X.W. Sun, H.S. Kwok, Optical properties of epitaxially grown zinc oxide films on sapphire by pulsed laser deposition, *J. Appl. Phys.* 86 (1999), <https://doi.org/10.1063/1.370744>.
- [40] J. Tauc, Optical properties and electronic structure of amorphous Ge and Si, *Mater. Res. Bull.* 3 (1968) 37–46, [https://doi.org/10.1016/0025-5408\(68\)90023-8](https://doi.org/10.1016/0025-5408(68)90023-8).
- [41] J.F. Scott, Uv resonant Raman scattering in ZnO, *Phys. Rev. B.* 2 (1970) 1209–1211, <https://doi.org/10.1103/PhysRevB.2.1209>.
- [42] C. Bundesmann, N. Ashkenov, M. Schubert, D. Spemann, T. Butz, E.M. Kaidashev, M. Lorenz, M. Grundmann, Raman scattering in ZnO thin films doped with Fe, Sb, Al, Ga, and Li, *Appl. Phys. Lett.* 83 (2003) 1974–1976, <https://doi.org/10.1063/1.1609251>.



# Thermal-induced structural and optical investigations of Ag–ZnO nanocomposite thin films

S.K. Singh<sup>\*</sup>, R. Singhal

Department of Physics, Malaviya National Institute of Technology Jaipur, JLN Marg, Malaviya Nagar, Jaipur 302017, Rajasthan, India



## ARTICLE INFO

### Article history:

Available online 25 April 2018

### Keywords:

Nanocomposite thin film  
RF-Sputtering  
X-ray photoelectron spectroscopy  
UV–Visible spectroscopy

## ABSTRACT

In the present paper, we have successfully synthesized Ag–ZnO nanocomposite thin films by RF-magnetron sputtering technique at room temperature. Systematic investigations of thermal-induced structural and optical modifications in Ag–ZnO thin films have been observed and described. The Ag–ZnO thin films were annealed at three different temperatures of 300 °C, 400 °C and 500 °C in vacuum to prevent the oxidation of Ag. The presence and formation of Ag nanoparticles were estimated by transmission electron microscopy. X-ray diffraction analysis revealed the structural information about the crystalline quality of ZnO. The crystallinity as well as the crystallite size of the films have been found to be improved with annealing temperatures. The estimated crystallite size was ~15.8 nm for as-deposited film and 19.0 nm for the film at a higher temperature. The chemical composition and structural analysis of as-deposited film were carried out by X-ray photoelectron spectroscopy. A very sharp absorption band appeared at ~540 nm for Ag NPs that is associated with the surface plasmon resonance band of Ag. A noticeable red shift of about ~12 nm has been recorded for films annealed at 500 °C. Atomic force microscopy has been utilized to examine the surface morphology of the as-deposited and annealed films. The grain size was found to be increase with increasing annealing temperature, while no significant changes were observed in the roughness of Ag–ZnO thin films. Raman spectroscopy revealed lattice defects and disordering in the films after the thermal annealing.

© 2018 Elsevier Ltd. All rights reserved.

## 1. Introduction

In the present scenario, crystalline nanomaterials emerged as useful due to their excellent electrical and optical properties. Such properties of nanomaterial yield an extraordinary effects in the diverse research area, especially due to the introduction of metallic particles in a ZnO matrix [1,2]. Commonly, nanocrystalline thin films can play a significant role in enhancing the material physical properties which cannot be possible in bulk materials [3,4]. Among of them, nanocomposite thin film is vastly growing research fields because of their diverse applications [5,6]. Incorporation of the metal nanoparticles in a parent matrix makes it very promising in optical applications since metal particles show exciting optical properties [7,8].

ZnO is an efficient material with the direct band gap of 3.4 eV at room temperature and a high exciton binding energy of 60 meV [9]. Nowadays, doped ZnO nanostructures have been subjected to great interest to the researchers, due to their wide

<sup>\*</sup> Corresponding author.

E-mail address: [singhshushant86@gmail.com](mailto:singhshushant86@gmail.com) (S.K. Singh).

applications in different technological fields such as optoelectronic devices [10], transparent electrodes formation [11], solar cell industry [12], photocatalytic activity [13], plasmonic [14], and thin film transistors devices [15]. Among of all, incorporation of Ag metal in ZnO matrix attract special attention owing to its superior optical properties [16,17]. The absorption/scattering cross section of Ag nanoparticle is larger than the geometrical cross-section that makes it superior to other class of the materials. Moreover, it showed higher interaction with the incident light [18]. Therefore, the presence of Ag nanoparticles in ZnO matrix gives plasmon-active SPR band in visible and near infrared region and offered new optical properties for different plasmonic applications [18,19].” Various reports are available for the modification in matrix properties using metal-metal nanocomposite thin films for different applications [19–21]. Though, the thermal induced SPR tuning of Ag in ZnO matrix is less studied. There are several method to synthesis Ag–ZnO nanocomposite thin films such as physical-vapour deposition [22], sol-gel method [23], dip coating [24], electron-beam deposition [25], molecular beam epitaxial growth [26], chemical vapour deposition [27], DC/RF sputtering method [28]. RF-sputtering is a unique technique to synthesize the metal-nanocomposite thin films with higher crystalline quality and good adhesion on different substrates. The structural and optical properties of such films depend significantly on the nature of embedded nanoparticles (i.e., shape and size of the nanoparticles) as well as the surrounding medium (ZnO matrix). Therefore, in order to trigger both structural and optical properties, thermal energy plays an important that can be provided by thermal annealing at higher temperatures [29,30]. Thermal annealing is very low-cost and unsophisticated technique for producing structural modifications, to further boost the device performance.

In the present study, Ag–ZnO nanocomposite thin films have been synthesized by RF-magnetron sputtering at the room temperature. Prepared thin films were annealed in vacuum at three different temperatures of 300 °C, 400 °C and 500 °C. Thermal-induced structural and optical modification have been investigated with various characterization techniques. The tunable structural and optical properties of these films might be useful in plasmonic and device fabrications.

## 2. Experimental plan

Ag–ZnO nanocomposite thin films were synthesized by RF-magnetron sputtering at room temperature. A target of pure ZnO was used for the deposition, prepared from ZnO powder (Merck) by the hydraulic press machine. A tubular furnace was used for the Sintering process of the target at a temperature of 1200 °C for 24 h in an oxygen environment. To prepare the Ag–ZnO nanocomposite, one small piece of Ag was glued on the target before mounting in the target holder. Silicon and glass substrates were used for the film deposition. RCA-1 cleaning method was applied to remove different redundant residues from the surface of the substrate. The sputtering chamber was connected with rotary and turbo pumps to maintain the desired vacuum in the chamber. After mounting the target and substrates, both pumps were switched on, to achieve the high vacuum in the chamber. In the first stage, the rotary pump created a rough vacuum in the chamber followed by the turbo-molecular pump. The vacuum in the chamber was noted from the reading of penning gauge and found to be  $\sim 2 \times 10^{-6}$  mbar before incorporating the argon gas. Then argon gas was introduced in the chamber to create the plasma, and vacuum of the chamber got down and recorded  $1.5 \times 10^{-2}$  during the film deposition. A  $\sim 60$  W power supplied to sputter the target material for  $\sim 40$  min. At the same time, the thickness of the deposited film was observed by the help of quartz crystal monitor and found to be  $\sim 80$  nm. The slow deposition  $0.2 \text{ \AA/second}$  rate was kept to maintain the homogenous film growth. After that, prepared Ag–ZnO thin films were annealed at three different temperature 300 °C, 400 °C and 500 °C. The annealing was performed in the vacuum (of the order of  $\sim 1.24 \times 10^{-2}$  mbar) to prevent oxidation of the Ag from the ZnO matrix.

After the synthesis and annealing of Ag–ZnO NC thin films, different characterization techniques were used to investigate the properties of the as-deposited and annealed thin films. X-ray diffraction spectroscopy (Cu-K $\alpha$  beam at the wavelength of 1.54 Å) was carried out to understand the structural information. Surface and chemical analysis were done by atomic force microscopy (Bruker) and X-ray photoelectron spectroscopy. The presence and formation of the nanoparticles were estimated by transmission electron microscopy (Tecnai G<sup>2</sup> 20-FEI). Optical properties of the films were carried out by UV–visible spectroscope (Perkin Elmer) and Raman spectra of the film were recorded by Raman microscope (AIRIX-STR 500) with the laser beam (wavelength 532 nm) at low power. All synthesis and characterization facilities were performed in Material Research Center (MRC) at Malaviya National Institute of Technology Jaipur.

## 3. Result and discussion

### 3.1. X-ray diffraction analysis

To observe the structural and crystalline behavior of the as-deposited and annealed films, X-ray diffraction analysis has been performed in the range of  $2\theta = 30\text{--}50^\circ$  degrees. Fig. 1 shows the X-ray pattern of as-deposited and annealed films at three different temperatures of 300 °C, 400 °C and 500 °C respectively. A most prominent Bragg peak was observed at an angle of  $34.33^\circ$  that corresponds to (002) plane of the hexagonal wurtzite structure. As the annealing temperature increases, the peak intensity of (002) plane increases significantly, indicating a gradual improvement in the crystallinity of the film.

Therefore, it is concluded that the crystallinity of the film increases with increasing the annealing temperature. According to basic crystal theory, it is well known for ZnO wurtzite system that the (002) orientation had higher growth rate due to small surface energy along the c-axis [31]. The c-axis orientation dominant in the as deposited and annealed films with higher

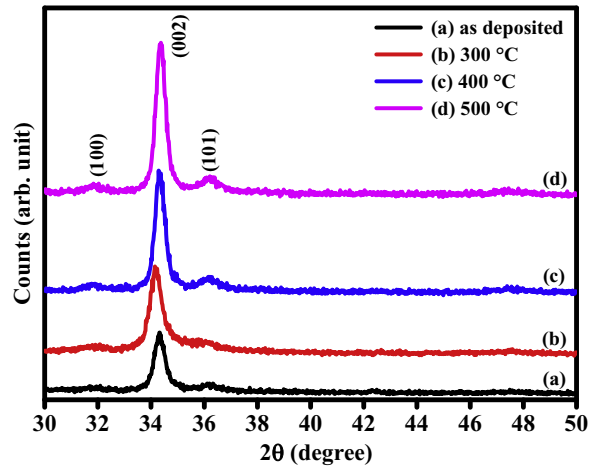


Fig. 1. X-ray diffraction spectra of as-deposited and annealed Ag–ZnO NCs thin films.

intensity of the (002) plane which represents the higher crystalline behavior with thermal annealing. No signature of Ag and other phases were observed in the spectra. We assume that this might be due to a low concentration of Ag and the formation of nanoparticles. The crystallite size of the as-deposited and annealed films was calculated using well known Scherrer's [32] formula as explained in the following manner:

$$\text{Crystallite size } (D) = \frac{0.9 \lambda}{\beta \cos \theta}$$

In above relation,  $\beta$  is the full width at half maxima (FWHM),  $\theta$  is the Bragg diffraction angle and  $\lambda$  shows the wavelength of X-ray beam (Cu-K $\alpha$  = 1.54 Å). The calculated crystallite size was 15.8 nm for as-deposited film and reached up to 19.0 nm for the film annealed at temperature 500 °C. Furthermore, lattice strain [33] and dislocation density [34] for the as-deposited and annealed films have also been calculated by the following relations:

$$\text{Lattice strain } (\epsilon) = \frac{\beta \cot \theta}{4}$$

and

$$\text{Dislocation density } (\delta) = \frac{1}{D^2}$$

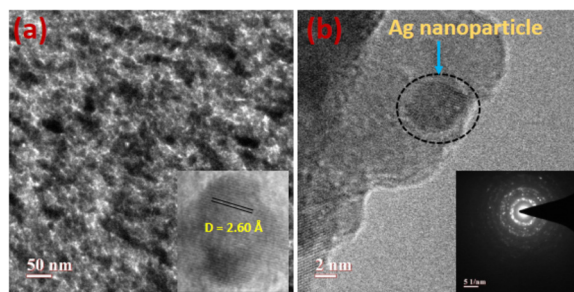
Lattice strain of the films was calculated to be 0.74% and decreases with increasing annealing temperature. The minimum value of the strain was found for film annealed at 500 °C. In addition, a large crystallite size of 19 nm was found for such film. This can be understood in the term of energy relaxation between the grains during the thermal annealing. A high dislocation density was found for as-deposited film. However, it decreases with increasing the annealing temperature as summarized in Table 1. The calculated value of dislocations density for as-deposited and annealed film are  $4.1 \times 10^{15}$  and  $2.7 \times 10^{15}$  line/m<sup>2</sup> respectively. The decrement in the dislocation density and lattice strain is related to the higher crystalline behavior of the films that is affected by thermal annealing.

Table 1

Crystallite size, lattice strain and dislocation density of the as-deposited and annealed Ag–ZnO NCs thin films.

Sr. No.	Sample detail	Crystallite size (nm)	Lattice Strain (%)	Dislocation density ( $\times 10^{15}$ line/m <sup>2</sup> )
1.	As-deposited Ag–ZnO	15.8 $\pm$ 0.9	0.74	4.1
2.	300 °C	17.1 $\pm$ 0.6	0.69	3.4
3.	400 °C	18.6 $\pm$ 0.8	0.64	2.9
4.	500 °C	19.0 $\pm$ 0.5	0.62	2.7





**Fig. 2.** TEM micrographs of as-deposited Ag–ZnO NCs thin film (a) surface image (HETEM image inset) (b) Ag nanoparticle (SAED pattern).

### 3.2. Transmission electron microscopy

Transmission electron microscopy is a very efficient technique to confirm the formation of the nanoparticles at nm scale. Fig. 2 depicts the TEM micrographs of the as-deposited Ag–ZnO nanocomposite thin film. A homogenous distribution of material was observed at the surface (see top view Fig. 2 (a)). In high-resolution image, the presence of Ag nanoparticle is clearly observed in Fig. 2 (b) as marked by a black circle and the size of the Ag nanoparticle was measured to be  $\langle D \rangle \cong 5.6$  nm for as-deposited Ag–ZnO film. HRTEM images of ZnO film were acquired for calculating the d-spacing as marked in the inset of Fig. 2 (a). Lattice fringes with d-spacing of 2.60 Å were observed that correspond to (002) plane of the wurtzite structure of ZnO. These results are in agreement with XRD analysis wherein a high intensity (002) peak was detected in the diffraction spectra. To further observe the crystallinity of the as-deposited film, selected area diffraction pattern (SAED) were acquired and the resulting diffraction pattern (inset of Fig. 2(b)) containing spots enclosed in a ring pattern.

### 3.3. X-ray photoelectron spectroscopy

X-ray photoelectron spectroscopy has been carried out to determine the elemental composition and electronic structure of the elements present in the film. In this case, XPS analysis was performed for the as-deposited Ag–ZnO thin film to better understand the formation and elemental composition. Full scan as well as core spectrum of the different elements (Ag, Zn and O) in the as-deposited film have been recorded and are shown in Fig. 3(a–d). The core spectra of Zn 2p region split into two different states  $2p_{3/2}$  and  $2p_{1/2}$  at the energy scale of 1022.33 eV and 1045.52 eV respectively, as displayed in Fig. 3 (d). The presence of oxygen group was also confirmed by two different peaks, which is clearly seen in the core spectra of the oxygen. The splitting of the peak in two regions Zn–O and O–H were observed at the energy scale of 530.61 eV and 532.14 eV respectively. Zn–O region support to the formation of ZnO while the appearance of O–H group observed due to the presence of hydroxyl group. This hydroxyl group may be arises presumably due to defects and contamination during the film growth [35]. The Ag 3d peak in the survey scan has confirmed the presence of Ag in ZnO matrix. The chemical composition of Ag was found to be ~9 at.%. A high-resolution spectrum of the Ag 3d doublet is shown in Fig. 4 (b). Furthermore, the de-convolution of Ag 3d doublet was carried out that revealed two different states  $3d_{5/2}$  and  $3d_{3/2}$  at the binding energy of 367.98 eV and 374.11 eV respectively. A small shoulder was observed with these two states this is associated with Ag 3d. The reason for the small shoulder could be attributed to the formation of other groups such as Ag–Zn–O and  $Ag_2$ –O. However, the contribution of these groups are negligible in the present case. XPS analysis confirms the presence of different species like Ag, Zn and O and their possible phase/group.

### 3.4. UV–visible spectroscopy

Thermal-induced optical modifications have been investigated by UV–visible spectroscopy in reflectance mode for as-deposited and annealed Ag–ZnO thin films. To find out the surface plasmon resonance (SPR) band of Ag nanoparticles, the absorbance of the films was calculated by the reflection data and plotted as the absorbance versus wavelength spectra of the films. Fig. 4 shows the absorption spectra of the as-deposited and annealed films at three different temperatures of 300 °C, 400 °C and 500 °C. A strong absorption band was identified at the wavelength of 540 nm for the as-deposited film. This strong absorption is known as SPR band of the Ag nanoparticles [36]. The position of SPR band has been found to be increase toward the higher wavelength side with increasing in the thermal annealing. The shifting in the SPR position towards the higher wavelength called as red shift. At the higher annealing temperature (500 °C), the SPR has been shifted to 552 nm wavelength. This shifting of ~12 nm in SPR band at 500 °C is attributed to the growth of the Ag nanoparticles during thermal annealing. The FWHM of the SPR band calculated by Gaussian fitting and found to be 90.07 for as deposited film and it decreased up to 69.49 for annealed film at the temperature of 500 °C with thermal annealing which support the growth of the particles. With the increasing of annealing temperature, the SPR band becomes sharper with red shift (~12 nm) which directly indicates the growth of the nanoparticles [37,38]. As the annealing temperature increases, the crystalline quality of the film increases with increase in crystallite size as estimated by XRD, which in turn support the growth of nanoparticles. This tailoring in the

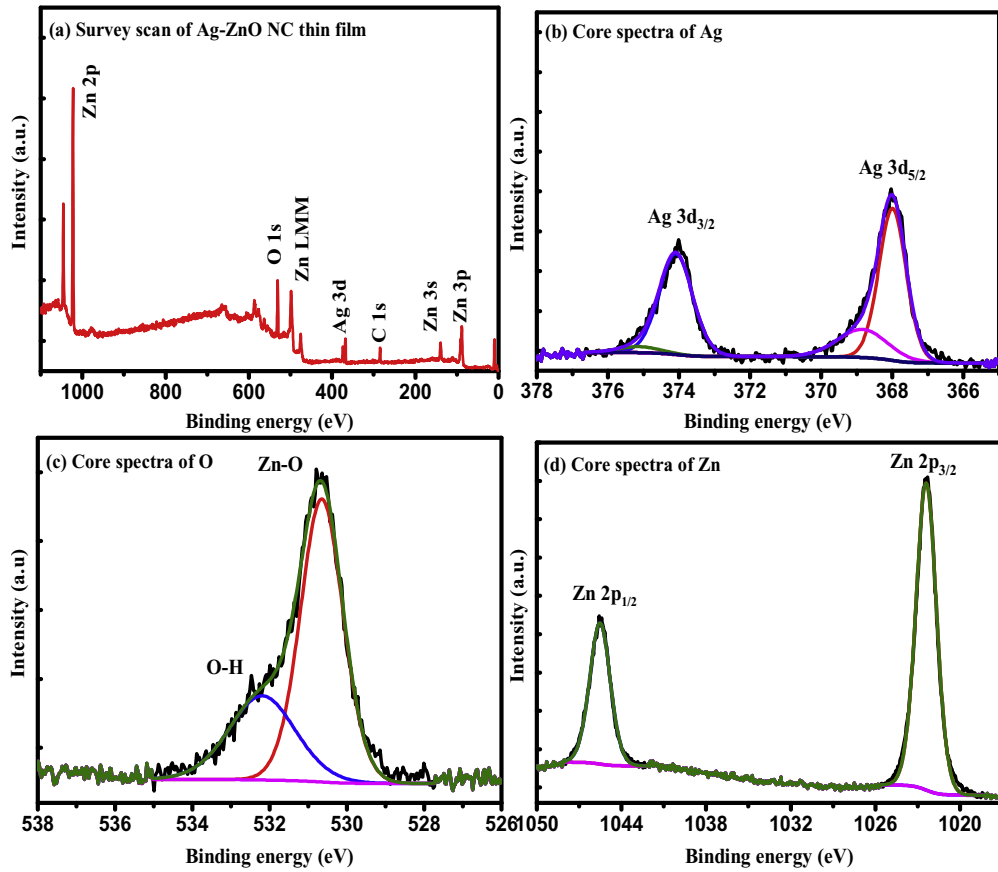


Fig. 3. XPS spectra (a) survey scan (b) core spectra of Ag (c) core spectra of O and (c) core spectra of Zn of as-deposited Ag–ZnO thin film.

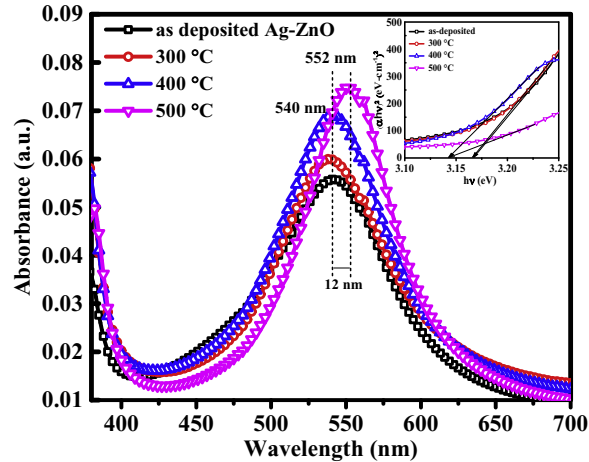


Fig. 4. UV–visible absorption spectra of Ag–ZnO nanocomposite thin film.

position of SPR band of the Ag nanoparticles with thermal annealing can be used for the plasmonic applications. The optical band gap of the as-deposited and annealed Ag–ZnO nanocomposite thin films was calculated by well-known Tau's relation [39] which can be expressed in the following manner:

$$\alpha h\nu = A (h\nu - E_g)^{1/2}$$

In the given Tau'c relation, symbol  $h\nu$  represents the photon energy which is falling on the sample film and  $E_g$  represents the energy band gap of the material. In the present experiment, the band gap of the as-deposited film was calculated and found to be 3.17 eV. It decreases with increasing the thermal annealing and found to be 3.14 eV for film annealed at a temperature of 500 °C as shown in Fig. 4 (inset). The marginal decrement in the band gap of the film with thermal annealing may be due to higher metal to oxygen ratio as well as higher crystallinity of the film. During the thermal annealing, the growth of Ag nanoparticles in ZnO matrix observed which is subjected to the band gap reduction [40]. Therefore, incorporation of Ag metal in ZnO matrix is also responsible for the lower band gap.

### 3.5. Atomic force microscopy

Thermal-induced surface modifications have been observed by atomic force microscopy (AFM). AFM was performed in the tapping mode during the measurements. Fig. 5 showed the 3-D AFM images of the as-deposited and annealed Ag–ZnO thin films. The film growth was homogeneously over the substrate in the as deposition stage. Similar results were observed by TEM analysis as explained in the previous section. Both AFM and TEM results support the uniformity of the film growth. The grains are perfectly connected to each another in a nearly circular shape. The grain size was estimated for the as-deposited film as well as annealed Ag–ZnO thin films. The value of grain size increases with increasing the annealing temperature. These results are in agreement with XRD where a large crystallite size was observed at a higher temperature. The larger grain size could be due to agglomeration of the neighboring grains at sufficiently higher temperature. It is possible that grains acquire energy during the thermal annealing which leads to the agglomeration as well crystallization of the material. The XRD results also endorse the AFM results in this case. The roughness of the film was not significantly differ during the thermal annealing as confirmed by following relation [41]:

$$R_{rms} = \left[ \frac{1}{N} \sum_{i=1}^N |Z_i - \bar{Z}|^2 \right]^{\frac{1}{2}}$$

Where, N and Z are the surface height and mean height distance respectively. The estimated value of the surface roughness and grain size of the as-deposited and annealed Ag–ZnO films are summarized in given Table 2. During the thermal annealing

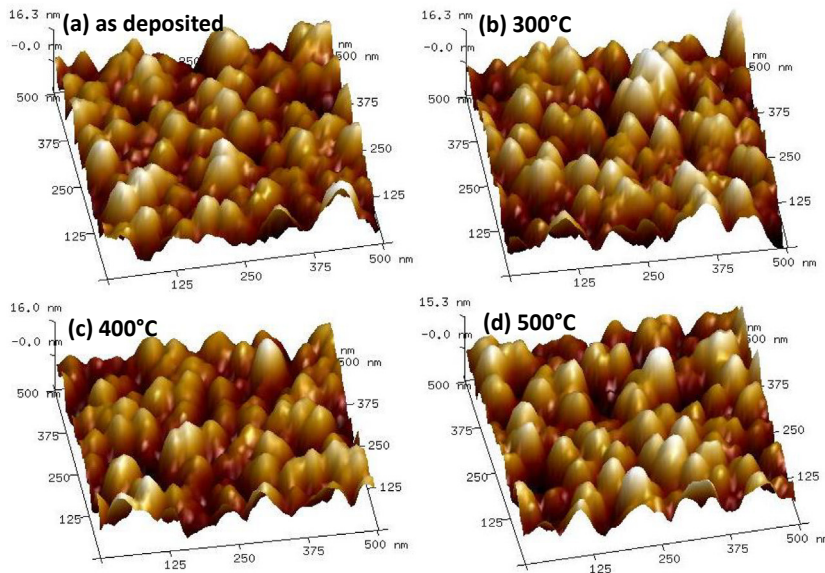


Fig. 5. 3-D AFM images of (a) as deposited and annealed (b) 300 °C (c) 400 °C and (d) 500 °C Ag–ZnO nanocomposite thin films.

**Table 2**  
Variation of roughness and grain size with different annealing temperatures.

SL. No.	Sample detail	Roughness ( $R_q$ )	Grain size
1.	as deposited Ag–ZnO	5.48 nm	49.82 ± 1.3 nm
2.	300 °C	5.45 nm	48.87 ± 1.9 nm
3.	400 °C	5.35 nm	59.41 ± 1.7 nm
4.	500 °C	5.10 nm	61.45 ± 2.3 nm

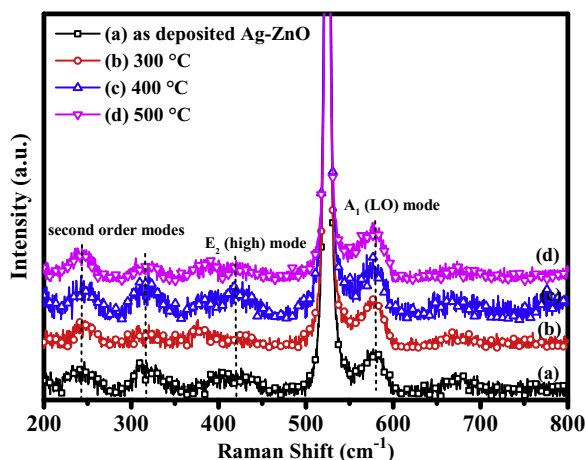


Fig. 6. Raman spectra of as Ag–ZnO nanocomposite thin films.

process, grains starting acquired energy and participated in the agglomeration process that might be responsible for the grain growth, size and shape of the grains.

### 3.6. Raman spectroscopy

To observe the different Raman active phonon modes of ZnO, Raman spectroscopy was carried out at room temperature. In general group theory suggested that, ZnO wurtzite structure has  $A_1+2E_2+E_1$  modes, where all atoms occupy  $C_{3v}$  sites [42]. Fig. 6 shows the typical Raman spectra of as-deposited and annealed films at three different temperatures of 300 °C, 400 °C and 500 °C. There are different Raman peaks observed in the spectra at different wavenumber such as 242, 315, 419 and 579  $\text{cm}^{-1}$ . Other than Raman peaks, a higher intense peak at  $\sim 524 \text{ cm}^{-1}$  was observed in the spectrum which is related to the silicon substrate and appears reproducible in all the films. The first two small intense peaks were assigned to second order modes and  $E_2$  high mode also observed at the position of 419  $\text{cm}^{-1}$  which is related to the crystalline nature of the sample. A peak appeared at 579  $\text{cm}^{-1}$  is assigned to the  $A_1$  (LO) mode. The presence of  $A_1$  (LO) mode in Raman spectra has been related to defects such as oxygen vacancies, Zn interstitials, free carriers and other complexes. The intensity of this mode is higher in the as deposited film in comparison to annealed films which indicates the more vacancies in the as grown film while the marginal decrement has been observed with thermal annealing at higher temperatures. The decrement in the intensity with thermal annealing implies that the concentration of defects decrease with the annealing temperature which also supported by defect density calculation by X-ray diffraction analysis [43,44].

## 4. Conclusions

Ag–ZnO nanocomposite thin films have been successfully synthesized by RF-magnetron sputtering and annealed in a vacuum environment at three different temperatures of 300 °C, 400 °C and 500 °C in sequential manner. Thermal-induced structural and optical modifications in Ag–ZnO nanocomposite thin films have been studied. X-ray diffraction analysis reveals the formation hexagonal wurtzite structure of ZnO and crystalline behavior of the films. TEM analysis confirmed the presence of Ag nanoparticles with the average size of the particle was  $\sim 5.6 \text{ nm}$  which also supported by XPS. A strong SPR band has been observed in as-deposited Ag–ZnO thin film at the position of 540 nm and significant red shift ( $\sim 12 \text{ nm}$ ) has been observed in the SPR band with annealing. Thermal annealing plays the important role to tune the optical and structural properties of the material. The tuning of SPR band might be very useful for the different plasmonic applications.

### Acknowledgment

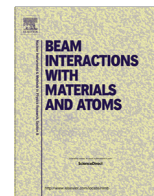
The author S.K. Singh highly thankful to “TEQIP” for providing the financial assistantship during the research work. Author is grateful to Material Research Center (MRC) at Malaviya National Institute of Technology Jaipur for providing synthesis and characterizations facility for the present study. This work is supported by IUAC Project Grant (UFR-54302) by Inter University Accelerator Center New Delhi.

### References

- [1] J.S. Chen, X.W. Lou, SnO<sub>2</sub>-based nanomaterials: synthesis and application in lithium-ion batteries, *Small* 9 (2013) 1877–1893, <https://doi.org/10.1002/sml.201202601>.

- [2] B. Baruwati, D.K. Kumar, S.V. Manorama, Hydrothermal synthesis of highly crystalline ZnO nanoparticles: a competitive sensor for LPG and EtOH, *Sensors Actuators, Biol. Chem.* 119 (2006) 676–682, <https://doi.org/10.1016/j.snb.2006.01.028>.
- [3] R.S. Mane, W.J. Lee, H.M. Pathan, S.-H. Han, Nanocrystalline TiO<sub>2</sub>/ZnO thin films: fabrication and application to dye-sensitized solar cells, *J. Phys. Chem. B* 109 (2005) 24254–24259, <https://doi.org/10.1021/jp0531560>.
- [4] R.E. Presley, C.L. Munsee, C.H. Park, D. Hong, J.F. Wager, D.A. Keszler, Tin oxide transparent thin-film transistors, *J. Phys. D Appl. Phys.* 37 (2004) 2810–2813, <https://doi.org/10.1088/0022-3727/37/20/006>.
- [5] F. Li, J. Song, H. Yang, S. Gan, Q. Zhang, D. Han, A. Ivaska, L. Niu, One-step synthesis of graphene/SnO<sub>2</sub> nanocomposites and its application in electrochemical supercapacitors, *Nanotechnology* 20 (2009) 455602, <https://doi.org/10.1088/0957-4484/20/45/455602>.
- [6] U. Schürmann, W. Hartung, H. Takele, V. Zaporozhchenko, F. Faupel, Controlled syntheses of Ag-polytetrafluoroethylene nanocomposite thin films by co-sputtering from two magnetron sources, *Nanotechnology* 16 (2005) 1078–1082, <https://doi.org/10.1088/0957-4484/16/8/014>.
- [7] Dongyan Zhang, Pangpang Wang, Ri-ichi Murakami, Xiaoping Song, Effect of an interface charge density wave on surface plasmon resonance in ZnO/Ag/ZnO thin films, *Appl. Phys. Lett.* 96 (2010) 233114, <https://doi.org/10.1063/1.3442916>.
- [8] S.K. Singh, R. Singhal, V.V. Siva Kumar, Study on swift heavy ions induced modifications of Ag-ZnO nanocomposite thin film, *Superlattice. Microst.* 103 (2017) 195–204, <https://doi.org/10.1016/j.spmi.2017.01.032>.
- [9] Ü. Özgür, Y.I. Alivov, C. Liu, A. Teke, M.A. Reshchikov, S. Doğan, V. Avrutin, S.J. Cho, H. Morko, A comprehensive review of ZnO materials and devices, *J. Appl. Phys.* 98 (2005) 1–103, <https://doi.org/10.1063/1.1992666>.
- [10] J.H. He, C.S. Lao, L.J. Chen, D. Davidovic, Z.L. Wang, Large-scale Ni-doped ZnO nanowire arrays and electrical and optical properties, *J. Am. Chem. Soc.* 127 (2005) 16376–16377, <https://doi.org/10.1021/ja0559193>.
- [11] X. Jiang, F.L. Wong, M.K. Fung, S.T. Lee, Aluminum-doped zinc oxide films as transparent conductive electrode for organic light-emitting devices, *Appl. Phys. Lett.* 83 (2003) 1875–1877, <https://doi.org/10.1063/1.1605805>.
- [12] D.G. Baik, S.M. Cho, Application of sol-gel derived films for ZnO/n-Si junction solar cells, *Thin Solid Films* 354 (1999) 227–231, [https://doi.org/10.1016/S0040-6090\(99\)00559-3](https://doi.org/10.1016/S0040-6090(99)00559-3).
- [13] R. Wang, J.H. Xin, Y. Yang, H. Liu, L. Xu, J. Hu, The characteristics and photocatalytic activities of silver doped ZnO nanocrystallites, *Appl. Surf. Sci.* 227 (2004) 312–317, <https://doi.org/10.1016/j.apsusc.2003.12.012>.
- [14] J.B. You, X.W. Zhang, Y.M. Fan, S. Qu, N.F. Chen, Surface plasmon enhanced ultraviolet emission from ZnO films deposited on Ag/Si(001) by magnetron sputtering, *Appl. Phys. Lett.* 91 (2007) 231907, <https://doi.org/10.1063/1.2822404>.
- [15] High Fridman, field-effect mobility zinc oxide thin film transistors produced at room temperature, in: *J. Non. Cryst. Solids*, North-Holland, 2004, pp. 806–809, <https://doi.org/10.1016/j.jnoncrsol.2004.03.096>.
- [16] G. Wang, Z. Li, S. Lv, M. Li, C. Shi, J. Liao, C. Chen, Optical absorption and photoluminescence of Ag interlayer modulated ZnO film in view of their application in Si solar cells, *Ceram. Int.* 42 (2016) 2813–2820, <https://doi.org/10.1016/j.ceramint.2015.11.014>.
- [17] J.S. Tawale, A. Kumar, A. Mohan, A.K. Srivastava, Influence of silver and graphite on zinc oxide nanostructures for optical application, *Opt. Mater.* 35 (2013) 1335–1341, <https://doi.org/10.1016/j.optmat.2013.01.034>.
- [18] D.D. Evanoff, G. Chumanov, Size-controlled synthesis of nanoparticles. 2. Measurement of extinction, scattering, and absorption cross sections, *J. Phys. Chem. B* 108 (2004) 13957–13962, <https://doi.org/10.1021/jp0475640>.
- [19] T. Ivanova, A. Harizanova, T. Koutzarova, B. Vertruyen, Sol-gel nanocrystalline ZnO: Ag films: structural and optical properties, *Superlattice. Microst.* 70 (2014) 1–6, <https://doi.org/10.1016/j.spmi.2014.03.007>.
- [20] U. Pal, J. Garcia-Serrano, G. Casarrubias-Segura, N. Koshizaki, T. Sasaki, S. Terahuchi, Structure and optical properties of M/ZnO (M = Au, Cu, Pt) nanocomposites, *Sol. Energy Mater. Sol. Cells* 81 (2004) 339–348, <https://doi.org/10.1016/j.solmat.2003.11.016>.
- [21] L. Duan, W. Gao, R. Chen, Z. Fu, Influence of post-annealing conditions on properties of ZnO: Ag films, *Solid State Commun.* 145 (2008) 479–481, <https://doi.org/10.1016/j.ssc.2007.12.013>.
- [22] Y.C. Kong, D.P. Yu, B. Zhang, W. Fang, S.Q. Feng, Ultraviolet-emitting ZnO nanowires synthesized by a physical vapor deposition approach, *Appl. Phys. Lett.* 78 (2001) 407–409, <https://doi.org/10.1063/1.1342050>.
- [23] L. Armelao, Sol-gel synthesis and characterisation of ZnO-based nanosystems, *Thin Solid Films* 394 (2001) 89–95, [https://doi.org/10.1016/S0040-6090\(01\)01158-0](https://doi.org/10.1016/S0040-6090(01)01158-0).
- [24] K. Thongsuriwong, P. Amornpitoksuk, S. Suwanboon, Structure, morphology, photocatalytic and antibacterial activities of ZnO thin films prepared by sol-gel dip-coating method, *Adv. Powder Technol.* 24 (2013) 275–280, <https://doi.org/10.1016/j.apt.2012.07.002>.
- [25] D.R. Sahu, S.Y. Lin, J.L. Huang, Deposition of Ag-based Al-doped ZnO multilayer coatings for the transparent conductive electrodes by electron beam evaporation, *Sol. Energy Mater. Sol. Cells* 91 (2007) 851–855, <https://doi.org/10.1016/j.solmat.2007.02.003>.
- [26] M.A.L. Johnson, S. Fujita, W.H. Rowland, W.C. Hughes, J.W. Cook, J.F. Schetzina, MBE growth and properties of ZnO on sapphire and SiC substrates, *J. Electron. Mater.* 25 (1996) 855–862, <https://doi.org/10.1007/BF02666649>.
- [27] J. Lu, Z. Ye, J. Huang, L. Wang, B. Zhao, Synthesis and properties of ZnO films with (1 0 0) orientation by SS-CVD, *Appl. Surf. Sci.* 207 (2003) 295–299, [https://doi.org/10.1016/S0169-4332\(02\)01502-7](https://doi.org/10.1016/S0169-4332(02)01502-7).
- [28] K.H. Kim, K.C. Park, D.Y. Ma, Structural, electrical and optical properties of aluminum doped zinc oxide films prepared by radio frequency magnetron sputtering, *J. Appl. Phys.* 81 (1997) 7764–7772, <https://doi.org/10.1063/1.365556>.
- [29] M.H. Habibi, R. Sheibani, Preparation and characterization of nanocomposite ZnO-Ag thin film containing nano-sized Ag particles: Influence of pre-heating, annealing temperature and silver content on characteristics, *J. Sol. Gel Sci. Technol.* 54 (2010) 195–202, <https://doi.org/10.1007/s10971-010-2177-x>.
- [30] E. Kusano, J. Kawaguchi, K. Enjouji, Thermal stability of heat-reflective films consisting of oxide–Ag–oxide deposited by dc magnetron sputtering, *J. Vac. Sci. Technol. A Vacuum, Surfaces, Film* 4 (1986) 2907–2910, <https://doi.org/10.1116/1.573658>.
- [31] V.A. Coleman, C. Jagadish, Basic properties and applications of ZnO, in: *Zinc Oxide Bulk, Thin Film. Nanostructures*, Elsevier, 2006, pp. 1–20, <https://doi.org/10.1016/B978-008044722-3/50001-4>.
- [32] A.L. Patterson, The scherrer formula for X-ray particle size determination, *Phys. Rev.* 56 (1939) 978–982, <https://doi.org/10.1103/PhysRev.56.978>.
- [33] P. Bindu, S. Thomas, Estimation of lattice strain in ZnO nanoparticles: X-ray peak profile analysis, *J. Theor. Appl. Phys.* 8 (2014) 123–134, <https://doi.org/10.1007/s40094-014-0141-9>.
- [34] R.K. Ham, The determination of dislocation densities in thin films, *Philos. What Mag.* 6 (1961) 1183–1184, <https://doi.org/10.1080/14786436108239679>.
- [35] K.W.J. Wong, M.R. Field, J.Z. Ou, K. Latham, M.J.S. Spencer, I. Yarovsky, K. Kalantar-Zadeh, Interaction of hydrogen with ZnO nanopowders - evidence of hydroxyl group formation, *Nanotechnology* 23 (2012) 15705, <https://doi.org/10.1088/0957-4484/23/1/015705>.
- [36] P. Mulvaney, Surface plasmon spectroscopy of nanosized metal particles, *Langmuir* 12 (1996) 788–800, <https://doi.org/10.1021/la950271i>.
- [37] U. Kreibitz, M. Vollmer, *Optical Properties of Metal Clusters*, Springer Berlin Heidelberg, Berlin, Heidelberg, 1995, <https://doi.org/10.1007/978-3-662-09109-8>.
- [38] Y.K. Mishra, S. Mohapatra, R. Singhal, D.K. Avasthi, D.C. Agarwal, S.B. Ogale, Au–ZnO: a tunable localized surface plasmonic nanocomposite, *Appl. Phys. Lett.* 92 (2008) 43107, <https://doi.org/10.1063/1.2838302>.
- [39] J. Tauc, R. Grigorovici, A. Vancu, Optical properties and electronic structure of amorphous germanium, *phys. Status Solidi* 15 (1966) 627–637, <https://doi.org/10.1002/pssb.19660150224>.
- [40] S.S. Xu, H.L. Lu, Y. Zhang, T. Wang, Y. Geng, W. Huang, S.J. Ding, D.W. Zhang, Bandgap narrowing and conductivity evolution of atomic-layer-deposited ZnO: Cu thin films under rapid thermal annealing, *J. Alloy. Comp.* 638 (2015) 133–135, <https://doi.org/10.1016/j.jallcom.2015.03.083>.
- [41] H.S. Zhang, J.L. Endrino, A. Anders, Comparative surface and nano-tribological characteristics of nanocomposite diamond-like carbon thin films doped by silver, *Appl. Surf. Sci.* 255 (2008) 2551–2556, <https://doi.org/10.1016/j.apsusc.2008.07.193>.

- [42] T.C. Damen, S.P.S. Porto, B. Tell, Raman effect in zinc oxide, *Phys. Rev.* 142 (1966) 570–574, <https://doi.org/10.1103/PhysRev.142.570>.
- [43] N. Garces, K. Stevens, G. Foundos, L. Halliburton, Electron paramagnetic resonance and optical absorption study of V<sup>4+</sup> centres in YVO<sub>4</sub>, *J. Phys. Condens. Matter* 16 (2004) 7095–7106, <https://doi.org/10.1088/0953-8984/16/39/0>.
- [44] D. Gao, Z. Zhang, J. fu, Y. xu, J. qi, D. Xue, Room temperature ferromagnetism of pure ZnO nanoparticles, *J. Appl. Phys.* 105 (2009) 119, <https://doi.org/10.1063/1.3143103>.



# Thermal annealing and SHI irradiation induced modifications in sandwiched structured Carbon-gold-Carbon (a-C/Au/a-C) nanocomposite thin film



S.K. Singh\*, R. Singhal

Department of Physics, Malaviya National Institute of Technology Jaipur, JLN Marg, Malaviya Nagar, Jaipur 302017, India

## ARTICLE INFO

### Article history:

Received 24 March 2017

Received in revised form 13 May 2017

Accepted 5 June 2017

### Keywords:

Nanocomposite thin film

SHI irradiation

Transmission electron microscopy

Surface plasmon resonance

## ABSTRACT

In the present work, we study the annealing and swift heavy ion (SHI) beam induced modifications in the optical and structural properties of sandwiched structured Carbon-gold-Carbon (a-C/Au/a-C) nanocomposite (NCs) thin films. The NCs thin films were synthesized by electron-beam evaporation technique at room temperature with  $\sim 30$  nm thickness for both carbon layer and  $\sim 6$  nm for gold layer. Gold-carbon NCs thin films were annealed in the presence of argon at a temperature of 500 °C, 600 °C and 750 °C. The NCs thin films were also irradiated with 90 MeV Ni ions beam with different ion fluences in the range from  $3 \times 10^{12}$ ,  $6 \times 10^{12}$  and  $1 \times 10^{13}$  ions/cm<sup>2</sup>. Surface plasmon resonance (SPR) of Au nanoparticles are not observed in the pristine film but, after annealing at temperature of 600 °C and 750 °C, it was clearly seen at  $\sim 534$  nm as confirmed by UV-visible absorption spectroscopy. 90 MeV Ni irradiated thin film at the fluence of  $1 \times 10^{13}$  ions/cm<sup>2</sup> also show strong absorption band at  $\sim 534$  nm. The growth and size of Au nanoparticle for pristine and 90 MeV Ni ion irradiated thin film with fluence of  $1 \times 10^{13}$  ions/cm<sup>2</sup>, were estimated by Transmission electron microscopy (TEM) images with the bi-model distribution. The size of the gold nanoparticle (NPs) was found to be  $\sim 4.5$  nm for the pristine film and  $\sim 5.4$  nm for the irradiated film at a fluence of  $1 \times 10^{13}$  ions/cm<sup>2</sup>. The thickness and metal atomic fraction in carbon matrix were estimated by Rutherford backscattering spectroscopy (RBS). The effect of annealing as well as heavy ion irradiation on D and G band of carbon matrix were studied by Raman spectroscopy.

© 2017 Elsevier B.V. All rights reserved.

## 1. Introduction

Nowadays, carbon-based nanocomposite materials have attracted researcher due to their application in a diverse field like biosensors, nonlinear optical devices and optoelectronic devices [1–5]. Carbon nanotube, graphite, fullerene, amorphous carbon (a-C), diamond and graphene are the many forms of carbon which can exist in natural environment. The change in optical properties with the appearance of surface plasmon resonance (SPR) is very interesting, when novel metal particles such as Ag and Au embedded in an amorphous carbon matrix [6–7]. These metals are particularly significant because of their strongest SPR appears in the visible range of the electromagnetic spectrum. When electromagnetic light imposed on these nanoparticles, free conduction electron cloud of nanoparticles shows the strong absorption. When

the frequency of collective oscillations of free electron cloud of metal NPs resonant with frequency of incident photons, strong absorption band appears due to these NPs. This strong absorption is known as SPR band for noble metal NPs. SPR band for the NPs depends on many factors such as size and shape, spatial distribution and sensitive to dielectric properties of surrounding host medium (matrix) [8–9]. Gold NPs shows the strong absorption band in visible range which makes it more applicable in the different application like sensors, photonic devices and plasmonic [10–11]. When novel metal nanoparticles embedded in an oxide matrix such as SiO<sub>2</sub> and Al<sub>2</sub>O<sub>3</sub>, they exhibit good optical transparency in visible region [12] but the Problem of instability and rapid oxidation arises due to large surface-to-volume ratio for these matrix. Carbon-based matrixes are more fascinating due to its multifunctional properties in magnetism, electronics, optics and catalysis and also protect these novel metal nanoparticles against oxidation process [13–17]. Mechanical stability and biocompatibility are two important properties which show only in metal-carbon NCs thin

\* Corresponding author.

E-mail address: [singhshushant86@gmail.com](mailto:singhshushant86@gmail.com) (S.K. Singh).

films [18]. Therefore carbon based matrices are provided to shield these nanoparticles against oxidation with very low reactivity.

Annealing is a technique to enhance the structural and optical properties of nanocomposite materials, while the swift heavy ion irradiation is a unique tool to modify the optical and structural properties in a controlled manner [19–23]. When swift heavy ions (SHI) traverse through the target material, it interact with the electron as well nuclei of the target material and loose huge amount of energy by two main mechanisms as: (a) Inelastic collisions between incident ions and electron cloud of the target atoms (dominant in higher energy regime, specially case for SHI irradiation  $>1$  MeV/nucleon), designate as electronic energy loss ( $S_e$ ) and other (b) elastic scattering from the nuclei of the target atoms and incoming ions (dominant in lower energy regime from  $\sim$ few keV to 1 MeV/nucleon), designate as nuclear energy loss ( $S_n$ ). A large amount of energy deposited by incident ions is responsible for the atomic displacement along the beam path and described by two different models approach; (i) Coulomb spike model (CSM) and (ii) Thermal spike model (TSM). The large amount of energy transfers from SHI ions to target material during irradiation which is responsible coherent radial atomic movements with in ion track and leads to excitations/ionizations towards the track in very short time scale of  $10^{-17}$  sec. These movements are lead to modifications in the material such as defects and mixing under the Coulomb force and explained as CSM. On the other hand, when the atomic subsystem of the material attain the energy form electronic subsystem due to SHI irradiation by electron-phonon coupling (EPC) phenomena which leads to increasing local lattice-temperature rapidly up to  $10^4$  K (formed the thermal spikes) and quenched very fast (rate  $\sim 10^{14}$  K/s). This process is also responsible for modifications in the material and known as thermal spike model (TSM) [24–25]. In the case of SHI irradiation,  $S_e$  is more leading and depend on many factors such as charge, mass and energy of the incident ions. In this case, if the range of incident ions is larger in the comparison of the thickness of the material, so all incident ions passed from NCs thin film and buried into the substrate. Size and shape of NPs can be easily tuned with SHI irradiation with the significant way which is very much useful for different plasmonic applications.

In this paper, a systematized study of thermal annealing as well SHI irradiation induced modifications in structural and optical properties of a-C/Au/a-C NCs thin films have been carried out. Modifications in the properties are evaluated by different characterization techniques such as X-ray diffraction analysis, Transmission electron microscopy (TEM), UV-visible and Raman spectroscopy. Optical absorption of the Au nanoparticles was found at  $\sim 534$  nm in annealed NCs thin film, and it again observed by 90 MeV Ni ions beam irradiation in the same manner. The growth of the nanoparticles is subjected to SHI irradiation confirmed by Transmission electron microscopy.

## 2. Experimental details

a-C/Au/a-C NCs thin films with a thickness of  $\sim 66$  nm, were deposited on glass, quartz, and silicon substrate by using the electron-beam evaporation technique at room temperature. The substrate glass, quartz, and silicon were cleaned with trichloroethylene, acetone, and alcohol in a sequential manner before the deposition. The distance between source to substrate and source to quartz crystal was kept at  $\sim 23$  cm. During deposition, the vacuum inside the chamber was kept at  $\sim 8.5 \times 10^{-7}$  mbar with a deposition rate of 0.1–0.2 nm/s. for Au and 0.5–0.6 nm/s for amorphous carbon respectively. The sandwiched NCs structure of the gold-carbon film was prepared in three steps (i) first a carbon layer of about 30 nm was deposited (ii) a second layer of Au with a

thickness  $\sim 6$  nm and (iii) again a carbon layer of about  $\sim 30$  nm was deposited. The thickness of the individual layers was estimated by quartz crystal monitor during deposition and also confirm by Rutherford backscattering spectroscopy. Copper-grids (carbon coated) for TEM analysis were placed on the substrate holder before film deposition in the chamber. Only NCs thin films that were deposited on glass and carbon coated grid were irradiated with 90 MeV Ni ions using the 15 UD pelletron accelerator at Inter University Accelerator Centre (IUAC), New Delhi. The NCs thin films were mounted on the ladder (made of copper) in irradiation chamber with a high vacuum of the order of  $4 \times 10^{-6}$  mbar and scanned over the area  $1 \times 1$  cm<sup>2</sup>. Then films were irradiated with different fluences of  $3 \times 10^{12}$  ions/cm<sup>2</sup>,  $6 \times 10^{12}$  ions/cm<sup>2</sup> and  $1 \times 10^{13}$  ions/cm<sup>2</sup>. For the 90 MeV Ni ions irradiation, value of electronic ( $S_e$ ) and nuclear ( $S_n$ ) energy losses in gold-carbon thin film are estimated  $\sim 8.36 \times 10^2$  eV/Å and 1.5 eV/Å respectively and the range of Ni ions in a-C/Au/a-C NCs thin film is found to be  $\sim 15.53$   $\mu$ m as determined by Stopping and Range of ions in matter (SRIM) simulation program. The NCs thin films which deposited on quartz substrate used for annealing study and they were annealed 60 min in the presence of Ar atmosphere at a temperature of 500 °C, 600 °C and 750 °C.

Metal atomic fraction and film thickness were calculated by Rutherford backscattering spectroscopy (RBS) with 2 MeV He<sup>+</sup> ions performed at Pelletron Accelerator RBS-AMS System (PARAS) facility at Inter University Accelerator Centre, New Delhi. X-ray diffraction analysis was performed with Panalytical X-pert Pro diffractometer by using the Cu-K $\alpha$  X-ray source at Material Research Center (MRC) Jaipur. The UV-visible absorption spectra of the pristine, annealed and irradiated films were observed by dual-beam LAMBDA 750 (Perkin Elmer) UV-visible NIR spectrometer. TEM observations of the pristine and irradiated carbon-coated Cu grid were investigated by TecnaiG<sup>2</sup>20 (FEI) microscope, operated at 200 kV. Pristine, annealed and irradiated films were characterized by Raman spectrometer AIRIX STR 500 Raman microscope with laser excitation at 532 nm at room temperature.

## 3. Results

### 3.1. Rutherford backscattering spectroscopy

RBS spectrum of the pristine and annealed sandwiched structured a-C/Au/a-C nanocomposites has been shown in Fig. 1. Fig. 1 (a and b) indicate the RBS spectra with depth profile for the pristine film which was deposited on Si substrate and Fig. 1(c and d) for annealed thin film which was annealed at 750 °C for quartz substrate. The atomic concentration and thickness of the film were calculated by fitting the RBS experimental data with Rutherford Universal Manipulation Program (RUMP) [26]. The thickness of the pristine film was estimated to be  $\sim 70$  nm which agrees well with the thickness measured ( $\sim 66$  nm) during deposition by quartz crystal monitor. The presence of Au, and Carbon in pristine NCs thin film were confirmed by RBS spectrum and the metal (Au) atomic concentration was estimated to be  $\sim 1.3$  at% by RUMP simulation program. In a next step, these films were subjected to a thermal treatment at three different annealing temperature of 500 °C, 600 °C and 750 °C. The RBS spectra of the annealed films (at 750 °C) did not show the presence of Carbon while the atomic fraction of Au nanoparticles was observed below  $\sim 1.3$  at% which is showing in the Fig. 1(c and d). Instead a clear signature of Si and O was detected which confirms that the disappearance of carbon and diffusion of the Au nanoparticles into the substrate. Also depth profile measurements of the annealed film revealed no Au atomic fraction after the depth of about  $\sim 120$  nm.



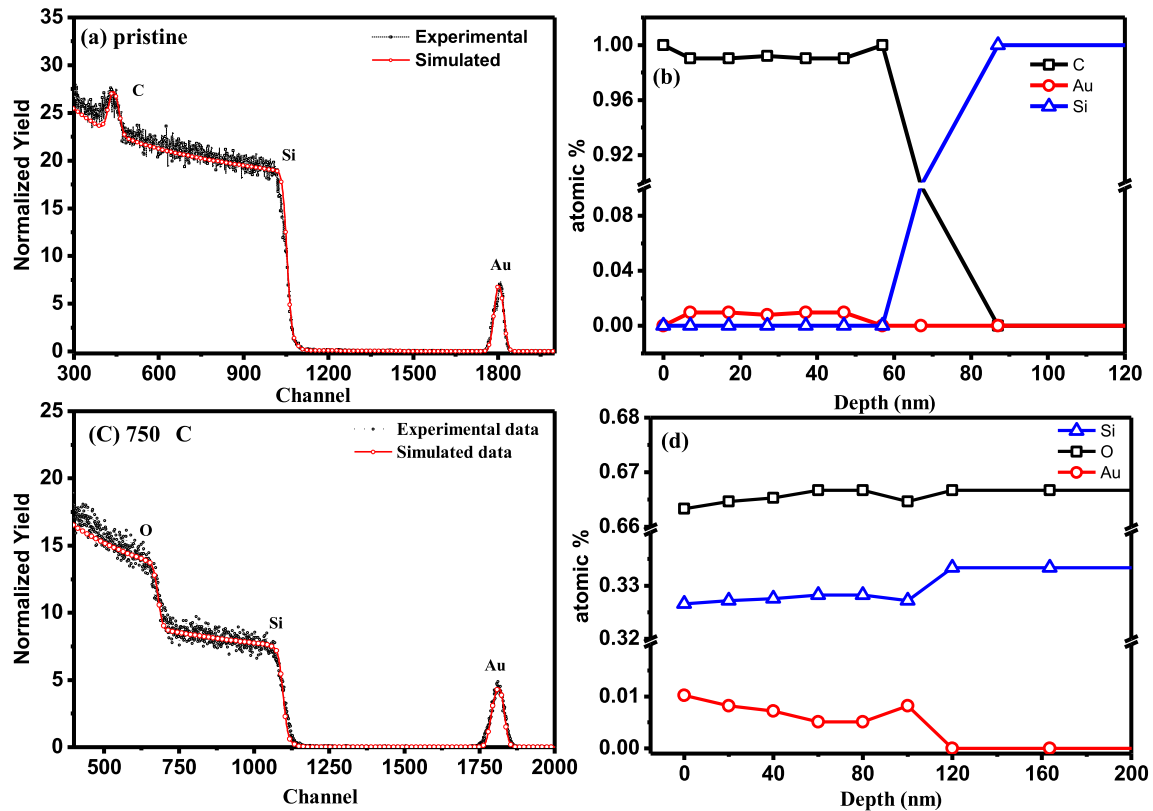


Fig. 1. Rutherford backscattering spectra and depth profile for the (a–b) pristine and (c–d) annealed a-C/Au/a-C nanocomposite thin film.

### 3.2. Transmission electron microscopy

Fig. 2(a and b) shows good high-resolution bright field images of the pristine and 90 MeV Ni ions irradiated a-C/Au/a-C NCs thin films respectively. The shape of Au nanoparticles is spherical which can be clearly seen in the TEM images (Fig. 2). The average size of the nanoparticles is  $\langle D \rangle = 4.5 \pm 0.1$  nm for the pristine films as estimated using a Gaussian size distribution function (Fig. 2 d). HRTEM image of Au nanoparticles shows the presence of cross lattice fringes which shows the crystalline quality of Au nanoparticles embedded in the amorphous carbon matrix. The  $d$ -spacing of Au nanoparticles can be measured and found to be 2.34 Å, which corresponds to the (111) reflection of a fcc crystal structure which shows in Fig. 2(c). The selected area electron diffraction pattern (SAED) of the pristine film is shown in Fig. 2(b) and confirms the poor crystallinity of the nanocomposites due to the absence of the ring patterns. When these films were irradiated at higher fluence ( $1 \times 10^{13}$  ions/cm<sup>2</sup>), growth of nanoparticles are observed, as can be seen in (see Fig. 3). Apparently, the average size of Au particles  $\langle D \rangle = 5.4 \pm 0.1$  nm, was slightly increased as compared with the pristine film. Furthermore, the SAED pattern showed the presence of sharp rings when irradiated at a fluence of  $1 \times 10^{13}$  ions/cm<sup>2</sup> (Fig. 3b). This clearly shows that the crystalline quality of Au nanoparticles can be significantly enhanced when subjected to a heavy ion irradiation process. The growth of Au nanoparticles in the carbon matrix is also confirmed by X-ray diffraction analysis. It was reported earlier that when high-energy ions pass through the material, they lose their energy into the film with a certain rate of incident energy per nm through the material. The loss in the electronic energy is mainly responsible for the high density of electronic excitation/ionization and structural changes in the target material [27]. The structural changes as observed in TEM images

after irradiation with a fluence of  $1 \times 10^{13}$  ions/cm<sup>2</sup>, such as increase in the particle size and the crystalline quality can be explained in the framework of the thermal spike model. For structures like Au-carbon nanocomposite films, Au is present in a form of nanoparticle with certain size and shape. However, it is likely that during ion irradiation apart of Au particles could be dissolved in the matrix as a solid solution. As a result the transient temperature of the nanocomposite materials increases rapidly around the ion path and form a latent track of deformed material due to rapid quenching process. During the formation of the latent track, Au nanoparticles and a-C matrix is also present in the transient molten state. The formation of bigger particles and diffusion of Au nanoparticles have occurred due to ion-induced diffusivity which is responsible for ripening of Au nanoparticles in latent track. The growth of NPs during the ion irradiation at higher irradiation doses depend significantly on the overlapping of the latent track which leads to agglomeration of Au nanoparticles due to enhance diffusivity around the ion path [18].

### 3.3. X-ray diffraction analysis

X-ray diffraction pattern of the pristine, irradiated ( $1 \times 10^{13}$  ions/cm<sup>2</sup>) and annealed (at 750 °C) a-C/Au/a-C NCs thin films have been shown in Fig. 4. There is no signature of Au peaks in the pristine films and films annealed at 750 °C. The reason of the peak disappearance is twofold: firstly, in case of pristine nanocomposites the presence of highly amount of carbon might suppress the Au peak and secondly, at sufficiently high temperatures it is more likely that Au nanoparticles diffuse into the carbon matrix, which results in a peak disappearance in the XRD data. In contrast, a-C/Au/a-C nanocomposites irradiated with a fluence of  $1 \times 10^{13}$  ions/cm<sup>2</sup> revealed the presence of (111) reflection of the Au crystal

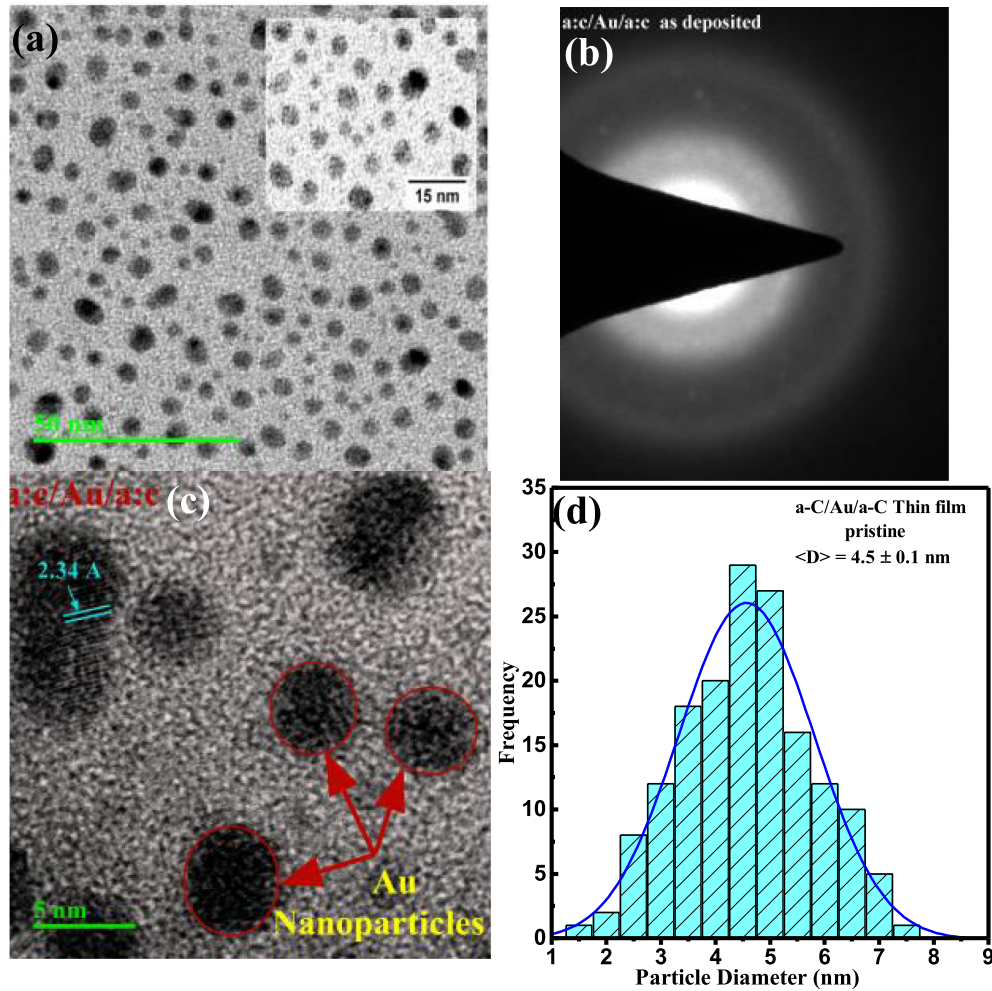


Fig. 2. (a–c) TEM image with SEAD pattern of pristine a-C/Au/a-C nanocomposite thin film and (d) particle size distribution.

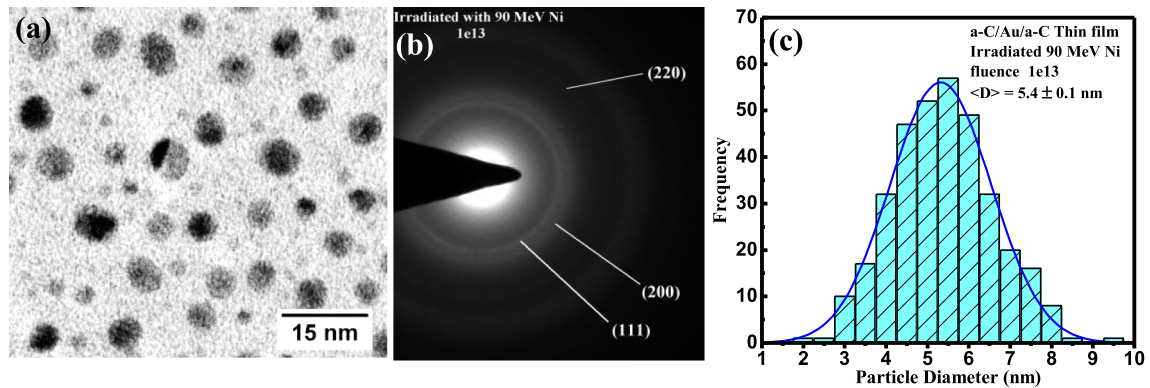


Fig. 3. (a–b) TEM image with SEAD pattern of irradiated thin film at fluence of  $1 \times 10^{13}$  ions/cm<sup>2</sup> and (c) particle size distribution.

structure. The particle size of Au nanoparticles at a fluence of  $1 \times 10^{13}$  ions/cm<sup>2</sup> was calculated by using Scherrer's formula [28] and found to be  $\sim 7.0$  nm, which agrees well with the observed TEM results. In summary, from XRD results we have shown that the ion irradiation is a very effective tool for improving the crystalline quality of the complex systems like a-C/Au/a-C nanocomposites thin film. In next section the presence of Au nanoparticles is also confirmed by UV–visible spectroscopy.

### 3.4. UV–visible spectroscopy

Fig. 5(a) shows the UV–visible absorption spectra of pristine and 90 MeV Ni ions irradiated a-C/Au/a-C NCs thin films with fluences of  $3 \times 10^{12}$ ,  $6 \times 10^{12}$  to  $1 \times 10^{13}$  ions/cm<sup>2</sup>, respectively. Fig. 5 (b) shows the absorption spectra obtained on the annealed a-C/Au/a-C nanocomposites films at temperatures of 500 °C, 600 °C and 750 °C respectively. There is no surface plasmon band was

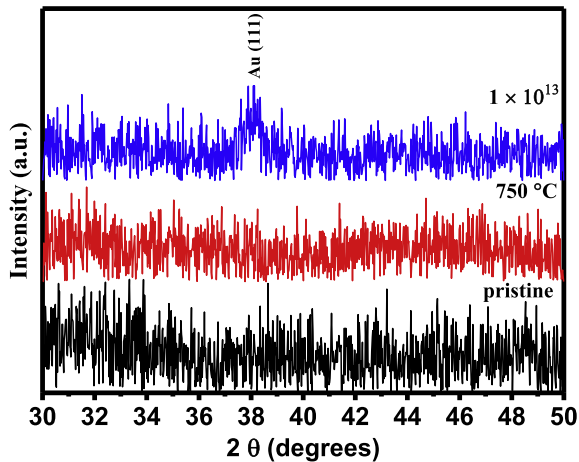


Fig. 4. X-ray diffraction spectra for the pristine, irradiated and annealed a-C/Au/a-C nanocomposite thin film.

observed for the pristine as well as irradiated thin films up to lower irradiation fluences. However, at higher fluences of  $1 \times 10^{13}$  ion/cm<sup>2</sup>, a clear peak at  $\sim 534$  nm wavelength was seen in the spectrum which is a unique characteristic (surface plasmon resonance) of the Au nanoparticles in carbon matrix. While in case of annealed films, there is no indication of surface plasmon peaks at 500 °C, but if the temperature increases from 500 °C to 600 °C, the absorbance of the film was drastically decreased with a good resonance at  $\sim 534$  nm (see fig 5 b). Similar results were observed on a-C/Au/a-C nanocomposites films annealed at even higher temperature of 750 °C. It is also evident that Carbon in the a-C/Au/a-C nanocomposites could be removed after the annealing process as confirmed by a large change in the absorbance spectra. The disappearance of the carbon at higher annealing temperature is also confirmed by RBS and Raman

spectroscopy. In this process, both the ion-induced annealing as well thermal annealing is responsible for the enhancement in the thermal energy of the carbon atoms. This would promote the reduction of carbon atom from the material.

### 3.5. Raman spectroscopy

Raman spectra of pristine and 90 MeV Ni ion irradiated a-C/Au/a-C NCs thin films with three different fluences of  $3 \times 10^{12}$ ,  $6 \times 10^{12}$  and  $1 \times 10^{13}$  ions/cm<sup>2</sup> have been shown in Fig. 6(a). Fig. 6(b) shows the comparison of Raman spectra of the pristine and annealed a-C/Au/a-C NCs thin films at three different annealing temperatures of 500 °C, 600 °C and 750 °C respectively. The spectra of the pristine film reveal the formation of D and G bands which are the characteristic of amorphous carbon structure with a significant degree of  $sp^2$  hybridization [29]. The position of D and G bands were found at  $\sim 1373$  cm<sup>-1</sup> and  $\sim 1544$  cm<sup>-1</sup> respectively. The spectra are fitted with Gaussian curves and the estimated parameters are summarized in Table 1 for irradiated and annealed NCs thin film. The FWHM of the D and G bands for the pristine films are 397.8 cm<sup>-1</sup> and 171.0 cm<sup>-1</sup>. When films were irradiated with 90 MeV Ni ions at different fluences, the FWHM of the D band decreases significantly as shown in Fig. 7. A similar trend was also found for the films annealed at different temperature while the position of G band shifted towards the higher wave number. The  $I(D)/I(G)$  ratio was calculated from the spectra and found the increment with increasing irradiation fluence as well annealing temperature. The  $I(D)/I(G)$  ratio of the pristine films was 1.6 but it changes drastically at 500 °C annealing temperature and increase up to 3.5. At the higher irradiation fluence of  $1 \times 10^{13}$  ions/cm<sup>2</sup> and higher temperatures of 600 °C and 750 °C, both D and G bands have been completely disappear, due to the absence of carbon in the thin films. These results clearly confirm that the disappearance of the carbon after ion irradiation especially at higher fluence as well higher annealing temperature.

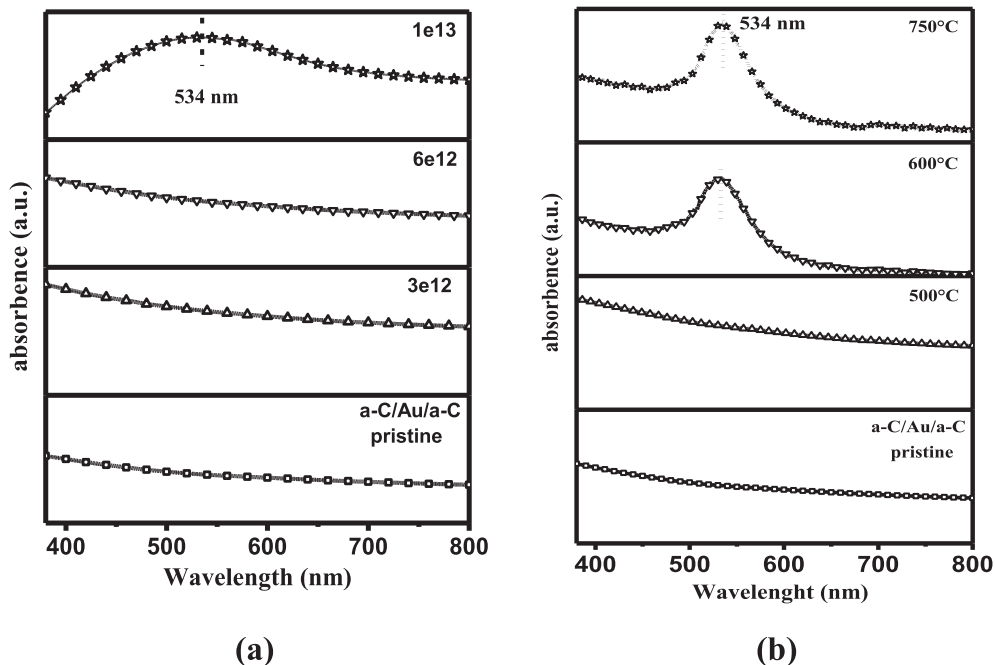


Fig. 5. UV-visible spectra for (a) irradiated and (b) annealed a-C/Au/a-C nanocomposite thin films.

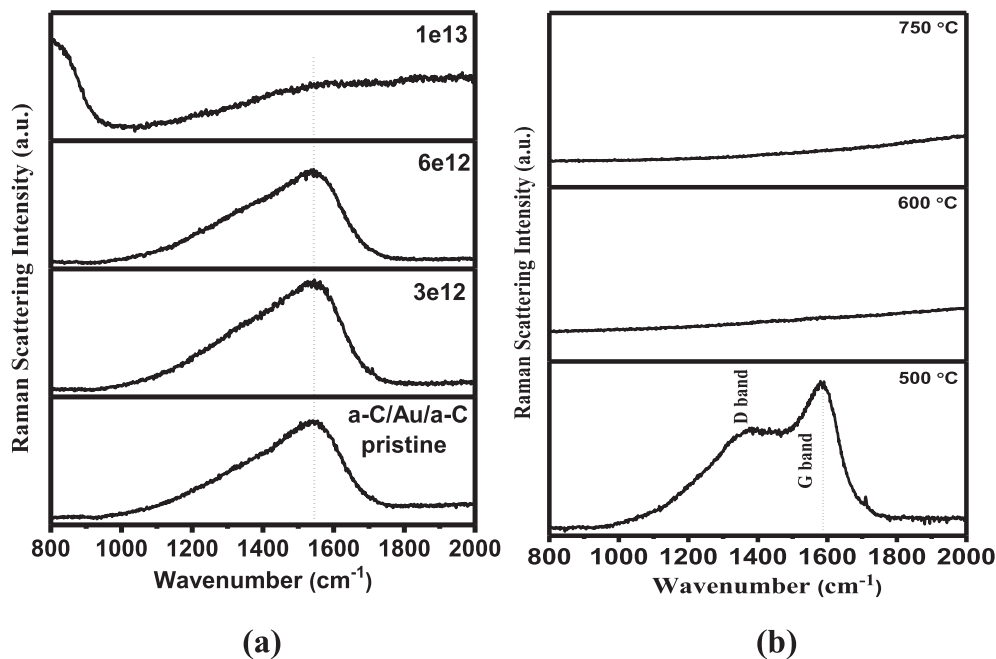


Fig. 6. Raman spectra for (a) irradiated and (b) annealed a-C/Au/a-C nanocomposite thin film.

Table 1

Sample detail	FWHM of D band (cm <sup>-1</sup> )	Position of G band (cm <sup>-1</sup> )	I(D)/I(G) ratio
Pristine	397.8	1544.6	1.6
$3 \times 10^{12}$ ions/cm <sup>2</sup>	364.6	1547.5	1.8
$6 \times 10^{12}$ ions/cm <sup>2</sup>	347.8	1551.7	1.9
500 °C annealed	397.8	1584.2	3.5

annealing as well SHI ion induce modification in optical and structural properties of the gold-carbon thin films have been investigated. The growth of gold nanoparticles was observed with SHI irradiation which can be explained in the terms of Thermal spike model during heavy ion irradiation. The strong absorption at  $\sim 534$  nm was observed at higher irradiation fluence and higher annealing temperature. The change in D and G band of the carbon is responsible for the matrix modifications by ion beam as well annealing which can be understood by Raman measurements.

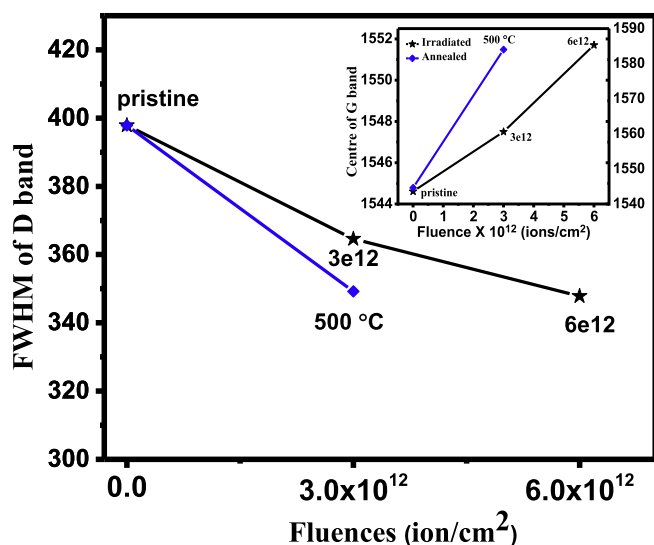


Fig. 7. Variation of FWHM of D band of the irradiated and annealed gold-carbon nanocomposite thin film. Inset figure shows the variation in center of G-band with irradiation and annealing.

#### 4. Conclusions

Sandwiched structured gold-carbon NCs thin films have been synthesized by electron beam deposition technique. Thermal

#### Acknowledgements

The author (S.K. Singh) would like to grateful for “Technical Education Quality Improvement Programme (TEQIP)”, MNIT Jaipur for a grant the financial assistantship for the research work. The authors gratefully acknowledge to Inter University Accelerator Centre (IUAC New Delhi - India) and thanks to the crew of IUAC pelletron group for providing stable beam during experiment. The authors are also thankful to the Materials Research Centre (MRC), MNIT Jaipur for providing the characterizations facility. One of the authors R. Singhal highly acknowledges the financial support provided by DST New Delhi (DST FAST young scientist project SR/FTP/PS-081/2011) and UGC New Delhi project in the term of IUAC New Delhi P.F. No. DRC-14/59/2013/10/169/00036.

#### References

- [1] H. Zhu, J. Wei, K. Wang, D. Wu, Sol. Energy Mater. Sol. Cells 93 (2009) 1461–1470.
- [2] A.M.M. Omer, S. Adhikari, S. Adhikary, H. Uchida, M. Umemo, Appl. Phys. Lett. 87 (2005) 161912.
- [3] D.K. Avasthi, Y.K. Mishra, R. Singhal, D. Kabiraj, S. Mohapatra, B. Mohanta, Nivedita K. Gohil, N. Singh, J. Nanosci. Nanotechnol. 10 (2010) 2705–2712.
- [4] S. Korchev, M.J. Bozack, B.L. Slaten, G. Mills, J. Am. Chem. Soc. 126 (2004) 10–11.
- [5] D.K. Avasthi, Y.K. Mishra, D. Kabiraj, N.P. Lalla, J.C. Pivin, Nanotechnology 18 (2007) 125604–125607.
- [6] J.D. Joannopoulos, P.R. Villeneuve, S. Fan, Nature 386 (1997) 143.
- [7] Z. Salamon, H.A. Macleod, T. Gordon, Biochim. Biophys. Acta 1331 (1997) 117.
- [8] R. Singhal, D.C. Agarwal, Y.K. Mishra, F. Singh, J.C. Pivin, R. Chandra, D.K. Avasthi, J. Phys. D Appl. Phys. 42 (2009) 155103.

- [9] U. Kreibig, M. Vollmer, *Optical Properties of Metal Clusters*, Springer Series in Materials Science, 1995.
- [10] T. Bhuvana, G.V.P. Kumar, C. Narayana, G.U. Kulkarni, *Nanotechnology* 18 (2007) 145702.
- [11] D.A. Schultz, *Curr. Opin. Biotechnol.* 14 (2003) 13–22.
- [12] M.D. Mchahon, R. Lopez, V. Meyer, L.C. Feldman, R.F. Haglund Jr., *Appl. Phys. B* 80 (2005) 915.
- [13] A. Sanchez, S. Abbet, U. Heiz, W.-D. Schneider, H. Hakkinen, R.N. Barnett, U. Landman, *J. Phys. Chem. A* 103 (1999) 9573.
- [14] R. Singhal, J.C. Pivin, D.K. Avasthi, *J. Nanopart. Res.* 15 (2013) 1641.
- [15] H.J. Fecht, *Europhys. News* 28 (1997) 89.
- [16] Y. Li, J.P. Tu, D.Q. Shi, X.H. Huang, H.M. Wu, Y.F. Yuan, X.B. Zhao, *J. Alloys Compd.* 436 (2007) 290.
- [17] F.R. Marciano, L.F. Bonetti, R.S. Pessoa, J.S. Marcuzzo, M. Massi, L.V. Santos, V. Trava-Airoldi, *Diamond Relat. Mater.* 17 (2008) 1674.
- [18] J. Robertson, *Phys. Rev. Lett.* 68 (1992) 220–223.
- [19] R. Singhal, D. Kabiraj, P.K. Kulriya, J.C. Pivin, R. Chandra, D.K. Avasthi, *Plasmonics* 8 (2013) 295.
- [20] R. Singhal, J.C. Pivin, R. Chandra, D.K. Avasthi, *Surf. Coat. Technol.* 229 (2013) 50–54.
- [21] A. Gupta, R. Singhal, J. Narayan, D.K. Avasthi, *J. Mater. Res.* 26 (2011) 2901–2906.
- [22] R. Singhal, D.C. Agarwal, Y.K. Mishra, F. Singh, J.C. Pivin, R. Chandra, D.K. Avasthi, *J. Appl. Phys. D* 42 (2009) 155103.
- [23] R. Singhal, D.C. Agarwal, S. Mohapatra, Y.K. Mishra, D. Kabiraj, F. Singh, D.K. Avasthi, A.K. Chawla, R. Chandra, G. Mattei, J.C. Pivin, *Appl. Phys. Lett.* 93 (2008) 103114.
- [24] S.K. Srivastava, D.K. Avasthi, W. Assmann, Z.G. Wang, H. Kucal, E. Jacquet, H.D. Carstanjen, M. Toulemonde, *Phys. Rev. B* 71 (2005) 193405.
- [25] W. Bolse, B. Schattat, *Nucl. Instr. Meth. Phys. Res. B* 190 (2002) 173–176.
- [26] M. Mayer, SIMNRA User's Guide, Technical Report IPP 9/113, Max Plank Institute of fur Plasmaphysik, Garching, Germany, 1997.
- [27] Florian. Banhart, *Rep. Prog. Phys.* 62 (1999) 1181.
- [28] B.D. Cullity, *Elements of X-Ray Diffraction*, Addison-Wesley, Reading, MA, 1970.
- [29] A.C. Ferrari, J. Robertson, *Phys. Rev. B* 61 (2000) 14095–14107.



## Study the Effect of Substrate on Thermally Evaporated PbS Thin Film

Sat Kumar<sup>1</sup>, Shushant Kumar Singh<sup>2</sup>, Rakesh Kumar<sup>3</sup>, Beer Pal Singh<sup>3</sup>

<sup>1</sup>Government Degree College, Nainidanda, Pauri Gharwal- 226277, Uttarakhand- India.

<sup>2</sup>Department of Physics, Malaviya National Institute of Technology Jaipur-302017, India.

<sup>3</sup>Department of Physics, Chaudhary Charan Singh University, Meerut 250004, India.

### Article history

Received: 24-Dec-2016

Revised: 02-Jan-2017

Available online: 23-Jan-2017

### Keywords:

Thin film,  
X-ray diffraction,  
Scanning electron  
microscopy (SEM),  
Atomic force microscopy  
(AFM)

### Abstract

In the present work, PbS thin films have been synthesized by thermal evaporation technique on two different types of substrate a) glass and b) ITO coated glass. PbS thin films were characterized by different characterization technique like X-ray diffraction (XRD), Scanning electron microscopy (SEM), Atomic force microscopy (AFM) and Energy dispersive analysis of X-rays (EDAX analysis). X-ray diffraction spectra of the film reveal higher crystallinity on ITO coated glass substrate in comparison of the film grown on a glass substrate. PbS thin films have been grown with good quality and more adhesion on the ITO coated glass as confirmed by scanning electron microscopy. The average roughness of the film is  $\sim 10$  nm for the film on ITO coated substrate and  $\sim 19$  nm for the film on a glass substrate as obtain by atomic force microscopy. The quality of the film is better with ITO coated substrate in comparison of glass substrate confirmed by different characterizations.

© 2017 JMSSE All rights reserved

### Introduction

Nowadays, the thin film science and technology playing a major role in the high-tech industries and different device fabrication area. In the recent years, thin film science has been grown worldwide into major research areas such as optoelectronic, solar cell and infrared detection application [1-3]. The thin film technology has been developed primarily for the need of the integrated circuits for many devices fabrication. Lead Sulphide (PbS) is relevant binary material which belongs to IV-VI semiconductor group material with direct narrow band gap ( $\sim 0.4$  eV at room temperature) and relatively large exciton Bohr radius ( $\sim 18$  nm)[4]. PbS thin films are advantageous in many fields like temperature sensors, photo resistance and solar absorption and also exhibit the semiconducting properties [5]. Its semiconducting behaviour plays a significant role in the development of detection system in which the infrared detectors were used. PbS thin film prosperous material for the infrared detector devices because it gives very good signal corresponds to incident photons by changing the detector element temperature [6-7], PbS thin films have also been employed for various application such as photo-resistance, diode lasers, temperature sensors, decorative and solar control coatings [8-10]. PbS thin film can be used in short-wavelength infrared application because it is sensitive material for the specific wavelength (1 to 2.5  $\mu\text{m}$ ) [11]. The properties of the PbS thin film can be easily controlled with the different film growth technique and different substrates. To tune the properties of the PbS thin film, many researchers have synthesized PbS thin film using various technique like electrodeposition, spray pyrolysis, photo accelerated chemical deposition, solid-vapor deposition, spin coating, microwave heating and thermal evaporation[12-18]. Thermal evaporation is a suitable technique to synthesize the PbS thin film because it gives high quality film with

homogeneous surface morphology and large area deposition which is very useful for device fabrication.

In the present paper, PbS thin films were synthesized by thermal evaporation technique at room temperature. The effect of the substrate on the characteristic of the deposited films is studied in present work. From the structural and surface morphology analysis, it is found that the film deposited on the ITO coated glass is of good quality.

### Experimental

Thin films of lead sulphide (PbS) have been synthesized by the thermal vacuum deposited technique at room temperature. Lead sulphide powder of AR grade (sigma Aldrich) was used to evaporate in deep-mouthed molybdenum boat. Highly cleaned glass and ITO coated glass substrates were used as substrate for the film deposition. Prior to a deposition, the glass and ITO coated glass substrates were cleaned in aquaregia, acetone, washed in distilled water and isopropyl alcohol (IPA). After loading the substrate into the deposition chamber they were thermally cleaned by keeping them at an elevated temperature 200°C for few minutes. The deposition is carried out in a vacuum of the order of  $10^{-5}$  torr with constant current for homogeneous film deposition. PbS thin films have been characterized by different characterization technique such as X-Ray diffraction, Scanning electron microscopy, Atomic force microscopy, EDX analysis. Structural analysis has been estimated by X-ray diffractometer (Bruker D8-Advance model) with  $2\theta$  ranging from  $10^\circ$  to  $90^\circ$  with step size  $0.02^\circ$  and step time 0.5 second. Surface morphology of the film has been confirmed by Scanning electron microscope (ZIESS microscope with 5 kV energy) and Atomic force microscope.

## Results and Discussion

### X-ray measurements

The XRD pattern of the PbS thin film on different substrate is shown in Figure 1. It shows different diffraction peaks at  $2\theta$  values of  $26.28^\circ$ ,  $30.39^\circ$ ,  $43.47^\circ$  and  $51.49^\circ$  which were assigned to the Monoclinic and cubic phase produced by (111), (200), (220) and (311) reflection planes respectively of PbS thin film. The dominant and sharp peak at  $30.39^\circ$  indicates that PbS nanocrystals are highly polycrystalline in monoclinic phase. The ITO coated glass provides a better crystalline surface for deposition of PbS films than glass, this is reflected and well define and sharp peak in XRD of PbS films deposited on ITO coated glass while the crystallinity of films deposited glass is not so good. The calculation of particle size of PbS thin films has been calculated using Debye-Scherrer formula using (200) plane from the XRD spectra [19].

$$D = \frac{0.9\lambda}{\beta \cos\theta} \quad (1)$$

In expression (1),  $\lambda$ ,  $\beta$ , and  $\theta$  are X-ray wavelength ( $\text{CuK}\alpha = 1.54\text{\AA}$ ), full width at half maximum (FWHM) and the Bragg diffraction angle respectively. The calculated size is found to be  $\sim 22$  nm for glass and  $\sim 27$  nm for ITO. The higher crystallite size of the film indicates the higher crystallinity of the film.

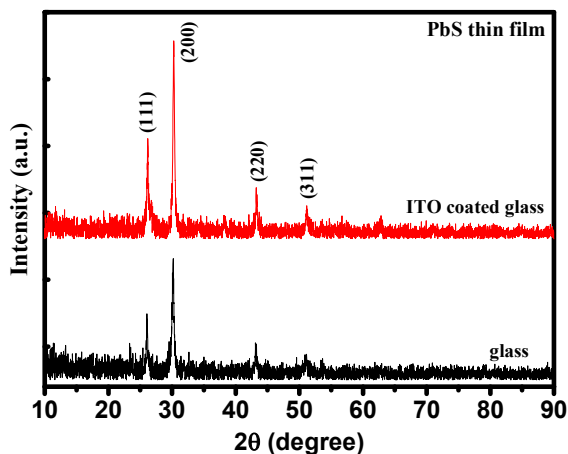
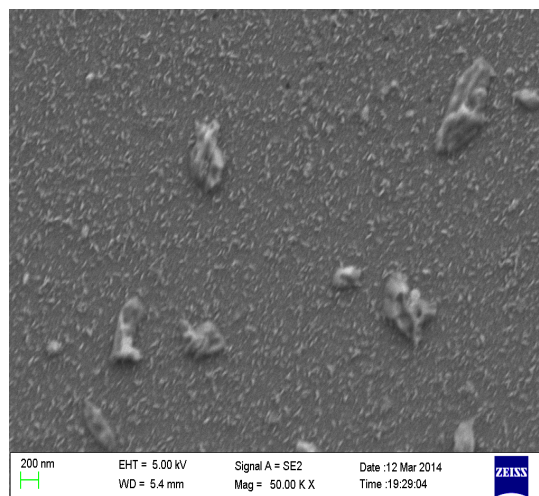


**Figure 1:** XRD spectra of PbS thin films on glass and ITO coated glass substrate.

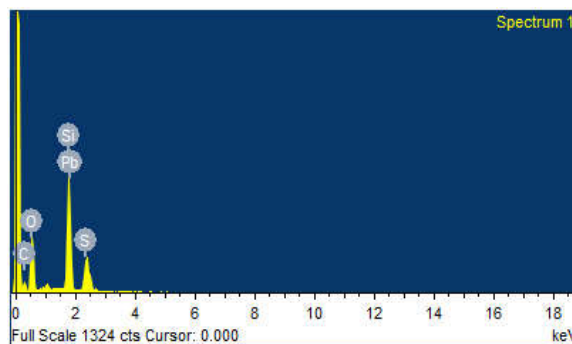
### Scanning electron microscopy

The SEM micrograph of polycrystalline PbS thin films at 200nm magnification deposited on both the substrates are shown in Fig. 2(a,b). PbS thin films have a uniform surface morphology with more adhesion over the ITO coated glass substrate rather than the glass substrate. The films deposited on ITO coated glass have fine grains and have good quality in comparison to the glass substrate. The SEM images show that the better surface is achieved on ITO coated glass comparison to the plane glass substrate.

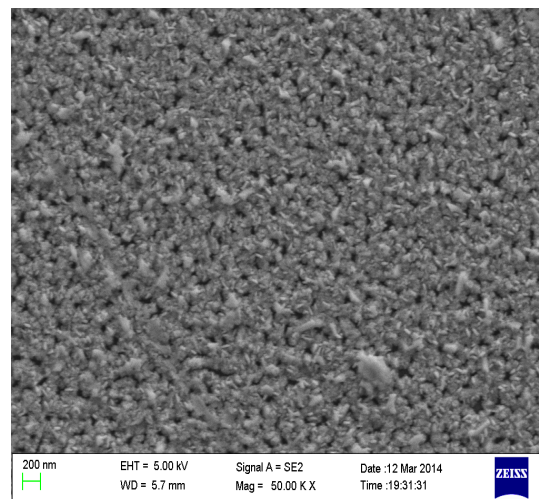
The EDAX Fig. 2(c,d) spectra revealed that the Pb:S ratio varied randomly. This may be due to the surface roughness effect as well as the presence of some intrinsic defects within the films (pores, etc.), which have some effects during the chemical analysis: the incident electron beam interact only with a particular portion of the film (spot analysis), thereby will not give the overall and the average chemical composition of the entire thin film. The EDAX ratio shows that films deposited on ITO glass substrate have good stoichiometry in comparison to the plane glass substrate.



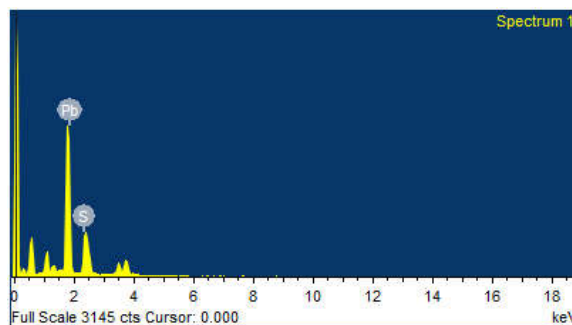
(a)



(b)



(c)



(d)

**Figure 2:** SEM Micrograph with EDX analysis of PbS Thin films Deposited on (a,b) Glass and (c,d) ITO Glass Substrate.

### Atomic force microscopy

Atomic force microscopy (AFM) micrographs of the vacuum evaporated PbS thin films which were deposited on glass and ITO coated glass substrate are shown in figure 4 (a, b c and d). All the AFM images were taken for an area of  $2 \times 2 \mu\text{m}$  orders show that the particles are closely packed. The AFM images of the PbS thin film revealed that the grains are more spherical in shape and are homogeneously distributed over the whole surface in comparison to the PbS film deposited on ITO coated glass substrate. The average roughness of PbS films deposited ITO coated glass and ordinary glass comes out 9.93 nm and 18.5 nm respectively. PbS film on ITO glass show cluster of particles with highly dense structure with high packing density and have advanced surface and typical columnar structure with highly dense grains. These results shows that the better crystalline and surface morphology of PbS thin films is achieved on ITO coated glass substrate which provides the better crystalline surface to deposited crystalline films.

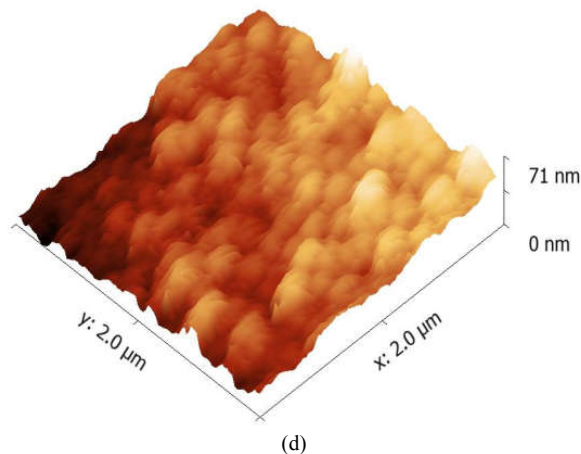
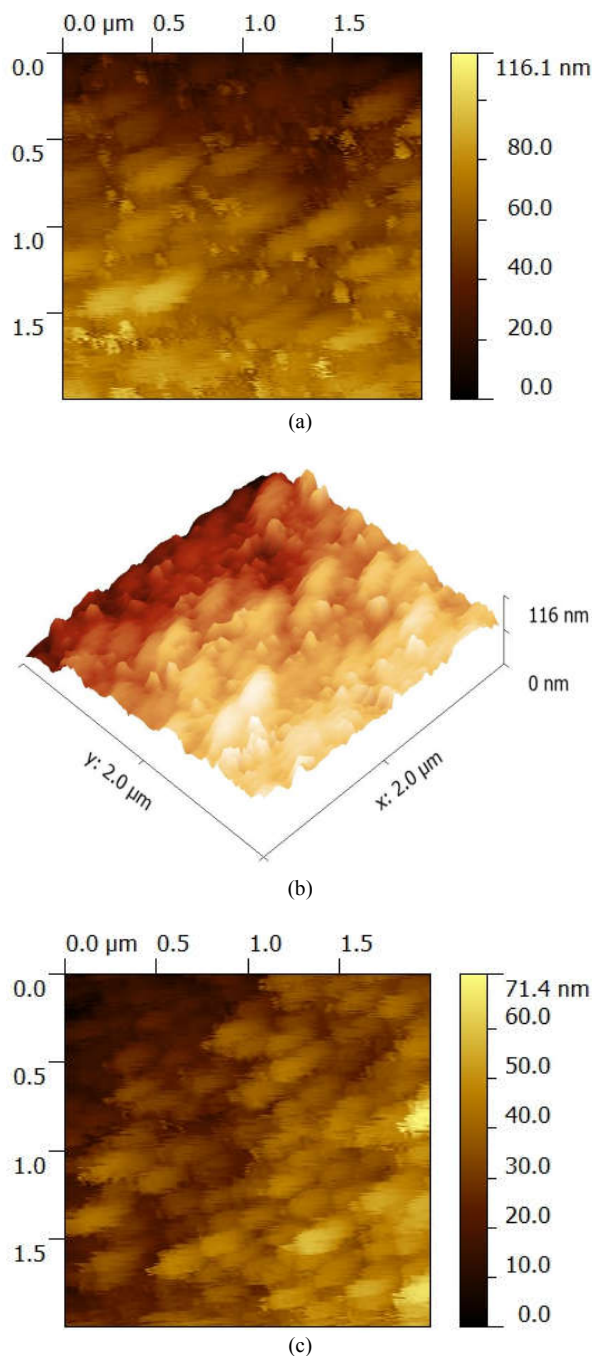


**Figure 3:** AFM micrograph of the PbS thin film (a,b) glass substrate; (c,d) ITO coated glass substrate.

### Conclusions

PbS thin films have been synthesized by thermal evaporation technique at room temperature. EDX analysis conforms the formation of PbS thin film. The crystallinity of the film is much better on ITO coated glass in comparison of plane glass substrate. Surface morphology of the films has been investigated by scanning electron microscopy and atomic force microscopy. The roughness of the film is lower for the ITO coated glass substrate while in high for plane glass substrate. From the structural analysis, we can conclude that ITO coated glass substrate is better for the film growth because the film has a good crystallinity and more adhesion on the ITO coated glass substrate by thermal evaporation. EDAX measurements of the film confirmed the present stoichiometric compound in the film.

### Acknowledgment

The author would like to thank Nano-materials lab, Dept. of Physics, C.C.S University, Meerut for providing the synthesis facility and IIT Roorkee for providing the characterization facility. Author is very much thankful to lab colleagues Gyanendra Panchal and Anuj Kumar for their help in this work.

### References

1. S. Seghaier, N. Kamoun, R. Brini, A.B. Amara Materials Chemistry and Physics 97 (2006) 71–80
2. Shushant Kumar Singh, Himanshu Sharma, R. Singhal, V. V. Siva Kumar, and D. K. Avasthi, AIP Conference Proceedings 1731, 080063 (2016); doi: 10.1063/1.4947941.
3. Maheshwar Sharon, K.S. Ramaiah, Mukul Kumar, M. NeumannSpallart, C. Levy-Clement, Electroanal. Chem. 436 (1997) 49–52.
4. J.L. Machol, F.W. Wise, R.C. Patel, D.B. Tanner Phys. Rev. B, 48 (1993), p. 2819.
5. S.A. McDonald, G. Konstantatos, S. Zhang, P.W. Cyr, E.J.D. Klem, L. Levina, E.H. Sargent Nat. Mater., 4 (2005), pp. 138–142
6. P. Gadenne, Y. Yagil, G. Deutscher, J. Appl. Phys. 66 (1989) 3019.
7. S. Jing, S. Xing, Y. Wang, H. Hu, B. Zhao, C. Zhao Mater. Lett., 62 (2008), p. 977
8. P.K. Nair, V.M. Garcia, A.B. Hernandez, M.T.S. Nair J. Phys. D: Appl. Phys., 24 (1991), pp. 1466–1472.
9. Ileana Pop, Cristina Nascu, VioletaIonescu, E. Indrea, I. Bratu Thin Solid Films, 307 (1997), pp. 240–244.
10. S. Kacia, A. Keffous, S. Hakoum, M. Trari, O. Mansri, H. MenariAppl. Surf. Sci., 305 (2014), pp. 740–746.
11. P. Gadenne, Y. Yagil, G. Deutsche J. Appl. Phys., 66 (1989), p. 3019



12. Maheshwar Sharon, K.S. Ramaiah, Mukul Kumar, M. NeumannSpallart, C. Levy-Clement, *Electroanal. Chem.* 436 (1997) 49–52.
13. Rakesh K. Joshi, AlopeKanjilal, H.K. Sehgal, *Appl. Surf. Sci.* 221 (2004) 43–47.
14. Thangaraju B, Kaliannan P (2000) *SemicondSci Tech* 15:849.
15. S. Kumar, T.P. Sharma, M. Zulfequar, M. Husain *Physica B*, 325 (2003), pp. 8-16
16. Yu Zhao, Xue-Hong Liao, Jian-Min Hong, Jun-Jie Zhu, *Mater. Chem. Phys.* 87 (2004) 149–153.
17. R. Das, Rajesh Kumar, *Materials Research Bulletin* 47 (2012) 239–246.
18. Sushil Kumar, T.P. Sharma, M. Zulfequar, M. Husain, *Physica B* 325 (2003) 8–16.
19. B.D. Cullity, *Elements of X-Ray Diffraction*, Addison-Wesley, Reading, MA, (1970).



## Bio-data

### **Shushant Kumar Singh**

M. Sc., M. Phil., Ph. D.

Department of Physics,

Malaviya National Institute of Technology Jaipur

JLN Marg, Malaviya Nagar, Jaipur- 302017 (Rajasthan)

Mob:- 9528412700, 9694462109

Email: [singhshushant86@gmail.com](mailto:singhshushant86@gmail.com), [2013rph9001@mnit.ac.in](mailto:2013rph9001@mnit.ac.in)



=====

### Carrier Objective:

Seeking a position in the academic/research field related to impart the learning of fundamental & applied physics and material sciences.

### Detail of Educational Qualifications:

Exam	Board/ University	Division	Year of passing	Percentage (%/CGPI*)	Subjects
B.Sc.	M.J.P Rohilkhand University, Bareilly	First	2008	64.44	Physics, Chemistry, Mathematics
M.Sc.	C.C.S University, Meerut	First	2011	79.22	Physics
M.Phil.	C.C.S University, Meerut	Second	2014	57.75	Physics
Ph.D.	Malaviya National Institute of Technology Jaipur-(Raj.)	First	2019	8.22	Physics (Nanocomposite thin films)

### Research Carrier:

- **Ph.D. (Physics)**

Thesis title: “*Synthesis, characterization and modifications of nanocomposite thin films*”

Supervisor: Dr. Rahul Singhal, Asst. Prof., Malaviya National Institute of Technology Jaipur.

- **M.Phil. (Physics)**

Thesis title: “*Synthesis and characterization of cerium oxide (CeO<sub>2</sub>) for fuel cell*”.

Supervisor: Prof. Beer Pal Singh, Head, Department of Physics, C.C.S University Meerut (U.P.).

### **Experimental Skills:**

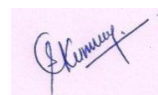
- **Synthesis area:** Thermal evaporation, E-beam evaporation, RF-magnetron sputtering, Spin-coating thin film deposition.
- **Software's and languages:** Origin 8.0, Digital micrograph analysis for TEM, Nano-scope analysis, WSxM solution, X-pert high-score, SRIM-TRIM simulation program, RUMP, SIMNRA, Casa-XPS, Image J, Crystal sleuth, C and C<sup>++</sup>, Fortran 77.
- **Characterization techniques:** Rutherford backscattering spectroscopy (RBS), Transmission electron microscopy (TEM), X-ray photoelectron spectroscopy (XPS), X-ray diffraction spectroscopy (XRD), UV-Visible spectroscopy, Atomic force microscopy (AFM), Scanning electron microscopy (SEM), Raman Spectroscopy, Electrical measurements, Photo-luminance spectroscopy (PL).

### **Teaching experience:**

- Working as a visiting faculty for teaching Applied Physics to B.Sc. (Computer Science) at Department of Professionals Courses, Meerut College Meerut (Affiliated form C.C.S. University Meerut) during 2011-12 session.

### **Personal Particulars:**

**Name:** Shushant Kumar Singh (S.K Singh)  
**Date of Birth:** 01-March-1988  
**Father's Name:** Mr. Ramesh Kumar Singh  
**Mother's Name:** Mrs. Saroj Singh  
**Marital Status:** Unmarried  
**Nationally:** Indian  
**Permanent Address:** Shushant Kumar Singh  
Vill + Post- Dilari,  
Dist. – Moradabad  
State- Uttar Pradesh (India)  
Pin- 244401.



**(Shushant Kumar Singh)**